GOETHE
UNIVERSITÄT
FRANKFURT AM MAIN

Signal integration by the ER-stress sensors Ire1 and PERK

Dissertation

Zur Erlangung des Doktorgrades

der Naturwissenschaften

vorgelegt beim Fachbereich Biochemie, Chemie und Pharmazie

der Johann Wolfgang Goethe-Universität

in Frankfurt am Main

von

Kristina Väth

aus Hanau

Frankfurt, 2020

(D30)

Vom Fachbereich Biochemie, Chemie und Pharmazie der

Johann Wolfgang Goethe-Universität als Dissertation angenommen.

Dekan: Prof. Dr. Clemens Glaubitz

Gutachter: 1. Prof. Dr. Robert Ernst

2. Prof. Dr. Martin Grininger

Datum der Disputation:

Teile der vorliegenden Arbeit wurden in folgenden Publikationen zusammengefasst:

Halbleib, K., **Pesek, K.**, Covino, R., Hofbauer, H.F., Wunnicke, D., Hänelt, I., Hummer, G., and Ernst, R. (2017). Activation of the unfolded protein response by lipid bilayer stress. Mol. Cell 6*7*, 673-684.

Cohen, N., Breker, M., Bakunts, A., **Pesek, K.**, Chas, A., Argemí, J., Orsi, A., Gal, L., Chuartzman, S., Wigelman, Y., Jonas, F., Walter, P., Ernst, R., Aragón, T., van Anken, E., and Schuldiner, M. (2017). Iron affects Ire1 clustering propensity and the amplitude of endoplasmic reticulum stress signaling. J Cell Sci. *130*, 3222-3233.

Radanovic, T., Reinhard, J., Ballweg, S., **Pesek, K.**, and Ernst, R. (2018). An emerging group of membrane property sensors controls the physical state of organellar membranes to maintain their identity. BioEssays *40*, 1-9.

Väth, K., Covino, R., Reinhard, J., Mattes, C., Stumpf, H., Hummer, G., and Ernst, R. Systematic cysteine-crosslinking in native environments establishes the transmembrane architecture in Ire1 clusters. (*in revision*)

Väth, K.,* Mattes, C.,* Reinhard, J.,* and Ernst, R. Cellular lipid composition during acute ER-stress" (*in preparation)* (*equal first)

Für meine Familie

Index

Declaration

Except where stated otherwise by references or acknowledgements, the work presented in this thesis was generated by myself under the supervision of my advisor during my doctoral studies. All contributions from colleagues are explicitly referenced in the thesis.

The data listed below were obtained in the context of collaborative research:

Figure 28: MD simulations of the TMH of Ire1 were performed by Dr. Roberto Covino from the Gerhard Hummer group (MPI of Biophysics, Frankfurt).

Figure 31B: The CPY/CPY* binding assay using $^{MBP}Ire1_{cLD\text{-}AH\text{-}TMH}$ reconstituted in EPL:DPPL was performed by Susanne Wolf during her bachelor thesis under my supervision.

Figure 40C,D: SEC experiments with $^{MBP}PERK_{AH\text{-}TMH}$ were performed by Julian Bruckert during his bachelor thesis under my supervision.

Figure 42: The replicates 2 and 3 of the cwEPR experiments of $^{MBP}PERK_{AH\text{-}TMH}$ WT were performed by Iryna Stasiuk during her master thesis under my supervision.

Figure 43: The replicates 2 and 3 of the cwEPR experiments of $^{MBP}PERK_{AH\text{-}TMH}$ WT and the spin-labeled controls were performed by Iryna Stasiuk during her master thesis under my supervision.

Figure 47: MD simulations of the TMH of Ire1 and PERK were performed by Dr. Roberto Covino from the Gerhard Hummer group (MPI of Biophysics, Frankfurt).

Whenever a figure, table or text is identical to a previous publication, it is stated explicitly in the thesis.

List of Figures

List of Tables

List of Abbreviations

aa	amino acid
AEBSF	4-(2-Aminoethyl)benzensulfonylfluorid
Agar	Agar agar
AH	Amphipathic helix
ATF4	Activation transcription factor 4
ATF6	Activating transcription factor 6
BiP	binding protein
bp	base pairs
$CaCl_2$	Calcium chloride
Chol	Cholesterol
CSM	Complete supplement mixture
$CuSO_4$	Copper(II)-sulfate
dNTP	Desoxyribonucleotide triphosphate
DMSO	Dimetylsulfoxid
DOPC	1,2-Dioleoyl-*sn*-glycero-3-phosphocholine
DPPC	1,2-Dipalmitoyl-*sn*-glycero-3-phosphocholine
DTT	Dithiothreitol
E. coli	*Escherichia coli*
EDTA	Ethyldiaminetetraacetic acid
eIF2	Eukaryotic initiation factor 2α
EPL	*E. coli* polar lipids
ER	Endoplasmic reticulum
ERAD	ER-associated degradation
Fwd	forward
HCl	Hydrochloric acid
HEPES	4-(2-hydroxyethyl)-1-piperazineethanesulfonic acid
GFP	Green fluorescent protein
GPI	Glycerolphosphatidylinositol
GPL	Glycerolphospholipids
IF	Interface
IPTG	Isopropyl- β-D-thiogalactopyranosid
Ire1	Inositol requiring enzyme 1
IRE1α	Inositol requiring enzyme 1 – alpha
KAc	Potassium acetate
KCl	Potassium chloride
kDa	Kilo Dalton
LiAc	Lithium acetate
MD	Molecular dynamic
$MgCl_2$	Magnesium chloride
$MgSO_4$	Magnesium sulfate
MHC-I	Major-histocompatibility complex I

$MnCl_2$	Mangan(II)-chloride
NaCl	Sodium chloride
Na_2CO_3	Sodium carbonate
NAFLD	non-alcoholic fatty liver disease
NaH_2PO_4	Sodium di-hydrogen phosphate
Na_2HPO_4	*di*-Sodium hydrogen phosphate
NaN_3	Sodium azide
NaOH	Sodium hydroxide
$(NH_4)_2SO_4$	Ammonium sulfate
NEM	N-ethylmaleimide
β-OG	β-Octylglucopyranoside
PA	Phosphatidic acid
PBS	Phosphate buffered saline
PC	Phosphatidylcholine
PCR	Polymerase chain reaction
PE	Phosphatidylethanolamine
PEG	Polyethylene glycol
PERK	Protein kinase-like ER kinase
PG	Phosphatidylglycerol
PI	Phosphatidylinositol
PIC	Protease inhibitor cocktail
PIPES	Piperazine-N,N'-bis(2-ethanesulfonic acid
PM	Plasma membrane
POPC	1-Palmitoyl-2-oleoyl-*sn*-glycero-3-phosphocholine
POPE	1- Palmitoyl-2-oleoyl-*sn*-glycero-3-phosphoethanolamine
PS	Phosphatidylserine
rev	reverse
RIDD	Regulated Ire1-depedent decay
RT-qPCR	Real time quantitative PCR
S. cerevisiae	*Saccharomyces cerevisiae*
SDS	Sodium dodecyl sulfate
SL	Sphingolipids
Soy-PI	L-α-phosphatidylinositol (Soy)
TM	Tunicamycin
TMD	Transmembrane domain
TMH	Transmembrane helix
Tris	Tris(hydroxymethyl)-aminomethan
UPR	Unfolded protein response
w/v	Weight per volume
v/v	Volume per volume
YNB	Yeast nitrogen base
XBP1	X box-binding protein 1

Zusammenfassung

Alle Zellen sind von einer biologischen Membran umgeben, die eine zweidimensionale Flüssigkeit aus Proteinen und Lipiden darstellt. Eukaryotische Zellen sind durch biologische Membranen zusätzlich in verschiedene Kompartimente (sogenannte Organelle) unterteilt, die spezifische Bedingungen bereitstellen und biochemische Prozesse voneinander trennen. Die Membranen dieser Organellen benötigen eine spezifische Lipid- und Proteinzusammensetzung, um sowohl ihre Aufgaben zu erfüllen als auch um ihre Identität zu bestimmen. Aufgrund der höheren molaren Abundanz der Lipide werden die kollektiven physiochemischen Eigenschaften der Membranen wie zum Beispiel ihr Phasenverhalten, die Packungsdichte der Lipide, sowie die Oberflächenladung der Membranen zu einem großen Anteil durch die Lipidzusammensetzung bestimmt. Im Gegensatz zur Proteinzusammensetzung kann die Lipidzusammensetzung sehr viel dynamischer reguliert werden. Lipide spielen daher eine zentrale Rolle in der lebenswichtigen Adaption von Membraneigenschaften auf äußere Reize. Entlang des sekretorischen Weges, dem Transportweg für sekretorische Proteinen, gibt es charakteristische Änderungen der Membranzusammensetzung und der daraus resultierenden kollektiven Eigenschaften der Zellorganellen. Für die Funktionalität von Membranproteinen, die durch die Eigenschaften der Membranumgebung auf vielfältige Weise beeinflusst werden, ist eine strikte Regulation der Membranzusammensetzung von zentraler Bedeutung.

Das Endoplasmatische Retikulum (ER) ist in der Regel das größte Organell einer eukaryotischen Zelle. Sein kontinuierliches Membrannetzwerk macht häufig mehr als die Hälfte der gesamten Membranmasse aus. Im Vergleich zur Plasmamembran ist die ER-Membran dünner und leichter verformbar. Als das zentrale Organell für die Lipidbiosynthese und die Faltung von sekretorischen und Membranproteinen, stellt das ER den Startpunkt des sekretorischen Weges dar. Die hohe Verformbarkeit der ER-Membran ermöglicht so die Insertion und Faltung von Membranproteinen, die sich in ihrer hydrophoben Dicke deutlich unterscheiden können. Die Faltung von Membran- und sekretorischen Proteinen wird durch Faltungshelfer, sogenannte Chaperone, unterstützt. Nur korrekt gefaltete Proteine können das ER verlassen und entlang des sekretorischen Weges zu ihrem Zielort in der Zelle transportiert werden. Fehlgefaltete Proteine werden im ER zurückgehalten, um entweder weitere Faltungsversuche zu durchlaufen oder – wenn diese erfolglos verlaufen – durch die ER-assoziierten Degradationsmaschinerie (ERAD) abgebaut zu werden. In der Gesamtheit werden diese Prozesse als die Protein-Qualitätskontrolle des ER bezeichnet. Wenn die Proteinfaltungskapazität des ERs überschritten wird und ungefaltete Proteine im Lumen des ERs akkumulieren, kann sie durch die Aktivierung der *unfolded protein response* (UPR) angepasst werden. Die UPR ist in allen bekannten eukaryotischen Zellen konserviert und

umfasst unter anderem ein breit angelegtes Transkriptionsprogramm, welches die Faltungskapazität des ERs erhöht und für die Homöostase der Proteinproduktion und Proteinfaltung von zentraler Bedeutung ist. In der Tat werden über fünf Prozent aller Gene im Genom des Hefepilz *Saccharomyces cerevisiae* (*S. cerevisiae*) durch die UPR reguliert – einschließlich einer Vielzahl an Genen, die für Faltungshelfer (Chaperone), Oxidoreduktasen und Komponenten der ERAD-Maschinerie sowie für Enzyme des Lipidmetabolismus kodieren. Eine dauerhafte Aktivierung der UPR kann in höheren Eukaryoten zum programmierten Zelltod (Apoptose) führen. Bezeichnenderweise ist eine chronische Aktivierung der UPR stark mit metabolischen Erkrankungen wie Typ II Diabetes oder der Nicht-alkoholischen Lebererkrankungen (*non-alcoholic fatty liver disease,* NAFLD) assoziiert.

Die UPR in der Bäckerhefe wird durch ein einziges Transmembranprotein im ER, das *inositol requiring enzyme 1* (Ire1), ausgelöst. Die Domänenstruktur und die grundlegenden Mechanismen seiner Aktivierung sind von der Hefe bis zum Menschen konserviert. Ire1 liegt im inaktiven Zustand als Monomer vor und interagiert mit dem ER-Chaperon Kar2 der Bäckerhefe oder dem *binding protein* (BiP) im Menschen. Gemäß kontrovers diskutierten Modellen dissoziiert Kar2 bei der Aktivierung von Ire1, sodass ungefaltete Proteine direkt an die ER-luminale Domäne von Ire1 binden können und dessen Oligomerisierung induzieren können. Diese Aktivierung führt zur Bildung von mikroskopisch sichtbaren, langlebigen Oligomeren von Ire1, die über spezifische Kontaktflächen innerhalb der luminalen und zytosolischen Domänen stabilisiert werden. Die Oligomerisierung führt zur Aktivierung der zytosolischen Domänen von Ire1 und somit zu einer Trans-Autophosphorylierung der Kinase-Domäne und zur Aktivierung der RNase Domäne. Diese schneidet hoch-spezifisch die mRNA von *HAC1* und vermittelt gemeinsam mit der tRNA Ligase Rlg1 ein unkonventionelles, zytosolisches Spleißen als Voraussetzung für die effektive Bildung des Proteins Hac1, dem zentralen Transkriptionsfaktor der UPR. In Säugerzellen beinhaltet die IRE1-vermittelte UPR nicht nur ein hoch-spezifisches Spleißen der mRNA von XBP1, dem funktionellen Homolog von Hac1 in der Bäckerhefe, sondern auch einen unspezifischen Abbau einer Vielzahl von mRNAs (*regulated IRE1 dependent decay of mRNA* (RIDD)). Dies vermindert die Syntheseleistung der Ribosomen und in Folge dessen auch die Faltungslast des ERs. Neben IRE1 existieren in Säugerzellen zwei weitere Sensorproteine der UPR: die *protein kinase (PRK)-like ER kinase* (PERK) und der *activating transcription factor* (ATF6). Ähnlich wie IRE1 wird auch PERK durch eine Oligomerisierung von einem inaktiven Zustand in einen aktiven Zustand überführt. Aktiviertes PERK phosphoryliert mit Hilfe seiner zytosolischen Kinase Domäne den eukaryotischen Initiationsfaktors 2 (eIF2) und vermindert somit global die Proteinbiosynthese durch Inhibition der Translationsinitiation. Gleichzeitig wird selektiv die Produktion des Transkriptionsfaktors ATF4 durch PERK erhöht, wodurch wiederum eine Vielzahl von UPR-Zielgenen reguliert werden. Das Sensorprotein ATF6 wird im Gegensatz zu

IRE1 und PERK nicht durch eine Oligomerisierung aktiviert. Laut gegenwärtigen Modellen liegt ATF6 im inaktiven Zustand als Dimer vor und wird zur Aktivierung als Monomer zum Golgi transportiert. Dort wird es proteolytisch prozessiert und als aktiver Transkriptionsfaktor zur Regulation von UPR-Zielgenen freigesetzt.

In den letzten Jahren zeigte sich, dass die UPR nicht nur auf fehlgefaltete Proteine reagiert, sondern auch auf verschiedenste, fehlerhafte Zusammensetzungen der ER-Membran. Zusammenfassend wird diese Form des ER-Stresses als *lipid bilayer stress* bezeichnet. Die Membran-vermittelte Aktivierung der UPR wurde für Ire1 aus der Bäckerhefe aufgeklärt und basiert auf einer ungewöhnlichen Architektur des Transmembranbereiches von Ire1. Die Transmembranhelix (TMH) ist relativ kurz und besitzt an ihrem N-Terminus eine ausgeprägte amphipathische Helix (AH). Dieser ungewöhnliche Aufbau der TMH Region führt zu einer „Quetschung“ der Membran (verminderte Membrandicke), was energetisch ungünstig ist. In einer ungestressten, überaus weichen ER-Membran sind die energetischen Kosten für diese Membranquetschung zu vernachlässigen. Eine Versteifung der Membran durch Veränderungen der Lipidzusammensetzung (z.B. ein erhöhter Anteil gesättigter Lipide) führen zu einer substantiellen Erhöhung dieser energetischen Kosten. Durch eine Oligomerisierung von Ire1 und eine damit verbundene Verschmelzung der gequetschten Membranbereiche können die Kosten allerdings minimiert werden. Die Quetschung der ER-Membran durch den ungewöhnlichen Transmembranbereich von Ire1 bildet somit die Grundlage für die Membran-vermittelte Aktivierung der UPR in der Bäckerhefe.

Der erste Teil dieser Doktorarbeit fokussiert sich auf die Oligomerisierung von Ire1. Es wurde untersucht, ob unterschiedliche Formen des ER-Stresses – proteotoxischer Stress und *lipid bilayer stress* – zu strukturellen Änderungen im Bereich der Transmembrandomäne (TMD) von Ire1 führen, um so möglicherweise die Oligomerisierung beeinflussen. Eine besondere Herausforderung bestand darin, die Architektur der TMD in ihrem natürlichen Kontext, also in Clustern von Ire1 und in der hochkomplexen Umgebung der ER-Membran zu etablieren. Als klassischer Ansatz diente dabei ein systematisches Cystein-vermitteltes *crosslinking* im Transmembranbereich. Als Voraussetzung wurde zunächst ein Cystein-loses Konstrukt von *IRE1* etabliert und funktional charakterisiert. Durch zielgerichtete Mutagenese wurden insgesamt zwölf Cysteine aus Ire1 durch Serine ersetzt. Die volle Funktionalität dieses Konstruktes wurde mittels sensitiver, Zell-basierten Assays validiert. Dabei wurde die zelluläre Resistenz gegenüber ER-Stress, der durch das Reduktionsmittel DTT ausgelöst wird, bestimmt. Zusätzlich zeigten Analysen mittels qPCR, dass die mRNA von *HAC1* durch die Zugabe von DTT und Tunicymycin (ein Inhibitor der N-Glykosylierung) durch ein Cystein-loses Ire1 gespleißt wird. Somit war die Funktionalität der Cystein-losen Variante von Ire1 bestätigt. Durch ein gezieltes Einbringen einzelner Cysteine in das ansonsten Cystein-lose Konstrukt,

wurde der Transmembranbereich von Ire1 systematisch mutiert. Mit Hilfe eines zu diesem Zweck etablierten *crosslinking*-Protokolls konnte im Anschluss die Anordnung benachbarter TMHs von Ire1 in Clustern charakterisiert werden. Dazu wurde zunächst die Bildung von Ire1-Clustern in Zellen mittels DTT und Tunicamycin oder durch Inositol-Depletion ausgelöst. Frühere Studien haben belegt, dass Inositol-Depletion *lipid bilayer stress* induziert, ohne eine Fehlfaltung von Proteinen auszulösen. Eine auffällig hohe Reaktivität zeigte hierbei die F544C Variante. In der Gesamtheit deuten die *crosslinking* Experimente daraufhin, dass der Rest F544 an einem Punkt lokalisiert ist, an dem sich zwei überaus schräg in der Membran liegenden TMHs von Ire1 kreuzen. Darüber hinaus deuten die Ergebnisse an, dass die Architektur im Transmembranberiech unabhängig von der Form des ER-Stresses ist. Es konnte also eine große strukturelle Veränderung von Ire1 im Transmembranbereich durch die verschiedenen Formen des ER-Stresses ausgeschlossen werden. Die N-Terminal der TMH gelegene AH spielt bei der Stabilisierung dieser TMH Architektur eine entscheidende Rolle. Molekulardynamische (MD) Simulationen, die in Zusammenarbeit mit Dr. Roberto Covino aus der Arbeitsgruppe von Gerhard Hummer (MPI für Biophysik, Frankfurt) durchgeführt wurden, halfen dabei die gewonnen Ergebnisse strukturell zu interpretieren.

Im zweiten Teil dieser Arbeit wurde untersucht, inwieweit ungefaltete Proteine und *lipid bilayer stress* sich gegenseitig bei der Aktivierung von Ire1 beeinflussen. Dazu sollte in einem vollständig definierten *in vitro* System getestet werden, ob die Lipidzusammensetzung der Membran einen Einfluss auf die Interaktion von Ire1 mit fehlgefalteten Proteinen hat. Hierzu wurde ein Fusionsprotein aus dem Maltosebindeprotein (MBP), der ER-luminalen Domäne und des Transmembranbereichs von Ire1 aus *S. cerevisiae* kloniert und heterolog in *Escherichia coli* (*E. coli*) hergestellt. Das Fusionsprotein wurde anschließend isoliert und in Liposomen mit verschiedenen Lipidkompositionen rekonstituiert. Die Bindung von fehlgefalteten Proteinen an Ire1 wurde mittels einer fehlgefalteten Variante der Carboxypeptidase Y (CPY) aus *S. cerevisiae* untersucht. Die Mutation G255R führt zur Fehlfaltung von CPY und das resultierende Protein wird als CPY* bezeichnet. CPY* kann unter denaturierenden Bedingungen gereinigt werden und aufgrund der Mutation nur teilweise rückgefaltet werden. Um den Einfluss der Membranumgebung auf die Bindung von CPY* an Ire1 zu untersuchen, wurde Ire1 in Lipsomen mit definierten Lipidzusammensetzungen rekonstituiert. Bindungsstudien im Dichtegradienten belegten, dass CPY* besser an das Ire1-basierte Fusionsprotein bindet, wenn die Lipidumgebung erhöhte Packungsdichten und insbesondere einen erhöhten PE-Gehalt aufwies. Diese Bindung konnte spezifisch auf das Fusionsprotein zurückgeführt werden, da eine Bindung von CPY* an leere Liposomen nicht erfolgte. Als weitere Kontrolle diente ein Konstrukt aus MBP und der AH und TMH von Ire1 ($^{MBP}Ire1_{AH\text{-}TMH}$). Weil das $^{MBP}Ire1_{AH\text{-}TMH}$ Konstrukt eine signifikante, aber dennoch verminderte Bindung an CPY* aufwies, scheint ein Teil der Bindung von CPY* an MBP zu erfolgen. Darüber

hinaus konnte eine Modulation der Bindung durch die Membranumgebung beobachtet und auf den ungewöhnlichen Transmembranbereich von Ire1 zurückgeführt werden. Die hier gewonnen Daten lassen den Schluss zu, dass die veränderte Bindung von CPY* durch die Membranumgebung moduliert wird und belegen ein beeindruckendes, regulatorisches Potential der Membranzusammensetzung. *Continous wave* Elektronenspinresonanz (cwEPR) Studien mit einem Methanothiosulfonat-Spinlabel (MTS-SL) markierten $^{MBP}Ire1_{AH\text{-}TMH}$ bestätigten, dass der ungewöhnliche Transmembranbereich von Ire1 ein PE-abhängiges Oligomerisieren vermitteln kann. Somit konnte in dieser Arbeit ein Zusammenspiel zwischen *lipid bilayer stress* und proteotoxischem Stress aufgezeigt werden. Die präsentierten Ergebnisse deuten darauf hin, dass die vermehrte Bindung von CPY* an Ire1 auf unterschiedliche Oligomerisierungszustände und somit auf Aviditätseffekte zurückzuführen ist. Anhand dieser Ergebnisse aus kontrollierten *in vitro* Experimenten ließ sich zum ersten Mal ein direktes Zusammenspiel zwischen Proteinfaltungsstress und *lipid bilayer stress* zeigen.

Der dritte Teil dieser Arbeit behandelt die Frage, inwieweit der Mechanismus der Membran-vermittelten Aktivierung konserviert ist. Bioinformatische Analysen legen nahe, dass auch das Sensorprotein PERK des Menschen einen ungewöhnlichen Transmembranbereich besitzt. Gemäß diesen Vorhersagen besitzt PERK eine überaus kurze TMH mit einer ausgeprägten, N-terminalen AH (vergleichbar mit dem Transmembranbereich von Ire1 aus der Bäckerhefe). Vergleichend wurde daher die Membran-vermittelte Oligomerisierung von PERK charakterisiert. Zunächst wurde ein auf PERK-basierendes Fusionsprotein konstruiert, das aus dem MBP sowie der AH und TMH des humanen PERK besteht ($^{MBP}PERK_{AH\text{-}TMH}$). Während der Reinigung wurde das Protein am nativ vorkommenden Cystein 532 (C532) in der TMH von PERK mit MTS-SL markiert und anschließend in Lipsomen mit unterschiedlich dicht packenden Lipidzusammensetzungen rekonstituiert. In cwEPR Analysen konnte eine Membran-abhängige Verbreiterung des Spektrums beobachtet werden, was auf eine Oligomerisierung (vermutlich Dimerisierung) des PERK-basierten Sensors zurückzuführen ist. Dies lässt den Schluss zu, dass der Mechanismus der Membran-vermittelten Aktivierung von der Hefe bis zum Menschen konserviert ist. Um eine zentrale Rolle der AH von PERK in der Membran-vermittelten Oligomerisierung zu etablieren, wurde diese systematisch mutiert. Überraschenderweise hatte eine Zerstörung des amphipathischen Charakters der AH durch Einführung geladener Reste auf der nicht-polaren Seite keinen Einfluss auf die Membran-vermittelte Dimerisierung. Interessanterweise führte allerdings der Austausch negativ geladener Reste auf der hydrophilen Seite der AH von PERK (D514 E525) zu veränderten cwEPR Spektren, was auf eine verminderte Membransensitivität dieser Sensorvarianten schließen lässt. Diese Ergebnisse legen nahe, dass die Membran-vermittelte Aktivierung von PERK – ähnlich wie bei Ire1 aus der Bäckerhefe – auf der besonderen Architektur des Transmembranbereichs liegt. Es werden weitere Studien nötig sein, um genau zu verstehen,

inwieweit die Membran-vermittelte Aktivierung von PERK auf spezifischen Interaktionen zwischen der hydrophilen Seite der AH und Lipidkopfgruppen beruht.

Diese Arbeit hat zentrale Fragen zur Aktivierung der UPR behandelt und liefert mindestens drei wichtige Ergebnisse: 1) Verschiedene Formen des ER-Stresses konvergieren in einer einzigen Architektur des Transmembranbereichs. Es liegt daher nahe, dass die UPR eine einzige Antwort auf verschiedene Formen des ER-Stresses darstellt. 2) Die Bindung von ungefalteten Proteinen an Ire1 wird dramatisch durch die Lipidzusammensetzung der Membranumgebung moduliert. 3) Die Membran-vermittelte Aktivierung der UPR und der zugrundeliegende Mechanismus sind von der Hefe bis zum Menschen mit signifikanten Unterschieden im Detail konserviert.

Die Erkenntnisse dieser Arbeit bilden den Grundstein für einen neuen Blickwickel auf die UPR und verstärkt die Wichtigkeit der Membran-vermittelten Aktivierung der UPR.

1 Summary

Eukaryotic cells separate biological processes in organelles with specific cellular and biochemical functions. Each organellar membrane has a characteristic lipid and protein composition, which has to be tightly controlled in order to maintain its identity and to fulfill its organelle-specific tasks. The endoplasmic reticulum (ER) marks the entry point to the secretory pathway as the transportation path for membrane proteins and soluble, secretory proteins. The ER membrane is a rather thin and very deformable membrane, which is characterized by loosely packed lipids. The deformability of the ER membrane is important for the insertion of membrane proteins into the ER membrane despite featuring rather distinct hydrophobic lengths in the transmembrane regions. The ER plays a central role for the protein quality control of secretory and membrane proteins. The folding process of these proteins is assisted by chaperones in the ER lumen. Correctly folded proteins can leave the ER in vesicular carriers, while misfolded proteins are retained in the ER until they are correctly folded or retrotranslocated into the cytosol for a terminal degradation via the ER-associated degradation (ERAD) pathway. If the folding capacity of the ER lumen is exceeded, unfolded proteins accumulate. This condition is generally referred to as ER-stress. The unfolded protein response (UPR) is a conserved pathway to counteract ER-stress by a wide-spread transcriptional program. More than 5% of all genes in the baker's yeast *Saccharomyces cerevisiae* (*S. cerevisiae*) are under the control of the UPR. These genes encode e.g. for ER-luminal chaperones or oxidoreductases, components of the ERAD pathway, and proteins involved in lipid metabolism. If the adaptive response fails to restore proteostasis, the homeostasis of protein production and folding, the UPR can activate apoptotic pathways in higher eukaryotes. Given its crucial importance in cellular physiology, it is not surprising that the UPR has been implicated in complex metabolic diseases such as type II diabetes and the non-alcoholic fatty liver disease (NAFLD).

In *S. cerevisiae*, the inositol-requiring enzyme 1 (Ire1) is the only UPR sensor. Its mechanism of activation is conserved from yeast to man. In an inactive state, Ire1 is monomeric and associated with the major ER-chaperone Kar2, the homolog of the human binding protein BiP. According to currently discussed models, the accumulation of unfolded proteins causes Kar2 dissociation. Unfolded proteins then interact directly with Ire1 and induce its oligomerization. The oligomerization of Ire1 leads to the activation of its cytosolic effector domains: trans-autophosphorylation of the kinase domain and activation of the RNase domain mediates and unconventional splicing of the *HAC1* mRNA. Splicing of the *HAC1* mRNA allows the production of the active transcription factor Hac1 leading to the upregulation of UPR target genes. An unconventional splicing occurs also in mammalian cells. Here, the mRNA of XBP1 is spliced and the mature transcription factor XBP1 controls the transcriptional arm of the UPR. Clustered

and active IRE1 in mammals also mediates an unspecific degradation of various mRNAs thereby reducing the load of the ER with unfolded proteins. Furthermore, mammalian cells use at least two more branches of the UPR defined by the upstream sensor proteins: One of these branches is mediated by the protein kinase (PRK)-like ER kinase (PERK), the other one by the activating transcription factor (ATF6). Very much alike IRE1, the activation of PERK is caused by a dimerization of the protein. The active kinase domain of PERK phosphorylates the eukaryotic initiation factor 2 (eIF2) and counteracts ER-stress by inhibiting the initiation of translation by cytosolic ribosomes. Furthermore, activated PERK up-regulates the expression of the transcription factor ATF4 regulating the expression of UPR target genes. According to current models, ATF6 relocalizes in a monomeric form to the Golgi, where it is activated by a proteolytic release by the Golgi-specific Site-1 and Site-2 proteases. In the last decade, it became evident that the UPR can also be activated by aberrant ER lipid compositions. All aberrant composition of the ER membrane leading to UPR activation, are referred to as lipid bilayer stress. The molecular mechanism of UPR activation by lipid bilayer stress was recently described in baker's yeast. The mechanism relies on an amphipathic helix (AH) adjacent to and overlapping with the transmembrane helix (TMH) of Ire1. This unusual architecture was proposed to induce a local compression of the ER membrane, which is accompanied by lipid acyl chain disordering. The compression and acyl chain disordering come at energetic costs, which are not very substantial in the unstressed, loosely packed and deformable ER membrane. However, any aberrant stiffening of the ER membrane during lipid bilayer stress, causes these energetic costs to increase. The membrane environment thus provides a driving force for the oligomerization of Ire1 because it allows for a coalescence of the squeezed membrane regions.

The first part of this thesis focusses on a central aspect of UPR activation: the oligomerization. The architecture of Ire1's TMH in signaling-active clusters was analyzed using single-cysteine crosslinking of the full-length Ire1 from baker's yeast. A functional cysteine-less variant was established and analyzed by functionality tests. ER-stress was induced by a treatment with the reducing agent DTT and Tunicamycin, an inhibitor of N-glycosylation. A procedure to induce crosslinking of single-cysteine variants in the native ER-derived membranes was established. The $CuSO_4$ mediated crosslinking was combined with a single-cysteine scan along the TMH to identify interfacial residues in signaling-active clusters of Ire1. The F544C variant exhibited the highest crosslinking efficiency irrespective of the nature of ER-stress. The crosslinks were observed, when cells were stressed either by DTT, Tunicamycin, or inositol-depletion, a condition of lipid bilayer stress. A systematic scanning along the entire TMH revealed an almost identical crosslinking pattern for all types of ER-stress and suggested an X-shaped conformation of the TMH region in signaling-active clusters of Ire1. Additional mutational studies revealed that this architecture is crucially stabilized by the AH of Ire1. Molecular

dynamics (MD) simulations of the transmembrane region of Ire1 performed by Dr. Roberto Covino (Hummer group, MPI for Biophysics, Frankfurt) provided a visualization of this extreme X-shaped configuration with F544 located at the crossing point of the two helices.

The UPR can be activated either by proteotoxic stress or by lipid bilayer stress. It is unclear whether these forms of ER-stress act independently or not. In the second part of this thesis, I studied the impact of the membrane lipid composition on the binding of misfolded proteins to Ire1. To this end, an *in vitro* binding assay and a new minimal construct of Ire1 was established. It was comprised of the maltose binding protein (MBP), the core ER-luminal domain of Ire1, its Kar2 binding site and its transmembrane region with the functionally important AH and the TMH. The fusion protein $^{MBP}Ire1_{cLD\text{-}AH\text{-}TMH}$ was heterologously produced in *Escherichia coli* (*E. coli*), isolated and reconstituted in liposomes of defined lipid compositions. The binding of the misfolded protein (CPY*) to Ire1 was analyzed and compared to the binding of the folded CPY. CPY*, but not the folded CPY, was found to bind to $^{MBP}Ire1_{cLD\text{-}AH\text{-}TMH}$. Strikingly, an increased binding of CPY* to the fusion protein was observed, at increased packing densities of lipids induced either by saturated lipids, cholesterol or PE content. These findings highlight a modulation of the binding of CPY* to Ire1 by the membrane environment. The construct $^{MBP}Ire1_{AH\text{-}TMH}$ that lacks the ER-luminal domain of Ire1 served as a control in these experiments. Even though, some binding of CPY* to this construct remained (suggesting a significant degree of interaction between MBP and CPY*), it became evident that the membrane lipid composition has a remarkable potential to tune the binding of misfolded (and potentially unfolded) proteins to a transmembrane receptor protein such as Ire1. Additional continuous wave electron paramagnetic resonance (cwEPR) experiments using $^{MBP}Ire1_{AH\text{-}TMH}$ revealed a PE-dependent dimerization of this construct. Together, these observations suggest that the membrane-dependent modulation of CPY* binding relies on the AH and TMH of Ire1. It can be speculated that different oligomeric states of Ire1 might increase the apparent affinity to misfolded proteins. While more work has to be done to reveal the underlying mechanism, it is clear that lipid bilayer and proteotoxic stress may be highly interdependent processes in cells, which cannot be entirely understood by genetic perturbation experiments.

The third part of this thesis focusses on a possible conservation of the membrane-based activation of the UPR. The TMH region of the human PERK was analyzed for its role in the activation of the UPR. Here, cwEPR was used to analyze the membrane-based dimerization of PERK. A construct consisting of the MBP as a solubility tag and the AH and TMH of PERK was designed, produced in *E. coli* and then isolated and spin-labeled at residue C532. The construct was reconstituted in various liposomes differing in lipid packing. The membrane-dependent oligomerization of $^{MBP}PERK_{AH\text{-}TMH}$ was then characterized by cwEPR. The predicted AH of PERK was mutagenized in order to identify a role of this AH in PERK oligomerization.

Intriguingly, the mutation of negatively charged residues (D514 E525) in the polar face of the AH reduced the response of PERK to increased lipid packing. These data strongly suggested that the membrane-based activation of PERK relies – similar to Ire1 from baker's yeast - on an unusual architecture of the TMH region.

In summary, this thesis focused on three central question in the field of the UPR and provided important insights into principles underlying signal integration by the ER-stress sensors: 1) Different ER-stress types converge in a single architecture of the TMH. This suggests that the UPR may provide only a single answer to distinct forms of ER-stress. 2) The binding of misfolded proteins to Ire1 can be drastically modulated by the lipid composition of the ER membrane. 3) The membrane-based UPR activation are conserved from yeast to man, despite significant differences in the employed mechanisms of membrane sensing.

2 Introduction

2.1 The complexity of biological membranes

The spontaneous self-assembly of lipids via the hydrophobic effect is the physical basis for the formation of biological membranes. Cellular membranes provide a diffusion barrier for polar solutes (Holthuis and Menon, 2014; van Meer et al., 2008; Singer and Nicolson, 1972). This property is one of the central hallmarks of life and a prerequisite for the formation of cells. Membranes separate the intracellular milieu from the external environment. Eukaryotic cells are further compartmentalized by intracellular organelles, which also are surrounded by biological membranes thereby separating specific processes and pathways from each other (Holthuis and Menon, 2014).

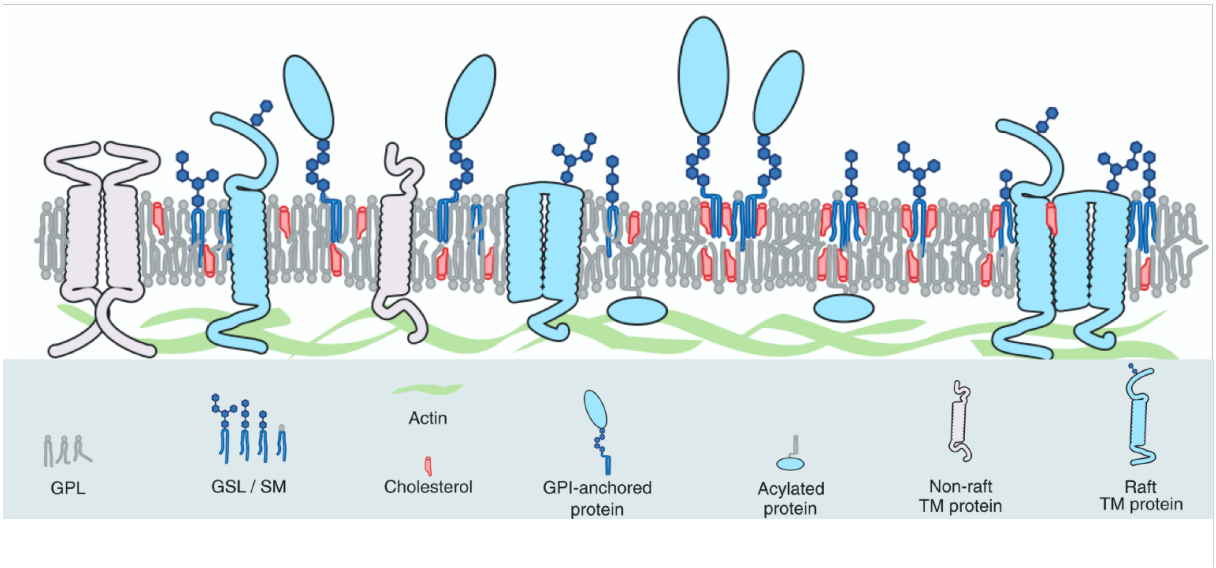

Figure 1: Model of a cellular membrane.

Biological membranes can be described by the fluid mosaic membrane model, first proposed in 1972. This model describes a membrane as a complex, fluid bilayer structure of lipids containing integral membrane proteins, membrane-associated cytoskeletal structures, lipid-anchored proteins and lipids. The illustration is adapted from a publication (Lingwood and Simons, 2010).

Even though a single lipid species is sufficient to form a planar, fluid bilayer, the membranes of eukaryotic cells are composed of hundreds, if not thousands of different membrane lipids with integral or peripherally attached membrane proteins (Figure 1) (Lingwood and Simons, 2010; Nicolson, 2014; Singer and Nicolson, 1972). The fluid mosaic model, proposed in 1972, was introduced to explain the structural and dynamic properties of biological membranes (Singer and Nicolson, 1972). This model described biological membranes as a matrix composed of a mostly fluid bilayer of phospholipids with mobile integral membrane proteins and glycoproteins intercalated into the bilayer (Nicolson, 2014; Singer and Nicolson, 1972). Updated versions of the fluid mosaic membrane model, proposed in 1976 and 2014, included

the interaction of the extracellular matrix and membrane-associated cytoskeletal components with the cellular membrane and the potential influence of this interaction on the mobility and distribution of membrane proteins (Figure 1) (Nicolson, 1976, 2014). Strikingly, biological membranes are non-homogenous and often show highly dynamic, nm-sized lateral specializations such as lipid rafts, which can locally enrich a specific subset of the cellular proteome (Lingwood and Simons, 2010). Cellular membranes exhibit an asymmetric distribution of phospholipids, polysaccharides and proteins between the two leaflets of the lipid bilayer (Nicolson, 2014; Singer and Nicolson, 1972). The asymmetry of integral membrane proteins is already determined for the vast majority of proteins already during their insertion into the membrane. The asymmetric distribution of phospholipids is the result of localized biosynthesized, passive flipflop between the leaflets and active transport by primary-active lipid transporters (Daleke, 2003; Nicolson, 2014). For example, the inner leaflet of the eukaryotic plasma membrane is enriched in amine-containing glycerophospholipids such as phosphatidylethanolamine (PE) and the negatively charged phosphatidylserine (PS). Also the signaling-active phosphatidylinositol phosphates (PIPs) are almost exclusively found in the inner leaflet of the plasma membrane (Daleke, 2003).

The organellar membranes of eukaryotic cells have characteristic lipid compositions. In fact, the lipid composition crucially contributes to define the identity of an organelle, which is essential for specific organelle interactions (Holthuis and Menon, 2014; Radanović et al., 2018). Membrane proteins harbor most of the chemical specificity of cellular organelles and mediate a selective exchange of material and information across the membrane. One third of all protein-encoding genes are thought to encode for membrane proteins (Pietzsch, 2004). Integral membrane proteins are anchored in the lipid bilayer either via their transmembrane domains (tail-anchored proteins, integral membrane proteins) or by a hydrophobic hairpin domain. Peripheral membrane proteins can either bind to lipids or membrane proteins or they can be covalently attached to lipid anchors such as glycosylphosphatidylinositol (GPI)-anchors (Lingwood and Simons, 2010; Nicolson, 2014; Pietzsch, 2004). Membrane proteins fulfill crucial roles in almost every aspect of cellular physiology. They are involved in inter- and intracellular signaling, selective transport of nutrients and waste products. They are thus crucially important for cellular growth, cell development, immune responses and many other functions (Holthuis and Levine, 2005). The functionality of membrane proteins depends on its physical state determined by the complex composition of the membrane at a given condition. Both, the membrane proteins and lipids impact on all physiochemical aspects of a membrane such as permeability, thickness, fluidity, phase behavior and membrane bending rigidity (Ernst et al., 2018) (2.1.2). It is therefore crucial to maintain these properties in a regime, which is acceptable for life. Lipids play the central role in maintaining membrane properties due to their molar abundance and quick turnover (Radanović et al., 2018). Perturbations in membrane

homeostasis are linked to cellular stress, and have been firmly associated with the pathogenesis of complex metabolic diseases such as type II diabetes, Alzheimer and cancer (Santos and Riezman, 2012).

2.1.1 The cellular lipidome

The cellular lipidome is complex. Eukaryotic cells invest substantial resources to generate thousands of different lipids: 5% of eukaryotic genes are used to synthesize, remodel and degrade different kinds of lipids (van Meer et al., 2008). The most abundant category of membrane lipids in eukaryotic cells, the glycerophospholipids, are amphiphilic molecules consisting of a hydrophilic headgroup and a hydrophobic portion formed by two acyl chains of different length (Holthuis and Levine, 2005; Holthuis and Menon, 2014; van Meer et al., 2008; Nicolson, 2014; Singer and Nicolson, 1972). Next to its role as building blocks for all cell membranes, lipids fulfill more functions in the cell. Lipids are also used for energy storage as triacylglycerol and steryl esters which are stored in lipid droplets. Lipids can also act in cellular signaling by acting as signaling molecules or by affecting signaling through influencing membrane functions (van Meer et al., 2008). This work mainly focuses on the role of cellular lipids as building blocks for cellular membranes and their role in mounting specific cellular stress responses in the endoplasmic reticulum (ER).

Eukaryotic membranes contain lipids from three distinct lipid categories: glycerophospholipids (GPL), sphingolipids (SL) and sterols (Figure 2). GPL, which are the most abundant in eukaryotic cells constituting up to 70% of all membrane lipids in yeast and most other eukaryotes (Holthuis and Levine, 2005). GPL consist of a glycerol backbone that is – in most cases – esterified with two acyl chains at the *sn1* and *sn2* positions. The fatty acyl chains can vary in length, number and position of double bonds (Ernst et al., 2016; Holthuis and Levine, 2005; Klose et al., 2013; De Kroon et al., 2013). The lipid headgroup located at the *sn3* position determines the lipid class. It can differ in charge, shape and chemistry: phosphatidylcholine (PC), phosphatidylserine (PS), phosphatidylethanolamine (PE), phosphatidylglycerol (PG), phosphatidylinositol (PI) and phosphatidic acid (PA). PE and PC are zwitterionic phospholipids, while PS, PI, PIPs and PA are anionic lipids (Holthuis and Menon, 2014; Klose et al., 2013). Due to the modular structure of the GPLs, the lipidome of eukaryotic cells can be remarkably complex with hundreds of distinct components (Holthuis and Levine, 2005; Klose et al., 2013; van Meer et al., 2008). Despite this huge variety, 50% of all phospholipids in most eukaryotes contain PC as the lipid headgroup and are usually linked to one *cis* unsaturated acyl chain (Ernst et al., 2016; Holthuis and Levine, 2005; Holthuis and Menon, 2014; Klose et al., 2013; van Meer et al., 2008).

The sphingolipids (SL) constitute a category of lipids, which is less abundant, but also extremely diverse. SLs are composed of a C18 sphingoid base linked to a saturated C16-C26 fatty acid forming a ceramide (Figure 2) (Holthuis and Levine, 2005). The types of ceramides vary among organisms. In mammals, the sphingoid base can be linked to phosphocholine (resulting in sphingomyelin), phoshoethanolamine (resulting in ethanolaminephosphoryl ceramide) or even to glucose or galactose forming cerebrosides or more complex glycosphingolipids. Sphingolipids in plants and fungi typically have a phosphoinositol headgroup linked to the sphingoid base to form inositolphosphorylceramide, that can further be mannosylated to form mannoylinositol phosphorylceramide (Holthuis and Levine, 2005). The complexity of SLs is further increased by one or several hydroxylation in the hydrophobic hydrocarbon chains (Holthuis and Levine, 2005).

The third, least complex category of membrane lipids are the sterols. They have a unique structure and function. Sterols are based on a planar four-ring structure (Figure 2). Cholesterol is the most abundant sterol in mammals, while ergosterol dominates in the membranes of baker's yeast (Holthuis and Levine, 2005).

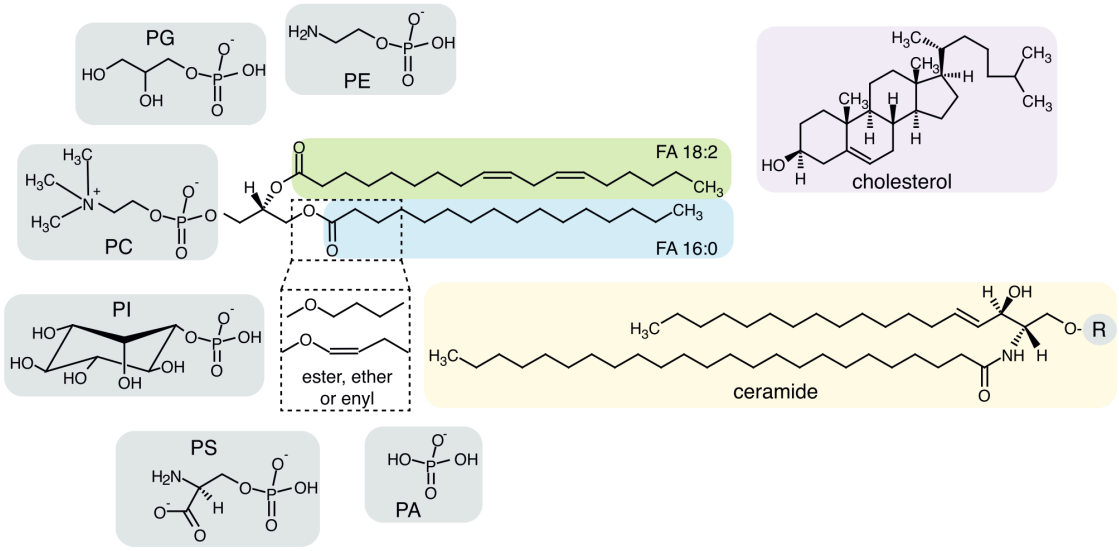

Figure 2: The molecular structure of the three major membrane lipid categories.

Biological membranes consist of three major lipid categories: Glycerophospholipids, sphingolipids and sterols. Glycerophospholipids contain a glycerol backbone with two acyl chains, which are most often esterified at position *sn1* and *sn2* and vary in length and double bonds (here 18:2, green, and 16:0, blue). The lipid headgroup at position *sn3* defines the lipid class (grey): phosphatidylcholine (PC), phosphatidylserine (PS), phosphatidylethanolamine (PE), phosphatidylglycerol (PG), phosphatidylinositol (PI) and phosphatidic acid (PA). Sphingolipids consist of a ceramide base (yellow) and a specific group at position R (grey), which can be phosphocholine or even a complex glucan. The third lipid category are the sterols (purple). Cholesterol is the most prevalent sterol in mammals and ergosterol in yeast. The illustration is taken from a recent review (Klose et al., 2013).

2.1.2 Lipid composition influences membrane property

The collective, physiochemical properties of cellular membranes such as thickness, fluidity, intrinsic curvature, the lateral pressure and their phase behavior are determined by the protein

and lipid content (Figure 3). To maintain these properties (and others) to external influences or to adjust them during differentiation processes, the lipid composition can be actively remodeled (Holthuis and Menon, 2014; Klose et al., 2013; Radanović et al., 2018).

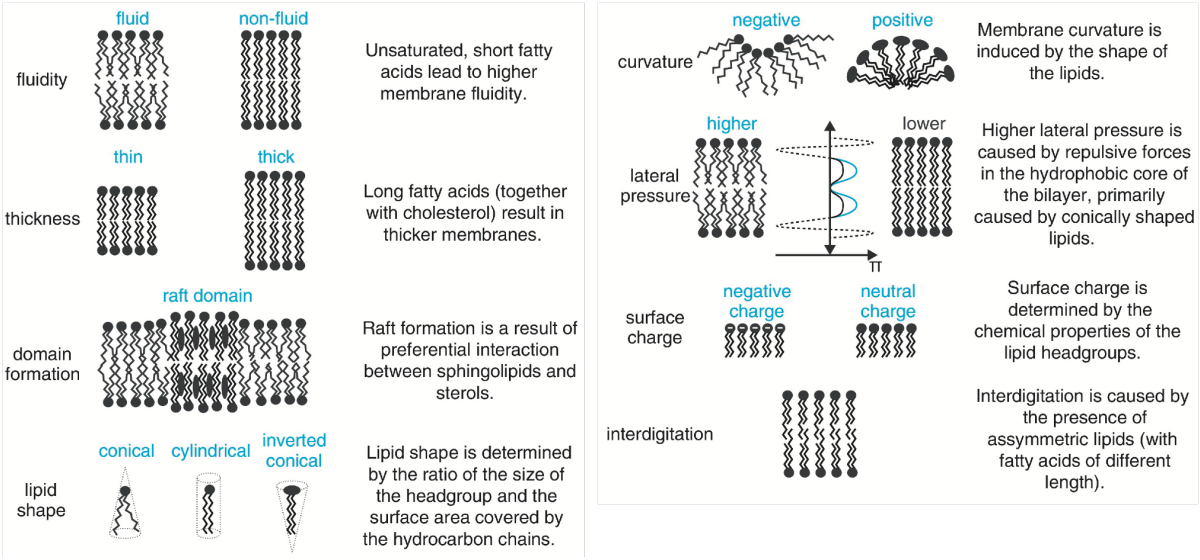

Figure 3: Membrane properties are influenced by the lipid composition.

The physiochemical properties of biological membranes are affected by the chemical character and the structure of the membrane lipids. The membrane fluidity and the spontaneous membrane thickness is influenced by the proportion of unsaturated acyl chains, the length of lipid acyl chains and the sterol content. The overall lipid shape is determined by the ratio between the area of the headgroup and the surface of the acyl chains and it can be described as conical, cylindrical and inverted conical. The overall shape also influences the intrinsic membrane curvature of the membrane and the lateral pressure profile within the lipid bilayer. The composition of lipid headgroups determines the surface charge density. The illustration is adapted from a recent publication (Klose et al., 2013).

One of the key factors influencing membrane fluidity, the rotational and translational mobility of membrane lipids and proteins, is the proportion of unsaturated and saturated lipid acyl chains (Radanović et al., 2018). Unsaturated fatty acyl chains with *cis* double bonds reduce the lipid packing and lower the phase transition temperature from a fluid bilayer to a solid, gel phase (Ernst et al., 2016; Holthuis and Menon, 2014). Long and saturated fatty acyl chains increase lipid packing thereby reducing membrane fluidity (Ernst et al., 2016). Sterols intercalate between the acyl chains and interfere with the packing of hydrophobic fatty acyl chains of the SLs and GPLs: they reduce the flexibility of the acyl chain rigidifying fluid membranes, but at the same time, they fluidize membranes that would tend to form solid gel phases (Holthuis and Menon, 2014). Furthermore, sterol has a particular impact on the transversal compressibility of the lipid bilayer by increasing the energetic costs associated with hydrophobic mismatches between transmembrane proteins and the lipid phase. It is important to realize that membrane fluidity is not only affected by the packing in the hydrophobic core of the membrane, but also substantially affected by the lipid headgroup composition (Radanović et al., 2018)

One way to approximate the impact of a certain lipid on the collective bilayer properties is by considering their molecular shape. The shape of a lipid can be described in a simplified fashion by the relative volumes occupied by the lipid headgroup and the lipid acyl chain region (Klose et al., 2013). If the relative volume occupied by the lipid headgroup is similar to the relative volume occupied by the acyl chains, the overall shape is cylindrical. This is the case for example for most PC lipids with two fatty acyl chains. Due to their distinct structure and acyl chain composition, most sphingolipids can pack more tightly than PC lipids. In contrast, lipids with a small headgroup such as PE have a smaller volume ratio between head and acyl chain thereby showing a conical shape. Consequently, most PC lipids can spontaneously self-assemble into planar lipid bilayers, while some PE lipids such as DOPE with two unsaturated 18:1 acyl chains tend to form non-lamellar structures (Ernst et al., 2016; Holthuis and Menon, 2014; Klose et al., 2013; van Meer et al., 2008; Radanović et al., 2018). The shape of lipids influences the lateral pressure profile within the membrane which is higher in the hydrophobic core of the bilayer for membranes containing both PC and PE lipids than in membranes composed solely of PC (Ballweg et al., 2020). The surface properties of biological membranes are greatly affected by the lipid headgroup composition. Different subcellular membranes expose very distinct densities of negative surface charges and these are critically contributing in determining the identity of these organelles (Klose et al., 2013). A central challenge, when studying the homeostasis of physiochemical membrane properties is the fact that most, if not all, membrane properties are non-additive, non-linear, and interdependent. It is almost impossible to change a specific bilayer property without affecting many others at the same time.

2.1.3 Cellular organelles and their lipid compositions

The secretory pathway describes the vesicular transport of secretory and membrane proteins from the endoplasmic reticulum to other organelles in the cell. It comprises the endoplasmic reticulum (ER), the Golgi apparatus, endosomes, lysosomes, transport vesicles and the plasma membrane (PM). These organelles have distinct lipid compositions reflecting their functions (Holthuis and Menon, 2014; Radanović et al., 2018). Despite constant exchange of membrane material by vesicular and non-vesicular transport, the organelles maintain their characteristic compositions.

The ER marks the starting point of the secretory pathway. It is a hotspot for lipid biosynthesis, the insertion, folding and quality control of membrane proteins, as well as the translocation, folding, and quality control of secretory proteins (Goyal and Blackstone, 2013). Its lipid composition results in a rather thin and loosely packed membrane with a neutral surface charge at the cytoplasmic leaflet. In contrast, the PM functions as a barrier between the intra-

and extracellular environment. Its protein and lipid composition lead to a thick and tightly packed membrane with negative surface charges at the cytoplasmic membrane leaflet (Figure 4) (Holthuis and Menon, 2014; van Meer et al., 2008). The most significant differences in physiochemical properties are achieved to a large extent by variations in the lipid content. The sterol content increases along the secretory pathway from 5 mol% in the ER to 30-40 mol% in the PM (Holthuis and Menon, 2014; van Meer et al., 2008). The PM additionally has a higher content of saturated and polyunsaturated glycerophospholipids and sphingolipids (Antonny et al., 2015; Holthuis and Menon, 2014). This composition allows a tighter lipid packing which is needed for a rigid and a low permeability barrier (Holthuis and Menon, 2014; van Meer et al., 2008). The differences in surface charge between PM and ER is caused by the asymmetric distribution of phospholipids between the two membrane leaflets. The content of anionic phospholipids increased from a few percent in the ER to more than 10 mol% in the PM (Holthuis and Menon, 2014; van Meer et al., 2008). In the ER membrane, the low amount of anionic phospholipids are enriched in the luminal leaflet, possibly through calcium-mediated interactions with luminal proteins (Daleke, 2003; Holthuis and Menon, 2014). The cytosolic leaflet of the PM is enriched in PS and PI leading to the negative surface charge in the cytoplasmic leaflet. The maintenance of the asymmetric distribution of phospholipids and the surface charge is essential for cellular survival (Daleke, 2003; van Meer et al., 2008).

The increase in membrane thickness along the secretory pathway is also reflected in the length of transmembrane domains of inserted membrane proteins (Figure 4). In the ER, the average length of a transmembrane helix (TMH) is 20 amino acids (aa) while it is 25 aa for a plasma membrane protein (Diaz-Rohrer et al., 2014; Holthuis and Menon, 2014; Lorent et al., 2017; van Meer et al., 2008; Sharpe et al., 2010). The ER is the starting point of the secretory pathway of various membrane proteins. Consequently, the ER membrane must be able to accommodate membrane proteins with TMHs of different length. A prerequisite for the insertion and folding of these diverse membrane proteins is a soft and deformable membrane. In summary, the contrasting lipid compositions of the ER and the PM lead to distinct physiochemical properties of these membranes, which reflect their cellular functions.

The Golgi apparatus, a polarized and multi-cisternal organelle, saves as a major lipid and protein sorting machinery. The trafficking route of vesicles from the ER to the PM is via the Golgi apparatus. Here, protein and lipid sorting occurs to preserve the unique membrane compositions of the ER and the PM (Holthuis and Menon, 2014). The Golgi is also the major site for the biosynthesis of lipids. It is specialized in sphingolipid biosynthesis (van Meer et al., 2008). The lipid composition of early endosomes, also a part of the secretory pathway, resembles the lipid content of the PM (van Meer et al., 2008).

Mitochondria, which are not part of the secretory pathway, play crucial roles in the cellular lipid metabolism and energy production. The lipid composition of mitochondria is distinct from the organelles of the secretory pathway and resembles, in line with their evolutionary origin, bacterial lipids. The mitochondrial membranes contain cardiolipin, PG and a high PE-to-PC ratio which has been implied to be required for oxidative phosphorylation (van Meer et al., 2008).

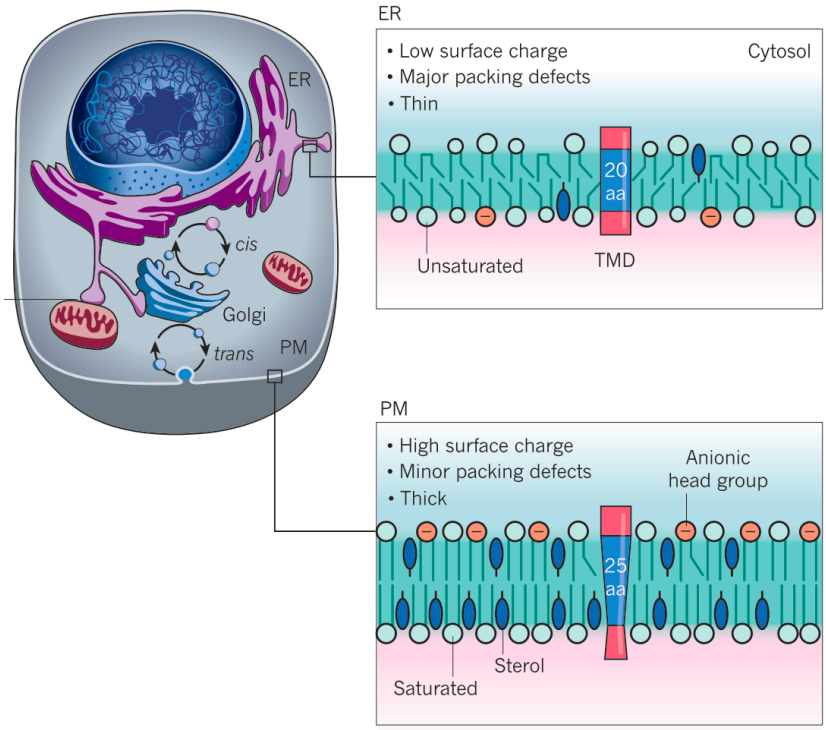

Figure 4: Organelles of the secretory pathway have different lipid compositions and physiochemical properties.

The ER membrane is characterized by a loosely packed, flexible lipid bilayer with a rather neutral surface on is cytosolic side. In contrast, the lipids of the plasma membrane are longer and more tightly packed. The content of sterols, saturated phospholipids and sphingolipids increases along the secretory pathway. The increased membrane thickness from the ER to the PM is reflected in the hydrophobic length of transmembrane helices of membrane proteins. It is on average ~20 aa for the ER and ~25 aa in the PM. Illustration adapted from a publication (Holthuis and Menon, 2014).

2.2 The endoplasmic reticulum and its cellular function

2.2.1 The architecture of the ER

The endoplasmic reticulum is the largest organelle in most eukaryotic cells. In some cell types, it comprises 50% of the total cell membrane mass (Goyal and Blackstone, 2013). It is a continuous and dynamic membrane system with structurally distinct domains. Using light microscopy, the ER can be differentiated in the nuclear and the peripheral ER (Figure 5A). The nuclear envelope, a part of the nuclear ER, consists of two separated lipidic bilayers: the inner

and outer nuclear membrane. The shape of this stacked membranes is maintained by inner nuclear membrane proteins, nuclear pores, and the cytoskeleton (Voeltz et al., 2002; Westrate et al., 2015).

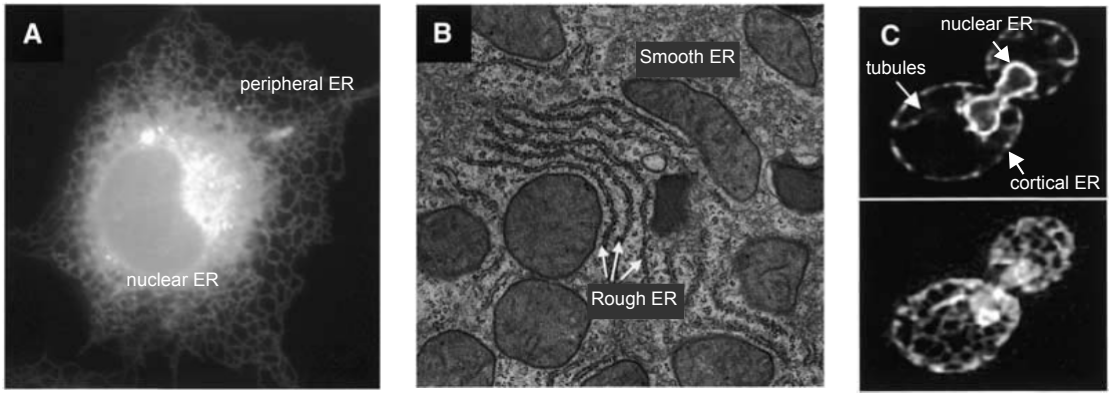

Figure 5: Structure of the endoplasmic reticulum (ER).

(A) Visualization of the nuclear and peripheral ER by GFP-Sec61β proteins expressed in COS cells. (B) An electron micrograph of an hepatocyte showing the smooth and rough ER subdomains. (C) Visualization of the nuclear and cortical ER of a yeast cell by Sec63-GFP. Illustration extracted from a publication (Voeltz et al., 2002).

The peripheral ER forms an extended membrane network with two structurally and functionally distinct domains: the rough and smooth ER (Figure 5B). The rough ER is decorated with ribosomes and it marks a hotspot for protein biosynthesis, translocation, modification and quality control. The rough ER is predominantly formed by membrane sheets (Westrate et al., 2015). The smooth ER is not studded with ribosomes and is regarded as a hotspot for lipid synthesis and the metabolism of carbohydrates. The smooth ER is a network of mostly ER tubules. They spread into the cell periphery thereby making membrane contact sites with other organelles (Goyal and Blackstone, 2013; Westrate et al., 2015). The relative abundance of smooth and rough ER correlates with cell function. Cells with a high secretory capacity such as exocrine, pancreatic cells, contain predominantly rough ER. Neurons or muscle cells have an extended network of smooth ER acting as a calcium reservoir. In hepatocytes, the smooth ER is enriched in enzymes for the metabolism of carbohydrates and detoxification (Goyal and Blackstone, 2013; Voeltz et al., 2002; Westrate et al., 2015).

In yeast, the ER can be subdivided into nuclear and cortical ER which is tethered to the plasma membrane (Figure 5C). The cortical and nuclear ER is connected by tubules. The shape of the cortical ER, constituting the major part of the ER in yeast, is a mixture between sheets and tubules (Voeltz et al., 2002; Westrate et al., 2015).

2.2.2 Cellular functions of the ER

The ER fulfills many important cellular functions. The ER requires a variety of proteins and unique physical properties to fulfill its tasks and to coordinate and response to changes in the intracellular milieu (Schwarz and Blower, 2016).

The rough ER is responsible for protein folding and co- and post-translational translocation of secretory and membrane proteins. The folding process of these proteins is assisted by chaperones and requires in most cases protein modifications such as N-linked glycosylation, or disulfide bond formation. Unfolded proteins are retained in the ER and in some cases undergo several folding-unfolding cycles until they are correctly folded. Finally misfolded proteins are retrotranslocated to the cytosol by the ER-associated degradation (ERAD) machinery where they are degraded (Görlach et al., 2006; Schwarz and Blower, 2016). The process of protein folding, unfolding and possible degradation in the cytosol can be summarized as the protein quality control. If the folding capacity of the ER is exceeded and misfolded proteins accumulate in the ER lumen, the unfolded protein response (UPR) is activated. The UPR is a conserved program that restores the folding capacity of the ER. More than 5 % of all genes in *Saccharomyces cerevisiae* (*S. cerevisiae*) are regulated by the UPR including chaperones, oxidoreductases, components of the ERAD machinery and enzymes of the lipid metabolism. A detailed description of this pathway can be found in 2.3.1 (Korennykh and Walter, 2012; Schwarz and Blower, 2016; Walter and Ron, 2011).

The ER is, next to the Golgi, one major site for lipid and steroid biosynthesis. The lipid synthesis predominantly occurs in the smooth ER (Görlach et al., 2006). Glycerophospholipids such as PE, PC or PS are synthesized in the ER and triacylglycerols for energy storage are also formed in the ER. The ER is also responsible for the synthesis of ceramides which are finally build up to complex sphingolipids in the Golgi (Fagone and Jackowski, 2009). The ER is also the main calcium storage compartment in mammalian cells. The Ca^{2+} concentration in the ER is around 100 – 800 µM, 1000 times higher as in the cytosol. Ca^{2+} functions as a second messenger in many cellular processes (Görlach et al., 2006; Schwarz and Blower, 2016).

2.2.3 Yeast as a model organism to study ER homeostasis

The yeast *S. cerevisiae* is wildly used as a model organism to study cell biology. In fact, three Nobel prizes were awarded since 2001 to research using *S. cerevisiae* as a model organism, (Nielsen, 2019). Genetic manipulations such as the introduction of mutations into the yeast genome or the knock-out of entire genes allows the biochemical description of the related functions, but also the cellular consequences (Botstein and Fink, 2011). A particularly valuable tool is the yeast deletion library. Here, nearly all open reading frames of the yeast genome

were individually deleted, thereby facilitating rapid, genome-wide screens. In addition, a localization library of most yeast proteins was established. To this end, the green-fluorescent protein (GFP) was fused to various proteins to allow the description of the cellular localization (Botstein and Fink, 2011; Santos and Riezman, 2012). Another important aspect for using *S. cerevisiae* is the fact that many biological pathways are conserved from yeast to man, especially in ER homeostasis (Nielsen, 2019; Santos and Riezman, 2012). ER homeostasis comprises the maintenance of the membrane composition and the resulting membrane properties, as well as protein quality control. Lipid metabolism, the UPR as well as the ERAD are pathways that are well conserved among eukaryotes. The use of *S. cerevisiae* as a model organism to study these processes gained important insights in their mode of operation and their regulation (Santos and Riezman, 2012) (2.2.4).

2.2.4 Exemplary membrane property sensors in *S. cerevisiae*

The organelles of a cell have characteristic membrane properties, which are actively maintained (Ernst et al., 2018; Radanović et al., 2018). The ER is the host for many such membrane property sensors. However, the mechanism of only a few sense-and-response systems have been characterized in detail (Ernst et al., 2018). Based on topological considerations, these sensors can be categorized in three classes. The first class of sensors senses membrane properties by surveying the membrane surface. The second class senses within the membrane and the third class of membrane property sensor uses a strategy to sense across the lipid bilayer (Covino et al., 2018; Ernst et al., 2018).

The first category surveys the membrane surface. Here, surface charges or hydrophobic membrane voids resulting from poor lipid packing are sensed (Figure 6A). The underlying mechanism relies on the folding of amphipathic helices (AH) into membranes (Ernst et al., 2018). The structure of an AH separates hydrophobic and hydrophilic residues on two faces of the helix. The AH folds upon the contact with a polar/non-polar interface or as for membrane property sensor upon the contact with a lipid bilayer (Giménez-Andrés et al., 2018). By attaching to the membrane, the non-polar face of the AH inserts into the membrane. Here, the AH interacts with the hydrophobic core, while the polar side faces the aqueous environment and interacts with the lipid headgroups (Puth et al., 2015). One example of this sensor type is the transcriptional repressor Opi1 that orchestrates the cellular decision between membrane biogenesis and fat storage. Opi1 uses an AH to sense the abundance of PA and the lipid packing density of the ER (Covino et al., 2018; Hofbauer et al., 2018). A high density of PA recruits Opi1 to the ER membrane. The binding of PA via the AH is stabilized by electrostatic interactions and membrane voids. At low PA levels, Opi1 detaches from the ER and is found in the nucleus to repress genes involved in membrane lipid biosynthesis. Opi1 uses a

combination of sensing PA levels and lipid packing to fine-tune the production of membrane lipids (Covino et al., 2018; Hofbauer et al., 2018). A mammalian example of a membrane property sensor, that uses an AH, is CCT (CTP:phosphocholine cytidylyltransferase). CCT resides at lipid droplets and the ER membrane. It senses lipid packing defects and regulates PC synthesis via the Kennedy pathway (Cornell, 2016; Giménez-Andrés et al., 2018; Krahmer et al., 2011; Puth et al., 2015).

The second class of membrane property sensors senses within the hydrophobic core of the membrane (Ernst et al., 2018; Radanović et al., 2018). One example is the sensing of lipid saturation, the balance between saturated and unsaturated lipids. In yeast, *OLE1* is the only fatty acid desaturase and its expression is controlled by the two transcriptional activators Mga2 and Spt23 (Ernst et al., 2018; Hoppe et al., 2000). The sensing mechanism of Mga2 and Spt23 relies on a tryptophan residue in the dimeric TMHs (Figure 6B). The two TMHs in the dimer rotate against each other, thereby populating distinct rotational conformations. The population of these configurations is affected by the lipid environment and coupled to the proteolytic activation of the transcription factors Mga2 and Spt23 (Ballweg and Ernst, 2017; Covino et al., 2016, 2018; Hoppe et al., 2000).

Class III membrane property sensors use a mechanism that senses across the lipid bilayer by deforming it altogether (Figure 6C) (Covino et al., 2018; Ernst et al., 2018). Here, the ER-stress sensor Ire1 serves as an example. Its mechanism of sensing is described in detail in section 2.3.2. In brief, this type of membrane sensor uses an unusual TMH composed of an AH and a short transmembrane region inducing a local compression (reduced membrane thickness) with lipid disordering in the ER membrane. With this sensing mechanism, Ire1 is able to react on stiffening of the ER membrane (Covino et al., 2018; Ernst et al., 2018; Halbleib et al., 2017).

This thesis is dedicated to a better understanding of the TMH architecture of Ire1, a prototypic class III membrane property sensor.

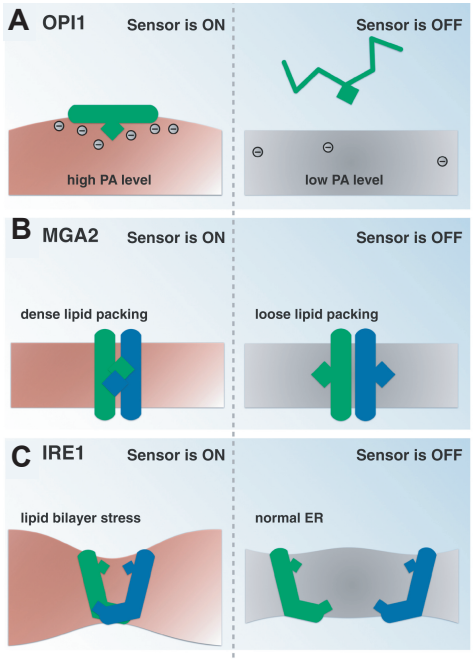

Figure 6: Three mechanism of sensing by exemplary membrane property sensors.

(A) Schematic representation of sensing at membrane surfaces. Here, the mechanism of Opi1 using an AH for sensing PA levels via electrostatic interactions and lipid packing via membrane voids is illustrated. The AH folds upon the attachment to a lipid bilayer and hydrophobic residues of the non-polar phase intercalate into the membrane. (B) Schematic representation of the sensing within the membrane. Here, the sensing of lipid saturation by Mga2, a transcriptional activator of the desaturase *OLE1*, via a rotational switch is shown. The sensing mechanism relies on highly dynamic dimers and on a bulky sensing residue, a tryptophan. In a saturated lipid environment, the bulky sensing residue is forced to hide in the dimer interface leading to the proteolytic activation of Mga2 and consequently of the *OLE* pathway. (C) Schematic representation of the sensing across the lipid bilayer. Here, the sensing of Ire1 with its unusual transmembrane helix is shown. Ire1's TMH is composed of an amphipathic helix and a short TMH. This unusual architecture induces a local compression compensated by the loosely packed and thin ER membrane. With increased lipid packing, the local compression gets energetically unfavored and the membrane forces Ire1 to oligomerize leading to its activation. The illustration is adapted from a previous publication (Covino et al., 2018).

2.3 How ER-stress is sensed

2.3.1 The unfolded protein response (UPR)

Organisms are often exposed to internal and external stresses that lead to protein misfolding and aggregation. It is not surprising that the cell has mechanism to sense and restore proteostasis – homeostasis of protein production and protein folding. The cell constantly monitors the level of potentially harmful misfolded proteins, as unfolded and misfolded proteins can saturate the available pool of chaperones. The pathway that is responsible for sensing accumulated misfolded proteins in the ER lumen is the unfolded protein response (UPR), a pathway conserved from yeast to man (Adams et al., 2019; Frakes and Dillin, 2017; Hetz and Papa, 2018; Korennykh and Walter, 2012; Walter and Ron, 2011). The UPR induces the activation of a wide-spreading transcriptional program to restore ER homeostasis by increasing the folding capacity of the ER. In yeast, more than 5% of all genes are regulated by the UPR including genes encoding for ER chaperones, oxidoreductases, components of the ERAD machinery and enzymes of lipid metabolism (Cox et al., 1993; Jonikas et al., 2009; Travers et al., 2000; Walter and Ron, 2011). However, the UPR is not under all circumstances

cytoprotective. Persistent activation of the UPR can also trigger cell death in mammalian cells (Walter and Ron, 2011). Such chronic activation of the UPR has been implicated in the pathogenesis of neurodegenerative and metabolic diseases such as type II diabetes or the non-alcoholic fatty liver diseases (NAFLD). The UPR plays also a two-sided role in several types of cancer (Frakes and Dillin, 2017).

2.3.1.1 The UPR in yeast

The inositol requiring enzyme 1 (Ire1) is the most conserved sensor of the UPR and the only one in yeast. Ire1 is an ER resident type I transmembrane protein and it belongs to the family of protein kinases (Cox et al., 1993; Mori et al., 1993). It senses misfolded proteins via its ER-luminal sensor domain. Its cytosolic part can be differentiated into a kinase and an RNase domain (Cox et al., 1993; Mori et al., 1993; Sidrauski and Walter, 1997). According to current models, Ire1 is activated by oligomerization upon binding of misfolded proteins and a concomitant dissociation of Kar2 (Figure 7) (Aragón et al., 2009; Gardner and Walter, 2011; Kimata et al., 2003, 2004, 2007). Kar2 is one of the most abundant chaperones in the ER lumen and a functional and structural homolog to the human binding protein (BiP). The oligomerization leads to an activation of the cytosolic effector domains of Ire1. While the activity of the kinase domain does not seem to be required for efficient signal transduction, it is an important modulator of the UPR activity (Korennykh and Walter, 2012; Rubio et al., 2011). Initially, autophosphorylation of Ire1 results in a stronger self-association (Korennykh et al., 2009). Increased autophosphorylation that occurs over time, however, leads to a faster deactivation of UPR signaling upon adaptation to ER-stress (Chawla et al., 2011; Korennykh and Walter, 2012; Rubio et al., 2011). The main effector domain is the RNase domain responsible for the unconventional splicing of the mRNA *HAC1* (Cox and Walter, 1996). The resulting fragments are joined by the tRNA ligase Rlg1 (Sidrauski and Walter, 1997; Sidrauski et al., 1996). The spliced mRNA is translated into the transcription factor Hac1 that enters the nucleus and activates the expression of UPR target genes (Cox et al., 1993).

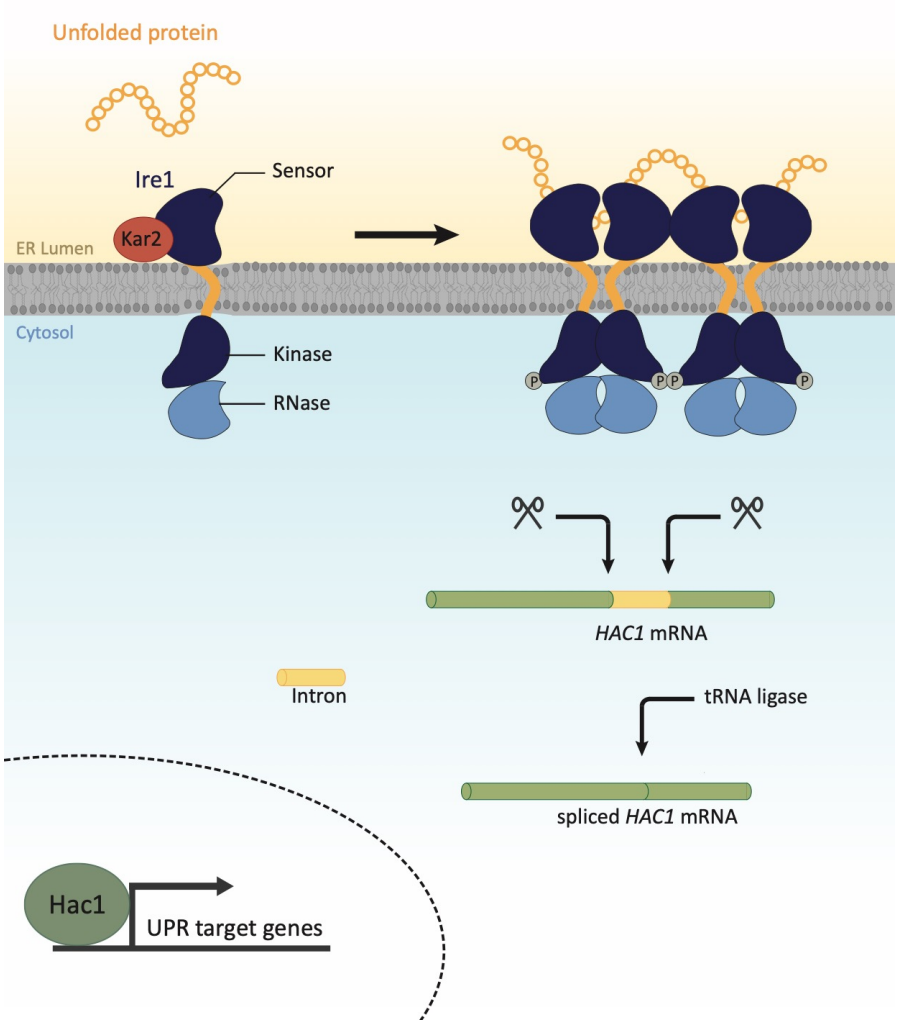

Figure 7: The unfolded protein response in *S. cerevisiae*.

The conserved UPR sensor Ire1 is composed of an ER-luminal domain that can sense unfolded/misfolded proteins, a TMH region, and cytosolic effector domains with kinase and RNase activity. Monomeric Ire1 is inactive and interacts directly with the major ER chaperone Kar2. Upon the accumulation of unfolded proteins in the lumen of the ER, Kar2 dissociates and Ire1 oligomerizes. Microscopically visible clusters of Ire1 are stabilized by a direct interaction with unfolded/misfolded proteins. The concomitant oligomerization of the cytosolic kinase domain leads to an autophosphorylation of Ire1 and the activation of its RNase domain. The function of the RNase domain together with the tRNA ligase Rlg1 is an unconventional splicing of the *HAC1* mRNA encoding for a transcription factor. The matured transcription factor targets genes with unfolded protein response elements (UPRE) and regulates hundreds of target genes.

2.3.1.2 The UPR in higher eukaryotes

In higher eukaryotes, the UPR relies on three sensory proteins in the ER membrane constituting the three branches of the mammalian UPR named after the upstream sensors: IRE1 (IRE1α/β) (Cox et al., 1993; Mori et al., 1993), the protein kinase (PRK)-like ER kinase PERK (Harding et al., 1999) and the activating transcription factor ATF6 (Haze et al., 1999) (Figure 8).

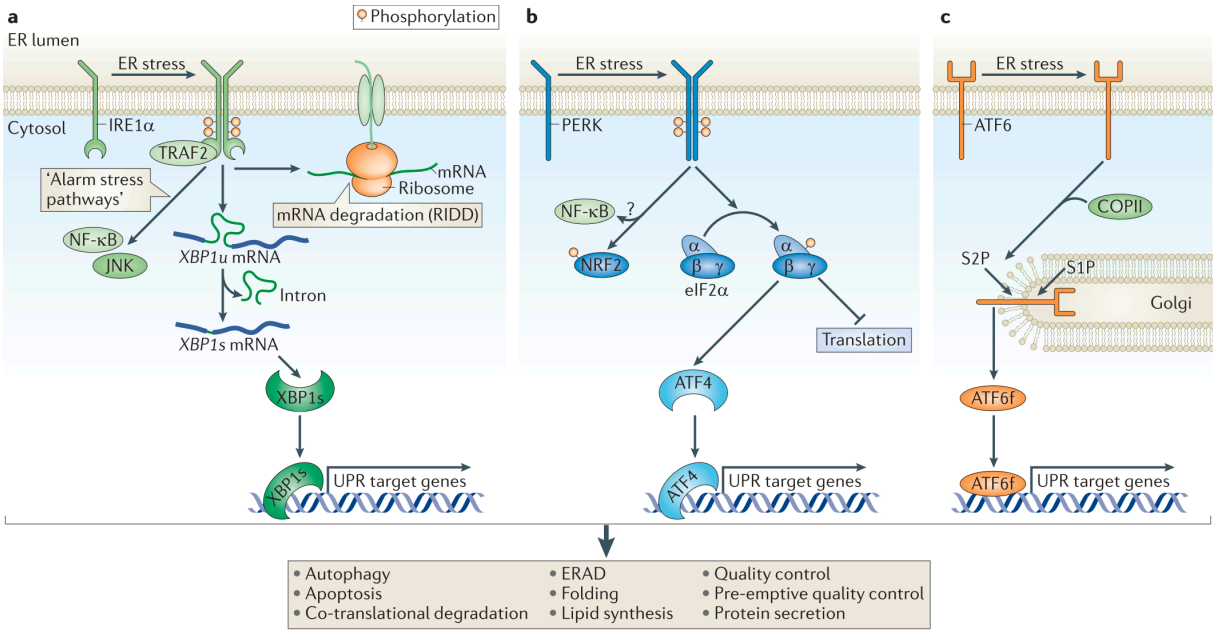

Figure 8: The unfolded protein response in higher eukaryotes.

The UPR in higher eukaryotes relies on three branches defined by their upstream signal transducers: IRE1, PERK and ATF6. (A) IRE1 oligomerization, followed by an autophosphorylation leads to the activation of its RNase domain resulting in the unconventional splicing of the mRNA encoding for X box-binding protein 1 (XBP1). XBP1 acts as a transcription factor for thousands of UPR target genes. The active RNase domain of IRE1 also regulates the non-specific degradation of mRNAs, which is referred to as the regulated IRE1-dependent decay (RIDD). Activation of IRE1 therefore leads to a global downregulation of protein translation. (B) PERK phosphorylates the eukaryotic initiation factor eIF2α to attenuate global protein translation and lower the load of the ER with unfolded proteins. Nevertheless, the phosphorylation of eIF2α allows for a selective translation of the ATF4 mRNA encoding for a transcriptional activator of many target genes of the UPR. (C) During the process of activation, the ER-resident UPR sensor ATF6 relocalizes from the ER to the Golgi apparatus via COPII vesicles. In the Golgi, ATF6 is processed by the proteases S1P and S2P thereby releasing a transcription factor domain referred to as ATF6f. The illustration is extracted from a publication (Hetz, 2012).

IRE1 is the most conserved UPR sensor and its domain structure and mechanism of activation is comparable to Ire1 from yeast (2.3.1.1) (Adams et al., 2019; Tirasophon et al., 1998). Two isoforms of IRE1 were described: IRE1α is ubiquitously expressed, while IRE1β is only expressed in the gut (Mori, 2009). During the process of activation, the ER chaperone BiP dissociates (Bertolotti et al., 2000), IRE1α oligomerizes (Li et al., 2010) and directly interacts with misfolded proteins via its luminal sensor domain (Karagöz et al., 2017). The oligomerization leads to a regulatory autophosphorylation (Prischi et al., 2014) and activation of its RNase domain. The RNase domain of IRE1α in mammals has two distinct functions. The first function is, similar to the role in unconventional splicing of *HAC1* in baker's yeast, to cleave the mRNA of the X box-binding protein 1 (XBP1) (Calfon et al., 2002). After maturation, spliced XBP1 functions as a transcriptional activator of UPR target genes similar to Hac1 in baker's yeast (Adams et al., 2019; Calfon et al., 2002; Korennykh and Walter, 2012). The second function of IRE1α is termed regulated IRE1-dependent decay (RIDD) pathway (Hollien and Weissman, 2006). Here, mRNAs are degraded by an rather unspecific RNase activity of active IRE1α. This reduces the load of the ER with unfolded proteins by lowering the overall cellular translation (Adams et al., 2019; Hollien and Weissman, 2006). Recently, it was shown that

IRE1α forms a complex with the SEC61 translocon (Plumb et al., 2015). By interacting with SEC61, IRE1α is recruited directly to the mRNA substrates of the RIDD pathway thereby potentially overcoming the limitations imposed by its low abundance in the ER membrane (Ghaemmaghami et al., 2003; Plumb et al., 2015).

The second UPR sensor PERK is also activated by an oligomerization upon sensing unfolded proteins in the lumen of the ER (Figure 8). PERK possesses an ER-luminal sensor domain, a single TMH and a cytosolic kinase domain. The luminal domain of PERK is structurally related to the ER-luminal domain of IRE1α (Adams et al., 2019; Korennykh and Walter, 2012). Upon accumulation of misfolded proteins, PERK dimerizes. The increased proximity of the cytosolic kinase domains then facilitates the activation of PERK by autophosphorylation in *trans* (Adams et al., 2019). The mechanism of sensing involves, similar to the case of IRE1α, an interaction with BiP (Bertolotti et al., 2000). Activated PERK mediates a translational attenuation by phosphorylating the eukaryotic initiation factor-2α (eIF2α). Phosphorylated eIF2α inhibits the initiation of translation thereby attenuating global cell translation (Harding et al., 1999). The activation of PERK also upregulates the expression of the activation transcription factor 4 (ATF4) that regulates the expression of many UPR target genes. Prolonged activation of the PERK branch can lead to cell death by apoptosis (Adams et al., 2019; Korennykh and Walter, 2012; Lin et al., 2009; Walter and Ron, 2011). Thus, PERK acts cytoprotective, but can also contribute signals to cell death (Lin et al., 2009; Walter and Ron, 2011).

The third UPR sensor ATF6 is different from PERK and IRE1α in its primary sequence, domain architecture and mode of operation (Figure 8) (Adams et al., 2019). AFT6 is a type II transmembrane protein, which is activated by proteolysis (Haze et al., 1999; Mori, 2009). According to current models, ATF6 exists as higher oligomers, dimers and monomers in the resting ER. Increased dissociation of ATF6 during ER-stress allows for the transport of monomeric ATF6 from the ER to the Golgi via the COPII vesicles. In the Golgi, ATF6 is processed by the site-1 protease (S1P) and site-2 protease (S2P) (Okada et al., 2003; Ye et al., 2000). The cytosolic fragment, referred to as ATF6f, is thus proteolytically released and can act as a transcriptional activator for the expression of chaperones and ERAD components (Haze et al., 1999; Korennykh and Walter, 2012; Walter and Ron, 2011).

Notably, the number of UPR sensors has increased during evolution. There is only one UPR sensor in *S. cerevisiae* (Ire1), two sensors in *Caenorhabditis elegans* and *Drosophila* (ire-1 and pek-2, IRE1 and PEK/PERK), and three in mammals (IRE1α, PERK and ATF6) (Mori, 2009).

2.3.2 Activation of the UPR by lipid bilayer stress

In the last decade, it became evident that the UPR is not only activated by unfolded or misfolded proteins, but also by signals from the ER membrane presumably from aberrant lipid compositions (Promlek et al., 2011; Surma et al., 2013; Thibault et al., 2012; Volmer and Ron, 2014). The general term for all aberrant composition of the ER membrane that activate the UPR is lipid bilayer stress (Surma et al., 2013). This includes for example a dysregulated sphingolipid biosynthesis (Han et al., 2010), disturbed sterol levels (Cohen et al., 2017; Pineau et al., 2009), impaired PC biosynthesis (Thibault et al., 2012), inositol depletion (Halbleib et al., 2017; Promlek et al., 2011), and an overly saturated lipidome (Pineau et al., 2009; Surma et al., 2013; Volmer et al., 2013). Interestingly, a variety of systematic, genetic studies identified an intense crosstalk of the UPR, the protein quality control machinery of the ER, and lipid metabolism (Jonikas et al., 2009; Surma et al., 2013). Genetic perturbation experiments and manipulation of UPR sensors suggested that lipid bilayer stress activates the UPR directly, and not indirectly by interfering with protein folding in the ER (Hou et al., 2014; Promlek et al., 2011; Volmer et al., 2013). This direct activation of the UPR by lipid bilayer stress was first shown in yeast. A mutant unable to bind misfolded proteins reacted on inositol depletion to the same extent as wildtype cells (Promlek et al., 2011). Studies focusing on the membrane-based activation of the UPR were also performed with mammalian UPR sensors. Truncation mutants of the human UPR sensors IRE1α and PERK consisting only of the TMH and the kinase domains were analyzed *in vitro.* These mutants were reconstituted in liposomes with an increased degree of lipid saturation and the kinase activity were analyzed. For both sensors, the kinase activity increased with an increase in the degree of lipid saturation. The activation by increased proportions of saturated lipids was described to be irrespective of the TMH sequence (Volmer et al., 2013).

Consequently, the question arises how does the UPR sensors sense aberrant lipid compositions? Bioinformatical and biophysical analysis of the TMH region of the yeast Ire1 identified unusual features. The TMH region of Ire1 can be separated in two parts: A rather short TMH that is extended on its N-terminal end with an AH (Figure 9A,B) (Halbleib et al., 2017). Molecular dynamics (MD) simulations revealed an unusual configuration of the TMH domain relative to the lipid bilayer: the AH tends to lie parallel to the membrane while the TMH is kept in a tilted orientation (Halbleib et al., 2017). Because the TMH is rather short and anchored by polar residues at the cytosolic end, this overall architecture leads to a substantial local compression (reduced membrane thickness) around the AH (Figure 9C) (Covino et al., 2018; Halbleib et al., 2017). These deformations are energetically disfavored. In a rather thin and loosely packed ER membrane the cost for this deformation are negligible. A stiffening of the membrane by a change in lipid composition (e.g. increased lipid saturation), however,

increases the cost for membrane deformation. Stiffening of the ER membrane therefore forces Ire1 to oligomerize, which leads to the coalescence of the deformed membrane regions and the minimization of the energetic costs associated with membrane compression (Figure 9C) (Covino et al., 2018; Halbleib et al., 2017). Mutational studies highlighted the importance of the AH for the membrane-based activation of the UPR (Halbleib et al., 2017). A disruption of the amphipathic character by the introduction of charged residues in the hydrophobic face of the AH destabilized and unfolded the helix, thereby preventing its insertion into the lipid bilayer (Figure 9C). These findings provided compelling evidence that the local compression induced by the AH is the molecular basis of the membrane-based activation of Ire1 from baker's yeast (Covino et al., 2018; Halbleib et al., 2017).

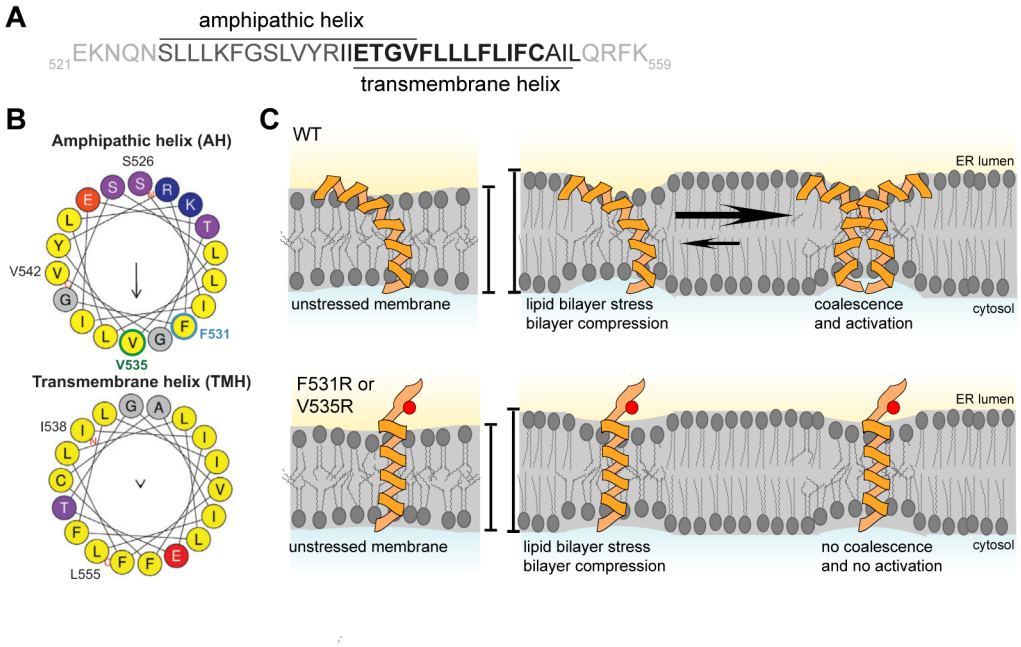

Figure 9: The mechanism of UPR activation by lipid bilayer stress in *S. cerevisiae.*

(A) Primary sequence of the AH and TMH of Ire1. (B) Heliquest analysis of the AH and TMH of Ire1. (C) Schematic model of the membrane-based activation mechanism of Ire1. The AH of Ire1 WT (Top) inserts into the bilayer and induces a local membrane compression. The energetic costs for membrane compression and acyl chain disordering is relatively low in the unstressed ER. Membrane stiffening upon lipid bilayer stress increases the energetic costs associated with membrane compression. These costs are minimized by an oligomerization of Ire1 and the coalescence of the compressed membrane regions. By disrupting the amphipathic character of the AH by mutations (e.g. V535R or the F531R) (Bottom), the area of membrane compression is much reduced and the driving force for the oligomerization of Ire1 by lipid bilayer stress is lost. The illustration is adapted from a previous publication (Halbleib et al., 2017).

Bioinformatical analysis of the mammalian UPR sensors PERK and IRE1α suggested a potential conservation of this unusual transmembrane architecture with an AH overlapping with a TMH (Halbleib et al., 2017). However, initial attempts to validate a role of this conserved AH in the membrane-based activation of IRE1α failed. It remains to be shown if Ire1 from baker's yeast and the mammalian IRE1α and PERK use similar mechanisms to sense membrane-based signals.

2.3.3 A closer look at Ire1: Structural and functional organization

The domain structure of the yeast Ire1 (Figure 10A) is well characterized. Several crystal structures of the ER-luminal sensor and the cytosolic kinase and RNase domains were obtained and helped to understand the mechanism of activation. Systematic deletion studies allowed the differentiation of the ER-luminal domain of Ire1 into five different subregions (Figure 10B) (Kimata and Kohno, 2011; Kimata et al., 2004): Subregion I comprises amino acids 32 – 111 and has a regulatory function by self-inhibiting Ire1 (Mathuranyanon et al., 2015). Subregions II, III and IV with amino acids 112 – 454 form the core ER-luminal domain of Ire1 and represents the core stress sensing region responsible for Ire1 clustering (Kimata et al., 2007; Oikawa et al., 2007). Subregion V comprising amino acids 455 - 524 is identified as the Kar2 binding site (Kimata et al., 2004).

The crystal structure of the core ER-luminal domain (112 – 454) (Figure 10C) revealed that subregion II and IV are tightly folded and that they are formed predominantly by β-sheets (Credle et al., 2005). Two parallel α-helices lie in parallel on top of this β-sheet platform thereby forming a peptide binding groove between them. The binding groove is decorated with aromatic residues at the bottom. The geometry of this groove shows striking similarities with the central peptide binding groove of major-histocompatibility complex I (MHC-I) molecules (Credle et al., 2005; Korennykh and Walter, 2012). The crystal structure of the core ER-luminal domain was obtained from higher-order oligomers that interact via specific interfaces. The oligomerization of the core ER-luminal domain requires two interfaces: Interface 1 is involved in the dimerization, which is required for forming the peptide binding groove. Interface 2 is involved in the formation of higher-order back-to-back oligomers of Ire1 (Credle et al., 2005; Korennykh and Walter, 2012). Mutations in both interfaces (IF_L1: T226A, F247A; IF_L2: W426A) substantially reduce the potential of Ire1 to form signaling-active clusters and desensitize Ire1 to the accumulation of unfolded proteins (van Anken et al., 2014; Aragón et al., 2009; Credle et al., 2005; Gardner and Walter, 2011; Halbleib et al., 2017; Kimata et al., 2007). The binding groove is only formed when Ire1 assembles into a dimer thereby allowing the direct binding of misfolded proteins with a preference for hydrophobic and basic peptides (Credle et al., 2005; Gardner and Walter, 2011; Korennykh and Walter, 2012).

The crystal structure of the cytosolic kinase and RNase domains revealed that both of them are predominantly formed by α-helices (Figure 10D) (Korennykh and Walter, 2012; Korennykh et al., 2009). The primary step in the activation of the kinase and RNase domains is oligomerization (Korennykh and Walter, 2012; Korennykh et al., 2009). Crystal structures of the cytosolic domains were solved as higher oligomers forming three distinct interfaces IF_C1, IF_C2 and IF_C3. Mutations within these interfaces result in a functional defect of the RNase domain (van Anken et al., 2014; Korennykh and Walter, 2012; Korennykh et al., 2009). IF_C1 is

the dimerization interface formed via RNase/RNase and kinase/kinase contacts (Figure 10D). IF_C2 is formed by a RNase/RNase interface. IF_C3 formed by kinase/kinase contacts is only found in a higher oligomer of Ire1. A dimer of Ire1 in a back-to-back arrangement forms the active site of the RNase function required for the splicing process of the *HAC1* mRNA. The *trans*-autophosphorylation of the kinase domain is mediated by the face-to-face dimer arrangement via interface IF_C3 (Korennykh and Walter, 2012).

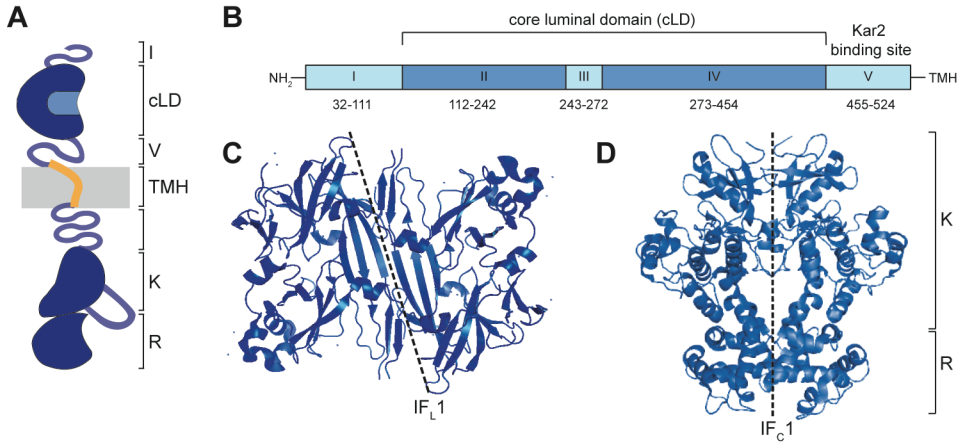

Figure 10: Schematic representation and crystal structures of Ire1 from *S. cerevisiae*.

(A) Schematic representation of the domain structure of Ire1 from baker's yeast. The ER-luminal domain consists of the subregion I, the core ER-luminal domain cLD and subregion V (Kimata and Kohno, 2011; Kimata et al., 2004). The cytosolic part of Ire1 can be subdivided in a loosely folded domain, a kinase domain and a RNase domain. (B) Organization of the ER-luminal domain of Ire1. The luminal domain can be separated in 5 subregions. Subregions II, III and IV form the core luminal domain, subregion V is the Kar2 binding site, while subregion I has a regulatory function. Subregion II and IV are tightly folded, the other three are loosely folded. (C) Crystal structure of the dimeric luminal domain of Ire1 (PDB 2BE1) (Credle et al., 2005). (D) Crystal structure of the dimeric cytosolic domain of Ire1 (PDB 3SDM) (Korennykh et al., 2009).

Despite a wealth of high-resolution, structural data on the cytosolic domains and the ER-luminal domain of Ire1, the role of the transmembrane domain remains rather poorly understood. Ire1 is a single-pass membrane protein and the structural flexibility in the TMH region represents a major challenge for structural biological work on the full-length protein. It is crucial to understand how Ire1 coordinates different types of signals from the lumen of the ER and the ER membrane to mount an adaptive response. This thesis is dedicated to a better understanding of the structure and function of the TMH of Ire1.

3 Aims

This thesis is dedicated to a better understanding of the signal integration by the ER-stress sensors Ire1 from baker's yeast and PERK from human. This thesis focuses on central questions in the field of UPR research: How is the TMH of Ire1 structurally organized in a cluster of Ire1? How does Ire1 coordinate different types of signals from the lumen of the ER and the ER membrane? Is it possible that proteotoxic stress and lipid bilayer stress are interdependent? Is the sensing mechanism of lipid bilayer stress conserved from yeast to man?

In the first part, this thesis focuses on identifying the architecture of the TMH region of Ire1. This ultimately addresses if the signaling-active conformation of Ire1 is different for all forms of ER-stress (proteotoxic and lipid bilayer stress) or if there is only one response to all input signals. To this end, a functional, cysteine-less variant of Ire1 will be constructed and used to perform a cysteine scanning and crosslinking approach in microsomal membranes. With the development of the crosslinking assay with single-cysteine mutants in the TMH of Ire1, the architecture of the TMH can be studied in the native lipid environment with the native protein-to-lipid ratio and in the context of the full-length protein.

In the second part, the interdependency between proteotoxic stress and lipid bilayer stress shall be addressed by analyzing the binding of a misfolded model substrate to Ire1 in different lipid environments. To this end, an *in vitro* binding assay with the reconstituted sensor domain of the yeast Ire1 shall be established. Here, the purification and reconstitution of a fusion protein consisting of MBP as a purification tag, the core ER-luminal domain of Ire1 and the TMH part is established. To analyze the binding of misfolded proteins to the ER-luminal domain, the fusion protein is reconstituted in liposomes with different lipid compositions. The modulation by the membrane environment will be analyzed using a binding assay that is based on a sucrose density gradient. With this assay, the binding of misfolded proteins in different lipid environments will be analyzed.

The third part of this thesis focusses on the membrane-based activation of the UPR in higher eukaryotes. Here, the hypothesis that the TMH region of the human UPR sensor PERK act as a sensor for lipid bilayer stress in mammals shall be investigated. The minimal sensor construct $^{MBP}PERK_{AH\text{-}TMH}$ will be reconstituted in liposomes with defined lipid compositions and the oligomerization of the construct will be studied by continuous wave electron paramagnetic resonance (cwEPR) spectroscopy.

4 Materials

4.1 Chemicals and reagents

All chemicals and reagents used in this study were of analytical or higher grad. Components, salts and additives used for buffers are listed in Table 1. All used solvents are listed in Table 2 and prepared protease inhibitor stock solutions are shown in Table 3. Components and additives for cultivation of *S. cerevisiae* and *Escherichia coli* (*E. coli*) are given in Table 4. Purchased lipids used in this study are listed in Table 5.

Table 1: Buffer components, salts and additives

Name	Source
4-(2-Aminoethyl)benzensulfonylfluorid (AEBSF)	Fluka
Acetic acid	Sigma-Aldrich
Agarose	Sigma-Aldrich
Antipain	Sigma-Aldrich
Biotin	Carl Roth
Bromphenol Blue	Carl Roth
Calcium chloride ($CaCl_2$)	Carl Roth
Chymostatin	Sigma-Aldrich
Copper (II)-sulfate ($CuSO_4$)	Carl-Roth
Desoxyribonucleotide triphosphate (dNTP) mix	NEB
Dithiothreitol (DTT)	Sigma-Aldrich
Ethidium bromide	Carl Roth
Ethyldiaminetetraacetic acid (EDTA)	Carl Roth
Glycerol 99.5%	Carl Roth
Glycine	Carl Roth
4-(2-hydroxyethyl)-1-piperazineethanesulfonic acid (HEPES)	Carl Roth
Hydrochloric acid (HCl)	NeoLab, Sigma-Aldrich
Imidazole	Sigma-Aldrich
Isopropyl- β-D-thiogalactopyranosid (IPTG)	Carl Roth
Lithium acetate (LiAc)	Sigma-Aldrich
Magnesium chloride ($MgCl_2$)	Carl Roth
Magnesium sulfate ($MgSO_4$)	Carl Roth
Mangan (II)-chloride ($MnCl_2$)	Carl Roth
(D+)-Maltose monohydrate	Carl Roth
Maltotriose	Sigma-Aldrich
β-Mercaptoethanol	Sigma-Aldrich
N-ethylmaleimide (NEM)	Sigma-Aldrich
β-Octylglucopyranoside (β -OG)	Calbiochem
Pepstatin	Sigma-Aldrich
Phosphate buffered saline (PBS)	Sigma-Aldrich
Piperazine-N,N'-bis(2-ethanesulfonic acid) (PIPES)	Carl Roth
Polyethylene glycol (PEG) 4000	Sigma-Aldrich
Potassium acetate (KAc)	Sigma-Aldrich
Potassium chloride (KCl)	Carl Roth
Salmon sperm DNA	Thermo Scientific
Skim milk powder	Carl Roth
Sodium azide (NaN_3)	GBioscience
Sodium carbonate (Na_2CO_3)	Sigma-Aldrich
Sodium chloride (NaCl)	Carl Roth
Sodium dodecyl sulfate (SDS)	Carl Roth
Sodium di-hydrogen phosphate (NaH_2PO_4)	Carl Roth
di-Sodium hydrogen phosphate (Na_2HPO_4)	Merck
Sodium hydroxide (NaOH)	Carl Roth

Name	Source
Sucrose	Carl Roth
Tris(hydroxymethyl)-aminomethan (Tris)	Sigma-Aldrich
Triton X-100	Carl Roth
Tunicamycin (TM)	Sigma-Aldrich
Tween 20	Sigma-Aldrich
Urea	Carl Roth

Table 2: Solvents

Name	Source
Chloroform > 99%	Carl Roth
Dimethylsulfoxid (DMSO)	Carl Roth
Ethanol 96% + 1% MEK	Carl Roth
Ethanol 96%	NeoLab
Isopropanol	AppliChem
Methanol	Carl Roth
RNase free water	Qiagen
Ultrapure water	Millipore

Table 3: Protease Inhibitor Stocks

Name	
5000x AEBSF	50 mg/ml AEBSF in ultrapure water
100x N-Ethylmaleimide (NEM)	1 M NEM dissolved in ultrapuree water
1000x protease inhibitor cocktail (PIC)	10 mg/ml chymostatin 10 mg/ml antipain 10 mg/ml pepstatin dissolved in DMSO

Table 4: Components and additives for culture media

Name	Source
Agar-Agar (Agar)	ForMedium
Ammonium sulfate ($(NH_4)_2SO_4$)	Carl Roth
Ampicillin sodium salt	Carl Roth
Chloramphenicol	Carl Roth, Sigma-Aldrich
Complete supplement mixture (CSM)	
w/o histidine	MP Biomedicals
w/o leucine	MP Biomedicals
w/o uracile	MP Biomedicals
G418 disulfate salt	Sigma-Aldrich
Galactose	Carl Roth
Glucose	Carl Roth
Tryptone/Peptone	Carl Roth
Yeast extract	Carl Roth
Yeast nitrogen base (YNB)	BD Bioscience, ForMedium
Yeast nitrogen base (YNB) w/o inositol	ForMedium

Table 5: Purchased lipids

Name	Source
1,2-Dioleoyl-*sn*-glycero-3-phosphocholine (DOPC)	Avanti Polar Lipids
1-Palmitoyl-2-oleoyl-*sn*-glycero-3-phosphocholine (POPC)	Avanti Polar Lipids

Name	Source
1,2-Dipalmitoyl-*sn*-glycero-3-phosphocholine (DPPC)	Avanti Polar Lipids
1- Palmitoyl-2-oleoyl-*sn*-glycero-3-phosphoethanolamine (POPE)	Avanti Polar Lipids
L-α-phosphatidylinositol (Soy) (Soy-PI)	Avanti Polar Lipids
E. coli polar lipids (EPL)	Avanti Polar Lipids
Cholesterol (Chol)	Avanti Polar Lipids

4.2 Commercially available systems

Commercially available systems as kits and standards are listen in Table 6 and used according to the manufacturer's protocol with the provided buffers if not stated otherwise.

Table 6: Kits and standards

Name	Source
Amylose-Resin	NEB
Bio-Beads™ SM-2 Adsorbent Media	BioRad
Clarity Western ECL Substrate	BioRad
DNA loading dye	NEB
EZview Red Anti-FLAG M2 affinity gel	Sigma-Aldrich
GeneRuler 1kb DNA ladder	NEB
GeneRuler 100 bp DNA ladder	NEB
High Capacity Streptavidin Agarose Resin	Thermo Scientific
Instant Blue™ Protein Stain	Expedeon
Mini-PORTEAN-TGX gels (4-15%, 7.5%)	BioRad
Ni-NTA Agarose	Qiagen
Oligo (dT) 12-18 primer	Life Technologies
ORA qPCR Green ROX L Mix	HighQu
PD-10 columns	GE Healthcare
Precision Plus Protein All Blue Prestained Protein Standard	BioRad
RiboLock RNase Inhibitor	Thermo Scientific
RNeasy Plus Mini Kit	Qiagen
Q5 Site-Directed Mutagenesis Kit	NEB
QIAprep Spin Miniprep Kit	Qiagen
QIAquick Gel Extraction Kit	Qiagen
QIAquick PCR Purification Kit	Qiagen
Quick Ligation Kit	NEB
SuperScript II Reverse Transcriptase	Invitrogen
SuperSignal West Femto ECL developing solution	Thermo Scientific

4.3 Enzymes

All enzymes used for molecular cloning and biochemical purposes are listed in Table 7. Unless stated otherwise, the enzymes were used according to the manufacturer's protocols and with the recommended buffers.

Table 7: Enzymes

Name	Source
*BamH*I	NEB
Benzonase	Sigma-Aldrich
*BssH*II	NEB
3C-Protease	Ernst Lab
*Dpn*I	NEB
*Hind*III	NEB

Name	Source
Phusion DNA Polymerase	NEB
Quick Ligase	NEB
TEV protease	Ernst Lab
*Xho*I	NEB

4.4 Antibodies

All antibodies used for immunoblotting are given in Table 8. Working solutions of primary and secondary antibodies were prepared in 3 – 5% skim milk powder dissolved in TBS-T. Dilutions of primary antibodies were stored in the presence of 0.01% sodium azide to prevent bacterial growth.

Table 8: Antibodies

Primary Antibodies	Dilution	Source
Anti-Dpm1 monoclonal, 5C5A7 (mouse)	1:2,000	Life Technologies
Anti-FLAG monoclonal, M2 (mouse)	1:2,000	Santa Cruz
Anti-HA monoclonal, 3F10 (rat)	1:5,000	Roche
Anti-MBP monoclonal (mouse)	1:20,000	NEB
Anti-Pgk1 monoclonal, 22C5 (mouse)	1:20,000	Invitrogen
Secondary Antibodies	**Dilution**	**Source**
Anti-mouse-HRP (goat)	1:20-40,000	Dianova
Anti-rat-HRP (goat)	1:20,000	Dianova

4.5 Supplies and Equipment

Consumables and laboratory equipment used in this study are listen in Table 9 and Table 10.

Table 9: Consumables

Name	Source
96-well plates, sterile and unsterile	Brand
96-deep-well plates	Genetix
Amicon Ultra, Ultracel 100 K	Millipore
BD Microlance 3 hypodermic needle (0.5 mm x 25 mm)	BD
Bottle Top Filter (0.22 µm, 0.45 µm)	Carl Roth, Sarstedt
Clear optical sealing film for Piko-PCR	Thermo Scientific
Cryogenic tubes NUNC with external thread (1.8 ml)	Sarstedt, VWR
Culture flasks (100 ml, 250 ml, 500 ml, 2 l)	VWR
Culture tubes with cap, sterile (14 ml)	Sarstedt, VWR
Cuvettes, disposable (semi-micro)	VWR
Eppendorff Gel Loader 20 µl Tips	Eppendorff
Falcon tubes (15 ml, 50 ml)	Sarstedt, VWR
Filter paper	BioRad
Glass beads	Carl Roth
Inoculation loops	VWR
Microcentrifuge tubes (0.2 ml, 0.5 ml, 1.5 ml, 2 ml)	Carl Roth, Eppendorf
Microcentrifuge tubes, (1.5 ml) (for TLA 55 rotor)	Beckmann
PD10 desalting column	GE Healthcare
Petri dishes, sterile (90 mm)	VWR
Piko PCR Plate, 96 well, white	Thermo Scientific
Pipette tips, refill, next generation (10 µl, 200 µl)	VWR
Pipette tips (1000 µl)	Carl Roth
PVDF membrane 0.45 µm	PALL

Name	Source
Ringcaps 50 µl	Hirschmann
Scalpel	Braun
Serological pipettes (5 ml, 10 ml, 25 ml)	VWR
Silicon stoppers SILICOSEN© C-type	VWR
Sterican hypodermic needle (0.9 mm x 40 mm)	Braun
Surphob SafeSeal filter pipette tips (10 µl, 20 µl, 200 µl, 1000 µl)	Biozym
Syringe filters (0.2 µm)	VWR
Syringes, luer-lock (1 ml, 5 ml)	Braun
Vacuum filtration systems (150 ml, 0.2 µm)	VWR
Vivaspin 2 (MWCO 100 kDa)	GE Healthcare
Zirkonia Beads (0.5 mm)	Carl Roth

Table 10: Laboratory equipment

Name	Source
96-well plate reader (BMG Fluostar Galaxy)	MTX Lab Systems
96-well plate reader (Infinite 200 PRO)	Tecan
ÄKTA™ Pure	GE Healthcare
Analytical balance	KERN & SOHN GmbH
Balance	Satorius
Bead Beater	BioSpec
Block Heater, Dual control	Stuart
Cell density meter, UltrospecTM 10 Classic	GE Healthcare
Centrifuge Avanti J-26 XP	Beckmann
ChemiDoc™ MP System	BioRad
Desiccator DN150 Duran	DURAN group GmbH
Disruptor Genie, analog	USA Scientific
Douncer	
Electrophoresis chamber	BioRad
FluroMax 4 fluorescence spectrometer	Horiba Scientific
Hellma® fluorescence cuvette, Suprasil® quartz, 100 µl	Sigma-Aldrich
Gyro-rocker SSL3	Stuart
Incubator Innova 42	Eppendorf
Magnetic stirrer with heating plate	Heidolph
Microcentrifuges (5415R, 5417R, 5424, 5804R)	Eppendorf
Mini-PROTEAN Tetra Cell	BioRad
MiniScope (MS-5000) ESR spectrometer	Magnettech
Multichannel pipette, motorized (100 µl, 300 µl)	Eppendorf
NanoDrop (ND-1000)	PeqLab
Nutating mixer	VWR
PCR thermal cycler	Analytik Jena AG
PikoReal™ Real-time PCR system	Thermo Scientific
Pipettes (10 µl, 20 µl, 200 µl, 1000 µl)	Gilson
Pipette (5 ml)	Eppendorf
Pipette boy 2	Integra
Polycarbonate Harvesting Bottle (for JLA 8.1000)	Beckmann
Power supply (PowerPacTM HC)	BioRad
Roller mixer SRT 6	Stuart
Rotors	
JLA 8.1000 (for Avanti)	Beckmann
TLA-120.1 (for Optima XP)	Beckmann
TLA-120.2 (for Optima XP)	Beckmann
TLA-55 (for Optima XP	Beckmann
Ti70 (for Optima XPN)	Beckmann
SWR 28.1 (for Optima XPN)	Beckmann
Sonifier cell disruptor	Branson Ultrasonic
Superdex 200 10/300 Increase column	GE Healthcare

Name	Source
Superose 6 10/300 Increase column	GE Healthcare
Thermal shaker	Eppendorf
TransBlot TurboTM transfer system	BioRad
Ultracentrifuge (Optima™ MAX, TL-100)	Beckmann
Ultracentrifuge (Optima XPN)	Beckmann
Ultracentrifuge Tubes	
Thinwall Polycarbonate Tubes 13 ml (for SW 28.1)	Beckmann
Thickwall Polycarbonate Tubes 1.0 ml (for TLA120.1)	Beckmann
Thickwall Polycarbonate Tubes 0.5 ml (for TLA120.2)	Beckmann
Centrifuge Bottles 26.3 ml (for Ti70)	Beckmann
Ultrasonic bath	VWR
Vortex Genie 2	USA Scientific

4.6 Plasmids

All plasmids used for *in vivo* and *in vitro* experiments are listen in Table 11 and Table 12.

Table 11: Plasmids for *in vivo* characterization of *S. cerevisiae*

Plasmid	Description	Source
pRS315	Empty vector (CEN6-ARS4, LEU2, Amp)	EUROSCARF
	pRS315-*IRE1*-GFP WT	Peter Walter lab (Aragón et al., 2009)
pRE451	pcDNA3.1(+)-*IRE1*-3xHA-GFP WT	Robert Ernst lab
pRE379	pcDNA3.1(+)-*IRE1*-3xHA-GFP cys-less	This study
pRE378	pcDNA3.1(+)-*IRE1*-3xHA-GFP cys-less C552	This study
pRE575	pcDNA3.1(+)-*IRE1*-3xHA-GFP cys-less E540C	This study
pRE576	pcDNA3.1(+)-*IRE1*-3xHA-GFP cys-less T541C	This study
pRE577	pcDNA3.1(+)-*IRE1*-3xHA-GFP cys-less G542C	This study
pRE578	pcDNA3.1(+)-*IRE1*-3xHA-GFP cys-less V543C	This study
pRE579	pcDNA3.1(+)-*IRE1*-3xHA-GFP cys-less F544C	This study
pRE570	pcDNA3.1(+)-*IRE1*-3xHA-GFP cys-less L545C	This study
pRE581	pcDNA3.1(+)-*IRE1*-3xHA-GFP cys-less L546C	This study
pRE691	pcDNA3.1(+)-*IRE1*-3xHA-GFP cys-less L547C	This study
pRE692	pcDNA3.1(+)-*IRE1*-3xHA-GFP cys-less F548C	This study
pRE693	pcDNA3.1(+)-*IRE1*-3xHA-GFP cys-less L549C	This study
pRE694	pcDNA3.1(+)-*IRE1*-3xHA-GFP cys-less I550C	This study
pRE695	pcDNA3.1(+)-*IRE1*-3xHA-GFP cys-less F551C	This study
pRE697	pcDNA3.1(+)-*IRE1*-3xHA-GFP cys-less F531R F544C	This study
pRE696	pcDNA3.1(+)-*IRE1*-3xHA-GFP cys-less F544A C552	This study
pRE698	pcDNA3.1(+)-*IRE1*-3xHA-GFP cys-less F531R C552	This study
pRE793	pcDNA3.1(+)-*IRE1*-3xHA-GFP cys-less W426A F544C	This study
pRE789	pcDNA3.1(+)-*IRE1*-3xHA-GFP cys-less W426A E540C	This study
pRE790	pcDNA3.1(+)-*IRE1*-3xHA-GFP cys-less W426A T541C	This study
pRE835	pcDNA3.1(+)-*IRE1*-3xHA-GFP cys-less L545C L546C	This study
pRE834	pcDNA3.1(+)-*IRE1*-3xHA-GFP cys-less I550C C552	This study
pRE571	pcDNA3.1(+)-*IRE1*-3xFLAG-GFP cys-less	This study
pRE572	pcDNA3.1(+)-*IRE1*-3xFLAG-GFP cys-less C552	This study
pRE699	pRS315-*IRE1*-3xFLAG-GFP cys-less	This study
pRE700	pRS315-*IRE1*-3xFLAG-GFP cys-less C552	This study
pRE618	pRS425-GAL1-Signal sequence-H14-3C-CPY*-SBP-HDEL	Alexander Stein lab (Stein et al., 2014)
pRE619	pRS425-GAL1-Signal sequence-H14-3C-CPY-SBP-HDEL	Alexander Stein lab (Stein et al., 2014)

Table 12: Plasmids carrying *in vitro* constructs for the isolation from *E. coli*

Plasmid	Description	Source
pRE424	pMALC-2x-MBP-*IRE1*-AH+TMH WT (S526 – L561)	Robert Ernst lab
pRE431	pMALC-2x-MBP-*IRE1*-AH+TMH C552S (S526 – L561)	Robert Ernst lab
pRE801	pMALC-2x-MBP-*IRE1*-cLD+AH+TMH cys-less (N111- L561)	Susanne Wolf (supervised bachelor thesis)
pRE811	pMALC-2x-MBP-*PERK*-AH+TMH+Rest (human) WT (K512 – Q551)	Julian Bruckert (supervised bachelor thesis)
pRE813	pMALC-2x-MBP-*PERK*-AH+TMH+Rest (human) cys-less (K512 – Q551)	Julian Bruckert (supervised bachelor thesis)
pRE819	pMALC-2x-MBP-*PERK*-AH+TMH+Rest (human) L518R	This study
pRE825	pMALC-2x-MBP-*PERK*-AH+TMH+Rest (human) D514K E525E	This study
pRE826	pMALC-2x-MBP-*PERK*-AH+TMH+Rest (human) D514N E525Q	This study

4.6.1 Construction of *IRE1* knock-in constructs

All plasmids used for genomic integration of *IRE1* were based on a previously established knock-in construct in a pcDNA3.1(+) vector system (Halbleib et al., 2017). The knock-in construct consists of a His3MX6 marker cassette, the endogenous promotor of *IRE1* (-1 to -551 bp) and the coding sequence of *IRE1* flanked at the 5' and 3' terminal sides by regions homologous to the *IRE1* locus for genomic insertion by recombination. A 3xHA-tag and a monomeric yeGFP variant (A206R) were inserted at position H875 of Ire1 (Figure 11).

Figure 11: Schematic representation of the knock-in construct for *IRE1*.

The knock-in construct of *IRE1* consists of a His3MX6 marker cassette (orange), 551 bp of *IRE1* promotor (light blue), coding regions for *IRE1* gene (blue), a 3xHA-tag (light grey) and a monomeric, codon-optimized yeGFP (A206R) (green). The knock-in construct is flanked by regions homologous to the *IRE1* locus at the 5' and 3' end (dark grey) for efficient genomic targeting and homologous recombination.

Site-directed mutagenesis of the plasmid was performed using a PCR-based strategy based on the QuickChange method (Stratagene) using the PHUSION polymerase (NEB). For faster substitution of several amino acids in one step, megaprimers containing all desired mutations were produced by a classical PCR reactions for a subsequent usage for a site-directed mutagenesis of *IRE1* (5.2.7.2). Oligonucleotides used for site-directed mutagenesis are listed in Table 14.

For transformation of *S. cerevisiae* YRE127, the plasmid containing the knock-in construct was linearized using the restriction enzymes *Hind*III and *Xho*I.

4.6.2 Construction of *IRE1 CEN*-based construct

In analogy to the knock-in construct, a *CEN*-based construct with a region encoding for a 3xFLAG-tag was cloned into the open reading frame of *IRE1* on the pEvA200 plasmid (van Anken et al., 2014). To this end, the original 3xHA-tag of the knock-in construct was substituted by a 3x-FLAG-tag using Q5 site-directed mutagenesis kit (NEB). The newly generated knock-in construct was amplified in a multi-step PCR reaction to add a long terminator sequence and *BssH*I and *Hind*III restriction sites in the last PCR reaction step. The entire $IRE1_{3xFLAG\text{-}GFP}$ sequence was transferred into the pEvA200 vector by classical, restriction-based cloning using the *BssH*I/*Hind*III restriction sites. Oligonucleotides used for the cloning of the *IRE1 CEN*-based construct are listed in Table 13.

4.6.3 Construction of constructs encoding for MBP fusion proteins

The minimal sensor constructs of Ire1 from baker's yeast and PERK encoded for MBP, a polyN linker, a TEV cleavage site and the predicted AH and TMH region of Ire1 and PERK, respectively. The cloning into the pMAL-C2x TEV *E. coli* expression vector of Ire1 was performed by Jonas Michaelis and is described in his diploma thesis (Michaelis, 2015). The $^{MBP}PERK_{AH\text{-}TMH}$ constructs were cloned together with Julian Bruckert in the course of his bachelor thesis. In brief, oligonucleotides coding for the predicted AH and TMH regions of the human UPR sensors were annealed, phosphorylated and cloned into pMAL-C2x TEV *E. coli* expression vector using *EcoR*I/*Hind*III restriction sites (Bruckert, 2016).

The region encoding for the core ER-luminal domain and its AH and TMH of *IRE1* (N111-L561) was cloned into the pMALC2x-TEV *E. coli* expression vector together with Susanne Wolf in the course of her bachelor thesis (Wolf, 2016). The $IRE1_{cLD\text{-}AH\text{-}TMH}$ sequence amplified by PCR was transferred into the pMALC2x-TEV *E. coli* expression vector via *EcoR*I/*Hind*III cloning. Oligonucleotides used for the cloning of $^{MBP}Ire1_{cLD\text{-}AH\text{-}TMH}$ can be found in Table 13. Mutagenesis was performed using the QuickChange method (Stratagene) using the PHUSION polymerase (NEB). Oligonucleotides used for this reaction are listed in Table 14.

4.7 Oligonucleotides

HPLC-purified oligonucleotides used in this study were purchased from Sigma-Aldrich. Oligonucleotides used for molecular cloning are shown in Table 13. Oligonucleotides used for site-directed mutagenesis on *IRE1* constructs are listed in Table 14. Oligonucleotides used for site-directed mutagenesis on *PERK* constructs are listed in Table 15. Oligonucleotides used for sequencing and for colony PCR are given in Table 16 and Table 17, respectively.

Oligonucleotides used for reverse transcription quantitative PCR (RT-qPCR) are specified in Table 18.

Table 13: Oligonucleotides used for molecular cloning

Name	Sequence	Description
TP334	CATGACATCGACTACAAGGATGACGATGACAAGTCTAAAGGTGA AGAATTATTCAC	Exchange of 3xHA to 3xFLAG by Q5 (fwd)
TP335	ATCTTTATAATCACCGTCATGGTCTTTGTAGTCGTGTTCC GTTTCGACTTG	Exchange of 3xHA to 3xFLAG by Q5 (rev)
KP33	CGCGCGGCCGCCTGAAACTCTGCTGCGCGCTGAAAAC	CGC-*Not*I-*BssH*II *IRE1*prom (fwd)
KP34	GGATGGTTACTACTAATGATCAAAGTAACATTAATGCAATA ATCAACCAAGAAGAAGCAG	*IRE1*term part I (rev)
KP35	GCGAAGCTTGTACAACTTTTTTTCATTTATGCAAGGGCGT AAAAATTATGGATGGTTACTACTAATGATC	GCG-*Hind*III-*IRE1*term part II (rev)
KP80	TAGGGATGAGAAAAGTAGTATAGGTTCATGAAGAAGTACA ACTTTTTTTCATTTATGCAAGGGC	*IRE1*term part III (rev)
KP94	GTTTATGAGATATGTATTTATAAAATTAAATGTCTGTCGGG TAGTTTATGTAGGGATGAGAAAAGTAGTATAGGTTC	*IRE1*term part IV (rev)
KP95	GCGAAGCTTTCCACCAAAAAAGTCAGTGTTGAATAACTGGAGTA GTATGTCGATGTTCGATGTTTATGAGATATGTATTTATAAAATTAA ATG	GCG-*Hind*III-*IRE1*term part V (rev)
KP70	CGCGGATCCAATCGTTCCTTGAACGAAC	CGC-*BamH*I-*IRE1* (bp 331 - 349) (fwd)
TP311	CGCAAGCTTTTACAAAATTTTGAATCTTTGTAG	CGC-*Hind*III-*IRE1* (bp 1663 – 1683) (rev)

Table 14: Oligonucleotides used for site-directed mutagenesis on *IRE1*

Name	Sequence	Description
KP9	GAGTCGAAATCGCTAAATTCTCCCTCTTCATCGGAAAATG	C589S (fwd)
KP10	CCATTAAAGCTATGTCAGAAAAATCAATTAACATTC	C709S (rev)
KP11	GTCATACGATACTACTCTTCAGAAACAACAGAC	C733S (fwd)
KP12	GAGTCTAGTTTTTTGGAAAGACCAAAGTCTG	C832S (rev)
KP13	GTATATTGCTTTAGAGCTCTCCAATTTGAACCTTCAAG	C748S (fwd)
KP14	GTTCCGTTTCGACTTGGGACTGCAAATTGTTTGATTC	C869S (rev)
KP15	GATATTTTTTCTATGGGATCTGTATTCTATTATATCC	C908S (fwd)
KP16	GGATCTATCATGTAGAGATTTCATTTCATCAAG	C943S (rev)
KP17	GAGCCAGAGTGTGGATTCCTCACCTGAGGAGAAG	C263S (fwd)
KP18	CGGAAAGGCGCTATGGACATGCCGTCCTTTG	C325S (rev)
KP19	GAGAAGATAAAACTTCAGGAATCTGAAAATATGATTGTAATAGGC	C274S (fwd)
KP20	GACCTTAAAATTTATTTCTACTACTGGTAAATTGC	GFP C48S (fwd)
KP22	GTGACCTAAAATGTTACCATCTTC	GFP (rev)
TP244	GTATTTCTGTTGTTATTTCTCATTTTTTCTGCAATACTACAAAGATTCAAA ATTTTG	C552S (fwd)
TP245	CAAAATTTTGAATCTTTGTAGTATTGCAGAAAAAATGAGAAATAACAACA GAAATACTCC	C552S (rev)
TP214	GAAGTTTGGAAGTCTAGTATATCGAATTATATGTACTGGAGTATTTCTGT TG	E540C (fwd)
TP215	GAAATAACAACAGAAATACTCCAGTACATATAATTCGATATACTAGACTT CCAAACTTCAG	E540C (rev)
TP216	AGTTTGGAAGTCTAGTATATCGAATTATAGAGTGTGGAGTATTTCTGTTG	T541C (fwd)
TP217	TGAGAAATAACAACAGAAATACTCCACACTCTATAATTCGATATACTAGA CTTCCAAAC	T541C (rev)
TP218	GAAGTTTGGAAGTCTAGTATATCGAATTATAGAGACTTGTGTATTTCTGT TGTTATTTCTCA	G542C (fwd)

Name	Sequence	Description
TP219	TGAGAAATAACAACAGAAATACACAAGTCTCTATAATTCGATATACTAGACTTCCAAAC	G542C (rev)
TP220	GTCTAGTATATCGAATTATAGAGACTGGATGTTTTCTGTTGTTATTTCTCAT	V543C (fwd)
TP221	ATGAGAAATAACAACAGAAAACATCCAGTCTCTATAATTCGATATACTAGAC	V543C (rev)
TP222	AGTATATCGAATTATAGAGACTGGAGTATGTCTGTTGTTATTTCTCATTTTTTCTGC	F544C (fwd)
TP223	TGCAGAAAAAATGAGAAATAACAACAGACATACTCCAGTCTCTATAATTCGATATACT	F544C (rev)
TP224	CGAATTATAGAGACTGGAGTATTTTGTTTGTTATTTCTCATTTTTTCTGCAATACTAC	L545C (fwd)
TP225	GTAGTATTGCAGAAAAAATGAGAAATAACAAACAAAATACTCCAGTCTCTATAATTCG	L545C (rev)
TP226	CGAATTATAGAGACTGGAGTATTTCTGTGTTTATTTCTCATTTTTTCTGCAATACTACAAAG	L546C (fwd)
TP227	CTTTGTAGTATTGCAGAAAAAATGAGAAATAAACACAGAAATACTCCAGTCTCTATAATTCG	L546C (rev)
TP228	CGAATTATAGAGACTGGAGTATTTCTGTTGTGTTTTCTCATTTTTTCTGCAATACTACAAAG	L547C (fwd)
TP229	CTTTGTAGTATTGCAGAAAAAATGAGAAAACACAACAGAAATACTCCAGTCTCTATAATTCG	L547C (rev)
TP230	AGAGACTGGAGTATTTCTGTTGTTATGTCTCATTTTTTCTGCAATACTACAAAGA	F548C (fwd)
TP231	TCTTTGTAGTATTGCAGAAAAAATGAGACATAACAACAGAAATACTCCAGTCTCT	F548C (rev)
TP232	AGACTGGAGTATTTCTGTTGTTATTTTGTATTTTTTCTGCAATACTACAAAGATTCAAAATTTTG	L549C (fwd)
TP233	CAAAATTTTGAATCTTTGTAGTATTGCAGAAAAAATACAAAATAACAACAGAAATACTCCAGTCT	L549C (rev)
TP234	AGACTGGAGTATTTCTGTTGTTATTTCTCTGTTTTTCTGCAATACTACAAAGA	I550C (fwd)
TP235	TGAATCTTTGTAGTATTGCAGAAAAACAGAGAAATAACAACAGAAATACTCCAGTCT	I550C (rev)
TP236	GACTGGAGTATTTCTGTTGTTATTTCTCATTTGTTCTGCAATACTACAAAGATTC	F551C (fwd)
TP237	GAATCTTTGTAGTATTGCAGAACAAATGAGAAATAACAACAGAAATACTCCAGTC	F551C (rev)
TP348	CCAAAATTCTTTGCTACTGAAGCGTGGAAGTCTAGTATATCG	F531R (fwd)
TP349	CTATAATTCGATATACTAGACTTCCACGCTTCAGTAGCAAAG	F531R (rev)
TP177	CTGGAGTAGCTCTGTTGTTATTTCTCATTTTTTG	F544A (fwd)
TP178	CAAAAAATGAGAAATAACAACAGAGCTACTCCAG	F544A (rev)
TP154	CGCTTCCAGTGACCGTGCGAGGGTGTCTTCAATTTTTG	W426A (fwd)
TP155	CAAAAATTGAAGACACCCTCGCACGGTCACTGGAAGCG	W426A (rev)
KP187	GGAAGTCTAGTATATCGAATTTGTGAGACTGGAGTATTTCTGTTG	I539C (fwd)
KP188	CAACAGAAATACTCCAGTCTCACAAATTCGATATACTAGACTTCC	I539C (rev)
KP189	GGAAGTCTAGTATATCGAATTTGTGAGTGTGGAGTATTTCTGTTGTTATTTC	I539C, T541C (fwd)
KP190	GAAATAACAACAGAAATACTCCACACTCACAAATTCGATATACTAGACTTCC	I539C, T541C (rev)
KP185	GAATTATAGAGACTGGAGTATTTTGTTGTTTATTTCTCATTTTTTCTGC	L545C, L546C (fwd)
KP186	GCAGAAAAAATGAGAAATAAACAACAAAATACTCCAGTCTCTATAATTC	L545C, L546C (fwd)
KP183	GTATTTCTGTTGTTATTTCTCTGTTTTTGTGCAATACTACAAAG	I550C, C552 (fwd)
KP184	CTTTGTAGTATTGCACAAAAACAGAGAAATAACAACAGAAATAC	I550C, C552 (rev)

Table 15: Oligonucleotides used for site-directed mutagenesis on *PERK*

Name	Sequence	Description
KP129	CAAAAAGGATCCTGTTCTTCGTTTACACTGGTGGAAAG	L518R (fwd)
KP136	CTTTCCACCAGTGTAAACGAAGAACAGGATCCTTTTTG	L518R (rev)
KP173	GCTAGCGAATTCAAAAAGAAACCTGTTCTTCTTTTACACTGGTGGAAAAA AATAGTTGCAACG	D514K E525K (fwd)
KP174	CGTTGCAACTATTTTTTTCCACCAGTGTAAAAGAAGAACAGGTTTCTTTT TGAATTCGCTAGC	D514K E525K (rev)
KP175	GCTAGCGAATTCAAAAAGAATCCTGTTCTTCTTTTACACTGGTGGAAACA AATAGTTGCAACG	D514N E525Q (fwd)
KP176	CGTTGCAACTATTTGTTTCCACCAGTGTAAAAGAAGAACAGGATTCTTTT TGAATTCGCTAGC	D514N E525Q (rev)

Table 16: Oligonucleotides used for sequencing

Name	Sequence	Description
TP5	CGCAGCCGACGTTGAGGGTGGACTTC	*IRE1* bp 371 – 398 (fwd)
TP6	CAAGTTGTCGTATGGATAAAGGCAG	*IRE1* bp 571 – 595 (rev)
TP7	GGACGGCATGTGCATAGCGCCTTTCCG	*IRE1* bp 962 – 990 (fwd)
TP8	GCTACTGAAGTTTGGAAGTCTAG	*IRE1* bp 1580 – 1604 (fwd)
TP9	GAGGAAAAGAGGTTCGAGAGGAG	*IRE1* bp 1932 – 1954 (fwd)
TP10	CTAGACTCTGGTCAGTCTTCATT	*IRE1* bp 2503 – 2526 (fwd)
TP11	GCAGAAGCTACAGATCTGATCTC	*IRE1* bp 2851 – 2873 (fwd)
TP31	ATGATTATACATGGGGATGT	His3MX6 cassette (rev)
TP34	CCCTCCTTGACAGTCTTGAC	Heukan (fwd)
TP67	GTTATAGACTTTTCACTGTTAG	*IRE1* prom bp -222 – - 220 (rev)
TP130	CAGACCGCTTCTGCGTTCTG	MBP-$IRE1_{cLD\text{-}AH+TMH}$ bp + 220 - +240 (rev)
RE450	GGTATTAACGCCGCCAGTCC	malE bp 2323 – 2342 (fwd)
lacOp-for	CGGATAACAATTTCACACAG	Lac operator Seqlab primer bp - 68 – - 88

Table 17: Oligonucleotides to check for integration of the knock-in construct

Name	Sequence	Description
TP11	GCAGAAGCTACAGATCTGATCTC	Check integration of *IRE1-3xHA-GFP* 5’ fwd
TP202	CGGGTAGTTTATGTAGGGATGAG	Check integration of *IRE1-3xHA-GFP* 5’ rev
TP201	GCAAGTATGAACTATTTGGAAACAC	Check integration of *IRE1-3xHA-GFP* 3’ fwd
RE133	GTCAAGACTGTCAAGGAGGG	Check integration of *IRE1-3xHA-GFP* 3’ rev

Table 18: Oligonucleotides used for RT-qPCR

Name	Sequence	Description
TP127	CTTTGTCGCCCAAGAGTATGCG	Spliced *HAC1* (fwd)
TP287	ACTGCGCTTCTGGATTACGC	Spliced *HAC1* (rev)
TP324	GATCGATTACGAGGGACCTAGA	*PDI1* (fwd)
TP325	GCGGAGGGCAAGTAAATAGAA	*PDI1* (rev)
TP169	TGTCACCAACTGGGACGATA	*ACT1* (fwd)
TP170	AACCAGCGTAAATTGGAACG	*ACT1* (rev)

4.8 Organisms

The *E. coli* strain DH5α was used for cloning and amplification of yeast and bacterial expression vectors. For the heterologous production of MBP-TMH fusion proteins using expression vectors, the *E. coli* strain BL21 carrying the pLysS plasmid was used, while the

E. coli strain CodonPlus was used for the heterologous expression of ^{MBP}Ire1$_{cLD\text{-}AH\text{-}TMH}$ constructs. The genotypes of *E. coli* strains are listed in Table 19.

Table 19: *E. coli* strains used in this study

Name	Genotype	Source
BL21 CodonPlus (DE3) RIL strain	*E. coli* B F$^-$ *ompT hsdS*($r_B^-m_B^-$) *dcm*$^+$ Tet^r *gal* λ(DE3) *endA* Hte [*argU ileY leuW* Cam^r]	Maike Bublitz lab (Agilent Technologies)
BL21 Star (DE3) pLysS	*E. coli* F$^-$ *ompT gal dcm lon hsdS*$_B$($r_B^-m_B^-$) *rne131* λ(DE3) pLysS(Cam^R)	Robert Tampé Lab
DH5α (K12 strain)	*E. coli* F$^-$ φ80*lacZΔ*(*lac*ZYA-*arg*F)U169 *rec*A *end*A1 *hsd*R17($r_K^-m_K^+$) *pho*A *sup*E44 λ$^-$ *thi*-1 *gyr*A96 *rel*A1	Invitrogen

All *S. cerevisiae* strains used in this thesis are listen in Table 20.

Table 20: *S. cerevisiae* used in this study

Strain number	Description	Genotype	Source	Plasmid
YRE001	BY4741	MATa; *his*Δ1; *leu2*Δ0; *met15*Δ0;*ura3*Δ0	EUROSCARF	
YRE046	Δ*IRE1*	MATa; *his*Δ1; *leu2*Δ0; *met15*Δ0; *ura3*Δ0; *ire1*ΔkanMX3	EUROSCARF	
YRE127	Δ*IRE1*Δ*IRE1prom*	MATa; *his*Δ1; *leu2*Δ0; *met15*Δ0; *ura3*Δ0; *ire1*Δ::URA	Ernst lab	
YRE425	*IRE1*-3xHA-GFP WT	MATa; *his*Δ1; *leu2*Δ0; *met15*Δ0; *ura3*Δ0; *ire1*Δ::URA; *IRE1*-3xHA-GFP::HIS	Ernst lab	pRE451
YRE343	*IRE1*-3xHA-GFP cys-less	MATa; *his*Δ1; *leu2*Δ0; *met15*Δ0; *ura3*Δ0; *ire1*Δ::URA; *IRE1*-3xHA-GFP::HIS	This study	pRE379
YRE342	*IRE1*-3xHA-GFP cys-less C552	MATa; *his*Δ1; *leu2*Δ0; *met15*Δ0; *ura3*Δ0; *ire1*Δ::URA; *IRE1*-3xHA-GFP::HIS	This study	pRE378
YRE530	*IRE1*-3xHA-GFP cys-less E540C	MATa; *his*Δ1; *leu2*Δ0; *met15*Δ0; *ura3*Δ0; *ire1*Δ::URA; *IRE1*-3xHA-GFP::HIS	This study	pRE575
YRE531	*IRE1*-3xHA-GFP cys-less T541C	MATa; *his*Δ1; *leu2*Δ0; *met15*Δ0; *ura3*Δ0; *ire1*Δ::URA; *IRE1*-3xHA-GFP::HIS	This study	pRE576
YRE532	*IRE1*-3xHA-GFP cys-less G542C	MATa; *his*Δ1; *leu2*Δ0; *met15*Δ0; *ura3*Δ0; *ire1*Δ::URA; *IRE1*-3xHA-GFP::HIS	This study	pRE577
YRE533	*IRE1*-3xHA-GFP cys-less V543C	MATa; *his*Δ1; *leu2*Δ0; *met15*Δ0; *ura3*Δ0; *ire1*Δ::URA; *IRE1*-3xHA-GFP::HIS	This study	pRE578
YRE534	*IRE1*-3xHA-GFP cys-less F544C	MATa; *his*Δ1; *leu2*Δ0; *met15*Δ0; *ura3*Δ0; *ire1*Δ::URA; *IRE1*-3xHA-GFP::HIS	This study	pRE579
YRE522	*IRE1*-3xHA-GFP cys-less L545C	MATa; *his*Δ1; *leu2*Δ0; *met15*Δ0; *ura3*Δ0; *ire1*Δ::URA; *IRE1*-3xHA-GFP::HIS	This study	pRE570
YRE535	*IRE1*-3xHA-GFP cys-less L546C	MATa; *his*Δ1; *leu2*Δ0; *met15*Δ0; *ura3*Δ0; *ire1*Δ::URA; *IRE1*-3xHA-GFP::HIS	This study	pRE581
YRE717	*IRE1*-3xHA-GFP cys-less L547C	MATa; *his*Δ1; *leu2*Δ0; *met15*Δ0; *ura3*Δ0; *ire1*Δ::URA; *IRE1*-3xHA-GFP::HIS	This study	pRE691
YRE718	*IRE1*-3xHA-GFP cys-less F548C	MATa; *his*Δ1; *leu2*Δ0; *met15*Δ0; *ura3*Δ0; *ire1*Δ::URA; *IRE1*-3xHA-GFP::HIS	This study	pRE692
YRE719	*IRE1*-3xHA-GFP cys-less L549C	MATa; *his*Δ1; *leu2*Δ0; *met15*Δ0; *ura3*Δ0; *ire1*Δ::URA; *IRE1*-3xHA-GFP::HIS	This study	pRE693
YRE720	*IRE1*-3xHA-GFP cys-less I550C	MATa; *his*Δ1; *leu2*Δ0; *met15*Δ0; *ura3*Δ0; *ire1*Δ::URA; *IRE1*-3xHA-GFP::HIS	This study	pRE694
YRE721	*IRE1*-3xHA-GFP cys-less F551C	MATa; *his*Δ1; *leu2*Δ0; *met15*Δ0; *ura3*Δ0; *ire1*Δ::URA; *IRE1*-3xHA-GFP::HIS	This study	pRE695
YRE724	*IRE1*-3xHA-GFP cys-less F531R F544C	MATa; *his*Δ1; *leu2*Δ0; *met15*Δ0; *ura3*Δ0; *ire1*Δ::URA; *IRE1*-3xHA-GFP::HIS	This study	pRE697
YRE722	*IRE1*-3xHA-GFP cys-less F544A C552	MATa; *his*Δ1; *leu2*Δ0; *met15*Δ0; *ura3*Δ0; *ire1*Δ::URA; *IRE1*-3xHA-GFP::HIS	This study	pRE696

Strain number	Description	Genotype	Source	Plasmid
YRE723	*IRE1*-3xHA-GFP cys-less F531R C552	MATa; *his*Δ1; *leu2*Δ0; *met15*Δ0; *ura3*Δ0; *ire1*Δ::URA; *IRE1*-3xHA-GFP::HIS	This study	pRE698
YRE776	*IRE1*-3xHA-GFP cys-less W426A F544C	MATa; *his*Δ1; *leu2*Δ0; *met15*Δ0; *ura3*Δ0; *ire1*Δ::URA; *IRE1*-3xHA-GFP::HIS	This study	pRE793
YRE773	*IRE1*-3xHA-GFP cys-less W426A E540C	MATa; *his*Δ1; *leu2*Δ0; *met15*Δ0; *ura3*Δ0; *ire1*Δ::URA; *IRE1*-3xHA-GFP::HIS	This study	pRE789
YRE774	*IRE1*-3xHA-GFP cys-less W426A T541C	MATa; *his*Δ1; *leu2*Δ0; *met15*Δ0; *ura3*Δ0; *ire1*Δ::URA; *IRE1*-3xHA-GFP::HIS	This study	pRE790
YRE791	*IRE1*-3xHA-GFP cys-less L545C L546C	MATa; *his*Δ1; *leu2*Δ0; *met15*Δ0; *ura3*Δ0; *ire1*Δ::URA; *IRE1*-3xHA-GFP::HIS	This study	pRE835
YRE790	*IRE1*-3xHA-GFP cys-less I550C C552	MATa; *his*Δ1; *leu2*Δ0; *met15*Δ0; *ura3*Δ0; *ire1*Δ::URA; *IRE1*-3xHA-GFP::HIS	This study	pRE834
YRE780	Δ*IRE1* *IRE1*-3xFLAG-GFP cys-less	MATa; *his*Δ1; *leu2*Δ0; *met15*Δ0; *ura3*Δ0; *ire1*ΔkanMX3; pRS315::LEU	This study	pRE571
YRE781	Δ*IRE1* *IRE1*-3xFLAG-GFP cys-less C552	MATa; *his*Δ1; *leu2*Δ0; *met15*Δ0; *ura3*Δ0; *ire1*ΔkanMX3; pRS315::LEU	This study	pRE572
YRE725	*IRE1*-3xHA-GFP cys-less + *IRE1*-3xFLAG-GFP cys-less	MATa; *his*Δ1; *leu2*Δ0; *met15*Δ0; *ura3*Δ0; *ire1*ΔkanMX3;*IRE1*-3xHA-GFP::HIS; pRS315::LEU	This study	pRE375 pRE571
YRE726	*IRE1*-3xHA-GFP cys-less + *IRE1*-3xFLAG-GFP cys-less C552	MATa; *his*Δ1; *leu2*Δ0; *met15*Δ0; *ura3*Δ0; *ire1*ΔkanMX3; *IRE1*-3xHA-GFP::HIS; pRS315::LEU	This study	pRE374 pRE572
YRE727	Δ*HRD3* Δ*ALG3*	MATa; *his*Δ1; *leu2*Δ0; *met15*Δ0; *ura3*Δ0; *hrd3*::KanR; *alg3*::HIS3;	Alexander Stein lab (Stein et al., 2014)	
YRE728	Δ*HRD3* Δ*ALG3* CPY*	MATa; *his*Δ1; *leu2*Δ0; *met15*Δ0; *ura3*Δ0; *hrd3*::KanR; *alg3*::HIS3; pRS425::LEU	Alexander Stein lab (Stein et al., 2014)	pRE618
YRE784	Δ*HRD3* Δ*ALG3* CPY	MATa; *his*Δ1; *leu2*Δ0; *met15*Δ0; *ura3*Δ0; *hrd3*::KanR; *alg3*::HIS3; pRS425::LEU	Alexander Stein lab (Stein et al., 2014)	pRE619
YRE416	Δ*IRE1* Empty Vector	MATa; *his*Δ1; *leu2*Δ0; *met15*Δ0; *ura3*Δ0; *ire1*ΔkanMX3; pRS315::LEU	This study	pRS315
YRE417	BY4741 Empty Vector	MATa; *his*Δ1; *leu2*Δ0; *met15*Δ0; *ura3*Δ0; pRS315::LEU	This study	pRS315

4.9 Media

4.9.1 Media and plates for cultivation of *E. coli*

The composition of media and plates to cultivate *E. coli* are listed in Table 21. All media were prepared with ultrapure water and sterilized by autoclaving. Cells carrying an expression vector or a plasmid for amplification were cultivated with the appropriate antibiotics for selection.

Table 21: Composition of media and plates used for cultivation of *E. coli*

Medium	Composition	
LB-Medium	1% (w/v)	Tryptone
	0.5% (w/v)	Yeast Extract
	1% (w/v)	NaCl
LB_{rich}-Medium	1% (w/v)	Tryptone

Medium	Composition	
	0.5% (w/v)	Yeast Extract
	1% (w/v)	NaCl
	0.2% (w/v)	Glucose
LB-Plates	1.5% (w/v)	Agar in LB
SOB-Medium	2 % (w/v)	Tryptone
	0.5% (w/v)	Yeast Extract
	10 mM	NaCl
	2.5 mM	KCl
	10 mM	$MgSO_4$
Antibiotics	100 µg/ml	Ampicillin
	34 µg/ml	Chloramphenicol

4.9.2 Media and plates for cultivation of *S. cerevisiae*

Media and plates used for the cultivation of *S. cerevisiae* can be found in Table 22. All media were prepared with ultrapure water and sterilized by autoclaving. The complete supplement mixture (CSM) was dissolved in ultrapure water and heated to 80°C to obtain a clear solution. The CSM was filtered with a 0.2 µm filter for sterilization.

Table 22: Composition of media and plates used for cultivation of *S. cerevisiae*

Medium	Composition	
YPD	2% (w/v)	Tryptone
	1% (w/v)	Yeast Extract
	2% (w/v)	Glucose
SCD complete	0.075% (w/v)	CSM complete
	0.5% (w/v)	Ammonium sulfate
	2% (w/v)	Glucose
	0.17% (w/v)	YNB
SCD complete w/o inositol	0.075% (w/v)	CSM complete
	0.5% (w/v)	Ammonium sulfate
	2% (w/v)	Glucose
	0.17% (w/v)	YNB w/o inositol
SCD – xx	0.075% (w/v)	CSM – xx
(- Leu, - His, - Ura)	0.5% (w/v)	Ammonium sulfate
	2% (w/v)	Glucose
	0.17% (w/v)	YNB
4x YEP	8% (w/v)	Peptone
	4% (w/v)	Yeast extract
YPD plates and SCD selective plates	1.5%	Agar in YPD or SCD media

4.10 General buffers

Buffers used in this study and their compositions are listed in Table 23. All buffers were prepared with ultrapure water.

Table 23: Compositions of buffers used in this study

Buffer	Composition	Application
5x MSB (non-reducing)	0.1 M Tris-HCl pH 6.8	SDS-PAGE
	8 M Urea	
	5 mM EDTA	
	3.2% SDS	

Buffer	Composition	Application
	0.15% (w/v) bromphenol blue 4% (v/v) glycerol	
5x MSB (reducing)	4% (v/v) β-mercaptoethanol in 5-MSB	SDS-PAGE
10x PBS	80 mM Na_2HPO_4 15 mM KH_2PO_4 1.37 M NaCl 27 mM KCl	1x PBS for washing of cell pellets
10x TEV Buffer	2 mM HEPES pH7.5 0.5 mM EDTA 1 mM DTT	TEV cleavage
Blocking buffer	3-5 % skim milk powder in TBS-T	Immunoblotting
Blotting buffer	25 mM Tris-base pH 8.3 190 mM Glycine 20% (v/v) Methanol	Immunoblotting
Buffer A	50 mM Tris-HCl pH 8 300 mM KCl 40 mM Imidazol	Purification of CPY*
Buffer AU	50 mM Tris-HCl pH 8 300 mM KCl 40 mM Imidazol 6 M Urea	Purification of CPY*
Buffer A+	50 mM Tris-HCl pH 8 300 mM KCl 100 mM Imidazol	Purification of CPY*
Buffer S	50 mM Tris-HCl pH 8 300 mM KCl 1 mM EDTA 1 mM DTT	Purification of CPY*
Elution buffer core	50 mM HEPES pH 7.5 250 mM NaCl 10% (w/v) Glycerol 50 mM OG 10 mM Maltose	Elution buffer for $^{MBP}Ire1_{cLD\text{-}AH\text{-}TMH}$
Elution buffer CPY* His	50 mM Tris-HCl pH 8 300 mM KCl 500 mM Imidazol	Elution buffer for His purification of CPY*
Elution buffer CPY* S	50 mM Tris-HCl pH 8 300 mM KCl 2 mM Biotin 1 mM EDTA 1 mM DTT	Elution buffer for Streptavidin purification of CPY*
Elution buffer TMH	50 mM HEPES pH 7.5 150 mM NaCl 1 mM EDTA 50 mM OG 10 mM Maltose	Elution buffer for $^{MBP}Ire1_{AH\text{-}TMH}$/ $^{MBP}PERK_{AH\text{-}TMH}$
IP-Wash	50 mM HEPES pH 7.5 150 mM NaCl 5 mM EDTA 0.2% (v/v) Triton X-100	IP-Washing buffer
LATE	10 mM Tris-HCl, pH 8 0.1 M LiAc 1 mM EDTA	Transformation of yeast cells
Lysis buffer core	50 mM HEPES pH 7.5 250 mM NaCl 10% (w/v) Glycerol + NEM, PIC, AEBF	Lysis buffer for $^{MBP}Ire1_{cLD\text{-}AH\text{-}TMH}$

Buffer	Composition	Application
Lysis buffer TMH	50 mM HEPES pH 7.5 150 mM NaCl 1 mM EDTA + PIC	Lysis buffer for $^{MBP}Ire1_{AH\text{-}TMH}$/ $^{MBP}PERK_{AH\text{-}TMH}$
Neutralization buffer	200 mM HEPES pH 7 150 mM NaCl	Membrane extraction assay
PLATE	10 mM Tris-HCl, pH 8 0.1 M LiAc 1 mM EDTA 40% PEG-4000	Transformation of yeast cells
Reconstitution buffer	20 mM HEPES pH 7.5 150 mM NaCl 5% (w/v) glycerol	Reconstitution of proteoliposomes Preparation of liposomes
Reconstitution buffer w/o glycerol	20 mM HEPES pH 7.5 150 mM NaCl	Reconstitution of proteolipsomes CPY* binding assay
SDS-electrophoresis buffer	25 mM Tris-base pH 8.3 190 mM Glycine 0.1% (v/v) SDS	SDS-PAGE
SEC buffer core	20 mM HEPES pH 7.5 150 mM NaCl 2 mM $CaCl_2$ 50 mM OG	SEC buffer for $^{MBP}Ire1_{cLD\text{-}AH\text{-}TMH}$
Storage buffer	20 mM HEPES pH 7.5 500 mM NaCl 0.5 mM DTT	Storage buffer for CPY*
TAE	40 mM Tris-Acetat pH 8 1 mM EDTA	Agarose gel electrophoresis
TB buffer	10 mM Pipes pH 6.7 55 mM $MnCl_2$ 15 mM $CaCl_2$ 250 mM KCl	Generation of competent *E. coli*
TBS-T	20 mM Tris-base pH 8.3 150 mM NaCl 0.1% (v/v) Tween 20	Immunoblotting
Washing buffer core	50 mM HEPES pH 7.5 250 mM NaCl 10% (w/v) Glycerol 50 mM OG	Washing buffer for $^{MBP}Ire1_{cLD\text{-}AH\text{-}TMH}$
Washing buffer TMH	50 mM HEPES pH 7.5 150 mM NaCl 1 mM EDTA 50 mM OG	Washing buffer for $^{MBP}Ire1_{AH\text{-}TMH}$/ $^{MBP}PERK_{AH\text{-}TMH}$
Yeast lysis buffer	50 mM HEPES pH 7.5 150 mM NaCl + PIC	Yeast lysis buffer

5 Methods

5.1 Microbiological methods

5.1.1 Generation of transformation-competent *E. coli*

Chemically competent *E. coli* cells of the strains DH5α or BL21 were generated according to standard protocols (Inoue et al., 1990). To this end, a small aliquot of competent DH5α and BL21 cells was used to inoculate 25 ml of SOB media and the cells were cultivated at 37°C for 8 h. 100 µl of the pre-culture was used to inoculate 250 ml of SOB media and the culture was cultivated over night at 18°C until an OD_{600} of 0.5 was reached. Cells were incubated 10 min on ice and harvested by centrifugation (3.155x g, 10 min, 4°C). The resulting cell pellet was washed with 16 ml of pre-cooled TB buffer and collected by centrifugation (3.155x g, 10 min, 4°C). Cells were resuspended in 10 ml TB buffer supplemented with 700 µl DMSO and 100 µl of competent cells were immediately snap frozen in aliquots in liquid nitrogen and stored at -80°C.

5.1.2 Transformation of competent *E. coli*

An aliquot of competent *E. coli* cells was thawed on ice and mixed with either 200 ng plasmid-DNA or 5 µl of a mutagenesis-reaction mix. The resulting suspension was incubated on ice for 30 min. After a heat shock at 42°C for 45 s, the suspension was mixed with 500 µl of LB media and incubated at 37°C for 45 min under constant agitation. Then, the cells were harvested by centrifugation (5.000x g, 5 min, 4°C), resuspended in fresh LB media and plated on selective LB-agar plates containing either ampicillin (for DH5α) or ampicillin plus chloramphenicol (BL21 pLys or CodonPlus). The plates were incubated at 37°C until single colonies had formed.

5.1.3 Cultivation and storage of *E. coli*

E. coli was cultivated at 37°C in LB liquid media under constant agitation (220 rpm) or on solid, selective LB-agar plates, if not stated otherwise. Cells carrying a plasmid were cultivated in selective media. For long-term storage, 500 µl of stationary overnight cultures were supplemented with 400 µl 50% (v/v) glycerol and stored at -80°C.

5.1.4 Generation of transformation-competent *S. cerevisiae*

Competent *S. cerevisiae* cells were generated by the lithium acetate-based method (Ito et al., 1983). To this end, a 3 ml culture in YPD was inoculated with a single colony. After overnight

cultivation at 30°C under constant agitation (220 rpm), the stationary cells were used to inoculate a 50 ml culture in YPD to an OD_{600} of 0.2. The cells were cultivated at 30°C until an OD_{600} of 1 was reached. The cells were harvested by centrifugation (3.000x g, 5 min, 4°C), washed with 1 ml LATE buffer and resuspended in 250 µl LATE buffer. The competent cells could be stored and used for up to one week at 4°C.

5.1.5 Transformation of competent *S. cerevisiae*

50 µl of competent yeast cells were mixed with either 1 µg plasmid-DNA or linearized DNA fragment. 5 µl of sperm ssDNA (10 mg/ml) were separately heated to 95°C, and – after a cooling down to room temperature (RT) – added to the mixture of competent cells and DNA. The entire mix was incubated at RT for 20 min. After incubation, 10 µl DMSO and 150 µl PLATE buffer were added and the mixture was gently mixed. The suspension was transferred to 30°C and incubated for 45 min. After a heat shock at 42°C for 15 min, the cells were harvested by centrifugation (6.000x g, 5 min, RT), washed with 1 ml sterile water and resuspended in 80 µl sterile water for plating on appropriate selective agar plates. Plates were incubated at 30°C for 2-4 days until single colonies had formed. The single colonies were obtained from three rounds of selection on selective agar plates until they were used for long-term storage (5.1.6). Yeast cells with genomic integration were analyzed for correct insertions by colony-PCR (5.2.10) prior to cultivation for long-term storage. The resulting genotype and the respective selection marker of all generated and used yeast constructs are listed in Table 20.

5.1.6 Cultivation and storage of *S. cerevisiae*

If not stated otherwise, liquid cultures of *S. cerevisiae* cells were grown at 30°C under constant shaking at 180 - 220 rpm. Single colonies were used to inoculate 3 ml cultures in either unselective YPD or selective minimal medium. After overnight cultivation, the main cultures were inoculated to an OD_{600} of 0.2, if not stated otherwise. Cells were further cultivated to the mid-exponential phase for subsequent experiments. For long-term storage, 500 µl of a stationary culture was mixed with 400 µl 50 % (v/v) glycerol and stored at -80°C. For each experiment, yeast cells stored as glycerol stocks were streaked out on selective agar plates, cultivated at 30°C for 2 – 3 days until single colonies became apparent.

5.2 Molecular biological methods

5.2.1 Polymerase chain reaction (PCR)

Polymerase chain reaction (PCR) was used for the amplification of specific DNA sequences, site-specific mutagenesis (5.2.7) and for the validation of correct genome insertions (5.2.10). The standard protocol for a PCR reaction is given in Table 24. Oligonucleotides used for PCR reactions are listed in Table 13 and Table 17.

Table 24: Standard protocol for PCR

Standard PCR reaction mixture	
Template (50 ng)	x
Primer fwd (10 pmol/µl)	2.5 µl
Primer rev (10 pmol/µl)	2.5 µl
5x HF-Buffer	10 µl
dNTPs (10 mM)	1 µl
DMSO (optional)	2.5 µl
PHUSION DNA polymerase	0.5 µl
ddH_2O	x
Total volume	50 µl

Standard PCR protocol			
Initial denaturation	1x	98°C	30 sec
Denaturation	32x	98°C	10 sec
Annealing	32x	x	10 sec
Elongation	32x	72°C	x
Final elongation	1x	72°C	5 min

The annealing temperatures and elongation times were adjusted for each PCR reaction to the predicted melting temperature of the primer pairs and the size of the PCR fragment, respectively. In general, the elongation time was adjusted to 30 sec per kb of the predicted product. The annealing temperature was adjusted to be roughly 5°C below the melting temperature of the respective primer pairs. Successful amplification of the PCR product was tested by agarose gel electrophoresis (5.2.4).

5.2.2 PCR purification

The purification of PCR products or linearized DNA fragments used for homologous recombination into the yeast genome was performed using the QIAquick PCR Purification Kit (Qiagen) according to the manufacturer's recommendations. The isolated DNA was eluted using 30 µl ddH_2O. The concentration was determined by absorption spectroscopy at 260 nm using a NanoDrop™ spectrophotometer. Isolated DNA fragments were stored at -20°C.

5.2.3 Restriction digestion

Digestion with restriction enzymes was used for standard molecular cloning purposes and for the linearization of *IRE1* knock-in fragments. A standard reaction mix is shown in Table 25.

Table 25: Standard reaction mixture for restriction digestion

Standard reaction mix	
Template (2 – 5 µg)	x
Restriction enzyme I	2 µl
Restriction enzyme II	2 µl
10x CutSmart buffer	5 µl
ddH_2O	x
Total volume	50 µl

The reaction mixture was either incubated overnight at RT or for 3 h at 37°C. For heat inactivation of the restriction enzymes, the mix was transferred to 80°C for 20 min. For cloning of the *CEN* based *IRE1* construct, the restriction with the enzymes *BssH*II and *Hind*III was performed in two consecutive steps because *BssH*II worked best at 50°C. The digested DNA fragments were analyzed by agarose gel electrophoresis (5.2.4) and purified by PCR purification (5.2.2) or gel extraction (5.2.5).

5.2.4 Agarose gel electrophoresis

To validate the PCR reactions and for separating DNA fragments after restriction digestion, agarose gel electrophoresis was performed. DNA-containing samples were mixed with 6x DNA-loading dye (NEB) and subjected to an agarose gel containing 1% (w/v) agarose in TAE buffer. The DNA fragments were separated by electrophoresis at 140 V. DNA was visualized by a post-run ethidium bromide staining (0.5 µg/ml) and UV light illumination.

5.2.5 DNA gel extraction

The extraction of DNA from agarose gels was performed using the QIAquick Gel Extraction Kit (Qiagen) according to the manufacturer's recommendations. The DNA was eluted in 30 µl ddH_2O. The concentration of the DNA was determined using the absorption at 260 nm measured with a NanoDrop™ spectrophotometer. DNA could be stored at -20°C for several months.

5.2.6 Ligation

The NEB Quick Ligation kit was used according to the manufacturer's protocol. 50 – 100 ng of a plasmid backbone was mixed with DNA insert at molar ratios between 1:3 and 1:5. Competent *E. coli* DH5α cells were transformed with 2 µl of this ligation mix (5.1.2).

5.2.7 Mutagenesis strategies

5.2.7.1 Site-directed mutagenesis by QuickChange

For site-directed mutagenesis, a PCR-based strategy based on the QuickChange method (Stratagene) was performed. Two complementary oligonucleotide pairs containing the desired mutation in the center of the primer were used. The relevant primers are listed in Table 14 and Table 15. A standard protocol for the site-directed mutagenesis is shown in Table 26. The template DNA was removed by adding 1 µl of *Dpn*I to the reaction mixture and an incubation of at least 1 h at 37°C. 5 µl of the resulting mix were used for transforming chemically competent *E. coli* DH5α cells (5.1.2). Successful mutagenesis was validated by sequencing of the resulting plasmid DNA (5.2.9).

Table 26: Protocol for site-directed mutagenesis PCR

SDM PCR reaction mixture	
Template (50 ng)	x
Primer fwd (10 pmol/µl)	0.5 µl
Primer rev (10 pmol/µl)	0.5 µl
5x HF-Buffer	10 µl
dNTPs (10 mM)	1.25 µl
PHUSION DNA polymerase	0.5 µl
ddH_2O	x
Total volume	50 µl

SDM PCR reaction protocol			
Initial denaturation	1x	98°C	30 sec
Denaturation	25x	98°C	10 sec
Annealing	25x	55°C	10 sec
Elongation	25x	72°C	12 min
Final elongation	1x	72°C	20 min

5.2.7.2 Site-directed mutagenesis using megaprimers

For the generation of cysteine-less *IRE1*, a megaprimer PCR combined with a subsequent site-directed mutagenesis PCR was performed (Table 27 and Table 28). Oligonucleotides for the generation of megaprimers are listed in Table 14. Template DNA was removed after each PCR step using the restriction enzyme *Dpn*I, which can be inactivated by incubating the reaction mixture for 20 min at 80°C. 2 µl of the resulting mix were used for the transformation of *E. coli* DH5α cells (5.1.2). Successful mutagenesis was verified by sequencing of the plasmid (5.2.9).

Table 27: Megaprimer PCR protocol

Megaprimer PCR reaction mixture	
Template (50 ng)	x
Primer fwd (10 pmol/µl)	2.5 µl
Primer rev (10 pmol/µl)	2.5 µl
5x HF-Buffer	5 µl
dNTPs (10 mM)	1 µl
DMSO (optional)	1.25 µl
PHUSION DNA polymerase	0.5 µl
ddH_2O	x
Total volume	25 µl

Megaprimer PCR reaction protocol			
Initial denaturation	1x	98°C	30 sec
Denaturation	18x	98°C	10 sec
Annealing	18x	59°C	10 sec
Elongation	18x	72°C	x
Final elongation	1x	72°C	5 min

Table 28: Protocol for site-directed mutagenesis PCR with megaprimers

SDM PCR with megaprimer reaction mixture	
Template (50 ng)	x
Megaprimer	3 µl
5x HF-Buffer	5 µl
dNTPs (10 mM)	1 µl
DMSO (optional)	1.25 µl
PHUSION DNA polymerase	0.5 µl
ddH_2O	x
Total volume	50 µl

SDM PCR reaction protocol			
Initial denaturation	1x	98°C	30 sec
Denaturation	18x	98°C	30 sec
Annealing	18x	55°C	10 sec
Elongation	18x	72°C	12 min
Final elongation	1x	72°C	20 min

5.2.7.3 Q5 site-directed mutagenesis

For the substitution of the 3xHA tag with a 3xFLAG-tag in the *IRE1* knock-in construct, a Q5 site-directed mutagenesis kit (NEB) was used according to the manufacturer's recommondations. Primers used for Q5 mutagenesis were designed with the NEBaseChanger® and are given in Table 13. To increase the cloning efficiency, the KLD (kinase ligation *Dpn*I) reaction time was raised to 15 min. Competent *E. coli* DH5α cells were afterwards transformed with 2 µl of the final reaction mix (5.1.2). Successful mutagenesis was verified by sequencing (5.2.9).

5.2.8 Plasmid preparation from *E. coli*

For the amplification and preparation of plasmids, a 5 ml culture in LB medium supplemented with ampicillin was inoculated with a single colony of freshly transformed *E. coli* DH5α cells. After an overnight cultivation at 37°C and constant agitation, the cells were subjected to a QIAprep Spin Miniprep Kit (Qiagen) according to the manufacturer's protocol. All recommended washing steps for the isolation procedure were included. The plasmid DNA was eluted with 30 µl ddH_2O. The concentration of the plasmid DNA was determined by absorption spectroscopy at 260 nm using a NanoDrop™ spectrophotometer. Plasmid-DNA were stored at -20°C.

5.2.9 DNA sequencing

Sequencing of plasmid-DNA was performed by the company Microsynth Seqlab (Göttingen). To this end, 200 ng DNA were mixed with an appropriate sequencing primer at a final concentration of 2 µM in a total volume of 10 µl. Oligonucleotides used for sequencing are listed in Table 16.

5.2.10 Colony-PCR

Colony-PCR was used to verify the correct genomic integration of the *IRE1* knock-in construct. Two PCR reactions were carried out to validate the correct insertion both at the 5' end (primers TP201 + RE133) and at the 3' end (primers TP11 + TP 202). Additionally, a colony-PCR was performed to amplify the entire knock-in cassette (TP201 + TP202). The oligonucleotides used for validation and their sequences are listed in

Table 17. A single colony from a selective agar plate was resuspended in 50 µl 20 mM NaOH and incubated at 95°C for 20 min. To remove cell debris, the mixture was centrifuged (16.000x g, 1 min, RT). 5 µl of the remaining supernatant was used as a template for the PCR reaction. The PCR reaction was carried out according to the standard PCR protocol given in Table 24 and analyzed by agarose gel electrophoresis (5.2.4).

5.2.11 RNA preparation from *S. cerevisiae*

A single colony from a selective agar plate was used to inoculate 30 ml culture in YPD. After an overnight cultivation at 30°C to the mid-exponential phase (OD_{600} 0.5 - 2), a fresh culture of 30 ml in YPD was inoculated to an OD_{600} of 0.2. After cultivation for 3 h at 30°C, ER-stress was induced by adjusting the medium either to 4 mM DTT or to 1.0 µg/ml Tunicamycin. As a control, a separate culture remained untreated. After cultivation of the stressed and unstressed cells for 1 h, 5 OD_{600} equivalents of each culture were harvested by centrifugation (3,155x g, 5 min, RT). The resulting cell pellet was snap frozen using liquid nitrogen and could be stored at -80°C. For lysis, the cells were resuspended in 700 µl lysis buffer (Buffer RLT Plus) supplemented with Ribolock and mixed with 100 µl Zirkonia beads. This mix was intensely agitated for cell disruption using a bead beater for 5 min. The RNA was isolated from this lysate using the RNeasy Plus RNA Isolation Kit (Qiagen) according to the manufacturer's instructions. The RNA was eluted with 30 µl RNase free ddH_2O. The RNA concentration was determined via the absorbance at 260 nm using a NanoDrop™ spectrometer. For further quality control, the isolated RNA was subjected to agarose gel electrophoresis on a 2 % (w/v) agarose gel.

5.2.12 Reverse transcription of isolated RNA

The reverse transcription was carried out using the Superscript™II Reverse Transcriptase (Invitrogen) according to the manufacturer's protocol. 500 ng RNA of each sample were mixed with 1 µl Oligo$(dT)_{12-18}$ primers and 1 µl dNTP mix and used for cDNA synthesis.

5.2.13 Quantitative Real-Time PCR (qPCR)

The quantitative real-time PCR (qPCR) was performed using the PikoReal Real-time PCR system (Thermo scientific) and HiQu SYBR Green reaction mix (HiQu) as previously described (Halbleib et al., 2017). After reverse transcription, the cDNA was analyzed for the relative content of species encoding for *ACT1*, *PDI1*, *KAR2* and spliced *HAC1.* The primers used for qPCR are listed in Table 18. All reactions were performed in technical duplicates. Additionally, non-template control (RNA) and non-reaction control (H_2O) were routinely performed. The qPCR program is shown in Table 29.

Table 29: qPCR protocol

qPCR reaction mixture	
DNA (1:10)	1 µl
Primer mix	1.5 µl
SYBR Green mix	2.5 µl
Total volume	5 µl

qPCR reaction protocol			
Initial denaturation	1x	95°C	15 min
Denaturation	40x	95°C	20 sec
Annealing	40x	58°C	20 sec
Elongation	40x	72°C	30 sec
Final elongation	1x	72°C	5 min

CT values of *PDI1*, *KAR2* and spliced *HAC1* of each sample were normalized to *ACT1* levels based on the comparative *ΔΔCT* method (StepOnePlus™ user manual, Applied Biosystems).

5.3 Biochemical methods

5.3.1 SDS polyacrylamide gel electrophoresis (SDS-PAGE)

SDS polyacrylamide gel electrophoresis (SDS-PAGE) was performed to separate proteins according to their molecular weight using precast 7.5% and 4 – 15 % Mini-PROTEAN-TGX gels (BioRad). If not stated otherwise, protein samples were mixed at a ratio of 5:1 with 5x MSB_{red} and incubated at 95°C for 10 min for full protein denaturation. Non-reducing conditions were chosen to analyze disulfide-linked protein oligomers. The samples were subjected to electrophoresis and separated using a constant voltage of 180 V for 30 – 45 min. The separated proteins were visualized by a staining with InstantBlue™ staining (Expedeon) or by immunoblotting using protein specific antibodies (5.3.2).

5.3.2 Immunoblotting

For the detection of proteins by immunoblotting, proteins separated by SDS-PAGE were transferred to a methanol-activated PVDF membrane by semi-dry Western-blotting in blotting buffer using the TransBlot® Turbo™ System (BioRad). The standard program (constant 25 V, 1.0 A, 25 min) was used for all applications. After blotting, the PVDF membrane was incubated in blocking buffer for 15 min and then with the primary antibody specific for the protein of

interest diluted in blocking buffer supplemented with 0.01% (v/v) NaN_3. The dilutions for the primary antibodies are listed in Table 8. The primary antibodies were incubated under constant agitation either 1 h at RT or overnight at 4°C. The membranes were washed 5-times in TBS-T for 5 min each to remove unbound antibodies. Then, the membranes were incubated for 45 min at RT with a secondary antibody coupled to a horseradish peroxidase (HRP). Again, the unspecifically bound antibody was removed by washing the membrane 5-times for each 5 mins with TBT-T. The specifically bound, HRP-coupled antibodies were detected by chemiluminescence using either the Clarity Western ECL substrate (BioRad) or the SuperSignal West Femto ECL developing solution (Fisher Scientific) for particularly low abundant proteins. The resulting signal was detected in a luminescence-imaging system (ChemiDoc™ MP System). If required, the immunoblot signals were quantified using the software ImageJ.

5.3.3 Preparation and characterization of liposomes

5.3.3.1 Liposome preparation

All lipids used for reconstitution of sensor proteins in liposomes (Table 5) were stored in a stock concentration at 20 mg/ml in chloroform. The following lipid mixtures were used for CPY* binding assays (5.3.6) and EPR experiments (5.5.1) (Table 30).

Table 30: Lipid mixtures used for the preparation of liposomes

Number	Composition
1	50% POPC, 50% DOPC
2	100% POPC
3	80% POPC, 20% Cholesterol
4	60% POPC, 30% Cholesterol, 10% DPPC
5	50% DOPC, 40% POPC, 10% POPE
6	50% DOPC ,30% POPC, 20% POPE
7	50% DOPC, 20% POPC, 30% POPE
8	50% DOPC, 10% POPC, 40% POPE
9	10% POPC, 40% POPE, 20% DPPC, 20% soy-PI, 10% Cholesterol

Lipids were mixed according to the molar fractions given in Table 30. The organic solvent was removed using a constant stream of nitrogen during an incubation at 60°C and a constant, gentle agitation. The resulting lipid cake was dried in a desiccator under vacuum conditions for 1 h to remove residual chloroform. The lipid cake was then hydrated in reconstitution buffer to obtain a final, total concentration of 10 mM glycerophospholipids. The rehydration was supported by an incubation for 20 min at 60°C under strong agitation followed by an incubation in an ultrasonic bath at 50°C for 30 min. Aliquots of the resulting multi-lamellar liposomes were snap frozen in liquid nitrogen and stored at -80°C until further use.

5.3.3.2 Determination of lipid packing by C-laurdan spectroscopy

C-Laurdan is a polarity-sensitive probe, which intercalates into the lipid bilayer and informs on the lipid packing density in the membrane (Kaiser et al., 2009). The integration of C-Laurdan into the lipid bilayer leads to a blue-shift of the emission peak. The degree of this blue-shift depends on the degree of water penetration into the bilayer. In a loosely packed membrane with a high degree of water penetration, the shift is less pronounced, and the emission peak lies at roughly 485 nm. In a densely packed membrane with a low degree of water penetration, the emission peak lies at roughly 440 nm. The generalized polarization (GP) value can be obtained by the ratio of blue and red emission band and serves as a measure for membrane order (eq. 1). In theory GP values can vary between -1 (less ordered) and +1 (most ordered) (Kaiser et al., 2009), but in reality, the range in biological membranes is much lower.

$$GP = \frac{I_{Ch1} - I_{Ch2}}{I_{Ch1} + I_{Ch2}}$$

(eq. 1)

In this study, liposomes at a concentration of 0.33 mM were mixed with 0.4 µM C-Laurdan dye in 150 µl reconstitution buffer and incubated for 5 min at 30°C. C-Laurdan was excited at 375 nm and an emission spectrum from 400 nm to 600 nm (bandwidth 3 nm) was recorded using the Fluormax-4 spectrometer (Horiba). GP values were calculated after blank correction (liposomes without C-Laurdan) by integrating the emission intensities between 400 – 460 nm (I_{Ch1}) and 470 nm – 530 nm (I_{Ch2}).

5.3.3.3 Estimation of lipid contents by Hoechst assay

Hoechst 33342 is an environment-sensitive fluorescent dye whose fluorescent intensity increases in hydrophobic environments. It is suitable to estimate relative lipid contents of an unknown sample in a semi-quantitative way. To this end, 135 µl of a liposome/proteoliposome-containing sample were mixed with 15 µl 70 µM Hoechst 33342 in a 96-well plate suitable for fluorescence applications. The fluorescence intensity was determined using a TECAN reader using an excitation at 355 nm and 459 nm as emission wavelength (bandwidth 20 nm).

5.3.4 Protein biochemical methods

5.3.4.1 Heterologous expression and purification of MBP fusion proteins

The heterologous expression and purification of minimal sensor constructs as MBP fusion proteins was previously established (Halbleib et al., 2017). Minimal sensor constructs of this study are $^{MBP}Ire1_{AH\text{-}TMH}$ (yeast) and $^{MBP}PERK_{AH\text{-}TMH}$ (human). Chemically competent *E. coli*

BL21 pLysS cells were transformed with the respective plasmids. A culture in LB medium supplemented with ampicillin and chloramphenicol was inoculated with a single colony and cultivated overnight at 37°C. The overnight pre-culture was used to inoculate a main culture at a ratio of 1:50 in 2 l of selective LB_{rich}-medium. The main culture was cultivated at 37°C and the gene expression was induced at an OD_{600} of 0.6 by the addition of IPTG to a final concentration of 0.3 mM. After further cultivation for 3 h at 37°C, the cells were harvested by centrifugation (5,000x g, 20 min, 4°C). Cell pellets were washed in lysis buffer TMH and stored at -20°C.

All purification steps were performed either at 4°C or on ice. The cell pellets from a 2 l culture were resuspended in 22.5 ml lysis buffer TMH supplemented with 2 µl Benzonase. The cells were then lysed by sonification (2x 90 sec, power 30%, pulse 0.7sec/0.3sec). For solubilizing $^{MBP}Ire1_{AH\text{-}TMH}$ or $^{MBP}PERK_{AH\text{-}TMH}$, the sample was adjusted to 50 mM OG and incubated at 4°C for 20 min under constant, gentle agitation. Cell-debris and non-solubilized material was removed by centrifugation (100,000x g, 30 min, 4°C). The supernatant was transferred to an amylose resin (NEB) (3 ml of settled material) and incubated for 30 min under constant agitation to allow binding of the MBP fusion protein. Then, the amylose resin was washed twice with each 20 ml washing buffer TMH. The MBP fusion proteins were eluted with elution buffer TMH. To subsequently support full elution of the fusion protein, the resin was incubated for 5 min for each elution step in elution buffer TMH. The protein was eluted in several rounds. The concentration of the isolated protein was determined using the absorption at 280 nm measured using a NanoDrop spectrophotometer and by using the protein-specific extinction coefficient. All steps of the purification and the purity of eluted protein were analyzed by SDS-PAGE (5.3.1) and subsequent InstantBlue staining. The eluted fractions were pooled, adjusted to 20% (v/v) glycerol and stored at the desired concentration. Aliquots were snap frozen with liquid nitrogen and stored at -80°C.

If the minimal sensor proteins were used for EPR studies, the constructs contained a single-cysteine, which was labeled during purification procedure with a methanethiosulfante spin label (MTS-SL) (Enzo Life Science). To prevent premature oxidation of the cysteine residue, the used lysis buffer TMH was supplemented with 2 mM DTT in this case. The MTS-SL labeling was performed on the amylose column after binding of the fusion protein and washing away unrelated proteins. For labeling, 1 mM MTS-SL was added to the washing buffer TMH and the entire resin was incubated in this buffer for 4 h at 4°C under constant agitation. Free spin labels were then washed away by two washing steps (20 ml each) with washing buffer TMH. The elution of the labeled protein was performed as the elution of the unlabeled protein.

5.3.4.2 Heterologous expression and purification $^{MBP}Ire1_{cLD\text{-}AH\text{-}TMH}$ constructs

The protocol for the heterologous production and purification of $^{MBP}Ire1_{cLD\text{-}AH\text{-}TMH}$ constructs was established together with Susanne Wolf in her bachelor thesis (Wolf, 2016). Here, chemically competent *E. coli* BL21 CodonPlus cells were transformed with the corresponding plasmids. A single colony was used to inoculate a 50 ml culture in LB medium supplemented with ampicillin and chloramphenicol. An overnight culture cultivated at 37°C was used to inoculate a main culture in 2 l of selective LB_{rich} medium to an OD_{600} of 0.05. This main culture was cultivated at 25°C until an OD_{600} of 0.25 was reached. Then, the culture was switched to 18°C until an OD_{600} of 0.6 was reached. Then, the gene expression was induced by the addition of IPTG to the medium to a final concentration of 0.3 mM. After further cultivation at 18°C for 18 h, the cells were harvested by centrifugation (5,000x g, 20 min, 4°C), washed in lysis buffer core and stored as cell pellets at -20°C.

All steps of the purification were either performed on ice or at 4°C. The cell pellets from a 2 l cultures were resuspended in 90 ml lysis buffer core supplemented with Benzonase. The cells were lysed by sonification (5x 60 sec, power 30%, pulse 0.7sec/0.3sec). For solubilization of the $^{MBP}Ire1_{cLD\text{-}AH\text{-}TMH}$ fusion protein, the lysate was adjusted to 50 mM OG and incubated for 10 min under constant agitation. Cell debris and non-solubilized material were removed by centrifugation (100,000x g, 30 min, 4°C) and the supernatant was transferred to 3.5 ml of an equilibrated and settled amylose resin. After binding of the fusion protein (10 min, 4°C, gently shaking), the amylose resin was washed twice with 30 ml washing buffer core each. To remove contaminations from nucleic acids, the resin was washed with 750 µl elution buffer core without collecting the protein. To subsequently support full elution of the fusion protein, the resin was incubated for 5 min for each elution step in elution buffer core. The protein was eluted in several rounds. To increase the purity of $^{MBP}Ire1_{cLD\text{-}AH\text{-}TMH}$ constructs, samples were further purified by size-exclusion chromatography (5.3.4.3).

5.3.4.3 Size-exclusion chromatography (SEC)

The separation of proteins according to their molecular weight by size-exclusion chromatography (SEC) was used 1) to remove impurities and aggregates from the protein sample on the preparative scale and 2) to analyze the concentration-dependent oligomerization of already purified proteins in detergent solution. For all applications, the Superose 6 Increase column on an Äkta Pure 25 FPLC system (GE Healthcare) was used. All buffers (SEC buffer core) were filtered and degassed prior to the application. All runs were performed at a constant flow rate at 0.5 ml/min and the separation was monitored by the

absorption at 280 nm. Before sample injection, it was centrifuged (20,000x g, 10 min, 4°C) to remove potential protein aggregates and other large particles.

For preparative SEC runs, the protein-containing samples was concentrated via Amicon centrifugal filters (100 kDa molecular weight cut off). Here, 500 µl of the sample was subjected to the column and fractions of 250 µl were collected.

For testing the concentration-dependent oligomerization in detergent solution, isolated and already gel filtrated protein samples were concentrated using an Amicon centrifugal filter (100 kDa molecular weight cut off) and then diluted to different concentrations prior to an analysis by analytical SEC. 100 µl of each sample was analyzed without collecting the elution fraction. For analysis of the oligomeric state, the peak elution volume was plotted against the tested concentration.

5.3.4.4 Reconstitution of MBP fusion proteins in liposomes

Purified proteins were reconstituted in liposomes with defined lipid compositions at a molar protein:lipid (P:L) ratio of 1:6000 and 1:400 for CPY* binding studies and EPR studies, respectively. For the reconstitutions at a P:L ratio of 1:6000, 200 µl liposomes (10 mM of glycerophospholipids) were mixed with 0.33 nmol MBP fusion protein in reconstitution buffer, adjusted to 37.5 mM OG and a final volume of 1 ml. For a reconstitution with a P:L ratio of 1:400, 160 µl liposomes (10 mM of glycerophospholipids) were mixed with 4 nmol $^{MBP}Ire1_{AH\text{-}TMH}$ or $^{MBP}PERK_{AH\text{-}TMH}$ fusion protein. The suspension was incubated for 10 min at RT on a rotator for complete solubilization of the liposomes. The detergent was removed stepwise by a first addition of 100 mg of BioBeads™ SM-2 Adsorbent Media (BioRad) equilibrated in reconstitution buffer and an incubation of 90 min at RT on a rotator and a second step with 400 mg BioBeads for additional 90 min. The proteoliposomes were harvested by centrifugation (450,000xg, 90 min, 4°C).

For EPR experiments, the harvested proteoliposomes were resuspended in 15 µl reconstitution buffer, transferred to EPR tubes, incubated at 30°C and then snap frozen with liquid nitrogen for storage at -80°C. For studying the interaction with misfolded model proteins, the proteoliposomes were resuspended in 160 µl reconstitution buffer w/o glycerol. Aliquots were snap frozen using liquid nitrogen and stored at -80°C.

5.3.4.5 Sucrose density gradient of reconstituted MBP fusion proteins

A sucrose density gradient can separate protein aggregates from proteoliposomes. To this end, a sucrose step gradient consisting of 30% (w/v), 20% (w/v), 10% (w/v), 5% (w/v) and 0%

sucrose in reconstitution buffer was used. Proteoliposomes (0.33 µM) resuspended in 300 µl reconstitution buffer were mixed with 300 µl 60% (w/v) sucrose solution and overlaid with 3 ml of each 30%, 20%, 10%, 5% and 0% sucrose solutions. The resulting sucrose gradient was centrifuged (100,000x g, 16h, 4°C) using a SW28.1 swing out rotor and then fractionated in 1 ml fractions from the top to the bottom.

5.3.4.6 Membrane-extraction assay

The membrane extraction assay was used to validate the correct integration of MBP fusion proteins into liposomes. Proteoliposomes (0.33 µM) in 1 ml reconstitution buffer were divided into four equal parts. These 250 µl samples were mixed either with 250 µl of reconstitution buffer, 5 M Urea in reconstitution buffer, 2% (w/v) SDS in reconstitution buffer or 200 mM Na_2CO_3 pH 11 in reconstitution buffer. After an incubation for 30 min at RT under constant agitation, the Na_2CO_3 sample was neutralized by adding 500 µl of neutralization buffer, while 500 µl of reconstitution buffer was added to the other three samples. Then, all samples were centrifuged (450,000x g, 90 min, 4°C) and analyzed by SDS-PAGE (5.3.1) and subsequent immunoblotting (5.3.2).

5.3.4.7 TEV cleavage

To analyze the topology of $^{MBP}Ire1_{cLD\text{-}AH\text{-}TMH}$ in proteoliposomes, the membrane-reconstituted proteins were treated with the TEV protease. A TEV cleavage site is located between the MBP and the core ER-luminal domain of Ire1 in $^{MBP}Ire1_{cLD\text{-}AH\text{-}TMH}$. It is only accessible if the fusion protein is reconstituted in the inside-out orientation. To this end, 2 µg of reconstituted $^{MBP}Ire1_{cLD\text{-}AH\text{-}TMH}$ was mixed with 0.2 µg TEV protease and 10x TEV buffer in a final volume of 20 µl. The mixture was incubated overnight at RT and analyzed by SDS-PAGE and InstantBlue staining (5.3.1).

5.3.5 Expression and purification of CPY*

Carboxypeptidase Y (CPY) was used as a model substrate for binding studies. CPY* is a mutant variant of CPY that can be isolated in a misfolded state (Stein et al., 2014). The production and purification of CPY* was based on an existing protocol and adapted as described below (Stein et al., 2014). CPY* was expressed in an ERAD defective yeast strain deleted for two genes: Δ*ALG3*Δ*HRD3*.

A culture in 100 ml SCD-Leu was inoculated using a single colony and cultivated for 24 h at 30°C under constant agitation. A main-culture in 750 ml SCD-Leu was inoculated 1:40 using

the stationary pre-culture and then cultivated for 24 h at 30°C under constant agitation. Gene expression was induced by the addition of 250 ml 4xYEP containing 8% galactose to the culture. After further cultivation for 12-16 h at 30°C under constant agitation, the cells were harvested by centrifugation (3,000x g, 30 min, 4°C), washed with ddH_2O and stored at -80°C.

All steps of the preparation of crude membrane extracts were performed on ice or at 4°C. First, cells from a 4 l culture were resuspended in 150 ml buffer A supplemented with PIC. Glass beads were added until they constituted a 1/3 of the volume of the cell suspension. The cells were disrupted using the BioSpec Bead Beater for 10 min using 30 sec ON and a 60 sec OFF cycle. Cell debris and glass beads were removed by centrifugation (2,000x g, 10 min, 4°C). Crude membrane extracts were harvested by centrifugation (42,000x g, 45 min, 4°C), washed twice in buffer A by resuspension and centrifugation. The resulting membranes were resuspended in a minimal amount of buffer A, snap frozen and stored at -80°C.

The crude membrane fraction was thawed on ice, dounced 80 times with a tight-fitting douncer, resuspended in 50 ml buffer AU, and incubated for 30 min at RT. Insoluble material was removed by centrifugation (100,000x g, 30 min, 4°C). The supernatant was then transferred to 7 ml of an equilibrated and settled NiNTA resin. The NiNTA resin was washed with 50 ml buffer AU, 50 ml buffer A, 25 ml of a 1:1 mix of buffer A and buffer A+ and finally with 25 ml buffer A+. The protein was eluted in several steps using the elution buffer CPY* His. The protein-containing fractions were pooled. EDTA and DTT to a final concentration of 1 mM were added to the pooled material. Then, the imidazole concentration was diluted by adding an identical volume of buffer S.

To further increase the purity of CPY*, a second purification step using Streptavidin agarose was performed. To this end, the pooled material from the first purification was incubated with 0.75 ml of equilibrated Streptavidin agarose beads for 30 min on a rotator. After binding, the beads were washed with 10 ml of buffer S. CPY* was then eluted in 1 ml fractions using elution buffer CPY* S. The concentration of the purified CPY* was determined by measuring the absorption on the NanoDrop spectrophotometer.

Fractions containing CPY* were pooled and incubated overnight at 4°C with the TEV and the 3C protease to remove the purification tags. After protease cleavage, the sample was adjusted to 30 mM Imidazole, and the proteases were removed using 1 ml of equilibrated NiNTA resin. The buffer of CPY* was exchanged to storage buffer containing 10% (w/v) glycerol using PD10 desalting columns.

5.3.6 CPY binding assay

The CPY binding assay was used to characterize the binding of misfolded proteins to $^{MBP}Ire1_{cLD\text{-}AH\text{-}TMH}$ reconstituted in liposomes. A sucrose step gradient consisting of 30% (w/v), 25% (w/v) and 2.5 (w/v) sucrose in reconstitution buffer w/o glycerol separates the unbound CPY* from CPY* that is bound to $^{MBP}Ire1_{cLD\text{-}AH\text{-}TMH}$ in the proteoliposomes.

80 µl reconstituted $^{MBP}Ire1_{cLD\text{-}AH\text{-}TMH}$ (0.17 nmol of protein assuming a 100% recovery during the reconstitution procedure) was mixed in a molar ratio of 1:2 either with CPY* or CPY (0.34 nmol) Then, the volume was adjusted to 150 µl using reconstitution buffer w/o glycerol. The mixture was incubated for 15 min at RT. Then, 100 µl of 75% (w/v) sucrose solution was added to the proteoliposomes to constitute the bottom layer of the gradient, which was then overlaid with 200 µl of 25% (w/v) sucrose solution and 50 µl 2.5% (w/v) sucrose solution. After centrifugation (240,000x g, 2 h, 22°C, no brake), the gradient was overlaid with 20 µl reconstitution buffer w/o glycerol. After an incubation for 5 min the gradient was fractionated in 160 µl fractions from top to the bottom. Each fraction was analyzed by SDS-PAGE and subsequent InstantBlue staining (5.3.1).

To minimize binding of CPY* to MBP, all buffers including the sucrose solutions were supplemented with 1 mM maltotriose. Prior to the addition of CPY*, the samples containing reconstituted $^{MBP}Ire1_{cLD\text{-}AH\text{-}TMH}$ were adjusted to a final concentration of 1 mM maltotriose and incubated for 10 min at RT. When maltotriose was used in the experimental setup, a statement about the maltotriose concentration was included in the figure legends of the relevant experiments.

5.4 Analytical methods for the characterization of the yeast sensor Ire1

5.4.1 Preparation of cell extracts for immunoblotting

For preparation of cellular extracts for immunoblotting, 20 OD_{600} equivalents of cells grown to the mid-exponential phase (OD_{600} = 1) were harvested by centrifugation (3.155x g, 5 min, 4°C), washed with 1xPBS and stored at -80°C until further use. For cell lysis, the cells were resuspended in 1 ml yeast lysis buffer and supplemented with 500 µl Zirkonia beads (Roth). Cells were disrupted by bead beating at 4°C for 5 min. Cell lysates were analyzed by SDS-PAGE (5.3.1) and subsequent immunoblotting (5.3.2) using specific antibodies.

5.4.2 Cultivation of yeast cells for crosslinking experiments

Proteotoxic stress: A stationary overnight culture was used to inoculate a fresh culture in 100 ml of SCD complete to an OD_{600} of 0.2. This culture was cultivated at 30°C until an OD_{600} of 0.7 was reached. Proteotoxic ER-stress was induced by adjusting the culture to either 2 mM DTT or 1.5 µg/ml Tunicamycin (TM). After 1 h cultivation, the stressed cells were harvested.

Lipid bilayer stress: A stationary overnight culture was used to inoculate a fresh culture in 50 ml SCD complete to an OD_{600} of 0.01. After cultivation for 16 h, the cells reached the mid-exponential phase (OD_{600} = 1-2) and then were washed twice with SCD complete medium w/o inositol (3.155xg, 5 min, 4°C). A fresh culture in 100 ml of SCD complete medium w/o inositol was then inoculated to an OD_{600} of 0.5 followed by a cultivation for 3 h at 30°C prior to harvesting.

80 OD_{600} equivalents of cells were harvested by centrifugation (3.155xg, 5 min, 4°C). Cell pellets were washed once with 2 ml ice-cold water, and then twice with 1 ml 1xPBS (8,000xg, 20 sec, 4°C). The cells were stored at -80°C.

5.4.3 Subcellular fractionation and membrane extraction

Subcellular fractionation was used 1) to validate correct insertion of Ire1 variants into the ER membrane and 2) to isolate Ire1-containing ER vesicles used for crosslinking with $CuSO_4$.

All steps were performed either on ice or at 4°C. Cells corresponding to 80 OD_{600} equivalents from a mid-exponentially grown culture (OD_{600} ~ 1) were resuspended in 1.5 ml yeast lysis buffer and supplemented with 500 µl Zirkonia Beads (Roth). Cells were disrupted by bead beating them twice for 5 min. Cell debris and nuclei were removed by centrifugation (800x, g, 5 min, 4°C) and the supernatant was further centrifuged (5,000xg, 10 min, 4°C) to sediment mitochondria. The Ire1-containing ER vesicles were harvested by centrifugation (100,000x g, 45 min, 4°C), resuspended in 1.5 ml yeast lysis buffer and sonicated for complete resuspension (power 50%, 5x 1 sec). Aliquots of microsomal membranes were snap frozen and stored at -80°C for crosslinking experiments.

For validation of the correct membrane insertion of different Ire1-variants, microsomal membranes were split into four equal parts and mixed either 1:1 with yeast lysis buffer, 5 M urea in yeast lysis buffer, 200 mM Na_2CO_3 pH11 in yeast lysis buffer and 2 % (v/v) Triton X-100 in lysis buffer. These samples were incubated for 1 h at 4°C under constant agitation and then centrifuged (100,000x g, 45 min, 4°C). Samples of the supernatant and the pellet fraction resuspended in yeast lysis buffer of each condition were analyzed by SDS-PAGE (5.3.1) and subsequent immunoblotting (5.3.2).

5.4.4 Crosslinking with $CuSO_4$

$CuSO_4$-mediated crosslinking of single-cysteine variants of Ire1 was performed in microsomal membranes (5.4.3). To this end, stored microsomes were thawed on ice and 8 µl sample was mixed with 2 µl of 50 mM $CuSO_4$ in ddH_2O. The crosslinking was catalyzed during an incubation for 5 min on ice. Then, the reaction was stopped by adding 8 µl stopping-mix (4 µl MSB, 2 µl 0.5 M EDTA, 2 µl 100x NEM). The degree of crosslinking was analyzed via SDS-PAGE (5.3.1) and subsequent immunoblotting (5.3.2) with anti-HA antibody.

5.4.5 Co-Immunoprecipitation combined with crosslinking

80 OD_{600} equivalents of unstressed and DTT-stressed cells expressing single-cysteine variants of Ire1 were used for the microsomal membrane preparation (5.4.2 and 5.4.3) and a subsequent co-immunoprecipitation was performed after $CuSO_4$-mediated crosslinking.

300 µl of microsomes were thawed on ice, adjusted to 10 mM $CuSO_4$ and incubated for 5 min on ice. The crosslinking reaction was stopped by adding EDTA to a final concentration of 50 mM and NEM to a final concentration of 111 mM. Untreated microsomes that were not exposed to $CuSO_4$ served as controls. The volume of each sample was adjusted to 1.3 ml using yeast lysis buffer. For solubilization, Triton X-100 was added to a final concentration of 2% (v/v) and the sample was incubated for 60 min at 4°C under constant agitation. Insolubilized material was removed by centrifugation (20,000x g, 10 min, 4°C) and the remaining supernatant was applied to 8 µl equilibrated FLAG-beads. After binding for 3 h at 4°C, the beads were pelleted (8,000x g, 30 sec, 4°C) and washed five times with IP-Wash. The co-immunoprecipitated material was eluted in 10 µl IP-wash mixed with 10 µl MSB_{red} and an incubation at 95°C for 5 min. Samples of input and IP were analyzed by SDS-PAGE (5.3.1) and a subsequent immunoblotting (5.3.2).

5.4.6 ER-stress resistance assay

A stationary overnight culture was used to inoculate a fresh 3 ml culture in either SCD complete or YPD to an OD_{600} of 0.2. After cultivation for 5-6 h at 30°C under constant agitation, the cells were mixed with fresh medium to an OD_{600} of 0.05. 50 µl of this suspension was then mixed in a 96-well plate with 200 µl fresh medium supplemented with different concentrations of DTT. The final concentration of DTT in minimal medium ranged from 0 – 2 mM DTT and was generated using a 4/5 dilution series. The final concentration of DTT in YPD ranged from 0 – 4 mM DTT and was also generated using a 4/5 dilution series. Cells were cultivated in a 96-well plate for 18 h at 30°C. The next day, the cells were thoroughly mixed and 200 µl of the

resulting suspension was transferred into a fresh 96-well plate. Here, either the OD_{620} or the OD_{600} were measured using a 96-well plate compatible photospectrometer (BMG Fluostar Galaxy).

5.5 Biophysical methods

5.5.1 Continuous wave EPR spectroscopy measurements

Continuous wave (cw) EPR spectroscopy was performed to analyze the oligomerization of spin-labeled minimal sensor constructs in different lipid environments. When two spin-probes are in a close proximity at a distance between 1 and 2 nm (which is frequently occurs when two spin-labeled transmembrane helices oligomerize), a dipolar coupling can become evident from the spectral line-broadening in the absorption spectrum of frozen samples (Bordignon and Steinhoff, 2007). The extent of line-broadening gives information on the average proximity of two spin-probes. Thus, spin-labeled sensor proteins were reconstituted in defined lipid environments (5.3.4.4) and the resulting proteoliposomes pellet was resuspended in only 15 µl reconstitution buffer to yield high concentrations of the spin-labeled material. The samples were analyzed in glass capillaries with inner diameter of 1 mm (Hirschmann). The cwEPR spectra were recorded at -115°C and 30°C using the MiniScope MS 400 spectrometer (Magnetech) using 10 mW microwave power and 0.15 mT field modulation amplitude.

The spin-labeling efficiencies were determined by double-integrating the EPR spectra. To analyze spin-labeling efficiencies, the spin-labeled proteins in detergent solution were concentrated to a minimum concentration of 100 µM before a cwEPR spectra was recorded at RT. The recorded spectrum was compared to the signal of a free MTS standard at 100 µM. The labeling efficiencies of all spin-labeled MBP fusion proteins ranged from 75 - 95%.

5.5.2 Analysis of cwEPR spectra

The analysis of cwEPR spectra was carried out as previously described (Covino et al., 2016; Halbleib et al., 2017). Recorded spectra illustrated as the first derivative of the absorption signal were baseline-corrected and normalized to the maximum intensity of the middle field peak. Spectra recorded at -115°C give information on inter-spin distances by spectral broadening and the polarity of the nano-environment of the spin-probe (Figure 12A). The polarity was determined from the difference in the field strengths (2Azz) of the low and the high field peak. The proximity between two spin-probes was determined semi-quantitatively as spectral broadening, which influences the intensity ratio of the low and the middle field peak ($I_{Lf}/2I_{Mf}$). Spin-diluted samples containing a 6-molar excess of unlabeled protein in the

reconstituted sample served as a control for unbroadened spectra. Spectra recorded at 30°C provide information about the mobility of the spin-probe, which was determined by the inverse of the line width of the middle field peak (Figure 12B).

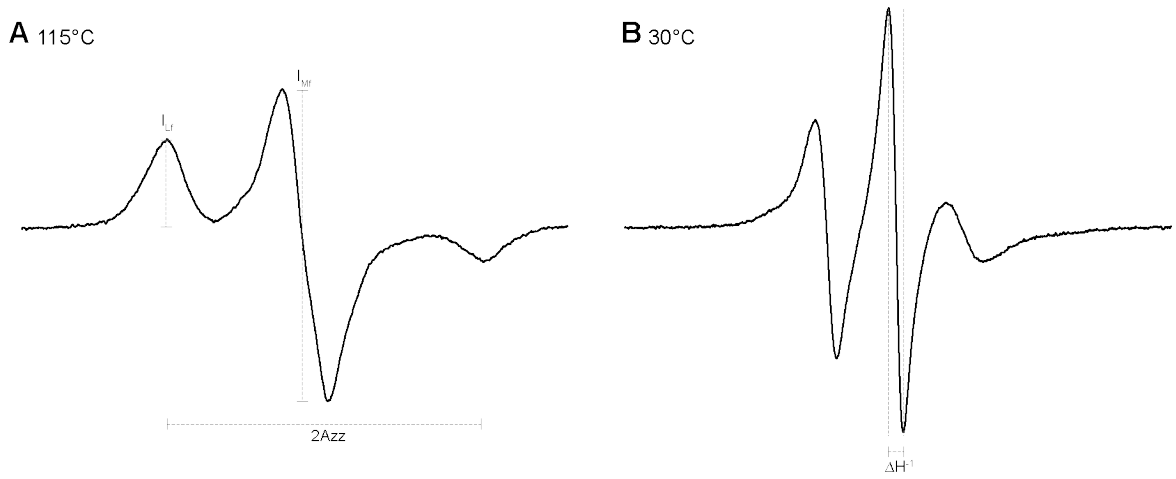

Figure 12: Representative cwEPR spectra and their characteristic feature.

(A) A cwEPR spectrum recorded at -115°C and intensity-normalized exhibits several peaks at characteristic field strengths. The difference in field strength between the low and the high field peak is referred to as 2Azz and informs on the polarity in the immediate environment of the spin-probe. High 2Azz values correspond to more polar environments. The ratio of the intensities of the low field and the middle field peak $I_{Lf}/2I_{Mf}$ provides a semi-quantitative information on the inter-spin distances. Here, a higher value informs on a low inter-spin distance. (B) A cwEPR spectrum recorded at 30°C gives information on the mobility of the spin-probe. The inverse line width ΔH^{-1} of the middle field peak is used as the semi-quantitative measure for the mobility. A higher value represents an increased flexibility of the spin-probe.

6 Results

6.1 Single-cysteine crosslinking establishes the TMH architecture in Ire1 clusters

X-ray crystallography has provided insights into the mechanisms of activation and signal transduction by the yeast UPR sensor Ire1 (Credle et al., 2005; Korennykh and Walter, 2012; Korennykh et al., 2009; Lee et al., 2008; Wiseman et al., 2010). However, all available structures were obtained from isolated domains and not from the full-length protein. It remains unclear, how the ER-luminal and the cytosolic domain are coupled to each other and how the TMH region of Ire1 is organized during ER-stress. In light of the membrane-based activation of the UPR, which has recently been established (Halbleib et al., 2017), it is important to better understand the contribution of the TMH to UPR signaling. Ire1 is a single-pass transmembrane protein with an unstructured juxta-membrane region. The inherent structural dynamics of this protein make it a challenging target for structural biology. The structures of most membrane proteins have been determined in the presence of detergents or in a reconstituted state using synthetic environments such as nanodiscs. Understanding the dynamics and function of a membrane property sensor in its native, complex environment therefore represents a particular challenge. This thesis employs a single-cysteine crosslinking strategy to establish the architecture of the TMH region in clusters of Ire1 in the native environment of the ER-derived membrane vesicles.

6.1.1 Generation of a functional cysteine-less Ire1 variant

In order to characterize the TMH architecture of Ire1 clusters by single-cysteine crosslinking, a cysteine-less variant of Ire1 was generated. The cysteine-less variant allowed a structural characterization of Ire1 at near-endogenous steady-state level, because the construct was produced from the endogenous locus and from the native promotor of *IRE1*. The previously established knock-in approach (Halbleib et al., 2017) was based on an integration of a plasmid-based knock-in construct that could be integrated into the yeast genome by homologous recombination at the *IRE1* locus.

The knock-in construct consists of a 3xHA-tag and a codon-optimized (Cormack et al., 1997) monomeric GFP variant (A206R) (Sheff and Thorn, 2004), referred to as yeGFP, inserted in Ire1 at the position H875 (van Anken et al., 2014; Halbleib et al., 2017). In order to generate a cysteine-less variant, twelve cysteines in Ire1 were substituted in this construct to serines. In the final construct, two cysteines located in the signal sequence remained unchanged in order to avoid a potential mistargeting or misintegration of Ire1 into the ER membrane. Notably, the

signal sequence is removed during maturation of Ire1. Wildtype Ire1 contains three cysteines in its ER-luminal domain, one in the TMH and eight in its cytosolic domain (Figure 13). Additionally, two cysteines C48 and C70 are present in the yeGFP variant. Only C48 was replaced by a serine. Substitution of position C70 would result in a loss-of-function of GFP (Costantini et al., 2015). It is known that C70 is not accessible to cysteine-modifying compounds.

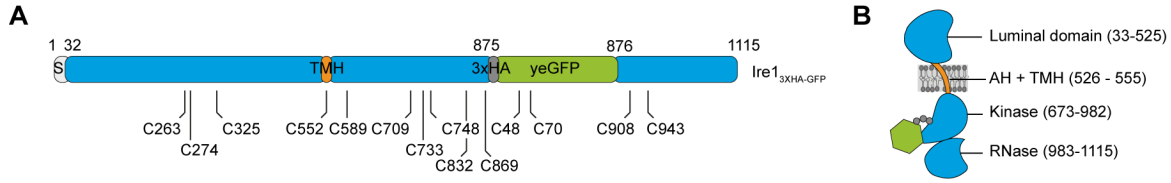

Figure 13: Schematic representation of the knock-in of *IRE1* construct and the location of cysteines.

(A) The *IRE1* knock-in construct contains the coding sequence of *IRE1*, and sequences encoding for a 3xHA-tag and a codon-optimized yeGFP inserted at position H875 of Ire1 (van Anken et al., 2014; Halbleib et al., 2017). Ire1 contains three luminal cysteines, one in its TMH and eight in its cytosolic domain. The engineered yeGFP contains two cysteines, C48 and C70, of which only C48 can be removed without compromising the fluorescent properties of yeGFP. (B) Schematic representation of Ire1's domain structure. The folded ER-luminal domain consists of amino acids 33 – 525. The TMH region is composed of an AH and a TMH formed by the amino acids 526 – 555. The cytosolic part encompasses a kinase (673 – 982) and a RNase domain (983 - 1115). S: Signal sequence, AH: amphipathic helix, TMH: Transmembrane helix.

To test the functionality of the cysteine-less variant of Ire1, ER-stress resistance assays were performed in minimal (SCD complete media) and full media (YPD media) (Figure 14A). Prolonged activation of ER-stress (18 h of ER-stress) by the stress-inducing agent dithiothreitol (DTT) that interferes with disulfide bridge formation revealed that cells producing the cysteine-less variant of Ire1 exhibit an indistinguishable resistance to DTT than cells producing the wild-type (WT) knock-in construct. However, cells lacking the *IRE1* altogether exhibit a marked sensitivity to DTT. Qualitatively similar results were obtained in full media with the notable difference that the cellular resistance of all strains was significantly higher in full medium (Figure 14A). As an alternative assay to study the functionality of cysteine-less Ire1, the cells were acutely stressed for 1 h and the relative degree of *HAC1* splicing was quantified using qPCR (Figure 14B). Either DTT or Tunicamycin (TM), an inhibitor of N-glycosylation in the lumen of the ER, were used to induce ER-stress. Cells expressing either the WT knock-in or the cysteine-less variant of *IRE1* show a significant increase of *HAC1* splicing levels in response to ER-stress. The level of the spliced *HAC1* mRNA in unstressed and stressed cells was indistinguishable between cells expressing the WT knock-in construct or the cysteine-less construct.

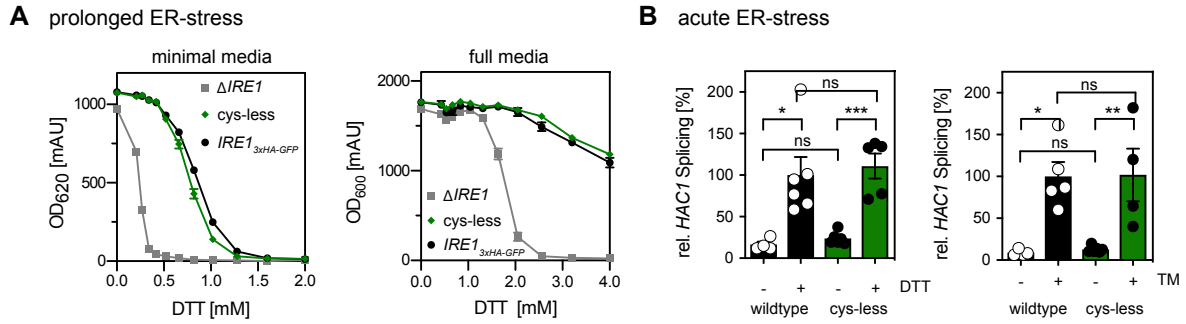

Figure 14: Cysteine-less Ire1 is functional.

(A) ER-stress resistance assays of the indicated strains in minimal (SCD complete) and full media (YPD) supplemented with different concentrations of DTT. A culture was inoculated to an OD_{600} of 0.01 with exponentially growing cells and cultivated for 18 h at 30°C. The final cell density was determined using the OD_{620} or OD_{600}. The error bars represent the mean ± SEM of at least three independent experiments. (B) The relative levels of spliced *HAC1* were analyzed by qPCR experiments. Exponentially growing cells in YPD were stressed for 1 h with DTT (4 mM) or Tunicamycin (1.0 µg/ml). The level of *HAC1* splicing was analyzed by RT-qPCR. Data were normalized to the level of spliced *HAC1* of stressed cells expressing WT *IRE1*$_{3xHA-GFP}$, which was set to 100%. The error bars represent the mean ± SEM of at least three independent experiments. Significance was tested with an unpaired, two-tailed Student's t-test. ***p<0.001, **p<0.01, *p<0.05.

As an important control, the steady-state protein levels of the cysteine-less and the WT variant of Ire1 were determined and compared (Figure 15A). The integration of cysteine-less Ire1 into the ER membrane was validated by a subcellular fractionation combined with a membrane extraction assay (Figure 15B). Pgk1 (phosphoglycerate kinase 1) served as a control for soluble cytosolic proteins and Dpm1 (dolichyl-phosphate mannosyltransferase 1) is a reference for an ER-transmembrane protein.

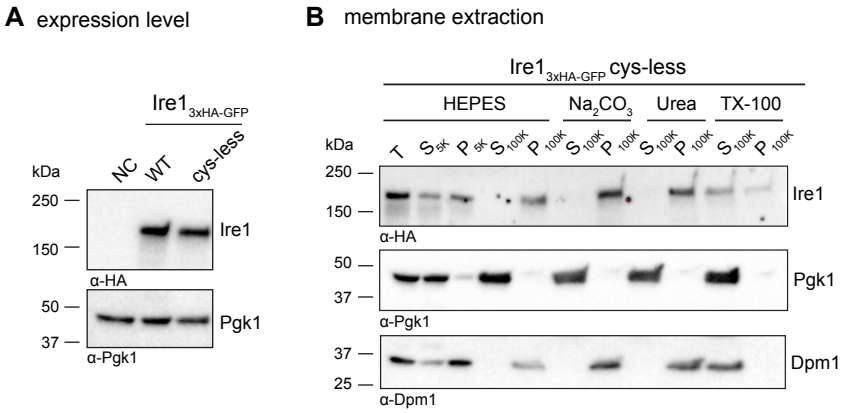

Figure 15: Steady-state level of cysteine-less Ire1 and its extraction from microsomal membranes.

(A) Expression levels of different Ire1 variants. Exponentially growing cells lacking an epitope-tagged variant of Ire1 (BY4741, NC) or expressing different knock-in construct of *IRE1* (either WT or cysteine-less) were harvested and lysed. The lysates were subjected to SDS-PAGE and immunoblotting with anti-HA antibodies. The isogenic wild-type strain BY4741 serves as a negative control for the anti-HA detection. Comparable loading was validated using anti-Pgk1 antibodies. (B) Subcellular fractionation and membrane extraction of cysteine-less Ire1. 80 OD_{600} equivalents of exponentially growing cells were used for the subcellular fractionation by differential centrifugation using 5,000x g and 100,000x g centrifugation steps. P100K samples containing microsomal membranes were treated either with HEPES, Na_2CO_3, urea or Triton X-100. The Na_2CO_3 and the urea treatments should remove peripherally attached membrane proteins, while Triton X-100 should solubilize the microsomal membranes. Samples of supernatant and pellet fraction after centrifugation of each condition were subjected to SDS-PAGE and immunoblotting using anti-HA antibodies. Anti-Pgk1 antibodies were used to track a soluble cytosolic protein, and anti-Dpm1 antibodies to track an unrelated ER membrane protein.

In conclusion, cysteine-less Ire1 is fully functional, correctly integrated into the ER membrane, and has a steady-state level similar to WT Ire1 produced from the same promotor and the same locus.

6.1.2 Cysteine crosslinking in microsomal membranes

6.1.2.1 Cysteine-mediated crosslinking of Ire1 requires $CuSO_4$ and pre-formed dimers

To study the architecture of the TMH region in clusters of Ire1 using single-cysteine crosslinking, a functional cysteine-less variant of Ire1 was established (6.1.1) and a crosslinking protocol compatible with membrane-exposed cysteine residues was employed.

$CuSO_4$ was chosen as a crosslinking reagent as it is known to function within the hydrophobic core of a lipid bilayer and to catalyze the oxidation of sulfhydryl groups of cysteines, which are in close proximity (Falke and Koshland, 1987; Kobashi, 1968; McIntosh and Freedman, 1980). In order to reduce the number of reactive cysteines in the crosslinking sample and to minimize unspecific crosslinking reactions, it was decided to prepare microsomal membranes by differential centrifugation prior to the crosslinking reaction. Microsomes were isolated from unstressed cells or from cells stressed either with DTT or TM to induce the formation of clusters of Ire1. The experimental procedure is illustrated in Figure 16A. Stationary cells of strains expressing the cysteine-less Ire1 or a single-cysteine variant with C552 (natively occurring cysteine in the TMH of Ire1) were used to inoculate a culture in SCD complete medium to an OD_{600} of 0.2. The cells were then cultivated at 30°C until an OD_{600} of 0.7 was reached. The formation of clusters of Ire1 was induced by adjusting the culture to either 2 mM DTT or 1.5 µg/ml TM followed by an additional cultivation for 1 h. The stressed and unstressed cells were harvested, washed and subjected to a differential centrifugation procedure to prepare crude microsomal membranes. Due to the low copy number of Ire1, which is estimated to be 260 (Ghaemmaghami et al., 2003), it can be assumed that the crude membrane fraction contains both vesicles with and without Ire1 molecules (Figure 16B). Importantly, Ire1 remains throughout the entire procedure in its native membrane environment with a complex lipid and protein composition present at the native protein-to-lipid ratio.

In order to induce crosslinking of neighboring cysteine-residues in clusters of Ire1, $CuSO_4$ was added to microsomes. The sample was then incubated on ice and the reaction was stopped after 5 min using EDTA for chelating Cu^{2+} ions and an excess of NEM to block all remaining free sulfhydryl groups (Falke and Koshland, 1987; Kobashi, 1968; McIntosh and Freedman, 1980). The samples were analyzed by SDS-PAGE and immunoblotting using anti-HA antibodies.

A prominent, HA-positive band corresponding to the monomeric Ire1 could be observed in all samples (Figure 16C). A less prominent, yet specific band that may correspond to a covalently crosslinked dimer of Ire1 was only observed when 1) a cysteine was present in the TMH region of Ire1 (C552), 2) when clusters of Ire1 were induced either by DTT or TM prior to the preparation of microsomes, and 3) when the microsomes were treated with $CuSO_4$ (Figure 16C). This suggests that C552 can be crosslinked by $CuSO_4$ with high specificity when present in pre-formed clusters of Ire1. This interpretation was further validated by a control experiment in which the crosslinked dimer was disrupted by an excess of DTT and heat, known to reduce disulfide bonds (Figure S 1).

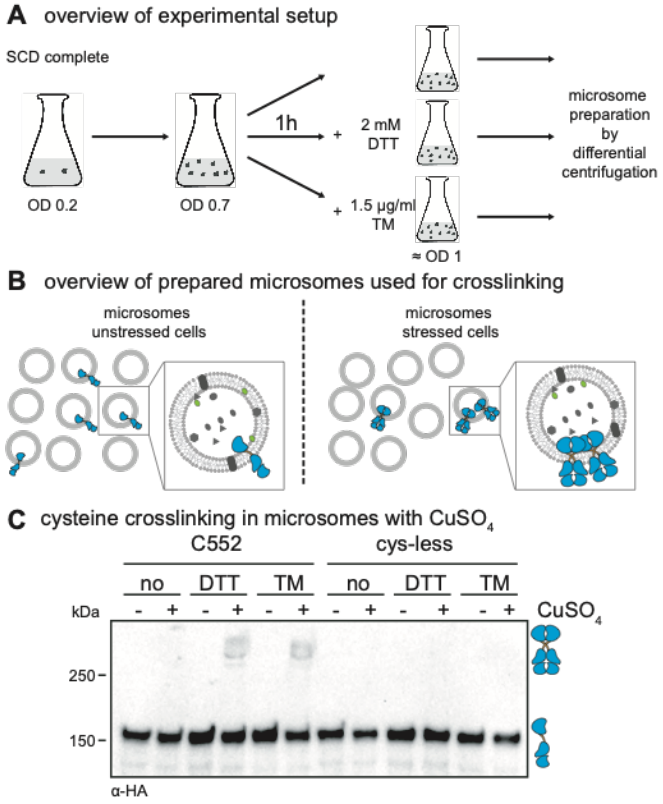

Figure 16: Single-cysteine crosslinking via $CuSO_4$ requires pre-formed dimers.

(A) Overview of experimental setup. Stationary cells were used to inoculate a culture in SCD complete medium to an OD_{600} of 0.2. After cultivation to an OD_{600} of 0.7, the cells were either stressed with 2 mM DTT, 1.5 µg/ml TM, or left untreated. After 1 h of additional cultivation, 80 OD_{600} equivalents were harvested and used for a microsomal membrane preparation by differential centrifugation. (B) Schematic overview of the expected distribution of Ire1 molecules in microsomes prepared from stressed and unstressed cells. The microsomal preparation is expected to contain a mixture of Ire1-containing and Ire1-free vesicles. Several copies of Ire1 in a single vesicle are only expected in preparation from stressed cells, where Ire1 forms stable, higher-oligomeric clusters. (C) Microsomes of unstressed and stressed cells were incubated for 5 min with 10 mM $CuSO_4$ on ice. The crosslinking reaction was stopped by a mix of EDTA, NEM and MSB. Samples were analyzed by SDS-PAGE and a subsequent immunoblotting using anti-HA antibodies.

6.1.2.2 Validation of Ire1 dimerization

In order to test if the immunoblot signal of lower electrophoretic mobility is indeed due to a covalently crosslinked dimer by Ire1 (Figure 16) and not due to the covalent crosslinking to an unrelated protein, a co-immunoprecipitation experiment was performed. HA-tagged and

FLAG-tagged variants of Ire1 with a single-cysteine (C552) were co-expressed in the same cell. Cysteine-less variants of Ire1 served as negative control in these experiments. After inducing the formation of clusters of Ire1 using DTT, microsomes were prepared and the crosslinking of cysteines was induced by $CuSO_4$. After an immunoprecipitation of the FLAG-tagged variant of Ire1 using anti-FLAG antibodies, immunoblots using anti-HA antibodies were used to test if HA-tagged Ire1 would be co-precipitated and would co-migrate due to a covalent crosslinking via C552 (Figure 17). This was indeed the case and validates the interpretation that Ire1 can form covalently crosslinked dimers in ER-derived microsomal membranes. These data are consistent with the prevailing model that Ire1 oligomerizes during ER-stress.

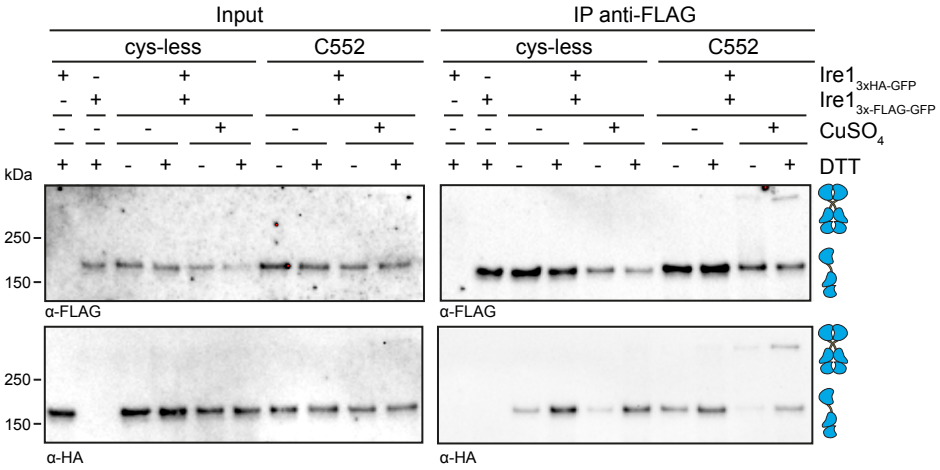

Figure 17: Co-immunoprecipitation validates the covalently crosslinked dimers of Ire1.

HA-tagged Ire1 was endogenously produced from the original gene locus of *IRE1*. FLAG-tagged Ire1 was expressed from a *CEN*-based plasmid. Stationary cells of the indicated strains were used to inoculate a culture in SCD complete medium to an OD_{600} of 0.2 After cultivation to an OD_{600} of 0.7, the cells were either stressed with 2 mM DTT or left untreated. After an additional hour of cultivation, 80 OD_{600} equivalents were harvested und subjected to a microsomal membrane preparation. Microsomes were incubated for 5 min with 10 mM $CuSO_4$ on ice and the crosslinking reaction was stopped by adding NEM and EDTA. After crosslinking reaction, the microsomes were solubilized using 1% Triton X-100 and subjected to a co-IP using anti-FLAG beads. The directly precipitated FLAG-tagged Ire1 and the co-immunoprecipitated HA-tagged Ire1 were analyzed by SDS-PAGE and a subsequent immunoblotting using anti-HA and anti-FLAG antibodies.

6.1.3 How do the TMHs interact with each other in clusters of Ire1?

6.1.3.1 Single-cysteine mutations and the impact on functionality

In order to characterize how the TMH region of Ire1 arranges in clusters of Ire1 and to identify the interface-forming residues, a systematic cysteine scanning and crosslinking screen was performed. The screen started with E540 and ended with C552 resulting in the analysis of three helical turns (Figure 18), which represent nearly the entire predicted TMH of Ire1.

Figure 18: Sequence of the TMH of Ire1.

(A) Sequence of the amphipathic helix and transmembrane helix of Ire1. (B) Helical wheel representation of Ire1's TMH.

In order to test if the substitution of single residues by cysteine affects the functionality of Ire1, ER-stress resistance assays were performed (Figure 19). Cells expressing the single-cysteine variants E540C, T541C or G542C variants were more sensitive to ER-stress caused by DTT than cells producing cysteine-less Ire1. This implies a subtle functional defect imposed by these mutations. All other single-cysteine variants were indistinguishable from cysteine-less Ire1 in their growth behavior and resistance to ER-stress. It is known that most mutations of E540 cause functional defects, while an Ire1 variant carrying a more conservative E540D mutation is fully functional (Halbleib, 2017). It remains unclear, why an acidic residue at the position E540 is important for Ire1's functionality. However, it is clear that E540 is functionally important and at a delicate position marking the transition from the TMH of Ire1 to the membrane-proximal amphipathic helix. It is therefore not surprising that the mutation E540C causes an increased sensitivity of the respective cells to DTT. Likewise, it is tempting to speculate that the neighboring T541 and G542 are structurally and functionally important by stabilizing the unique conformation of the TMH region thereby affecting the protein-membrane interaction of Ire1.

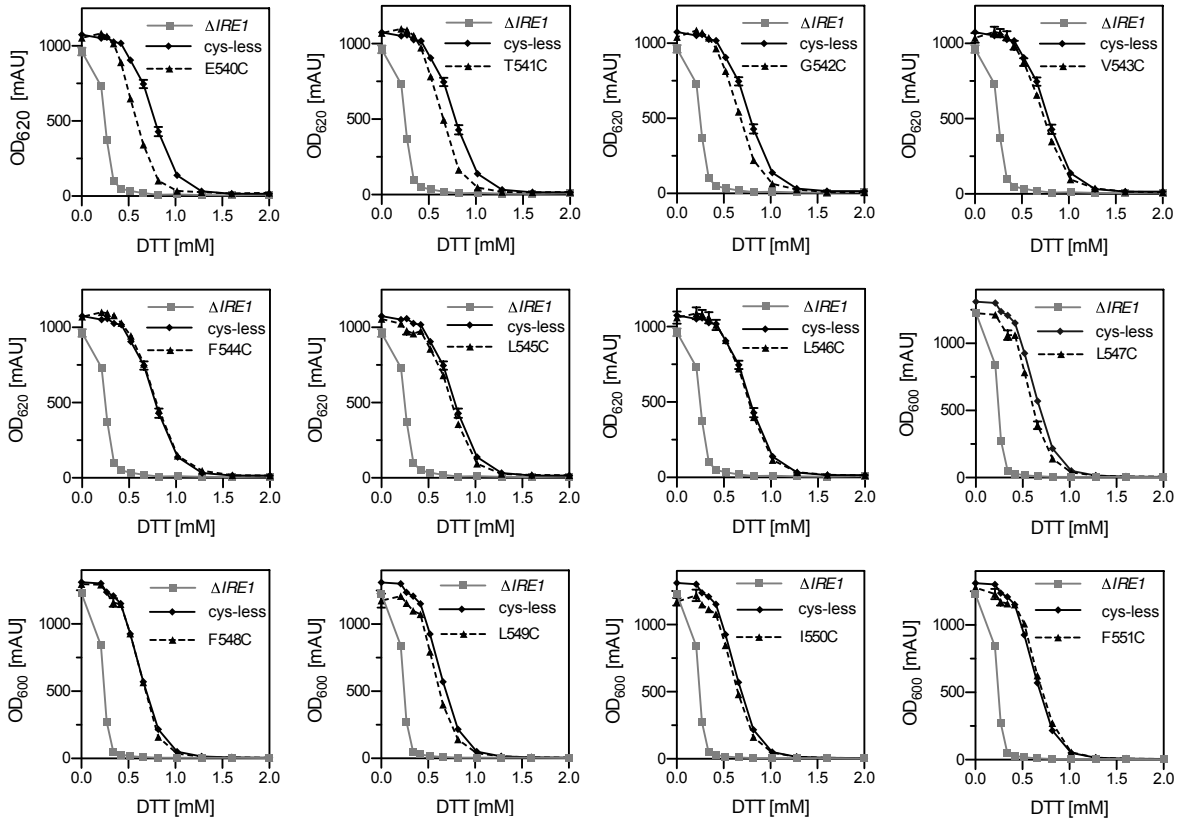

Figure 19: Functionality of single-cysteine variants of Ire1.

ER-stress resistance assays of the indicated strains in minimal media supplemented with different DTT concentrations. A culture was inoculated to an OD_{600} of 0.01 with exponentially growing cells and cultivated for 18 h at 30°C. The final cell density was determined using either the OD_{620} or OD_{600}. The error bars represent the mean ± SEM of at least two biological clones.

As an important control for all functional, cell-based analyses, the Ire1 steady-state protein level of each single-cysteine variant was determined by immunoblot analyses of cell lysates from exponentially growing cells. The analysis validated that the substitution of individual TMH residues by cysteine did not substantially affect the steady-state protein level of Ire1 (Figure 20).

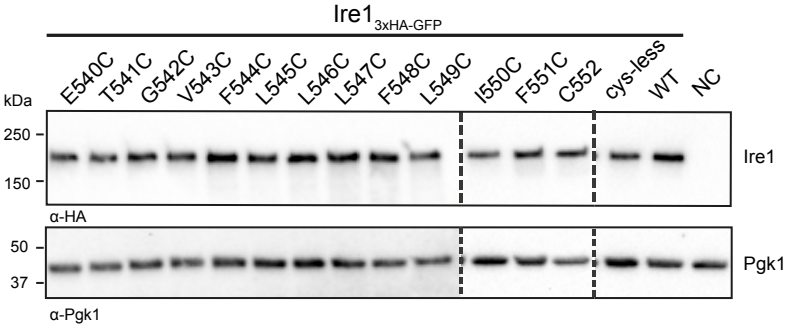

Figure 20: Single-cysteine variants do not affect the steady-state level of Ire1.

20 OD equivalents of exponentially growing cells (indicated strains) were harvested and lysed. 0.1 OD equivalents of the cell lysates were analyzed by SDS-PAGE and a subsequent immunoblot using anti-HA and anti-Pgk1 antibodies. Pgk1 serves as an equal loading control.

To conclude, most mutant variants of Ire1 generated in this thesis are produced at a similar rate and are present at comparable level in exponentially growing cells. Furthermore, most of the mutant variants are functional thereby allowing for a structure-function analysis using cell-based assays. The functional defect observed for the mutant variants E540C, T541C and G542C is subtle compared to the effect of an *IRE1* knock-out. This suggest a substantial residual activity of the mutant variant of Ire1. The reduced functionality of these variants, however, is likely reflecting a lower degree of oligomer formation thereby directly impacting on the crosslinking efficiency. This fact has to be considered when evaluating the crosslinking data for these functionally compromised variants with the other single-cysteine variants of Ire1.

6.1.3.2 Cysteine crosslinking reveals a X-shaped configuration of the TMHs

In order to identify the residue that contribute to the TMH-TMH interface in clusters of Ire1, microsomes were prepared from cells producing single-cysteine variants. The formation of Ire1-containing clusters was induced prior to the isolation of microsomes by supplementing the medium with Tunicamycin or DTT, or by depleting the medium of inositol (to induce lipid bilayer stress). The microsomes were then treated with $CuSO_4$ to induce the crosslinking of unpaired cysteines in close proximity.

Immunoblot analyses of the samples after crosslinking revealed substantial differences in the proportion of reacted Ire1 for different single-cysteine variants (Figure 21). The variants G542C, L546C, L547C, F548C and F551C of Ire1 could not be crosslinked at all, while all other variants could be crosslinked to different degree. The most striking signal was consistently observed for the F544C variant. Expectedly, almost no crosslinking was observed in microsomes prepared from unstressed cells (Figure 21). The minimal crosslinking observed for the F544C in the absence of ER-stress could be due to a low basal activity of the UPR, which has been previously described (Kimata et al., 2007; Promlek et al., 2011). Intriguingly, the pattern of crosslinks was comparable, irrespectively from the nature of ER-stress (proteotoxic or lipid bilayer stress) (Figure 22).

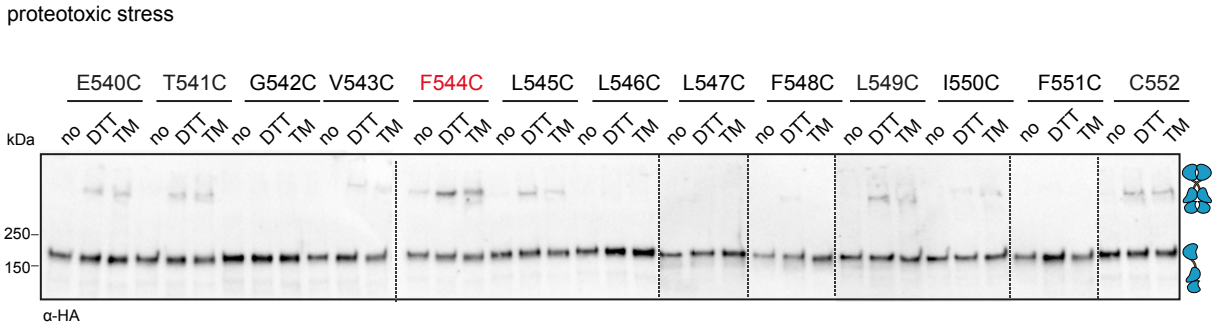

Figure 21: Single-cysteine crosslinking highlights F544C as the mutation with the highest crosslinking potential in clusters of Ire1 induced by DTT and TM.

Cysteine crosslinking in microsomes of the indicated stressed and unstressed cells. Stationary cells were used to inoculate a culture in SCD complete medium to an OD_{600} of 0.2. Cells were cultivated to an OD_{600} of 0.7 and then stressed with either 2 mM DTT, 1.5 µg/ml TM or left untreated. After 1 h of additional cultivation, 80 OD_{600} equivalents were harvested and subjected to a microsomal membrane preparation by differential centrifugation. To catalyze the crosslinking of cysteine residues, the microsomes were incubated for 5 min with 10 mM $CuSO_4$ on ice. The crosslinking reaction was stopped by a mix of EDTA, NEM and MSB. Samples were analyzed by SDS-PAGE and subsequent immunoblotting using anti-HA antibodies.

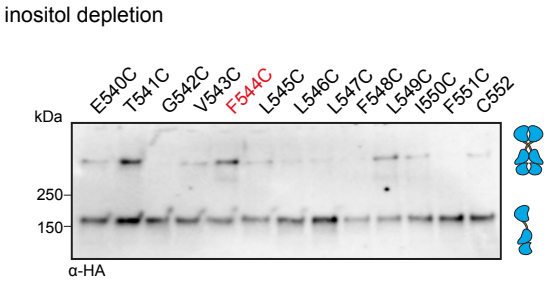

Figure 22: Single-cysteine crosslinking highlights F544C as the mutation with the highest crosslinking potential in clusters of Ire1 induced by inositol depletion.

Cysteine crosslinking in microsomes of the indicated cells depleted for inositol during growth. Exponentially growing cells were washed and used to inoculate a culture in SCD-inositol to an OD_{600} of 0.5. After cultivation for 3 h, 80 OD_{600} equivalents were harvested and microsomal membranes were prepared. To catalyze the crosslinking of cysteine residues, the microsomes were incubated for 5 min with 10 mM $CuSO_4$ on ice. The crosslinking reaction was stopped by a mix of EDTA, NEM and MSB. Samples were analyzed by SDS-PAGE and a subsequent immunoblotting using anti-HA antibodies.

Notably, the crosslinking patterns did not follow a simple helical pattern with a periodicity of three to four. This would be expected for a strict parallel association of two TMH's in the lipid bilayer (Figure 23A,B). This observation disfavors the model that the TMHs of Ire1 could be associate in a parallel fashion in signaling-active clusters. More likely is an association of the TMHs in a X-shaped configuration with the crossing point marked by the position of F544, where the highest degree of crosslinking was observed (Figure 23C). Strikingly, these observations suggest that different forms of ER-stress, caused by proteotoxic and lipid bilayer stress, converge in a single TMH architecture. Consequently, different signaling outcomes of the UPR are unlikely not to rely on different TMH architectures in clusters of Ire1.

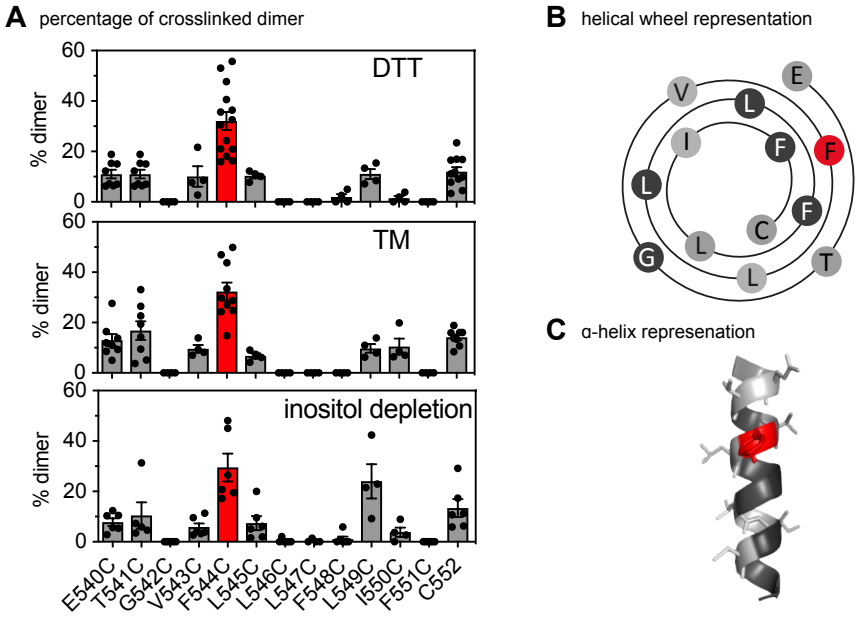

Figure 23: F544C crosslinks best in all tested conditions.

(A) Quantification of cysteine crosslinking from three distinct conditions of ER-stress. The percentage of dimer for each single-cysteine variant was determined with the software Image J (n>4, mean ± SEM). (B) Helical wheel representation of the TMH of Ire1. Residues, which did not crosslink are colored in dark grey. Residues showing some crosslinking are illustrated in light grey and F544C, the best crosslinking residue, is highlighted in red. (C) α-helix representation of Ire1's TMH. Color code as described in (B).

6.1.3.3 The amphipathic helix stabilizes the X-shaped conformation

The unusual configuration of Ire1's TMHs raises the question how this conformation is stabilized. Is the amino acid at position F544 important for the stability of the signaling-active state of Ire1? To test the influence of F544 on the stability of Ire1, the amino acid at position F544 was substituted with alanine and the effect of this mutation on Ire1's functionality and the crosslinking behavior of C552 was investigated (Figure 24). Surprisingly, the ER-stress resistance phenotype of cells producing the F544A variant was indistinguishable from cells expressing the cysteine-less variant (Figure 24A). Also, the crosslinking at position C552 was not affected by the F544A mutation (Figure 24B). This suggests that the unusual X-shaped configuration of Ire1's TMH in signaling-active clusters is not stabilized by a specific interaction of the residue at position 544 (Figure 24B).

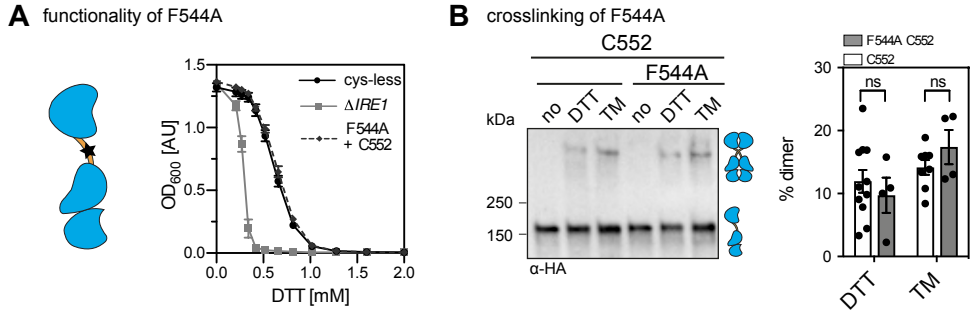

Figure 24: A F544A mutation does not impair the function of Ire1 and its crosslinking behavior.

(A) ER-stress resistance assays of the indicated strains in minimal media supplemented with different DTT concentrations. A culture was inoculated to an OD_{600} of 0.01 with exponentially growing cells and cultivated for 18 h at 30°C. The final cell density was determined using the OD_{600}. (B) Cysteine crosslinking in microsomes of the indicated cells. Cysteine crosslinking in microsomes of the indicated stressed and unstressed cells. Stationary cells were used to inoculate a culture in SCD complete medium to an OD_{600} of 0.2. Cells were cultivated to an OD_{600} of 0.7 and then stressed with either 2 mM DTT, 1.5 µg/ml TM or left untreated. After 1 h of additional cultivation, 80 OD_{600} equivalents were harvested and subjected to a microsomal membrane preparation by differential centrifugation. To catalyze the crosslinking of cysteine residues, the microsomes were incubated for 5 min with 10 mM $CuSO_4$ on ice. The crosslinking reaction was stopped by a mix of EDTA, NEM and MSB. Samples were analyzed by SDS-PAGE and subsequent immunoblotting using anti-HA antibodies. The percentage of dimer was quantified as the ratio of dimer to whole Ire1 signal by the software Image J. The error bars in (A) and (B) represent the mean ± SEM of at least three independent experiments. Significance was tested by an unpaired, two-tailed Student's t-test.

Next, the role of the AH adjacent to the TMH of Ire1 was tested. The crosslinking of F544C and C552 was analyzed in combination with a F531R mutation that disrupts the membrane-integration of the AH adjacent to the TMH and thus membrane-sensitivity of Ire1 (Halbleib et al., 2017) (Figure 25).

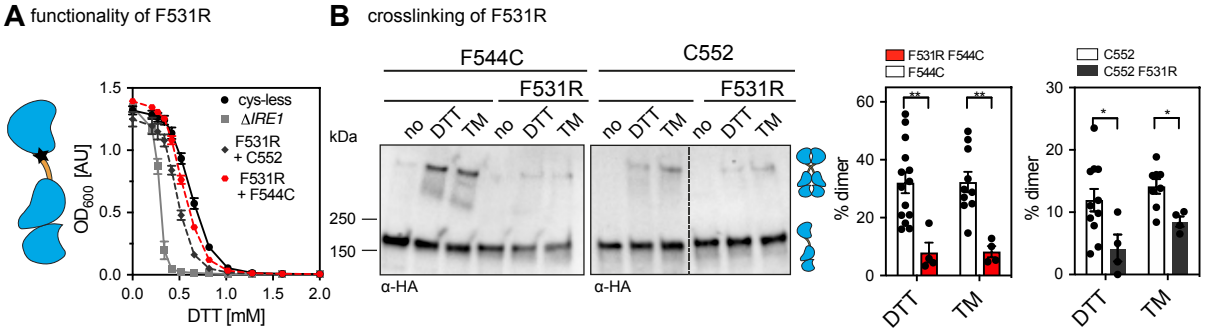

Figure 25: An AH-disruptive mutation (F531R) lowers the crosslinking potential of Ire1.

(A) ER-stress resistance assays of the indicated strains in minimal media supplemented with different DTT concentrations. A culture was inoculated to an OD_{600} of 0.01 with exponentially growing cells and cultivated for 18 h at 30°C. The final cell density was determined using the OD_{600}. (B) Cysteine crosslinking in microsomes of the indicated cells. Cysteine crosslinking in microsomes of the indicated stressed and unstressed cells. Stationary cells were used to inoculate a culture in SCD complete medium to an OD_{600} of 0.2. Cells were cultivated to an OD_{600} of 0.7 and then stressed with either 2 mM DTT, 1.5 µg/ml TM or left untreated. After 1 h of additional cultivation, 80 OD_{600} equivalents were harvested and subjected to a microsomal membrane preparation by differential centrifugation. To catalyze the crosslinking of cysteine residues, the microsomes were incubated for 5 min with 10 mM $CuSO_4$ on ice. The crosslinking reaction was stopped by a mix of EDTA, NEM and MSB. Samples were analyzed by SDS-PAGE and subsequent immunoblotting using anti-HA antibodies. The percentage of dimer was quantified as the ratio of dimer to whole Ire1 signal by the software Image J. The error bars in (A) and (B) represent the mean ± SEM of at least three independent experiments. Significance was tested by an unpaired, two-tailed Student's t-test.

When testing the sensitivity of the single-cysteine mutants F544C and C552 to DTT in combination with the AH-disruptive mutant F531R (Halbleib et al., 2017), it became clear that the F531R mutant affects Ire1's function (Figure 25A). However, when the F531R mutation of

the AH was combined with the F544C single-cysteine mutation, the functional defect was less pronounced. I speculate that the polar cysteine residue at position F544 might stabilize the dimeric form of Ire1 thereby potentially rescuing some of the functional defect caused by the disruption of the AH. However, the molecular details underlying these observations remain to be studied in greater detail. The AH-disrupting mutation F531R lowers the crosslinking observed for C552 and for F544C (Figure 25B). The reason for the lower crosslinking rate could be 1) less dimer formation, which was recently shown (Halbleib et al., 2017) or 2) a different orientation of the two TMHs in a dimer relative to each other. MD simulations revealed that a disruption of the AH leads to a local unfolding and a reorientation of the short TMH towards the normal of the lipid bilayer (Halbleib et al., 2017). This conformational change in Ire1's TMH is likely to contribute to a perturbed crosslinking potential of F544C.

6.1.3.4 The impact of an oligomer breaking mutation on the crosslinking of Ire1

The cysteine-mediated crosslinking that was observed for different single-cysteine variants of Ire1 could arise either from 'within dimers' or 'across dimers' of Ire1 in higher oligomeric clusters. To further characterize this point in greater detail, the effect of the W426A mutation, which disrupts higher oligomers of Ire1 by disrupting the ER-luminal IF2 interface, was analyzed. The mutation W426A inhibits the formation of higher oligomers with no impact on the formation of dimers of Ire1.

To study the effect of the IF2 mutation on the functionality of Ire1, ER-stress resistance assays were performed in full media. Notably, cells expressing the E540C and T541C variant exhibited no increased sensitivity to DTT. In fact, their growth was indistinguishable from cells expressing the cysteine-less Ire1 (Figure 26A). In contrast, the IF2-disruptive mutation W426A causes a significantly increased sensitivity of the respective cells to DTT and even more so, when this mutation was combined with E540C and T541C mutation. These double mutants were indistinguishable from cells lacking *IRE1* altogether. Several attempts were made to clone the IF2 mutation in the cysteine-less background. Unfortunately, this cloning was not successful. This is the reason why the effect of the IF2 mutation was tested in combination with L545C. Cells producing the IF2 mutation in combination with a L545C mutation showed a decreased resistance to ER-stress, but still a significantly higher resistance than a Δ*IRE1* strain. Surprisingly, cells producing the IF2 mutation in combination with F544C mutation were more resistant to DTT than these cells. It seems that the cysteine at position F544 can partially compensate for a functional defect caused by a W426A mutation. A similar effect of the F544C mutation was also observed, when this mutation was combined with the AH-disruptive mutation F531R (Figure 25A). It is tempting to speculate that the polar nature of the cysteine at position F544 or a minor degree of crosslinking already occurring in cells might contribute

to the increased resistance to DTT. In order to distinguish between crosslinked Ire1 formed between dimers or higher oligomers, the crosslinking of E540C, T541C and F544C combined with the IF2-disruptive mutation was analyzed. The IF2-disruptive mutation significantly affects the crosslinking of E540C (Figure 26B and C). In contrast, the crosslinking of the T541C and F544C variants was only marginally affected. Interestingly, the combination of the mutations T541C and W426A led to a loss of function of Ire1, but, the crosslinking and consequently the orientation of the TMH to each other was not affected by the IF2 mutation. This implies that the crosslink via T541C is formed within a dimer of Ire1, but not across dimers in a higher oligomeric arrangement. In contrast, the ability to form crosslinked dimers seemed to be completely abolished for E540C with the IF2-disruptive mutation (Figure 26B and C). It can be speculated that this interaction formed by E540C is formed between a higher oligomer of Ire1 and consequently inhibited by the IF2 mutation. Alternatively, it is possible that under these conditions, no higher oligomers and dimers of Ire1 form at all. Like the crosslinked species formed by T541C, the crosslinking of F544C is only marginally affected by the W426A mutation. One can therefore assume that this covalent link is formed within dimers of Ire1.

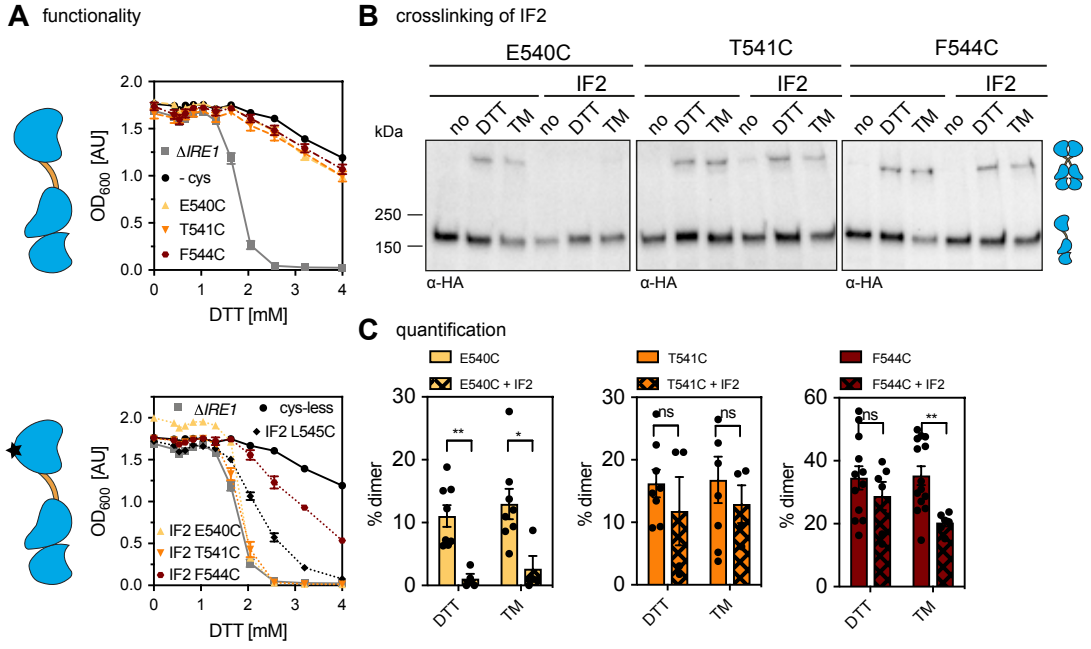

Figure 26: An oligomer breaking mutation (IF2 W426A) lowers the functionality of Ire1 and affect its crosslinking behavior.

(A) ER-stress resistance assays of the indicated strains in minimal media supplemented with different DTT concentrations. A culture was inoculated to an OD_{600} of 0.01 with exponentially growing cells and cultivated for 18 h at 30°C. The final cell density was determined using the OD_{600}. (B) Cysteine crosslinking in microsomes of the indicated cells. Cysteine crosslinking in microsomes of the indicated stressed and unstressed cells. Stationary cells were used to inoculate a culture in SCD complete medium to an OD_{600} of 0.2. Cells were cultivated to an OD_{600} of 0.7 and then stressed with either 2 mM DTT, 1.5 µg/ml TM or left untreated. After 1 h of additional cultivation, 80 OD_{600} equivalents were harvested and subjected to a microsomal membrane preparation by differential centrifugation. To catalyze the crosslinking of cysteine residues, the microsomes were incubated for 5 min with 10 mM $CuSO_4$ on ice. The crosslinking reaction was stopped by a mix of EDTA, NEM and MSB. Samples were analyzed by SDS-PAGE and subsequent immunoblotting using anti-HA antibodies. The percentage of dimer was quantified as the ratio of dimer to whole Ire1 signal by the software Image J. The error bars in (A) and (B) represent the mean ± SEM of at least three independent experiments. Significance was tested by an unpaired, two-tailed Student's t-test.

6.1.3.5 Crosslinking of double-cysteine variants validates the X-shaped dimer

The here employed strategy of single-cysteine crosslinking has a number of specific strengths but also weaknesses. Some specific arrangements, such as piston-type motions of the TMHs cannot be detected. The cysteines in the TMH would be moved apart from each other and, consequently, a covalent bond would not be formed in the presence of $CuSO_4$. In order to verify the X-shaped configuration of the TMHs and the possibility that they moved against each other in a piston-type arrangement, double cysteine mutants were generated. The double cysteine variants were chosen such that the cysteines are located on opposite sides of the helix. The crosslinking of the double-cysteine variants L545C + L546C and I550C + C552 were compared to the crosslinking of their corresponding single-cysteine variants. If the percentage of crosslinking of double-cysteine mutants is significantly increased compared to the single-cysteine variants, a piston-type arrangement of the TMHs would be likely. For both tested double-cysteine variants (L545C + L546C and I550C + C552), the percentage of crosslinking was not significantly increased over the crosslinking observed for the corresponding single-cysteine variants (Figure 27). This implies that the X-shaped configuration of the TMH is more likely than an arrangement in which the two TMHs are associated towards each other in a piston-type arrangement. While the here presented data cannot fully exclude the formal possibility of alternative relative orientations, the concordance of crosslinking data, functional data, and MD simulation data (see below) make an X-shaped arrangement of the TMH most likely and most reasonable.

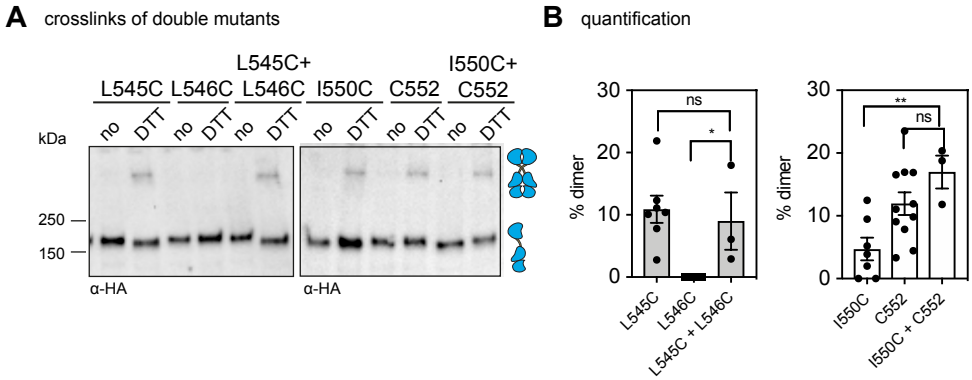

Figure 27: Crosslinking of double cysteine variants validate the X-shaped dimer.

Cysteine crosslinking in microsomes of the indicated cells. Cysteine crosslinking in microsomes of the indicated stressed and unstressed cells. Stationary cells were used to inoculate a culture in SCD complete medium to an OD_{600} of 0.2. Cells were cultivated to an OD_{600} of 0.7 and then stressed with 2 mM or left untreated. After 1 h of additional cultivation, 80 OD_{600} equivalents were harvested and subjected to a microsomal membrane preparation by differential centrifugation. To catalyze the crosslinking of cysteine residues, the microsomes were incubated for 5 min with 10 mM $CuSO_4$ on ice. The crosslinking reaction was stopped by a mix of EDTA, NEM and MSB. Samples were analyzed by SDS-PAGE and subsequent immunoblotting using anti-HA antibodies. The percentage of dimer was quantified as the ratio of dimer to whole Ire1 signal by the software Image J. The error bars represent the mean ± SEM of at least three independent experiments. Significance was tested by an unpaired, two-tailed Student's t-test.

6.1.4 MD simulations showed a similar X-shaped orientation of Ire1's TMH

MD simulations of the TMH region of Ire1 performed by Dr. Roberto Covino (Hummer group, MPI Biophysics Frankfurt) gain an insight into the architecture and structural dynamics of the TMH of Ire1. To this end, two peptides comprising the AH and the TMH of Ire1 (aa 516 – 571) were placed in a lipid bilayer containing two lipids that result in tight lipid packing to simulate a condition of lipid bilayer stress: POPC and cholesterol (80 mol% : 20 mol%). They were modelled based on a peptide structure that was taken from a previous 10 µs long atomistic MD simulation. The equilibrated peptide was then duplicated to yield two peptide configuration, which were arranged in a way that the two residues F544 were facing each other in a distance range between the Cβ of roughly 0.7 nm. A short energy minimization was performed to resolve all steric clashes between the side chains. After this energy minimization and quick relaxation, the dimer model was equilibrated again by running a 50 ns long simulation and restraining the position of the protein atoms. After this final equilibration, all restrains were relieved and a 500 ns long MD simulation was performed. Snapshots from this MD simulation highlighted the putative, overall and bend architecture of the TMH and the location of the F544 at the crossing point of the two TMH arranged in a X-shaped conformation (Figure 28). This MD simulation also demonstrates the membrane thinning of the membrane and a substantial water penetration in this area.

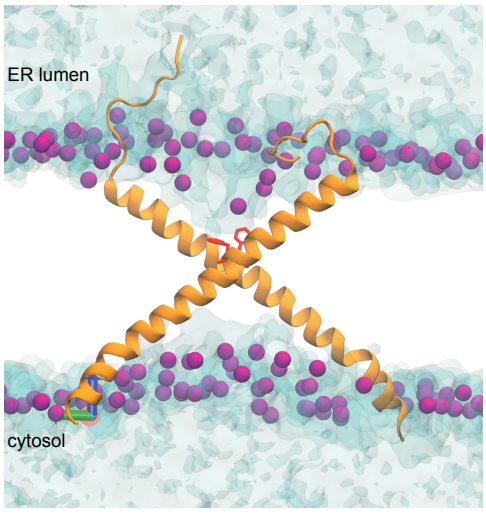

Figure 28: MD simulations indicate a X-shaped architecture of the TMH in Ire1 clusters.

Structural model of the dimeric TMH region of Ire1 derived from atomistic molecular dynamics simulations. The two protomers of Ire1 are shown as an orange ribbon, with the residues F544 highlighted in red. Water is shown in a transparent surface representation. The purple spheres indicate the positions of phosphate atom from the glycerophospholipids to illustrate the striking membrane deformation apparent on both sides of the membrane. The illustration was kindly provided by Dr. Roberto Covino.

In summary, the crosslinking studies in this thesis reveal an X-shaped configuration of the TMHs in clusters of Ire1. In this configuration, F544 lies at the interface of the protomers marking the crossing point of the X. Mutational analysis suggest that this overall configuration

is stabilized by the AH of Ire1. MD simulations and the use of double-cysteine mutants further validate this characteristic X-shaped configuration present in signaling-active clusters of Ire1. The here presented data suggest that proteotoxic and lipid bilayer stress converge – at least in the TMH region – in a single signaling-active configuration.

6.2 The interdependency of proteotoxic stress and lipid bilayer stress

The collective properties of biological membranes affect the interaction, localization and function of membrane proteins (Ernst et al., 2018; Radanović et al., 2018). The activity of Ire1 is regulated by oligomerization, which was shown to be influenced by the membrane environment (Halbleib et al., 2017; Surma et al., 2013; Thibault et al., 2012; Volmer et al., 2013). Recently, the AH adjacent to the TMH of Ire1 was identified as an important structural element that mediates the membrane-dependent oligomerization of Ire1 upon lipid bilayer stress. In this work, the influence of the membrane environment on the binding of misfolded proteins to the core ER-luminal domain of Ire1 is characterized. With these experiments, an interdependency between unfolded/misfolded proteins and lipid bilayer stress could be identified.

6.2.1 An *in vitro* system to study the interdependency of proteotoxic stress and lipid bilayer stress

To analyze if the binding of misfolded proteins to Ire1 is modulated by the membrane environment, an *in vitro* binding assay to study the interaction of a misfolded protein with Ire1 was established. Specifically, a membrane-reconstituted sensor construct ($^{MBP}Ire1_{cLD\text{-}AH\text{-}TMH}$) and a misfolded protein CPY* were used to study the role of the membrane on CPY* binding to Ire1.

6.2.1.1 Purification and characterization of the $^{MBP}Ire1_{cLD\text{-}AH\text{-}TMH}$ fusion protein

The sensor construct $^{MBP}Ire1_{cLD\text{-}AH\text{-}TMH}$ was based on the yeast Ire1 and consisted of a maltose binding protein (MBP) as solubilization and purification tag, the core ER-luminal domain of Ire1 with its C-terminal, loosely folded Kar2 binding site and the TMH region of Ire1. This construct was generated in a collaborative effort with Susanne Wolf during her bachelor thesis (Figure 29A) (Wolf, 2016). To enable a use of this construct for cysteine-specific labeling experiments, it was generated based on the cysteine-less variant of Ire1 established in this thesis (6.1.1).

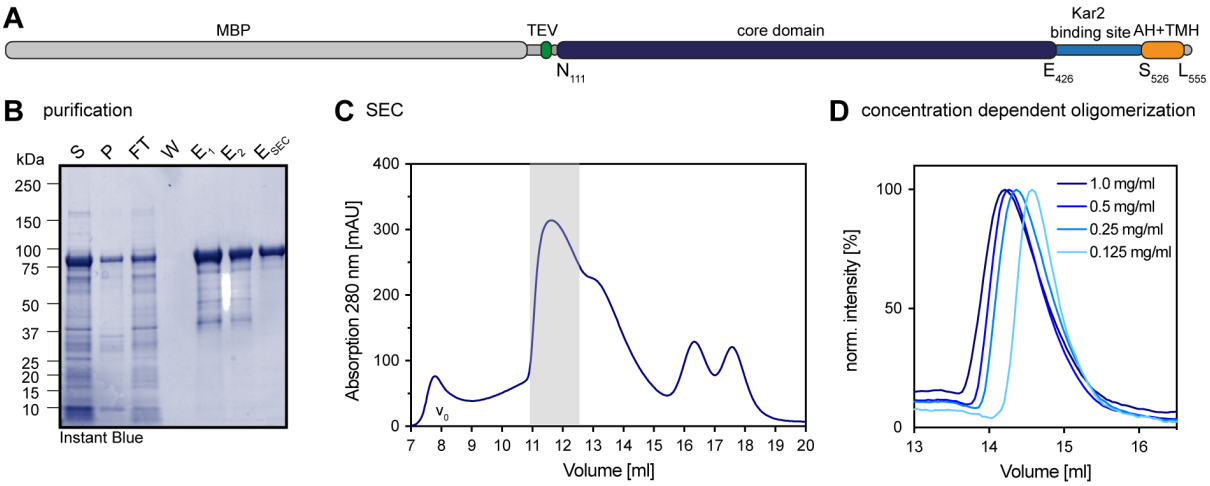

Figure 29: Purification of $^{MBP}Ire1_{cLD\text{-}AH\text{-}TMH}$ for *in vitro* studies.

(A) Illustration of the *in vitro* $^{MBP}Ire1_{cLD\text{-}AH\text{-}TMH}$ construct. The construct contained N-terminally an MBP-tag, a linker, a TEV cleavage site and the core ER-luminal domain of Ire1, the Kar2 binding site and the amphipathic and transmembrane helix of Ire1. (B) Affinity purification of $^{MBP}Ire1_{cLD\text{-}AH\text{-}TMH}$ from *E. coli.* The purification was monitored by subjecting 0.1 OD_{600} equivalents of supernatant (S), pellet (P), flow-through (FT), washing steps (W) and eluate (E) and 1 µg of SEC purified protein to SDS-PAGE and a subsequent InstantBlue™ staining. (C) SEC purification of $^{MBP}Ire1_{cLD\text{-}AH\text{-}TMH}$ using a Superose 6 Increase Column to increase purity of the protein. Volumes with a grey background were pooled and used for further experiments. (D) SEC of purified protein in detergent containing buffer analyzing the concentration-dependent oligomerization of the construct. Purified protein was concentrated using an Amicon (cut off 100 kDa) and the protein concentration was adjusted to the indicated concentrations prior to loading 100 µl onto a Superose 6 Increase column.

The purification of $^{MBP}Ire1_{cLD\text{-}AH\text{-}TMH}$ was established together with Susanne Wolf during her bachelor thesis (Wolf, 2016). $^{MBP}Ire1_{cLD\text{-}AH\text{-}TMH}$ was produced in the cytosol of *E. coli* and purified in the presence of the detergent β-OG by affinity chromatography using amylose columns (Figure 29B). The affinity-purified protein was further isolated using size-exclusion chromatography (SEC). The yield of the isolation was 1-2 mg of purified protein per liter of bacterial culture (Figure 29C). The homogeneity of the purified protein was verified by applying a sample again to a SEC. The protein eluted in a single peak from the column. The elution volume of $^{MBP}Ire1_{cLD\text{-}AH\text{-}TMH}$ did not correspond to the size of a monomer suggesting that the $^{MBP}Ire1_{cLD\text{-}AH\text{-}TMH}$ exists as an oligomer in detergent. This is not surprising as the core ER-luminal domain alone is known to form dynamic oligomers (Gardner and Walter, 2011). To further analyze the oligomeric state of $^{MBP}Ire1_{cLD\text{-}AH\text{-}TMH}$, the purified protein was first concentrated and then subjected in different dilutions to a SEC experiment. The peak of the elution was dependent on the protein concentration, thereby indicating a dynamic equilibrium of $^{MBP}Ire1_{cLD\text{-}AH\text{-}TMH}$ in detergent solution (Figure 29D).

6.2.1.2 Reconstitution of $^{MBP}Ire1_{cLD\text{-}AH\text{-}TMH}$ in liposomes

The reconstitution of the $^{MBP}Ire1_{cLD\text{-}AH\text{-}TMH}$ in liposomes was established in a collaborative effort with Susanne Wolf during her bachelor thesis. Previously, $^{MBP}Ire1_{cLD\text{-}AH\text{-}TMH}$ was reconstituted in liposomes composed of *E. coli* polar lipids (EPL) supplemented with DPPC (70

mol%:30mol%) (Wolf, 2016). Here, $^{MBP}Ire1_{cLD\text{-}AH\text{-}TMH}$ was inserted in the lipid bilayer at a protein:lipid molar ratio of 1:6000 . The correct insertion was verified using a sucrose density gradient and carbonate and urea extraction (Wolf, 2016). However, a liposome composition containing EPL resembles a rather unnatural environment for an ER membrane protein. In fact, C-laurdan spectroscopy suggest that the lipid packing in EPL is much higher than in the ER (data not shown) (Wenzel et al., 2018). Additionally, EPL are a complex mixture of different, rather poorly characterized lipid species. In order to systematically explore the role of specific lipid headgroup and lipid acyl chains, a synthetic lipid mixture would be much more suitable. Therefore, I decided to reconstitute $^{MBP}Ire1_{cLD\text{-}AH\text{-}TMH}$ in liposomes composed of simple lipid mixtures (Figure 30). As a simple, and loosely packing lipid composition, I used a mixture of 50% POPC and 50% DOPC (all mixtures are given in mol%). This most loosely packed lipid composition was referred to as ‘composition 1’. It mimics the acyl chain composition of an unstressed ER membrane. Densely packed liposomes containing different lipids such as ‘composition 4’ (60% POPC, 10% DPPC, 30% Cholesterol) and ‘composition 9’ (10% POPC, 40% POPE, 20% DPPC, 20% Soy-PI, 10% Cholesterol), were used to mimic conditions of ER-stress, characterized by a higher percentage of tightly packed lipids. Notably, for ‘composition 9’ several characteristic features of the stressed ER were combined (2.3.2).

To reconstitute $^{MBP}Ire1_{cLD\text{-}AH\text{-}TMH}$ in liposomes, it was mixed with multilaminar vesicles of the desired lipid composition. The lipids were completely dissolved by the addition of β-OG to a final concentration of 37.5 mM to a 1 ml solution. After a short incubation, the detergent was removed using SM-2 Bio-Beads™ and the resulting proteoliposomes were harvested by ultracentrifugation (Figure 30A). The proteoliposomes were subjected to an analytical sucrose density gradient centrifugation. As expected for a successful reconstitution, $^{MBP}Ire1_{cLD\text{-}AH\text{-}TMH}$ cofractionated with the lipids in the gradient after centrifugation (Figure 30B). Only a minor fraction of $^{MBP}Ire1_{cLD\text{-}AH\text{-}TMH}$ was found as an aggregate in the bottom fraction of the gradient. The orientation of the protein was tested using a TEV protease, which is membrane impermeable and cleaves between the MBP tag and the core ER-luminal domain of Ire1 (Figure 30C). This protease accessibility assay revealed that >65% of MBP was cleaved from $^{MBP}Ire1_{cLD\text{-}AH\text{-}TMH}$ thereby showing that >65% of the core ER-luminal domain of Ire1 is oriented towards the aqueous environment and that <35% is facing the lumen of the proteoliposomes.

The proper integration of the construct into the membrane of proteoliposomes was further analyzed by an extraction assay using sodium carbonate, urea and the detergent SDS. Sodium carbonate and urea treatment would remove peripherally attached proteins, while SDS should solubilize even properly integrated, transmembrane proteins. For the reconstitution of $^{MBP}Ire1_{cLD\text{-}AH\text{-}TMH}$ in densely packed liposomes, the membrane integration assay validated a robust membrane insertion of $^{MBP}Ire1_{cLD\text{-}AH\text{-}TMH}$ (Figure 30D). For the reconstitution in loosely

packed liposomes, we found that the conditions to harvest the proteoliposomes were not entirely sufficient for a full recovery of the protein in the pellet fraction (Figure 30D, HEPES control). Despite this minor technical issue in pelleting proteoliposomes, the extraction assay validated the proper integration of $^{MBP}Ire1_{cLD\text{-}AH\text{-}TMH}$ into densely packed and most likely also into the more loosely packed membrane environments (Figure 30D).

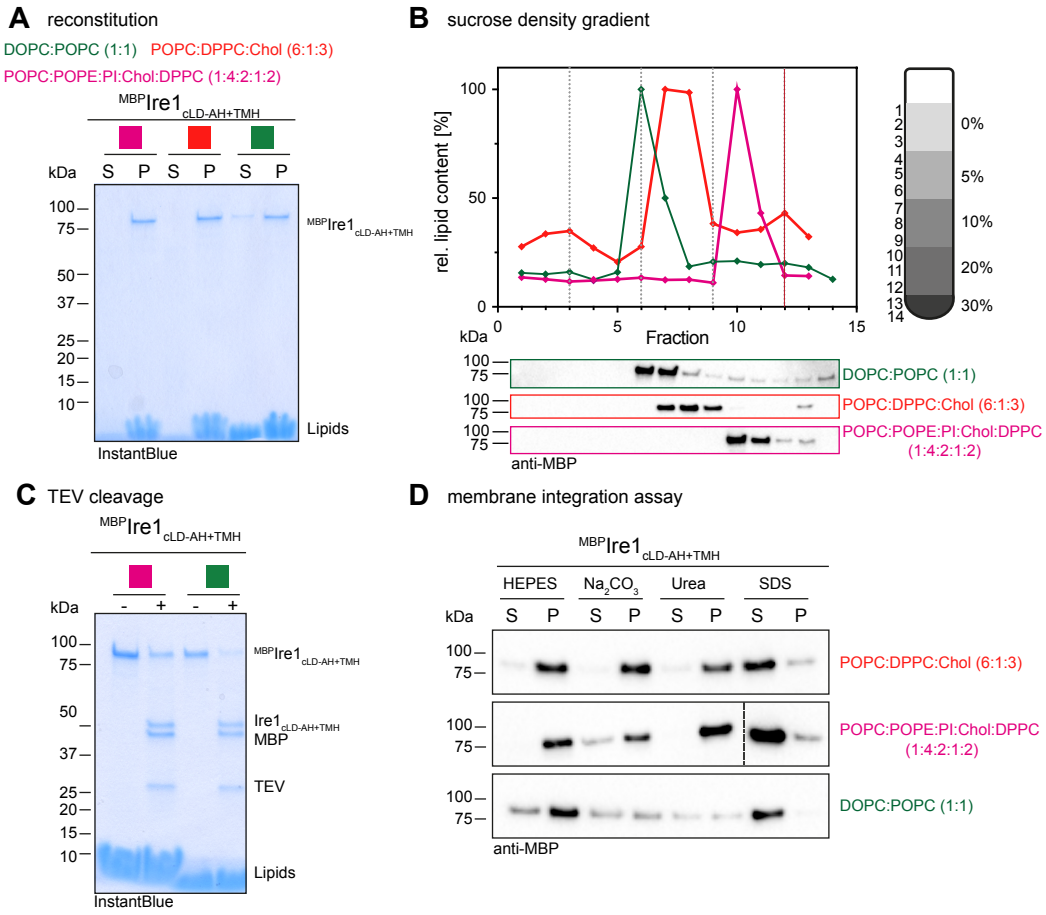

Figure 30: Reconstitution of $^{MBP}Ire1_{cLD\text{-}AH\text{-}TMH}$ for *in vitro* studies.

(A) The purified $^{MBP}Ire1_{cLD\text{-}AH\text{-}TMH}$ construct was reconstituted into composition 9 (10% POPC, 40% POPE, 20% DPPC, 20% Soy-PI, 10% Cholesterol), composition 4 (60% POPC, 10% DPPC, 30% Cholesterol) and composition 1 (50% DOPC, 50% POPC) liposomes in a protein-to-lipid molar ratio of 1:6000. The proteoliposomes were harvested by centrifugation (400.000x g, 90 min, 4°C) and the supernatant (S) and pellet (P) fraction were analyzed by SDS-PAGE and a subsequent InstantBlue staining. (B) Analysis of protein aggregates in proteoliposome samples by sucrose density gradient. The proteoliposomes were adjusted to 30% sucrose and overlaid with several buffers containing different sucrose concentrations (20%, 10%, 5%, 0%). The gradient was centrifuged (100.000x g, 16 h, 4°C). After ultracentrifugation, fractions were taken, and the relative lipid content was determined by Hoechst 33342 fluorescent staining. The amount of $^{MBP}Ire1_{cLD\text{-}AH\text{-}TMH}$ in the fractions was detected by immunoblotting using anti-MBP antibodies. (C) Analysis of $^{MBP}Ire1_{cLD\text{-}AH\text{-}TMH}$ orientation in proteoliposomes by TEV cleavage. Proteoliposomes were incubated with TEV protease overnight at RT. Samples of untreated and TEV treated samples were analyzed by SDS-PAGE and subsequent InstantBlue staining. (D) The proteoliposomes were adjusted to 0.1 M Na_2CO_3 pH 11 and 2.5 M urea to remove peripherally attached proteins. Samples treated with SDS was used for complete solubilization. An untreated sample that was only diluted with HEPES buffer served as a control for pelleting proteoliposomes. Samples were centrifuged (400.000x g, 90 min, 4°C) and supernatant (S) and pellet (P) fraction were analyzed by SDS-PAGE and a subsequent immunoblotting using anti-MBP antibody.

6.2.2 Does the membrane environment influence the binding of misfolded proteins to Ire1?

6.2.2.1 Establishing an *in vitro* binding assay

The yeast protein carboxypeptidase Y (CPY) was chosen as a model protein. While CPY is a folded protein, its G255R variant (referred to as CPY*) does not fold properly thereby making it to a well-studied substrate of the ERAD pathway (Finger et al., 1993; Stein et al., 2014). Notably, CPY* was already used to characterize the mechanism of Ire1 activation by misfolded proteins (Gardner and Walter, 2011). A direct binding of the core ER-luminal domain of Ire1 to mutant CPY* was demonstrated using co-immunoprecipitation analysis and *in vitro* binding assays (Gardner and Walter, 2011). Both, CPY and CPY*, can be purified from *S. cerevisiae* using a recently published protocol (Stein et al., 2014) (Figure S 2).

Membrane-reconstituted $^{MBP}Ire1_{cLD\text{-}AH\text{-}TMH}$ was mixed with either CPY or CPY* and incubated for 15 min at RT to allow for binding (Figure 31A). The core ER-luminal domain of Ire1 can distinguish between folded and misfolded proteins (Gardner and Walter, 2011; Promlek et al., 2011). Therefore, the misfolded variant CPY* should bind to $^{MBP}Ire1_{cLD\text{-}AH\text{-}TMH}$ while the folded CPY should remained unbound. To separate all unbound proteins from the proteoliposomes containing $^{MBP}Ire1_{cLD\text{-}AH\text{-}TMH,}$ a sucrose density gradient was used. The $^{MBP}Ire1_{cLD\text{-}AH\text{-}TMH}$ containing proteoliposomes and all stably bound protein should float to the top of the gradient upon centrifugation, while unbound proteins should remain at the bottom fraction (Figure 31A).

For pilot experiments, a densely packed membrane environment containing *E. coli* polar lipids (EPL) supplemented with 30% DPPC was used. This lipid composition should mimic a tightly packing membrane environment. Expectedly, $^{MBP}Ire1_{cLD\text{-}AH\text{-}TMH}$ was found in the top fraction of the gradient after sucrose density gradient centrifugation (Figure 31B). CPY* co-migrated with reconstituted Ire1 and was also found in the top fraction of the gradient indicating that the misfolded variant was bound to Ire1. In contrast, CPY remained at the bottom of the gradient. Notably, the poorly folded CPY* did not interact unspecifically with the surface of the proteoliposomes. When CPY or CPY* were mixed with empty, protein-free liposomes of the same composition, they remained in the bottom fractions indicating that the interaction of CPY* to the Ire1-containing liposomes was specific. With this experimental procedure, it is possible to study the influence of the membrane environment on the binding of misfolded proteins to Ire1.

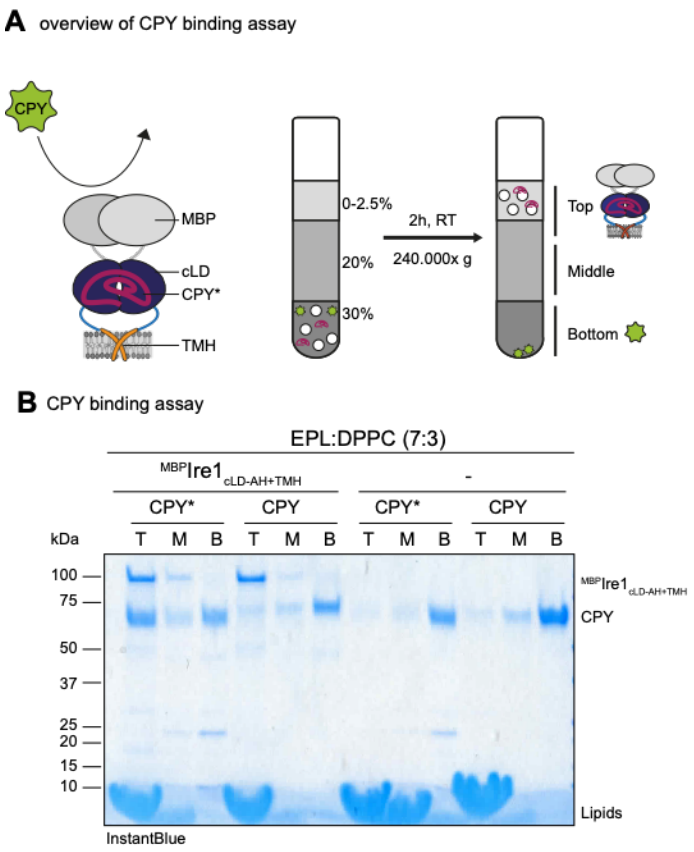

Figure 31: Reconstituted $^{MBP}Ire1_{cLD\text{-}AH\text{-}TMH}$ distinguishes between a correctly folded and unfolded protein.

(A) Overview of the CPY binding assay. Reconstituted $^{MBP}Ire1_{cLD\text{-}AH\text{-}TMH}$ were either mixed with CPY, the folded variant, or CPY*, the misfolded mutant. After a 15 min incubation at RT, the sample was mixed with sucrose to a final sucrose concentration of 30% and overlaid with 25% and 0-2.5% sucrose buffer. The sample was centrifuged (2 h, 240.000x g, 22°C) and fractionated in top, middle and bottom fractions. Samples of top, middle and bottom fractions were analyzed by SDS-PAGE and a subsequent InstantBlue staining. (B) CPY binding assay. $^{MBP}Ire1_{cLD\text{-}AH\text{-}TMH}$ was reconstituted in EPL:DPPC (7:3) and incubated with CPY or CPY* in a mass ratio of 1:1. Empty liposomes served as a control. This CPY binding assay performed by Susanne Wolf was performed without the addition of maltotriose. Illustration adapted from a supervised bachelor thesis (Wolf, 2016).

6.2.2.2 Influence of the membrane environment on binding of misfolded proteins

What is the impact of lipid saturation and the PC-to-PE ratio in the membrane on the binding of misfolded proteins to $^{MBP}Ire1_{cLD\text{-}AH\text{-}TMH}$? To address these questions, we used two series of lipid compositions and generated based on these formulations $^{MBP}Ire1_{cLD\text{-}AH\text{-}TMH}$-containing proteoliposomes (Figure 32).

The first set of lipid compositions exhibited a different degree of lipid saturation and was based mostly on PC lipids (Figure 32A). By changing the degree of lipid saturation, the lipid packing in the resulting liposomes was modulated as validated by C-laurdan spectroscopy (Figure 32B). GP values calculated from the fluorescence spectra increased with the proportion of saturated lipid acyl chains as expected. To further increase the lipid packing in this series of lipid mixtures, cholesterol was used as additional component (Figure 32C).

The second set of liposomes (Figure 32D) was used to study the impact of the PC-to-PE ratio on the binding of misfolded proteins to $^{MBP}Ire1_{cLD\text{-}AH\text{-}TMH}$. To this end, liposomes featuring

different PC-to-PE ratios were generated and used to prepare proteoliposomes. Notably, the acyl chain composition was kept constant for these formulations. There is *in vivo* evidence that both an increased and decreased PE-to-PC ratio can induce lipid bilayer stress to activate the UPR (Fu et al., 2011; Thibault et al., 2012). Expectedly, the PE-to-PC ratio has also a major impact on the molecular packing of lipids as studied by C-laurdan spectroscopy (Figure 32F). This is because the headgroup of PE is smaller than the one of PC thereby allowing for tighter lipid packing (Holthuis and Menon, 2014; Klose et al., 2013; Radanović et al., 2018). The more complex composition (referred to as 'composition 9') combined several features characteristic for different forms of lipid bilayer stress, which are all related to increased lipid packing: a high content of saturated lipids, cholesterol, a relatively high PE-to-PC ratio and a relatively low PI content. Consistently, these liposomes featured the highest degree of lipid packing as evidenced by the highest GP values (Figure 32F).

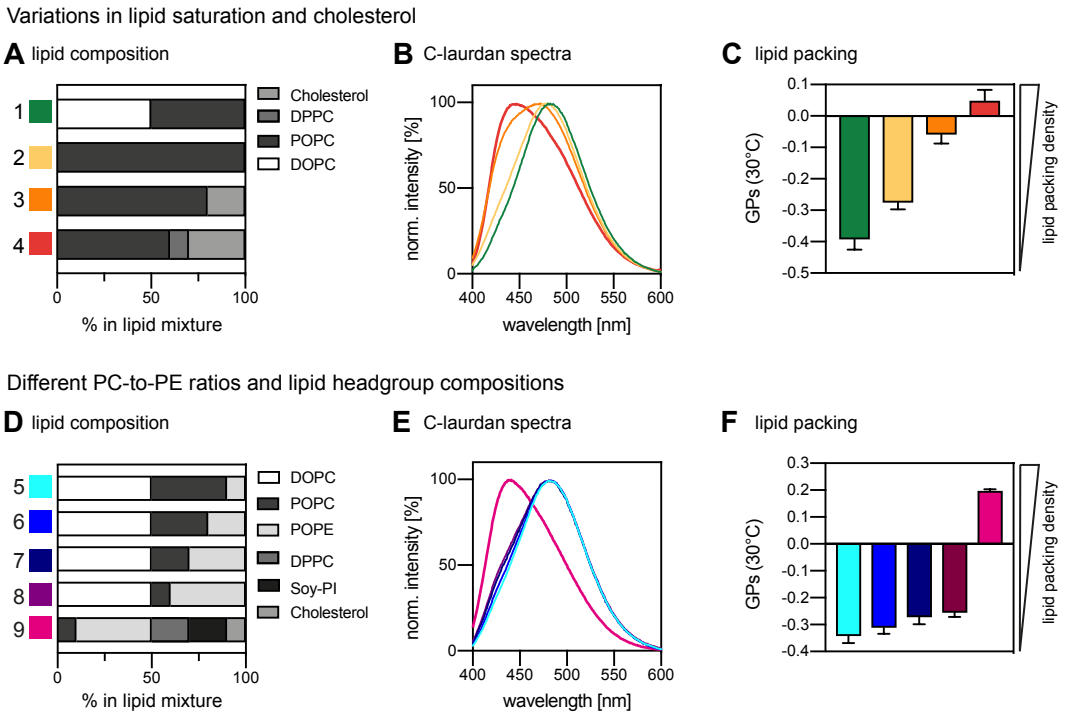

Figure 32: Determination of lipid packing of liposomes by C-laurdan measurements.

(A) Liposomes with defined lipid saturation: 1) 50% DOPC, 50% POPC, 2) 100% POPC, 3) 80% POPC, 20% Cholesterol, 4) 60% POPC, 10% DPPC, 30% Cholesterol. The color code for the liposome compositions is maintained in (B) and (C). (B) C-laurdan fluorescence spectroscopy of the indicated liposome compositions. The measurements were performed at 30°C. (Ex. 375 nm, Em. 400 – 600 nm). (C) The order parameter GP was determined form the spectra in (B). The mean ± SEM of four independent measurements is shown. (D) Liposomes with defined lipid head groups: 5) 50% DOPC, 40% POPC, 10% POPE, 6) 50% DOPC, 30% POPC, 20% POPE, 7) 50% DOPC, 20% POPC, 30% POPE , 8) 50% DOPC, 10% POPC, 40% POPE, 9) 10% POPC, 40% POPE, 20% DPPC, 20% Soy-PI, 10% Cholesterol. The color code for the liposome compositions us maintained in (E) and (F). (E) C-laurdan fluorescence spectroscopy of the indicated liposome compositions. The measurements were performed at 30°C. (Ex. 375 nm, Em. 400 – 600 nm). (F) The order parameter GP was determined form the spectra in (B). The mean ± SEM of four independent measurements is shown.

With this set of lipid compositions, the effect of both increased lipid saturation and increased PE-to-PC ratios on the binding of misfolded proteins to $^{MBP}Ire1_{cLD\text{-}AH\text{-}TMH}$ was characterized (Figure 33). When $^{MBP}Ire1_{cLD\text{-}AH\text{-}TMH}$ was reconstituted in membrane environments with

increased fractions of saturated lipid acyl chains (compositions 1 - 4), increased quantities of CPY* were found associated with Ire1-containing proteoliposomes in the top fractions of the gradient (Figure 33A). While the effect of lipid saturation was rather mild, a significant increase of CPY* binding was observed with increasing PE-to-PC ratios (liposome composition 5 – 8) (Figure 33B). Consistent with the hypothesis that increased lipid packing increases binding, most CPY* binding to $^{MBP}Ire1_{cLD\text{-}AH\text{-}TMH}$ was observed when Ire1 was reconstituted in liposomes with the lipid composition 9 (Figure 35). With these experiments, it could be directly shown that the membrane composition has a substantial impact on the binding of a misfolded model protein to the Ire1-based sensor $^{MBP}Ire1_{cLD\text{-}AH\text{-}TMH}$. The modulatory potential of the lipid headgroup composition was particularly striking. This thesis therefore provides a first, direct evidence that the ER-stress caused by misfolded proteins may modulated by conditions of lipid bilayer stress. It reveals remarkable potential of collective lipid bilayer properties in regulating receptor-ligand interactions.

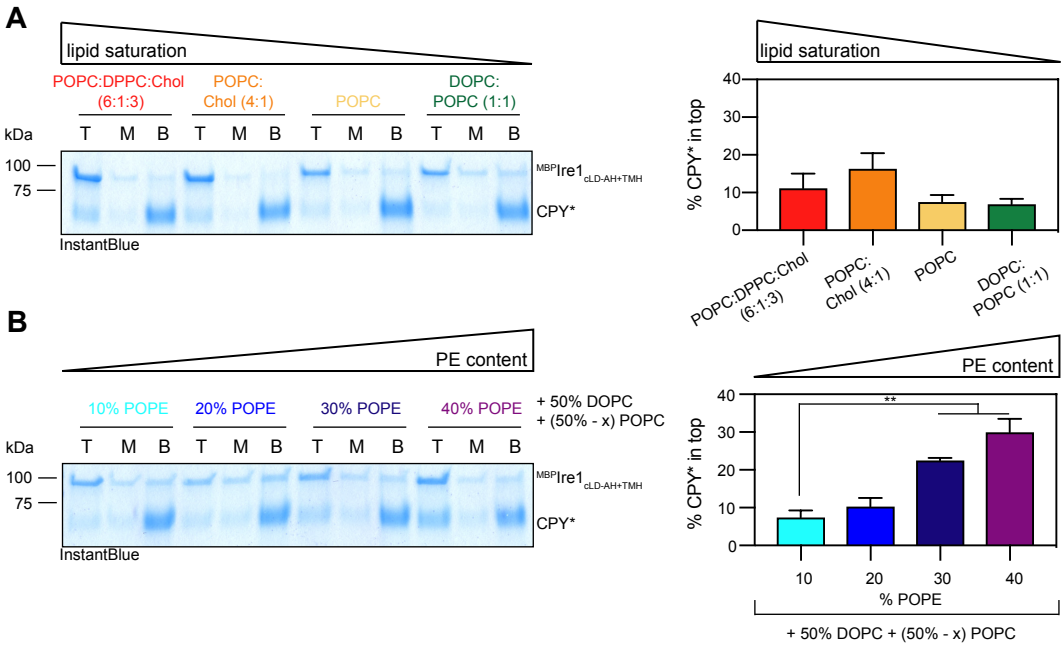

Figure 33: The binding of CPY* to reconstituted $^{MBP}Ire1_{cLD\text{-}AH\text{-}TMH}$ is modulated by the membrane environment.

(A) Effect of increased lipid saturation on the binding of CPY* to $^{MBP}Ire1_{cLD\text{-}AH\text{-}TMH}$. $^{MBP}Ire1_{cLD\text{-}AH\text{-}TMH}$ reconstituted in liposome compositions 1) 50% DOPC, 50% POPC, 2) 100% POPC, 3) 80% POPC, 20% Cholesterol and 4) 60% POPC, 10% DPPC, 30% Cholesterol was first incubated with 15 mM maltotriose for 10 min at RT. CPY* was added and the mix was again incubated for 15 min at RT. After incubation, the sample was mixed with sucrose to a final sucrose concentration of 30% containing 1 mM maltotriose and overlaid with 25% and 2.5% sucrose buffer containing 1 mM maltotriose. The samples were centrifuged (2 h, 240.000x g, 22°C) and fractionated in top, middle and bottom fractions. Samples of top, middle and bottom fractions were analyzed by SDS-PAGE and a subsequent InstantBlue staining. (B) Effect of PE increase on the binding of CPY* to reconstituted $^{MBP}Ire1_{cLD\text{-}AH\text{-}TMH}$. $^{MBP}Ire1_{cLD\text{-}AH\text{-}TMH}$ was reconstituted in liposome compositions 5) 50% DOPC, 40% POPC, 10% POPE, 6) 50% DOPC, 30% POPC, 20% POPE, 7) 50% DOPC, 20% POPC, 30% POPE and 8) 50% DOPC, 10% POPC, 40% POPE.The samples were treated as described in (A). The error bars represent the mean ± SEM of three independent experiments. Significance was tested by an unpaired, two-tailed Student's t-test. **p<0.01.

In order to verify that the core ER-luminal domain of Ire1 specifically binds CPY*, control experiments with $^{MBP}Ire1_{AH\text{-}TMH}$ were performed (Figure 34). The binding pocket of MBP for

maltose is structurally very distinct to the binding groove for misfolded proteins described for the core ER-luminal domain of Ire1. However, they share some common features. The binding groove of the core ER-luminal domain of Ire1 is rather hydrophilic with aromatic residues and is thought to bind the peptide backbone via hydrogen bonds. Furthermore, it contains hydrophobic pockets at both ends for non-polar residues (Credle et al., 2005; Korennykh and Walter, 2012). The binding pocket of MBP is decorated with aromatic and hydrophilic residues able to form hydrogen bonds with the polar groups of a bound sugar molecule (Quiocho et al., 1997). Additionally, the MBP binding pocket has the ability to bind and stabilize hydrophobic TMHs (Kapust and Waugh, 1999). This is the reason why MBP is often used as a purification tag for single-spanning transmembrane proteins (Contreras et al., 2012; Covino et al., 2016; Halbleib et al., 2017) . Due to these similarities of the binding regions of MBP and Ire1, it was not entirely surprising that some interactions between CPY* to MBP could be observed. CPY* is a misfolded protein that probably exposes hydrophobic portions on its surface, which might interact with the somewhat sticky surface of MBP in its binding pocket. Notably, the binding to MBP was lower compared to the binding of CPY* to $^{MBP}Ire1_{cLD\text{-}AH\text{-}TMH}$ (Figure 34 and Figure 35). Nevertheless, the binding of CPY* to MBP was also modulated by the membrane environment, as an increase of binding was observed with an increase in PE content of the membrane environment (Figure 34). Interestingly, by the addition of maltotriose (a ligand of MBP), reduced the binding of CPY* to MBP by roughly 50% in the lipid composition 9 (data not shown), This is likely because maltotriose binds to MBP and ‘closes’ the binding pocket of this substrate binding domain thereby lowering the surface accessible for an interaction with other binding partners such as the sticky, misfolded model protein CPY*. This observation indicates that the binding pocket of MBP is responsible for the background binding of CPY*.

These data indicate that MBP can contribute to the binding of CPY* to $^{MBP}Ire1_{cLD\text{-}AH\text{-}TMH}$. However, most strikingly is the observation that the membrane environment has a significant influence on the binding of CPY* to both $^{MBP}Ire1_{cLD\text{-}AH\text{-}TMH}$ and $^{MBP}Ire1_{AH\text{-}TMH}$. Consistent, with previous findings (Halbleib et al., 2017), it seems that the unusual TMH region of Ire1, which is equipped with an AH, renders these proteins sensitive to the lipid bilayer. Given that CPY* exhibits some binding to MBP alone, it would be ideal to study the interaction of CPY* with Ire1 in the absence of a fused MBP. However, in the course of this thesis, it was not possible to remove the purification tag without causing aggregation of the remaining protein (data not shown). More work using new sets of Ire1-based constructs will be required to fully understand and reconstitute the crosstalk of lipid bilayer stress *in vitro.*

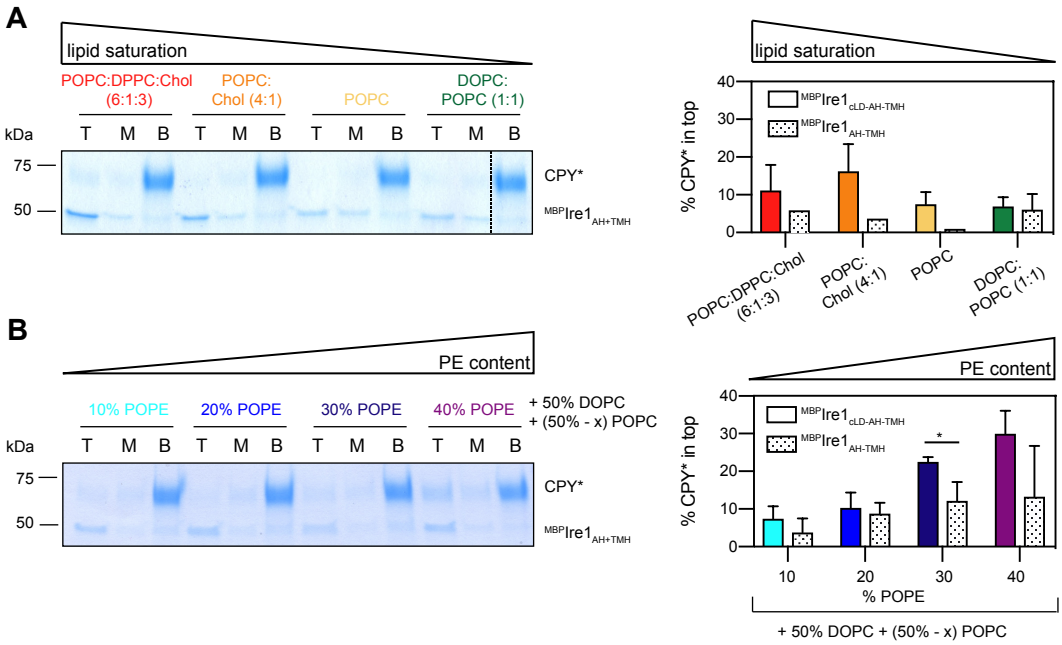

Figure 34: The binding of CPY* to reconstituted $^{MBP}Ire1_{AH-TMH}$ is modulated by the membrane environment.

(A) Effect of increased lipid saturation on the binding of CPY* to reconstituted $^{MBP}Ire1_{AH-TMH}$. $^{MBP}Ire1_{AH-TMH}$ reconstituted in liposome composition 1) 50% DOPC, 50% POPC, 2) 100% POPC, 3) 80% POPC, 20% Cholesterol and 4) 60% POPC, 10% DPPC, 30% was first incubated with 15 mM maltotriose for 10 min at RT. CPY* was added and the mix was again incubated for 15 min at RT. After incubation, the sample was mixed with sucrose to a final sucrose concentration of 30% containing 1 mM maltotriose and overlaid with 25% and 2.5% sucrose buffer containing 1 mM maltotriose. The samples were centrifuged (2 h, 240.000x g, 22°C) and fractionated in top, middle and bottom fractions. Samples of top, middle and bottom fractions were analyzed by SDS-PAGE and a subsequent InstantBlue staining. (B) Effect of PE increase on the binding of CPY* to reconstituted $^{MBP}Ire1_{AH-TMH}$. $^{MBP}Ire1_{AH-TMH}$ was reconstituted in liposome compositions 5) 50% DOPC, 40% POPC, 10% POPE, 6) 50% DOPC, 30% POPC, 20% POPE, 7) 50% DOPC, 20% POPC, 30% POPE and 8) 50% DOPC, 10% POPC, 40% POPE. The samples were treated as described in (A). The error bars of $^{MBP}Ire1_{cLD-AH-TMH}$ data represent the mean ± SEM of three independent experiments. The error bars of $^{MBP}Ire1_{AH-TMH}$ data in lipid composition 1, 5 – 8 represent the mean ± SEM of two independent experiments. Significance was tested by an unpaired, two-tailed Student's t-test. *p<0.05.

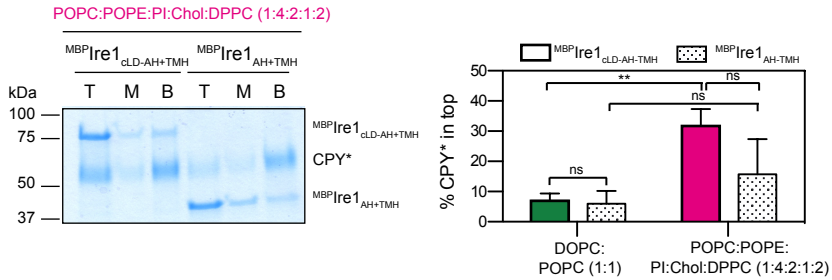

Figure 35: The binding of CPY* to $^{MBP}Ire1_{cLD-AH-TMH}$ and $^{MBP}Ire1_{AH-TMH}$ in densely packed liposomes.

$^{MBP}Ire1_{AH-TMH}$ and $^{MBP}Ire1_{cLD-AH-TMH}$ reconstituted in liposome composition 9 (10% POPC, 40% POPE, 20% DPPC, 20% Soy-PI, 10% Cholesterol) were first incubated with 15 mM maltotriose for 10 min at RT. CPY* was added and the mix was again incubated for 15 min at RT. After incubation, the sample was mixed with sucrose to a final sucrose concentration of 30% containing 1 mM maltotriose and overlaid with 25% and 2.5% sucrose buffer containing 1 mM maltotriose. The samples were centrifuged (2 h, 240.000x g, 22°C) and fractionated in top, middle and bottom fractions. Samples of top, middle and bottom fractions were analyzed by SDS-PAGE and a subsequent InstantBlue staining. Significance was tested by an unpaired, two-tailed Student's t-test. **p<0.01.

6.2.3 The impact of PE on the oligomerization of ^{MBP}Ire1$_{AH-TMH}$

In order to test the role of PE on the oligomerization of Ire1, I used cwEPR experiments with a spin-labeled variant of ^{MBP}Ire1$_{AH-TMH}$ that was reconstituted in different PE-containing lipid environments. The MTS-spin label was installed during isolation of ^{MBP}Ire1$_{AH-TMH}$ at the native C552 in the TMH of Ire1. The isolated, spin-labeled minimal sensor construct ^{MBP}Ire1$_{AH-TMH}$ was then reconstituted at a protein:lipid molar ratio of 1:400 in liposomes with defined lipid compositions. The impact of the lipid environment on the oligomeric state of ^{MBP}Ire1$_{AH-TMH}$ was studied using cwEPR spectroscopy with spectra recorded at -115°C. Here, spectral broadening indicates inter-spin distances between 1 – 2 nm which occur more when the TMH of ^{MBP}Ire1$_{AH-TMH}$ forms dimers or higher oligomers. Other spectra recorded at 30°C provide information on the mobility of the spin-label (Bordignon and Steinhoff, 2007; Covino et al., 2016; Halbleib et al., 2017) (For more information see 5.5.2).

The impact of the PE-to-PC ratio in the oligomerization of Ire1 was studied with ^{MBP}Ire1$_{AH-TMH}$ reconstituted in liposomes containing different molar fraction of PE (0%, 10%, 20% und 40%) (Figure 36).

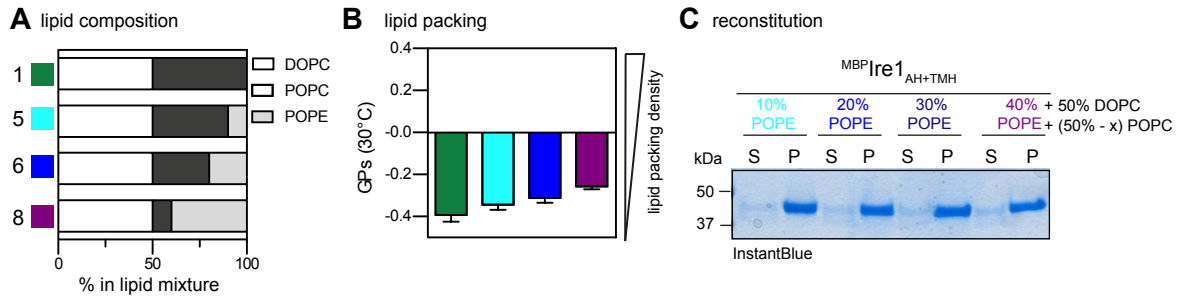

Figure 36: Reconstitution of spin-labeled ^{MBP}Ire1$_{AH-TMH}$ in different lipid environments.

(A) Lipid composition used for EPR studies with ^{MBP}Ire1$_{AH-TMH}$. The indicated lipid compositions were used for studying the membrane-dependent dimerization of the minimal sensor construct ^{MBP}Ire1$_{AH-TMH}$. (B) Lipid packing of the indicated lipid compositions. The lipid packing of the liposomes with the indicated lipid compositions were determined by fluorescence spectroscopy using C-laurdan. The degree of lipid packing is represented as the generalized polarization (GP) value at 30°C. (C) Reconstitution of the spin-labeled ^{MBP}Ire1$_{AH-TMH}$. The minimal sensor construct was reconstituted in a lipid:protein molar ratio of 400:1 in the indicated lipid compositions. After reconstitution using BioBeads, the proteoliposomes were harvested by centrifugation (400.000x g, 90 min, 4°C) and resuspended in reconstitution buffer with glycerol. Samples of supernatant and pellet were subjected to SDS-PAGE and a subsequent InstantBlue staining.

The spectra recorded at -115°C revealed an increased spectral broadening with an increasing PE-to-PC ratio in the proteoliposomes (Figure 37A). Consistently, the semi-quantitative proximity index Lf/Mf, calculated from the low temperature spectra, increases with higher PE levels (Figure 37C). This indicates a higher degree of dimerization of the minimal sensor construct ^{MBP}Ire1$_{AH-TMH}$ in PE-containing liposomes. Such an oligomerization of Ire1 might explain the increased binding of CPY* to ^{MBP}Ire1$_{AH-TMH}$ as well as to ^{MBP}Ire1$_{cLD-AH-TMH}$ in membrane environments with increased PE-to-PC ratios via avidity effects. The cwEPR spectra recorded at -115°C provided also information about the environment of the spin-label.

The semi-quantitative index 2Azz is a measure for the polarity in the nano-environment of the spin-probe. At increased PE-to-PC ratios, an increased polarity in the environment of the spin-probe installed on $^{MBP}Ire1_{AH\text{-}TMH}$ was observed (Figure 37D). CwEPR spectra recorded at 30°C showed the existence of an immobile phase indicating a decreased mobility of the spin-probe at increased PE-to-PC ratios (Figure 37B,E). It is tempting to speculate that the increase in polarity and decrease in mobility is due to the dimerization of the TMHs, which would also involve the establishment of a new dimerization interface (Bordignon and Steinhoff, 2007). If the spin-label faces the dimerization interface, the mobility should be reduced and the polarity would change from a non-polar, lipidic environment to a more polar proteinaceous environment. The crosslinking data provided in a previous chapter of this thesis performed with full-length Ire1 (6.1.3.2) significantly support this possibility: the native C552 residues formed covalent crosslinks in signaling-active clusters of Ire1, thereby demonstrating a suitable distance and appropriate orientation of the cysteine side chain relative to the dimerization interface.

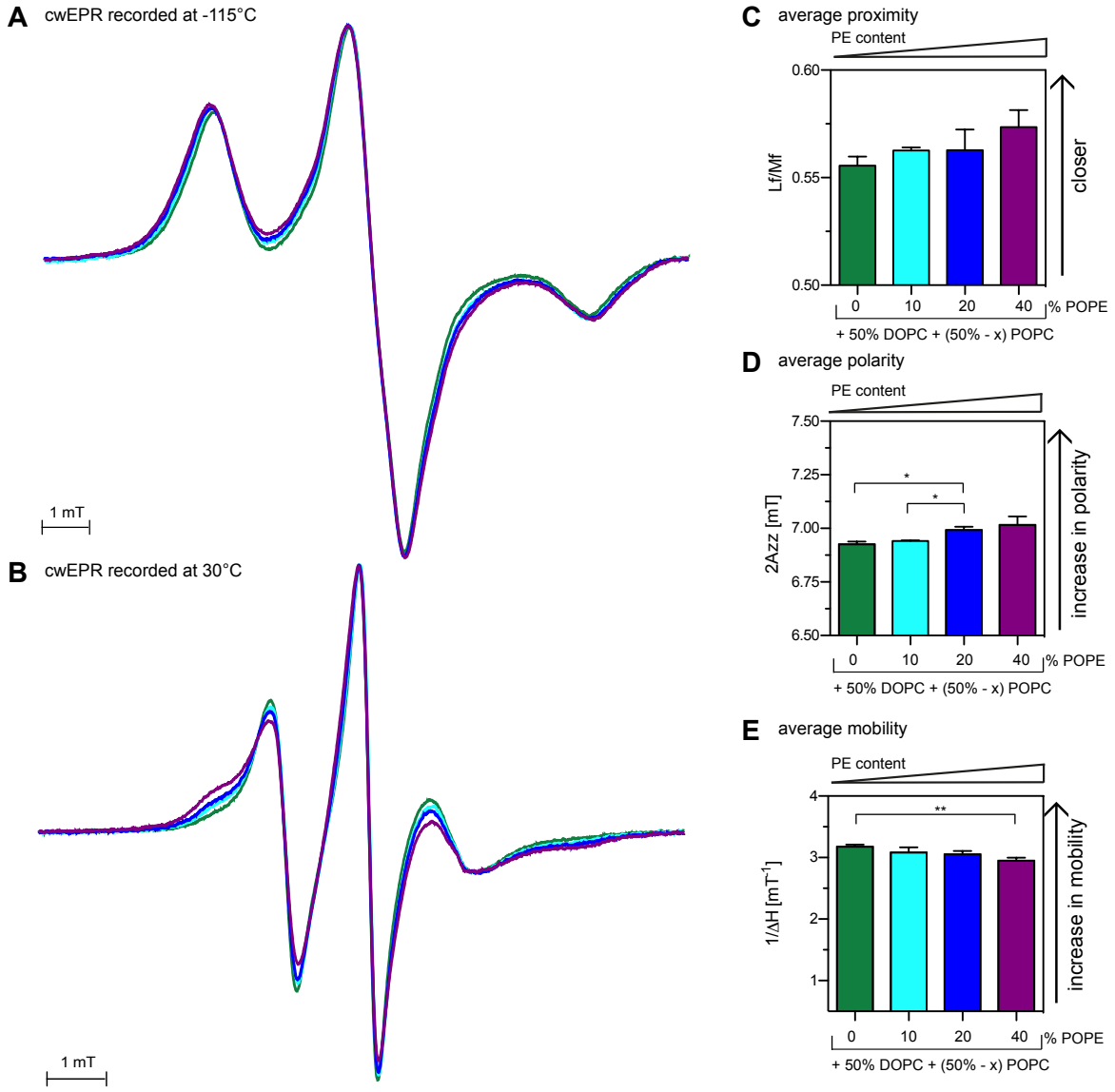

Figure 37: The impact of PE on the oligomerization of ^{MBP}Ire1$_{AH-TMH}$.

(A) Intensity-normalized cwEPR spectra of spin-labeled ^{MBP}Ire1$_{AH-TMH}$ recorded at -115°C. Spin-labeled ^{MBP}Ire1$_{AH-TMH}$ reconstituted in 1) 50% DOPC, 50% POPC, 5) 50% DOPC, 40% POPC, 10% POPE, 6) 50% DOPC, 30% POPC, 20% POPE , 8) 50% DOPC, 10% POPC, 40% POPE show spectral broadening when reconstituted in liposomes with increased POPE content. The intensities of the middle ($2IM_F$) and the low field peak (I_{LF}) are derived from these spectra and used for the calculation of the proximity index LF/Mf. (B) Intensity-normalized cwEPR spectra of spin-labeled ^{MBP}Ire1$_{AH-TMH}$ recorded at 30°C. The line width of the middle field peak (ΔH_0) is extracted from 30°C cwEPR spectra and used as a reporter for the mobility of the spin-probe. (C) Semi-quantitative analysis of the inter-spin distances. The proximity index Lf/Mf was extracted from spectra recorded at -115°C and plotted against the used lipid compositions. Higher values indicate lower average distances. (D) Semi-quantitative analysis of the average polarity of the nano-environment of the spin-label. The 2Azz value is derived from the spectra recorded at -115°C and plotted against the lipid composition. (E) Semi-quantitative analysis of the average mobility of the spin-label. The line width of the middle field peak (ΔH_0) was extracted from spectra recorded at 30°C and plotted against the lipid composition. (C), (D), and (E) The error bars represent the mean ± SEM of three independent experiments. Significance was tested by an unpaired, two-tailed Student's t-test. *p<0.05. **p<0.01

By recording cwEPR spectra with spin-diluted controls samples (Figure 38), it was tested if the spectral changes in membranes with high PE-to-PC ratios were indeed due to spin-spin interactions. The spin-labeled minimal sensor construct ^{MBP}Ire1$_{AH-TMH}$ was mixed with unlabeled ^{MBP}Ire1$_{AH-TMH}$ at a 5-fold excess and then reconstituted in liposomes. For these spin-diluted samples, no spectral broadening was observed in liposomes containing as much as

40% POPE (Figure 38A). Based on these data, it can be concluded that the spectral broadening observed at high PE-to-PC ratios is indeed due to an increased dimerization of $^{MBP}Ire1_{AH\text{-}TMH}$ and an increased spin-spin interactions (Figure 38A). Notably, the spin-diluted control also indicated an increase in polarity and a decrease in mobility (Figure 38D,E). These changes may be caused by the dimerization of two TMHs if the spin-labeled is located in the dimerization interface. However, a direct influence of the lipid environment on polarity and mobility of the spin-probe cannot be excluded with these experiments. This would be possible, by repeating these experiments with a dimerization-defective variant of Ire1. We can conclude that increased PE-to-PC ratios affect the oligomeric state of $^{MBP}Ire1_{AH\text{-}TMH}$ thereby providing a means to understand how conditions of lipid bilayer stress can affect the oligomeric state of Ire1 and consequently affect the sensitivity of Ire1 for unfolded proteins via avidity effects.

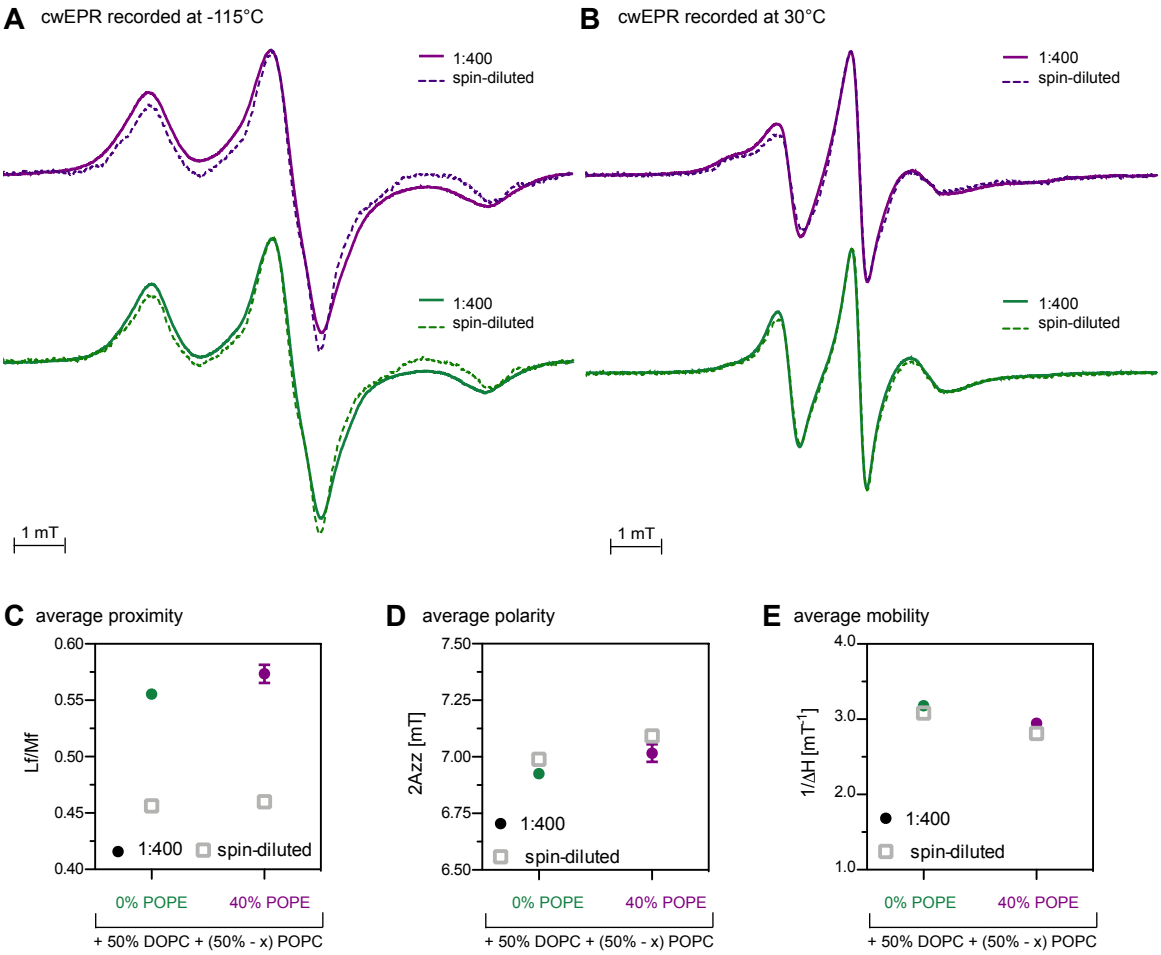

Figure 38: cwEPR spectra of $^{MBP}Ire1_{AH\text{-}TMH}$ in proteoliposomes including spin-diluted controls.

(A) Intensity-normalized cwEPR spectra recorded at -115 of $^{MBP}Ire1_{AH\text{-}TMH}$ reconstituted in lipid compositions 1) 50% DOPC, 50% POPC, 8) 50%DOPC, 10% POPC, 40% POPE. Spectra of spin-diluted samples, containing a 5-fold excess of unlabeled $^{MBP}Ire1_{AH\text{-}TMH}$ were recorded as a control. (B) Intensity-normalized cwEPR spectra recorded at 30°C of $^{MBP}Ire1_{AH\text{-}TMH}$ reconstituted in the indicated lipid compositions. (C) The semi-quantitative index Lf/Mf derived from spectra shown in (A) represents the average proximity of the spin-labels in the different lipid compositions. (D) The index 2 Azz derived from spectra shown in (A) represents the average polarity of the spin-labels in the different lipid compositions. (E) The line width of the middle field peak (ΔH_0) was extracted from spectra recorded at 30°C and represents the average mobility of the spin-labels in the different lipid compositions. (C), (D) and (E) The error bars represent the mean ± SEM of at least two independent experiments.

6.3 Do human transducers of the UPR use the same activation strategy for lipid bilayer stress as the yeast sensor Ire1?

The activation of the yeast Ire1 by lipid bilayer stress is based on an AH that is located N-terminally to the TMH and overlapping with the TMH (Figure 18) (2.3.2) (Covino et al., 2018; Halbleib et al., 2017). Recent evidence suggests that also the mammalian UPR sensors IRE1α and PERK can react to aberrant lipid environments (Cho et al., 2019; Volmer et al., 2013). The question arises whether human UPR sensors use the same strategy to sense for lipid bilayer stress as Ire1 from *S. cerevisiae*.

6.3.1 Bioinformatic analysis of the TMH region of PERK from humans

We performed a bioinformatical analysis of PERK to identify the TMH region and to identify a putative juxta-membrane AH adjacent to the TMH (Figure 39A). Heliquest analysis (Gautier et al., 2008) of the TMH region of PERK (aa 521 - 542) revealed a putative, juxta-membrane AH directly N-terminally of the TMH (Figure 39B). This putative AH has a predicted hydrophobic moment <μH> of 0.460 and a hydrophobicity <H> of 0.709. The predicted hydrophobicity <H> of the adjacent TMH region is 1.084. Interestingly, the predicted TMH region of PERK is relatively short and comprises only 11 amino acids (not counting all residues contributing to the predicted AH). This is similar to the TMH region of Ire1 from baker's yeast. There, the TMH is comprised of only 12 amino acids (not counting the residues contributing to the AH) (Figure 18) (Halbleib et al., 2017).

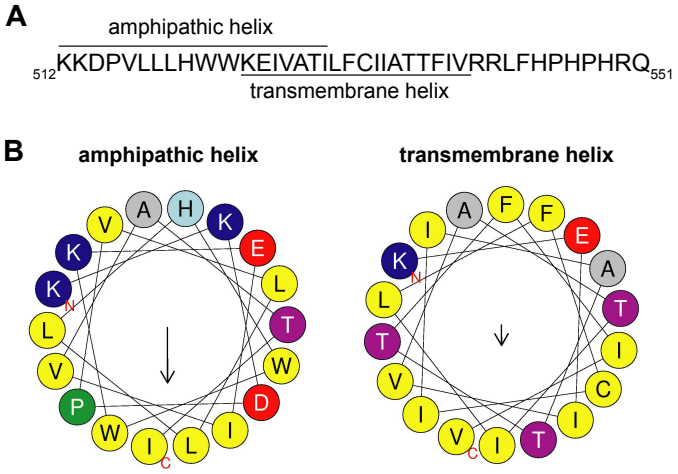

Figure 39: Bioinformatic analysis of the TMH region of human PERK.

(A) Primary sequence of the predicted AH and TMH region of the human UPR sensor PERK. (B) Heliquest analysis of the predicted AH and TMH of PERK (Gautier et al., 2008).

6.3.2 Establishing an $^{MBP}PERK_{AH\text{-}TMH}$ construct for *in vitro* studies

We constructed a minimal sensor construct based only on the TMH region of PERK to study its membrane-sensitivity. This minimal sensor was constructed in collaboration with Julian Bruckert during my supervision of his bachelor thesis (Bruckert, 2016). The sequence encoding for the AH and TMH of PERK (512 - 551) was cloned into a pMAL-C2x TEV *E. coli* expression vector. The resulting construct $^{MBP}PERK_{AH\text{-}TMH}$ encoded for a fusion protein composed of an N-terminal MBP tag for purification and solubilization, a polyN-linker, a TEV cleavage site and the TMH region of PERK encompassing the predicted AH and TMH of PERK (Figure 40A). The fusion protein was purified according to an established protocol (Halbleib et al., 2017). $^{MBP}PERK_{AH\text{-}TMH}$ was produced in the cytosol of *E. coli* and purified in the presence of the detergent β-OG by amylose chromatography. The yield from 1 l of bacterial culture was roughly 4 mg (Figure 40B). The tendency for oligomerization of $^{MBP}PERK_{AH\text{-}TMH}$ in detergent solution was examined by size-exclusion chromatography (Figure 40C,D). Our data are consistent with $^{MBP}PERK_{AH\text{-}TMH}$ forming a concentration-dependent dynamic equilibrium of monomeric, dimeric and potentially higher oligomeric species (Figure 40C,D). A similar dynamic and concentration-dependent oligomerization was previously observed for the $^{MBP}Ire1_{cLD\text{-}AH\text{-}TMH}$ construct (Figure 29D). This indicates that the TMH region of PERK bears features and properties that render it similar to the TMH region of Ire1 from baker's yeast.

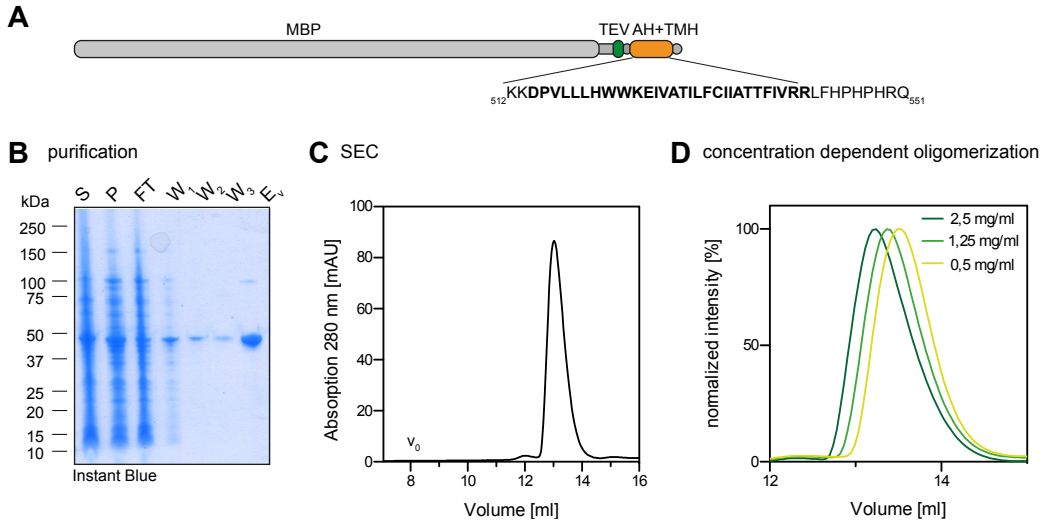

Figure 40: Purification of $^{MBP}PERK_{AH\text{-}TMH}$.

(A) Illustration of the minimal sensor construct of the human UPR sensor PERK. The construct contained N-terminally an MBP-tag, a linker, a TEV cleavage site and the AH and TMH of PERK. (B) Affinity purification of $^{MBP}PERK_{AH\text{-}TMH}$ from *E. coli.* The purification was monitored by subjecting 0.1 OD_{600} equivalents of supernatant (S), pellet (P), flow-through (FT), washing steps (W) and eluate (E) and 1 µg of SEC purified protein to SDS-PAGE and a subsequent InstantBlue™ staining. (C) SEC analysis of $^{MBP}PERK_{AH\text{-}TMH}$ using a Superdex 100/300 Column. (D) SEC of purified protein in detergent containing buffer analyzing the concentration dependent oligomerization of the construct. Purified protein was concentrated using an Amicon (cut off 50 kDa) and the protein concentration was adjusted to the indicated concentrations prior to loading 100 µl onto a Superdex 100/300 Column. Experiments illustrated in (C) and (D) were performed by Julian Bruckert during his bachelor thesis (Bruckert, 2016).

In order to study the membrane-based oligomerization of $^{MBP}PERK_{AH\text{-}TMH}$, we reconstituted spin-labeled $^{MBP}PERK_{AH\text{-}TMH}$ in liposomes. The native cysteine 532 in the TMH of PERK (C532) was used for labeling the protein. $^{MBP}PERK_{AH\text{-}TMH}$ was reconstituted at a protein:lipid molar ratio of 1:400 in liposomes with different lipid compositions (Figure 41). In order to study the impact of lipid packing on the oligomerization of the PERK TMH region, we used rather extreme lipid compositions, which differed in the degree of lipid saturation, the sterol content, and the lipid headgroup composition (Figure 41A). The success of the reconstitution procedure was validated together with Iryna Stasiuk during her master thesis (Stasiuk, 2017). Control experiments suggested that $^{MBP}PERK_{AH\text{-}TMH}$ was inserted properly into the lipid bilayer with only a minimal loss during the reconstitution from protein aggregation.

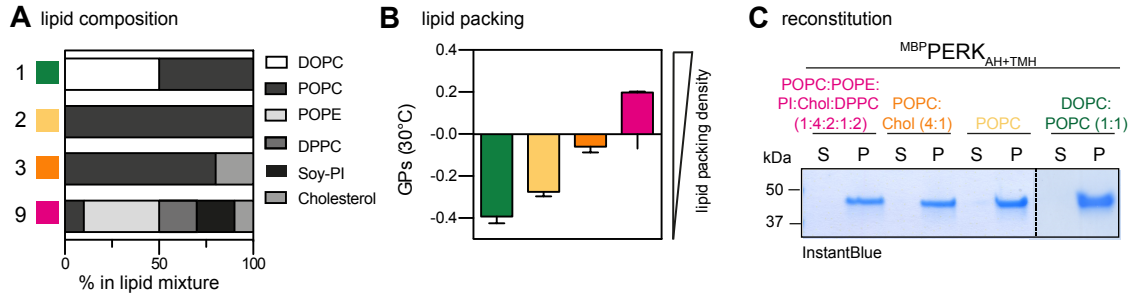

Figure 41: Reconstitution of spin-labeled $^{MBP}PERK_{AH\text{-}TMH}$ in different lipid environments.

(A) Lipid composition used for EPR studies with $^{MBP}PERK_{AH\text{-}TMH}$. The indicated lipid compositions were used for studying the membrane-dependent dimerization of the minimal sensor construct $^{MBP}PERK_{AH\text{-}TMH}$ (1) 50% DOPC, 50% POPC, 2) 100% POPC, 3) 80% POPC, 20% Cholesterol 9) 10% POPC, 40% POPE, 20% DPPC, 20% Soy-PI, 10% Cholesterol). (B) Lipid packing of the indicated lipid compositions. The lipid packing of the liposomes with the indicated lipid compositions were determined by fluorescence spectroscopy using C-laurdan. The degree of lipid packing is represented as the generalized polarization (GP) value at 30°C. (C) Reconstitution of the spin-labeled $^{MBP}PERK_{AH\text{-}TMH}$. The minimal sensor construct was reconstituted a lipid:protein molar ratio of 400:1 in the indicated lipid compositions. After reconstitution using BioBeads, the proteoliposomes were harvested by centrifugation (400.000x g, 90 min, 4°C) and resuspended in reconstitution buffer with glycerol. Samples of supernatant and pellet were subjected to SDS-PAGE and a subsequent InstantBlue staining.

6.3.3 A membrane-dependent oligomerization of $^{MBP}PERK_{AH\text{-}TMH}$

Spin-labeled $^{MBP}PERK_{AH\text{-}TMH}$ was reconstituted in liposomes with lipid compositions 1, 2, 3 and 9 (Figure 41) and cwEPR spectra were recorded at -115°C. The spectra were broadened, when $^{MBP}PERK_{AH\text{-}TMH}$ spin-labeled at C532 was reconstituted in a more tightly packed membrane environment and the degree of broadening correlated with the degree of lipid packing (Figure 41A and Figure 42A). This implies that $^{MBP}PERK_{AH\text{-}TMH}$, similar to $^{MBP}Ire1_{AH\text{-}TMH}$ (Figure 37A), dimerizes in tightly packed membrane environments. The semi-quantitative average proximity index Lf/Mf (Covino et al., 2016; Halbleib et al., 2017) of three independent experiments highlights that the changes of the inter-spin distances in different lipid compositions are indeed significant (Figure 42C). The average polarity in the nano-environment of the spin-probe was not dependent on the lipid composition (Figure 42D). Likewise, there was no significant impact of the membrane environment on the mobility of the

spin-probe, as suggested by cwEPR spectra recorded at 30°C (Figure 42B,E). These cwEPR experiments therefore suggest that $^{MBP}PERK_{AH-TMH}$ derived from the human UPR sensor PERK exhibits a similar membrane-dependent oligomerization as $^{MBP}Ire1_{AH-TMH}$ derived from baker's yeast (Halbleib et al., 2017). This suggests that the mechanism of the membrane-based oligomerization may be conserved from yeast to man.

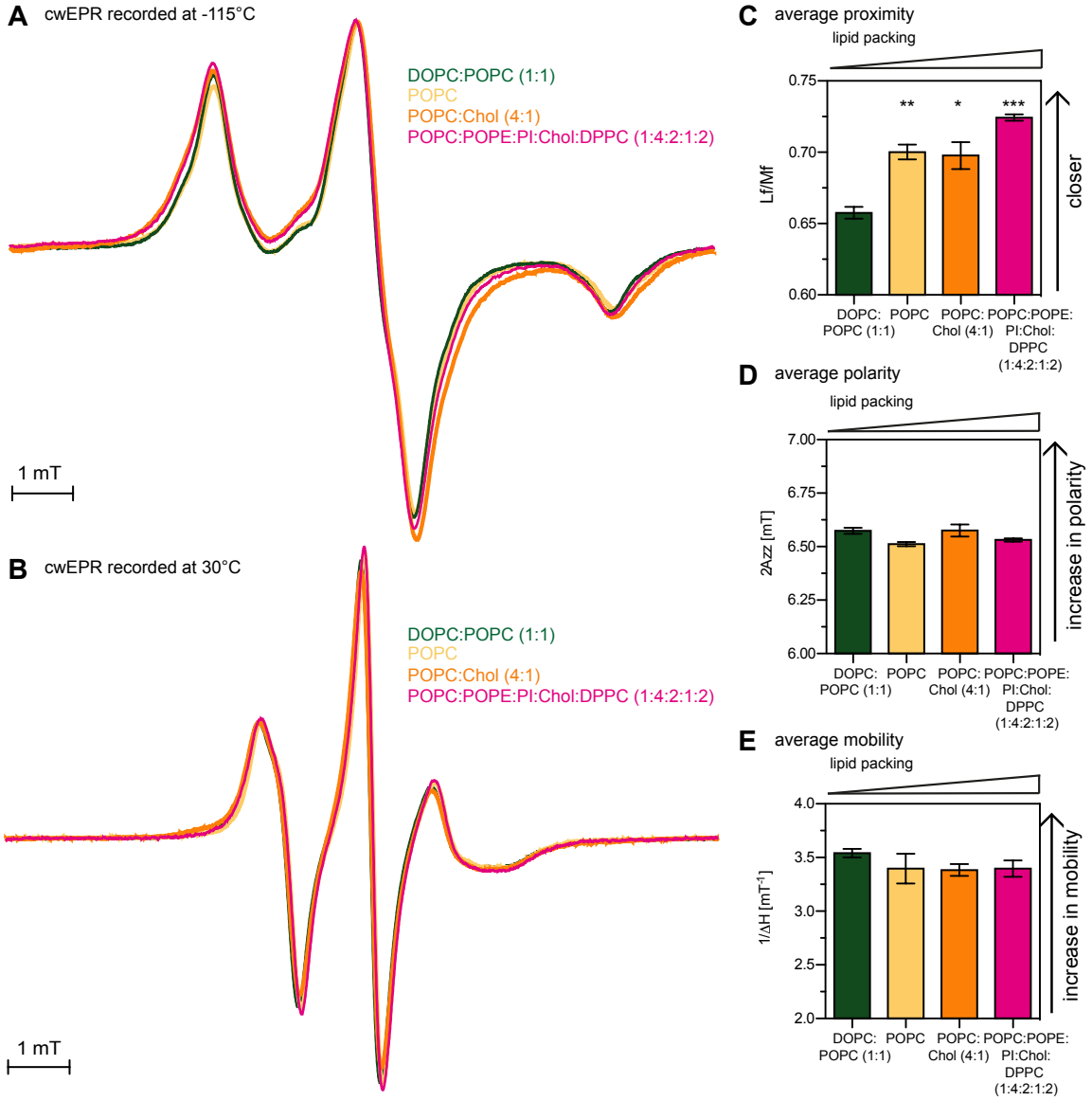

Figure 42: cwEPR spectroscopy of spin-labeled $^{MBP}PERK_{AH-TMH}$ in proteoliposomes indicates a membrane-dependent oligomerization.

(A) Intensity-normalized cwEPR spectra of spin-labeled $^{MBP}PERK_{AH-TMH}$ recorded at -115°C. Spin-labeled $^{MBP}PERK_{AH-TMH}$ reconstituted in 1) 50% DOPC, 50% POPC, 2) 100% POPC, 3) 80% POPC, 20% Cholesterol 9) 10% POPC, 40% POPE, 20% DPPC, 20% Soy-PI, 10% Cholesterol show spectral broadening when reconstituted in liposomes with increased lipid packing. The intensities of the middle ($2IM_F$) and the low field peak (I_{LF}) are derived from these spectra and used for the calculation of the proximity index LF/Mf. (B) Intensity-normalized cwEPR spectra of spin-labeled $^{MBP}PERK_{AH-TMH}$ recorded at 30°C. The line width of the middle field peak (ΔH_0) is extracted from 30°C cwEPR spectra and used as a reporter for the mobility of the spin-probe. (C) Semi-quantitative analysis of the inter-spin distances. The proximity index Lf/Mf was extracted from spectra recorded at -115°C and plotted against the used lipid compositions. Higher values indicate lower average distances. (D) Semi-quantitative analysis of the average polarity of the nano-environment of the spin-label. The 2Azz value is derived from the spectra recorded at -115°C and plotted against the lipid composition. (E) Semi-quantitative analysis of the average mobility of the spin-label. The line width of the middle field peak (ΔH_0) was extracted from spectra recorded at 30°C and plotted against the lipid composition. (C), (D), and (E) The error bars represent the mean ± SEM of three independent experiments. Experiments of replicates 2 and 3 were performed by Iryna Stasiuk during her master thesis (Stasiuk, 2017). Significance was tested by an unpaired students t-test. ***p<0.001, **p<0.01, *p<0.05.

Spin-diluted control spectra were recorded in order to exclude the possibility that the observed spectral broadening of the cwEPR spectra in tightly packed membranes were due to an unspecific interaction of the spin-probe with the lipid environment (Figure 43). To this end, spin-labeled $^{MBP}PERK_{AH\text{-}TMH}$ was mixed with a 5-fold molar excess of unlabeled $^{MBP}PERK_{AH\text{-}TMH}$ thereby minimizing inter-spin interactions. For these controls, no spectral broadening of the cwEPR spectra was observed in tightly packed membrane environments (Figure 43A, B, C, D). This validates the interpretation that $^{MBP}PERK_{AH\text{-}TMH}$ indeed undergoes a membrane-dependent oligomerization in tightly packed membrane environments.

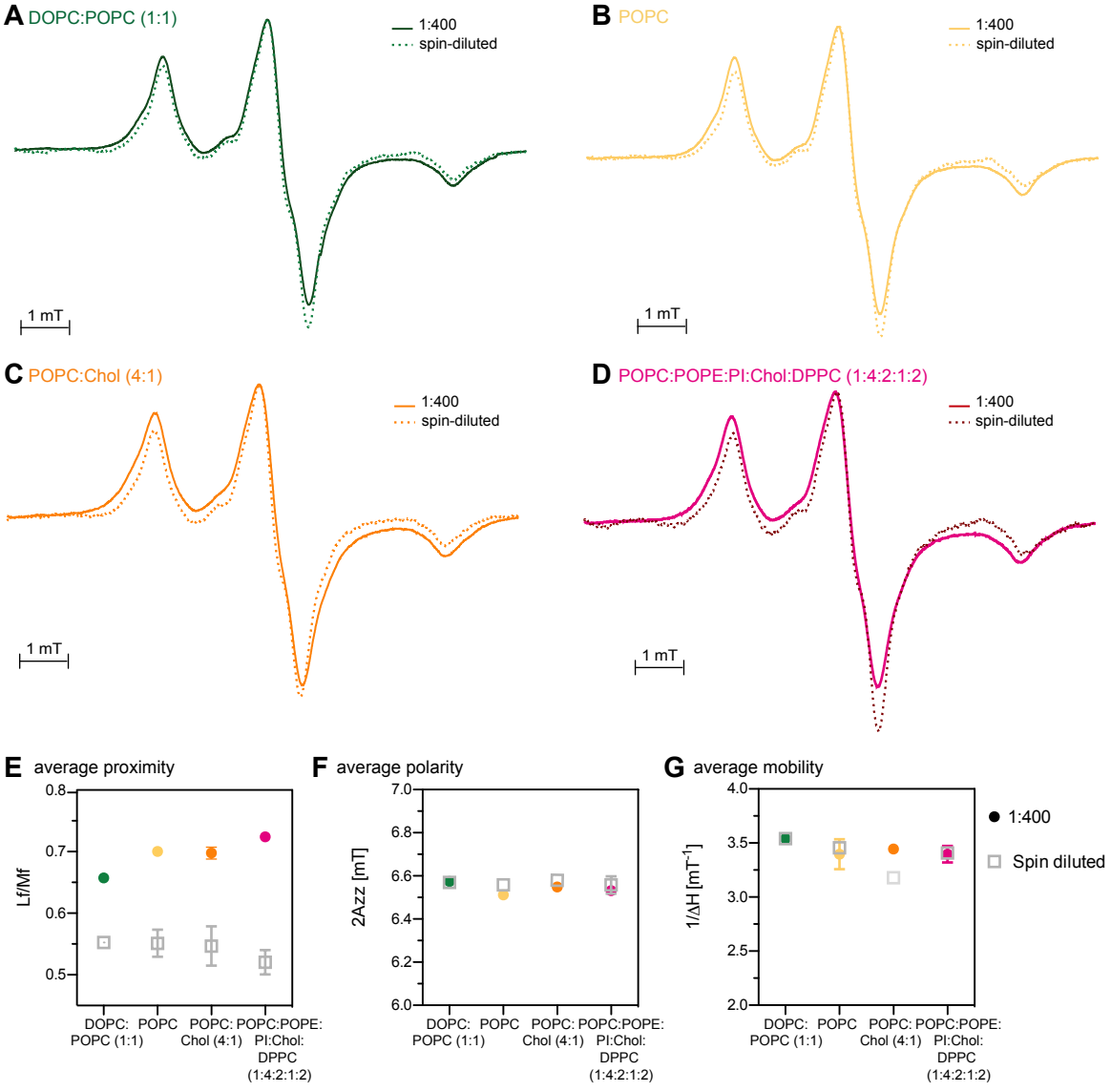

Figure 43: cwEPR spectra of $^{MBP}PERK_{AH\text{-}TMH}$ with spin-diluted controls.

(A), (B), (C) and (D) Intensity-normalized cwEPR spectra recorded at -115 of $^{MBP}PERK_{AH\text{-}TMH}$ reconstituted in the indicated lipid compositions. $^{MBP}PERK_{AH\text{-}TMH}$ was reconstituted in 1) 50% DOPC, 50% POPC, 2) 100% POPC, 3) 80% POPC, 20% Cholesterol 9) 10% POPC, 40% POPE, 20% DPPC, 20% Soy-PI, 10% Cholesterol. Spectra of spin-diluted samples, containing a 5-fold excess of unlabeled $^{MBP}PERK_{AH\text{-}TMH}$ were recorded as a control. (E) The semi-quantitative index Lf/Mf represents the average proximity of the spin-labels in the different lipid compositions. (F) The index 2 Azz represents the average polarity of the spin-labels in the different lipid compositions. (G) The line width of the middle field peak (ΔH_0) was extracted from spectra recorded at 30°C and represents the average mobility of the spin-labels in the different lipid compositions. (E), (F) and (G) The error bars represent the mean ± SEM of three independent experiments. Experiments of replicates 2 and 3 and the spin-diluted controls were performed by Iryna Stasiuk during her master thesis (Stasiuk, 2017).

6.3.4 The role of the AH in the oligomerization of $^{MBP}PERK_{AH-TMH}$

If the AH of PERK plays an analogous role to the AH of Ire1 from baker's yeast for the oligomerization of the UPR transducer, it should be possible to block the membrane-based oligomerization by disrupting the AH.

To test this hypothesis, a charged amino acid (arginine) was introduced on the hydrophobic side of the AH at the position L518 in the $^{MBP}PERK_{AH-TMH}$ construct. A spin-labeled variant of this $^{MBP}PERK_{AH-TMH}$ mutant was reconstituted in different lipid environments and characterized by cwEPR (Figure 44). Even though, the L518R variant should have a disruptive effect on the AH of $^{MBP}PERK_{AH-TMH}$, the cwEPR spectra recorded at -115°C broadened with the packing density of the lipid environment. Compared to the WT variant of $^{MBP}PERK_{AH-TMH}$, the broadening was even more pronounced (Figure 44A). The semi-quantitative index Lf/Mf further supports this impression (Figure 44C). Furthermore, the mutation L518R did not have a major effect on the nano-environment of the spin-probe, as the polarity was unperturbed (Figure 44A,D). However, the L518R did have an impact on the mobility of the spin-probe installed at C532 of $^{MBP}PERK_{AH-TMH}$. Spectra recorded at 30°C showed - irrespectively of the membrane environment - an increased mobility of the spin-label for the L518R mutant compared to WT variant of $^{MBP}PERK_{AH-TMH}$ (Figure 44B,E). Similar results were obtained for other $^{MBP}PERK_{AH-TMH}$ mutants that were constructed to disrupt the amphipathic character of the AH (L518D and W522R; data not shown). Thus, the introduction of charged residues on the non-polar face of the AH of PERK did not seem to disrupt the membrane-controlled oligomerization of $^{MBP}PERK_{AH-TMH}$. This could mean that 1) the introduced mutations do not drastically affect the folding of the AH and thereby the potential of PERK to react to increased lipid packing or 2) PERK uses a slightly distinct strategy to sense and react to lipid bilayer stress than Ire1 from baker's yeast.

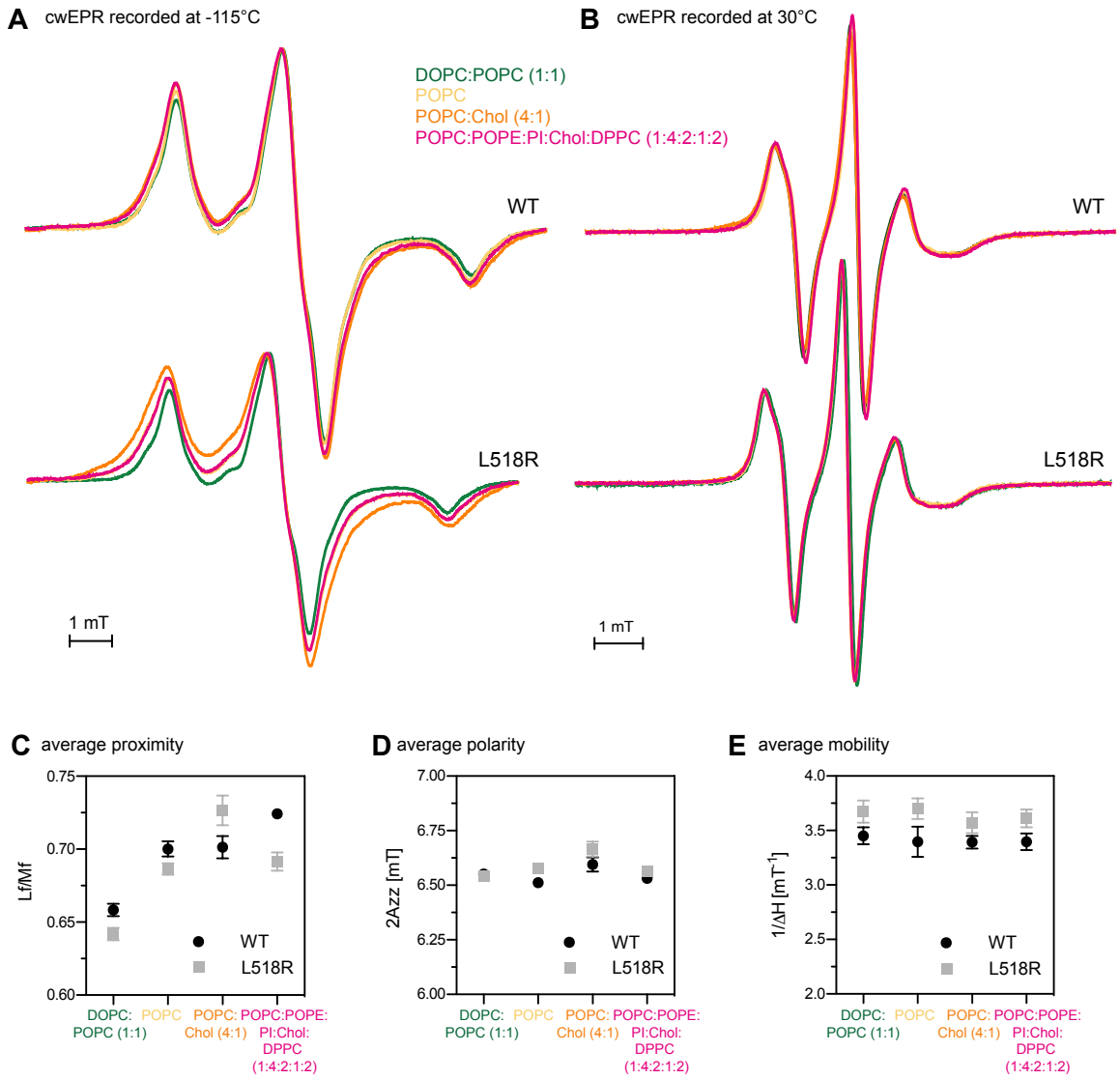

Figure 44: cwEPR spectra of $^{MBP}PERK_{AH\text{-}TMH}$ WT and of L518R variant.

(A) Intensity-normalized cwEPR spectra recorded at -115°C of $^{MBP}PERK_{AH\text{-}TMH}$ WT and L518R reconstituted in the indicated lipid compositions. (B) Intensity-normalized cwEPR spectra recorded at 30°C of $^{MBP}PERK_{AH\text{-}TMH}$ WT and L518R reconstituted in the indicated lipid compositions. (C) The semi-quantitative index Lf/Mf derived from spectra shown in (A) represents the average proximity of the spin-labels in the different mutants reconstituted in the indicated lipid compositions. (D) The index 2 Azz derived from spectra shown in (A) represents the average polarity of the spin-labels labels in the different mutants reconstituted in the indicated lipid compositions (E) The line width of the middle field peak (ΔH_0) was extracted from spectra recorded at 30°C and represents the average mobility of the spin-labels in the different lipid compositions. (C), (D) and (E) The error bars represent the mean ± SEM of three independent experiments. Experiments of replicates 2 and 3 of WT construct were performed by Iryna Stasiuk during her master thesis (Stasiuk, 2017).

As the introduction of a positively charged residue on the non-polar face of the AH did not disrupt the membrane-dependent oligomerization of $^{MBP}PERK_{AH\text{-}TMH}$, another set of mutants on the hydrophilic face of the AH was generated. Two negatively charged residues D514 and E525 were either substituted with positively charged lysines or with two polar, but uncharged residues (D514N, E525Q). These mutant variants of $^{MBP}PERK_{AH\text{-}TMH}$ were spin-labeled at the native cysteine C532 and subjected to cwEPR experiments.

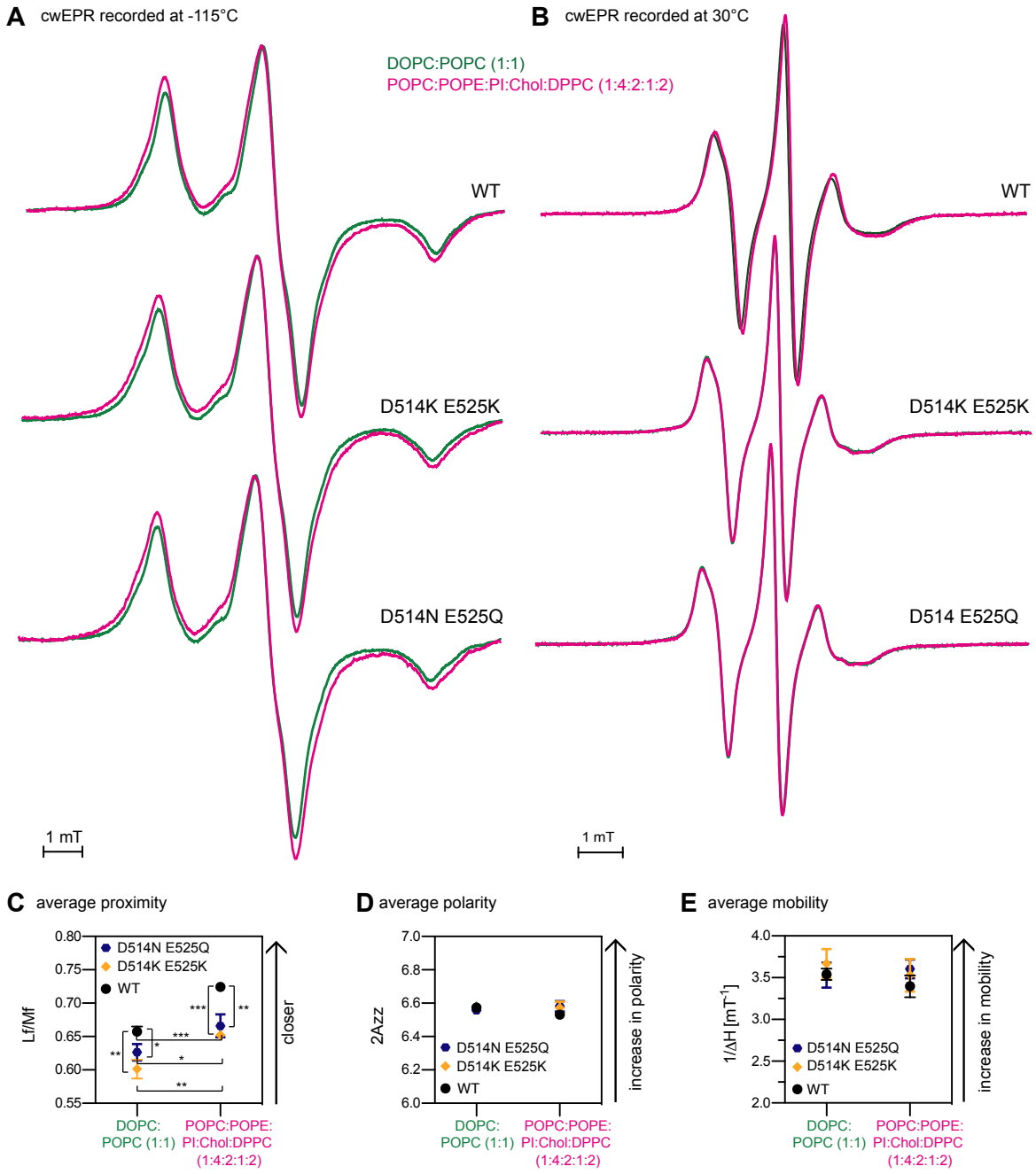

Figure 45: cwEPR spectra of $^{MBP}PERK_{AH\text{-}TMH}$ WT and variants with mutations in the polar face of the AH.

(A) Intensity-normalized cwEPR spectra recorded at -115°C of $^{MBP}PERK_{AH\text{-}TMH}$ WT and the AH mutants reconstituted in the indicated lipid compositions. (B) Intensity-normalized cwEPR spectra recorded at 30°C of $^{MBP}PERK_{AH\text{-}TMH}$ WT and the AH mutants reconstituted in the indicated lipid compositions. (C) The semi-quantitative index Lf/Mf derived from spectra shown in (A) represents the average proximity of the spin-labels in the different mutants reconstituted in the indicated lipid compositions. (D) The index 2 Azz derived from spectra shown in (A) represents the average polarity of the spin-labels labels in the different mutants reconstituted in the indicated lipid compositions (E) The line width of the middle field peak (ΔH_0) was extracted from spectra recorded at 30°C and represents the average mobility of the spin-labels in the different lipid compositions. (C), (D) and (E) The error bars represent the mean ± SEM of three independent experiments. Experiments of replicates 2 and 3 of WT construct were performed by Iryna Stasiuk during her master thesis (Stasiuk, 2017). Significance was tested by an unpaired students t-test. ***p<0.001, **p<0.01, *p<0.05.

The EPR experiments revealed that the spin-labeled double mutants of $^{MBP}PERK_{AH\text{-}TMH}$ (D514K/E525K or D514/E525Q) show slightly, but significantly reduced spectral broadening in tightly packed membrane environments compared to WT $^{MBP}PERK_{AH\text{-}TMH}$ (Figure 45A,C). This

lower spectral broadening of the double mutants can be interpreted as a reduced responsiveness to increased lipid packing (Figure 45C). The polarity as well as the mobility of the spin-label were not influenced by the double mutants in the polar face of the AH (Figure 45). Collectively, these experiments suggest that the polar face of the AH of PERK is involved in sensing lipid bilayer stress, possibly via specific interactions with the lipid headgroup region. This would further suggest that PERK might uses a related, yet distinct mechanism than Ire1 from baker's yeast for sensing lipid bilayer stress.

7 Discussion

7.1 Cysteine crosslinking to study the TMH architecture in Ire1 clusters

Single-pass membrane proteins such as Ire1 are structurally highly dynamic, which makes them challenging targets for structural biology. The problems arising from this dynamics are often circumvented by separately solving the structures of individual, soluble domains of these proteins (Hubert et al., 2010). However, the transmembrane regions of many such proteins such as receptor tyrosine kinases are crucial to transduce a signal across the membrane and often intimately involved in mounting signal-specific responses. To better understand the mechanism of signal transduction by the UPR transducer Ire1, it was studied in this thesis as a full-length protein in its native membrane context.

To this end, single-cysteine scanning and crosslinking of Ire1 from yeast was established to better understand the architecture of the transmembrane region in signaling-active clusters. Compared to other structural approaches, such as X-ray crystallography or NMR spectroscopy, the TMH was studied in its native membrane context and as a full-length protein. It is important to realize that the crosslinking approach established in this thesis allowed for a characterization of Ire1 in the environment of the complex and crowded ER, with a naturally complex composition of lipids and membrane proteins. With this approach the TMH architecture in conditions comparable to the ones in living cells was analyzed. To study the TMH architecture of Ire1 under most native conditions, this thesis uses a strategy for producing variants of Ire1 at the near-endogenous levels and with little variation in cellular levels across an individual culture (Halbleib et al., 2017). Working close to the endogenous level is crucial, as Ire1 has a only low copy number in cells of ~260 per cell (Ghaemmaghami et al., 2003) and it is activated by homo-oligomerization, which is – of course – concentration-dependent (Credle et al., 2005; Kimata et al., 2007; Korennykh et al., 2009). In the last years, a large number of studies investigated the cellular function of Ire1 by rescuing an *IRE1* knock-out with *IRE1* expressed from *CEN*-based 2µ plasmids and its endogenous promotor (van Anken et al., 2014; Aragón et al., 2009; Kimata et al., 2004, 2007; Oikawa et al., 2007; Promlek et al., 2011). It should be noted, that the expression from those plasmids results at least in a 2.5-fold increased expression compared to the knock-in construct (Halbleib et al., 2017). Such subtle, but significant overexpression results in an increased tendency for Ire1 activation, likely to constitutive activation of the UPR, and consequently, aberrant signaling. Two independent functional assays (ER-stress resistance assay and *HAC1* splicing analysis) confirmed that a cysteine-less variant of Ire1, which was produced in the course of this thesis, is functional, thereby providing a means to study the TMH architecture in signaling-active clusters of Ire1 (6.1.1). For the crosslinking of cysteine after microsome isolation, $CuSO_4$ was used to catalyze

the oxidation of sulfhydryl groups of cysteines in close proximity to disulfides (6.1.2). The reaction required only a 5 min incubation on ice, which lies well within the lifetime of individual, trackable Ire1 clusters (Belyy et al., 2020; Cohen et al., 2017; Kimata et al., 2007). To systematically scan through the TMH of Ire1 and to gain insights into its structural organization, 13 residues starting from E540 were individually mutated to cysteine. With this approach, the entire TMH of Ire1, which is unusually short compared to other ER membrane proteins, was analyzed. Each of the single-cysteine variants was tested for their functionality (6.1.3.1). Three variants, namely E540C, T541C and G542C, were identified to exhibit a functional defect as judged from an increased sensitivity of the respective cells to DTT. Notably, these mutations are close to the AH of Ire1 and may disrupt the normal membrane-sensitivity of Ire1 (Halbleib et al., 2017). In fact, it was previously observed that a negatively charge at position E540 is crucial for Ire1's full functionality (Halbleib, 2017). MD simulations performed by Dr. Roberto Covino from the Gerhard Hummer group showed that E540 is located near the phospholipid headgroup region within the water-lipid interface (Halbleib, 2017). It is possible that the negative charge of E540 is crucial for a charge repulsion of glycerophospholipids in this region. This could help to correctly place the TMH relative to the lipid bilayer and may contribute to the local membrane compression of the membrane, which is crucial for the sensitivity of Ire1 to the membrane environment.

7.2 The AH of Ire1 is crucial for the configuration of the TMH region and the sensing of lipid bilayer stress

The single-cysteine crosslinking of Ire1 revealed an X-shaped conformation of the TMH in Ire1 clusters irrespective of the nature of the underlying ER-stress. The crosslinking experiments showed that F544C crosslinked the best both during proteotoxic and lipid bilayer stress (Figure 23). This led to the conclusion that this residue is positioned at the crossing point of the two helices. A full, parallel orientation of two TMHs in dimers of Ire1 could be excluded as residues showing no crosslinking are located along the TMH on all sides. Furthermore, pattern of crosslinks observed for the TMH of Ire1 did not match a helical pattern with a periodicity of three to four. Together with the observations from MD simulations, which suggested an unusual, tilted conformation of Ire1's TMH region (Figure 28) (Halbleib et al., 2017), we proposed an X-shaped configuration of Ire1's TMH region in signaling-active clusters. This also provided important insights into the crucial role of the AH for Ire1's functionality. Disrupting the AH character resulted in an increased sensitivity of Ire1 to ER-stress, reduced cluster formation and a rearrangement of the TMH (Figure 25) (Halbleib et al., 2017). MD simulations of the dimeric TMH of Ire1 supported the data from systematic cysteine crosslinking and further highlighted an important role of membrane deformation for the oligomerization of Ire1. The AH

and charged residues at the cytosolic end of the TMH locally distort the bilayer, which is best evidenced by a decrease in membrane thickness. Such membrane deformations cause lipid acyl chain disordering and come at an energetic cost. Conditions of lipid bilayer stress, e.g. increased lipid saturation or perturbed PC-to-PE ratios, increase the energetic costs associated with this membrane deformation. By coalescing those membrane deformations upon oligomerization of Ire1, the energetic costs can be reduced. Therefore, membrane deformations can provide a driving force for the oligomerization of Ire1 in aberrant membrane environments.

The membrane-based activation of the UPR was also reported for sensors in higher eukaryotes (Cho et al., 2019; Hou et al., 2014; Volmer et al., 2013). A recent study suggested that the mammalian UPR sensor IRE1α uses a conformational switch in the TMH region, which relies on a tryptophan (W457) as a putative sensing residue and a conserved leucine zipper motif (SSxxLxx) involving serine 450 (Cho et al., 2019). Interestingly, such a mechanism of sensing was proposed for the lipid saturation sensor Mga2 from baker's yeast which controls the expression of the essential fatty acid desaturase Ole1 (Covino et al., 2016). However, it is clear from the data in this thesis that Ire1 from baker's yeast uses a mechanism distinct from the mammalian IRE1α based on the following evidences: 1) Mutagenesis of the entire TMH causes no functional defect unless the AH is disrupted (Figure 19) (Halbleib et al., 2017). 2) Mutagenesis of aromatic residues including F544 does not result in relevant functional defects (Figure 19). 3) The crosslinking data provide no evidence for a rotational re-organization of the TMHs during lipid bilayer stress (Figure 21, Figure 22 and Figure 23).

7.3 Different strategies to arrange TMHs in clusters of single-pass transmembrane proteins

Many receptor tyrosine kinases are known to form inactive dimers that can be activated by a ligand-induced conformational change (Brooks et al., 2014; Hubert et al., 2010). Crystal structures of domains of these receptors with unbound or bound ligand showed only minor conformational changes which do not explain the ligand-induced conformational change required for activation (Brooks et al., 2014). The structure of the full-length insulin receptor by cryo-EM revealed dramatic structural changes in the extracellular domain upon binding of insulin, which are likely to affect the TMH region (Gutmann et al., 2019). However, the TMH region was not clearly visible in this structural work. This is an important detail which is missing to better understand the structural organization within the membrane an its role in signal transduction.

Single-cysteine crosslinking is a common method to gain insights into the structural organization of TMH regions of single-spanning transmembrane signaling proteins. The self-association of the TMH of the thrombopoetin receptor was analyzed by single-cysteine crosslinking using Cu^{2+} phenantroline and identified a parallel dimer of the TMH: a helical crosslinking pattern was observed. (Matthews et al., 2011). Also, the TMH region of the human growth receptor JAK2 and its role in dimer formation was analyzed by single-cysteine crosslinking using Cu^{2+} phenantroline. Here, a parallel helix pair of the TMHs in the inactive dimer was inferred from crosslinking data, which showed a helical periodicity of crosslinks (Brooks et al., 2014). Based on a combination of MD simulations and experimental data, a switch to a left-handed crossover arrangement was proposed to occur upon a ligand-induced activation of the JAK2 receptor (Brooks et al., 2014). Thus, cysteine crosslinking in the TMH is a reliable method to study the TMH architecture of single-pass transmembrane proteins. Our crosslinking data showed that the TMH region of Ire1 does not randomly orientate in clusters of Ire1 and revealed a remarkably similar crosslinking pattern under different forms of ER-stress. The observed X-linked configuration of the TMHs is not unusual and a possible strategy to rearrange subdomains leading to an activation of a specific receptor, such as Ire1 or JAK2 (Brooks et al., 2014). Still, one has to consider the limitations of this method. Analysis of very dynamic interactions by cysteine crosslinking have to be carefully evaluated as the crosslink would reflect the average population of different states. These dynamic interactions can only be studied if the crosslink has not yet reached steady-state and still increases over time, which has to be tested. Otherwise, less abundantly visited structures may be overrepresented in the crosslinking analysis. Another weakness of this approach is that not all possible configurations, arising from piston-type movements of the TMHs for example, are equally detected by single-cysteine crosslinking. However, our additional controls using double-cysteine mutants helped to disfavor such scenario for the clusters of Ire1 (6.1.3.5).

7.4 TMH architecture in Ire1 cluster is independent of the form of ER-stress

TMH architecture of Ire1 was studied in the context of proteotoxic and lipid bilayer stress (6.1.3.2). This thesis provides a first, direct evidence that different forms of ER-stress converge in a single signaling-active configuration. As an extension to this finding, it is tempting to speculate that all forms of ER-stress may lead to the same activation of Ire1 despite other claims (Ho et al., 2019). If this is the case, differences of the signaling outcomes as recently phenomenologically described (Ho et al., 2019) would be mere a consequence from the crosstalk of UPR signaling with other signaling pathways rather than directly a consequence of distinct signaling by Ire1.

Interestingly, proteotoxic and lipid bilayer stress are typically analyzed after different durations of ER-stress. The stress from misfolded proteins as induced by DTT or TM is acute and peaks already after a relatively short time of ER-stress (30 min to 1 h) (Halbleib et al., 2017; Kimata et al., 2004, 2007; Oikawa et al., 2007; Promlek et al., 2011). In contrast, lipid bilayer stress has to build up over a longer time period (at least 3 h) (Halbleib et al., 2017; Promlek et al., 2011; Surma et al., 2013; Thibault et al., 2012). Consequently, lipid bilayer stress is a consequence of prolonged ER-stress condition, while proteotoxic stress is more acute. Lipid bilayer stress is induced in yeast either by depleting the medium of inositol more than 3 h or in the use of yeast deletion strains lacking a specific gene involved in lipid metabolism (Halbleib et al., 2017; Promlek et al., 2011; Surma et al., 2013; Thibault et al., 2012). This prolonged form of ER-stress is prone to cause indirect, secondary effects. Other signal transduction pathways may be perturbed due to the reorganization of the entire transcriptome (Ire1 regulates more than 5% of all genes in the genome). While such secondary effects are less likely to occur after short periods of ER-stress, they are expected to be more pronounced when ER-stress is maintained over prolonged periods of time. In the example of the chronic lipid bilayer stress condition caused by *OPI3* knock-out (Ho et al., 2019), it is quite likely that secondary effects from the chronic activation of the UPR are a major cause for the perturbed cellular transcriptome. A conformational change in the TMH region of Ire1 is not required to explain the observed changes in the cellular transcriptome caused selectively by conditions of lipid bilayer stress.

7.5 An *in vitro* system to study the interdependency of proteotoxic stress and lipid bilayer stress

The interdependence of protein and lipid homeostasis has previously been documented by systematic genetic experiments (Jonikas et al., 2009; Surma et al., 2013). The fact that UPR activation leads to increased lipid synthesis and the growth of the ER metabolism (Cox et al., 1993; Jonikas et al., 2009; Travers et al., 2000; Walter and Ron, 2011), highlights a role of the UPR in lipid metabolism. In the recent years, the membrane-based activation of the UPR sensors attracted significant attention. The sensing of aberrant ER membrane compositions, collectively referred to as lipid bilayer stress, was shown to rely on the TMH region of the UPR sensor and is independent of misfolded proteins (Halbleib et al., 2017; Promlek et al., 2011; Volmer et al., 2013). Most studies in this context have focused either on proteotoxic stress or lipid bilayer stress as independently processed signals. This thesis addresses the possibility that proteotoxic stress and lipid bilayer stress interdepend from each other via the oligomeric state of Ire1. Does lipid bilayer stress can modulate the binding of misfolded proteins to Ire1?

To address these questions, an *in vitro* binding assay was established that could quantify the binding of misfolded proteins to a membrane-reconstituted version of Ire1 (6.2.2). By reconstituting the sensor domain for misfolded proteins in defined lipid environments, it becomes possible to directly study the crosstalk between both different types of stress without any interference from other cellular pathways. Changing lipid environments *in vivo* relies in general on a genetic knock-out of genes involved in a specific lipid metabolic pathway. However, this specific effect is in most cases associated with changes throughout the entire lipid metabolic network thereby affecting the composition of cellular membranes and their membrane properties. Consequently, understanding the interdependency of lipid bilayer stress and misfolded proteins in regulating the UPR is virtually impossible by *in vivo* experiments.

The *in vitro* system established in this thesis uses $^{MBP}Ire1_{cLD\text{-}AH\text{-}TMH}$ with the core ER-luminal domain to sense unfolded proteins and the membrane-sensitive TMH region of Ire1. The binding of the misfolded model protein CPY* to this UPR sensor protein is systematically studied. $^{MBP}Ire1_{cLD\text{-}AH\text{-}TMH}$ construct reconstituted in densely packed liposomes binds only to the misfolded CPY* and therefore distinguishes between a correctly folded protein and a misfolded substrate (Figure 31). Increased binding of CPY* to $^{MBP}Ire1_{cLD\text{-}AH\text{-}TMH}$ is observed at increased lipid packing densities, which is particularly prominent in liposomes with an increased POPE content (Figure 33). It can be concluded that the membrane bears a strong modulatory potential on the UPR activation by controlling the propensity of Ire1 to bind misfolded proteins. A similar degree of modulation of background binding was observed for $^{MBP}Ire1_{AH\text{-}TMH}$, which lacks the entire core ER-luminal domain of Ire1 (Figure 34). This background binding was probably due to a weak interaction of CPY* with the MBP, as it could be reduced in the presence of maltotriose, a ligand of the MBP. These observations lead to the assumption that the AH and TMH of Ire1 are one key for the membrane-based modulation of misfolded protein binding. It would be interesting to know whether the AH-disruptive mutant F531R does also interfere with the binding of CPY* to MBP by modulating the oligomeric state. More experiments without the interference from a background binding of CPY* to the MBP should be performed to truly investigate the interdependency between proteotoxic and lipid bilayer stress in a clean and robust *in vitro* setup.

In the course of this thesis, several attempts have been made to remove the purification tag MBP (data not shown). However, several indications suggested a crucial role of the MBP in stabilizing the fused protein and suggested that it might aggregate in the absence of MBP. This is not entirely unexpected for such a protein that is activated through the formation of higher oligomers (van Anken et al., 2014; Kimata et al., 2007). In order to fully establish the here described interdependency between lipid bilayer stress and proteotoxic signals, it could help to use the core ER-luminal domain from UPR sensors in other organism such as a

thermotolerant or thermophilic yeast such as *Saccharomyces telluris* or *Candida slooffiae* (Arthur and Watson, 1976; Buzzini et al., 2018), which might exhibit a higher stability.

7.6 The interdependency of proteotoxic stress and lipid bilayer stress is based on oligomerization of Ire1

Having observed an interdependency of proteotoxic and lipid bilayer stress, the question arises how the membrane can modulate the binding of CPY* on the molecular level. Conditions that cause lipid bilayer stress, such as increased lipid saturation or an increased PE-to-PC ratio, might modulate the binding of misfolded proteins to Ire1 via avidity effects and an increased apparent affinity (Figure 34). In cwEPR experiments performed with the $^{MBP}Ire1_{AH\text{-}TMH}$, that lacks the core ER-luminal domain of Ire1 altogether, an environment-sensitive spectral broadening could be observed, which was indicative for an increased oligomerization in membranes containing increased levels of PE (Figure 38). Similarly, increased lipid packing resulted in increased oligomerization of the same minimal construct (Halbleib et al., 2017). It seems therefore likely that the membrane composition and its resulting properties control the oligomeric state of Ire1 and – consequently – the apparent affinity for unfolded/misfolded proteins such as CPY*. This leads to the model that Ire1 is inactive in its monomeric form in the “unstressed” ER membrane. Under this condition, Ire1 can only be activated by the accumulation of large numbers of unfolded proteins (Figure 46). This allows Ire1 to sense and react to misfolded proteins only above a certain threshold of protein misfolding in the lumen of the ER. Under conditions of lipid bilayer stress, however, Ire1 oligomerizes already independently of the presence of misfolded/unfolded proteins (as described in 2.3.2). This oligomerization increases the potential of Ire1 to bind misfolded proteins thereby sensitizing the UPR to unfolded proteins via avidity effects. Under conditions of lipid bilayer stress, the activation of Ire1 would have a lower threshold. The interdependency between proteotoxic and lipid bilayer stress in activating Ire1 is thus mediated by the oligomeric states of Ire1. To validate this model, it would be highly informative to follow the binding of misfolded proteins to Ire1 and its oligomerization in the membrane simultaneously for example by fluorescence-based methods.

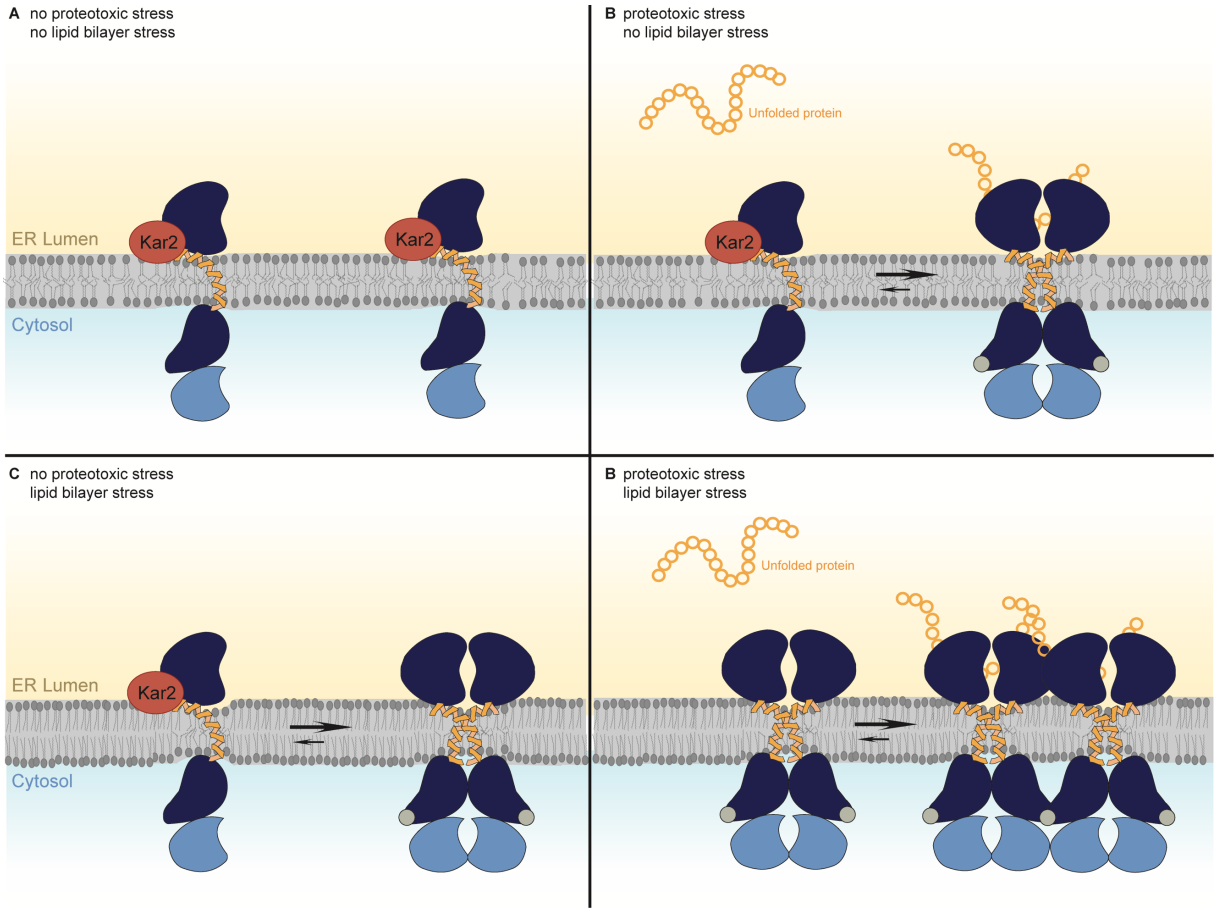

Figure 46: Current model of signal integration by the UPR.

(A) Oligomeric state of Ire1 with no ER-stress. Under non-stressed conditions, Ire1 is monomeric. The UPR is inactive. (B) Oligomeric state of Ire1 under proteotoxic stress. If misfolded proteins accumulated in the lumen of the ER, Ire1 is activated by oligomerization. The activation of Ire1 relies on accumulated misfolded proteins in the ER lumen with a specific concentration that is required for Ire1 activation. (C) Oligomeric state of Ire1 under lipid bilayer stress. Aberrant ER membrane composition activate the UPR through Ire1 oligomerization which requires a correctly folded AH. (D) Oligomeric state of Ire1 under proteotoxic and lipid bilayer stress. Ire1 is already oligomerized through the activation by lipid bilayer stress. The accumulation of misfolded proteins leads to a further oligomerization of Ire1 and interaction with misfolded proteins. The already activated oligomeric state thereby allows Ire1 to react to accumulated misfolded proteins at lower concentrations. The “stressed” ER membrane increases the affinity of Ire1 for misfolded proteins. The described interdependency between proteotoxic stress and lipid bilayer stress relies on the oligomerization of Ire1.

7.7 How human UPR sensors sense lipid bilayer stress

Given that the membrane-dependency of UPR transducers is conserved from yeast to man (Cho et al., 2019; Hou et al., 2014; Kono et al., 2017; Volmer et al., 2013), the question arises if they also employ a similar mechanism of sensing. In fact, it was shown that deletion mutants of the human IRE1α and PERK lacking their ER-luminal domains still respond to abnormally increased degrees of lipid saturation (Volmer et al., 2013). Bioinformatical analyses using Heliquest (Gautier et al., 2008) identified an AH adjacent to and overlapping with the TMH of IRE1α and PERK thereby suggesting a possible conservation of the membrane-based mechanism of activation (Figure 39) (Halbleib et al., 2017; Kono et al., 2017). In this thesis, the membrane-dependent activation of the human UPR sensor PERK was investigated. Using cwEPR and spin-labeled $^{MBP}PERK_{AH\text{-}TMH}$, a broadening of EPR spectra was observed when

$^{MBP}PERK_{AH-TMH}$ was reconstituted in liposomes featuring tight lipid packing (Figure 42). Control experiments with spin-diluted $^{MBP}PERK_{AH-TMH}$ confirmed that the observed spectral broadening is indeed due to an oligomerization of the minimal sensor construct (Figure 43). This observation is consistent with the findings for the yeast UPR sensor Ire1 (Halbleib et al., 2017). In yeast, however, the AH could be disrupted by charged residues introduced on the non-polar face of the AH (Halbleib et al., 2017). This does not seem to be the case for PERK (Figure 44). Charged residues in the apolar face of the AH of PERK did not disrupt the oligomerization of $^{MBP}PERK_{AH-TMH}$ in tightly packed membranes as identified by a spectral broadening of cwEPR (Figure 44). However, this thesis provides evidence that mutations in the polar face of the AH lead to a reduced spectral broadening, thereby suggesting an impaired responsiveness of this mutant to the membrane environment (Figure 45). This preliminary observation suggests that PERK compared to Ire1 from yeast uses a similar but not identical mechanism to sense lipid bilayer stress. It is intriguing to speculate that specific protein-lipid interactions between the polar lipid headgroups and the polar face of the AH may contribute to the membrane-based activation of PERK.

Preliminary MD simulations of the AH and TMH of the human UPR sensor PERK performed by Dr. Roberto Covino support this view. Here, a tilted configuration of the TMH region of PERK in the lipid bilayer similar to the one observed for Ire1 from baker's yeast was observed (Figure 47). The question if PERK uses the same or a similar sensing mechanism to sense lipid bilayer stress should be further addressed in the future. More extensive MD simulations in different membrane environments, cwEPR experiments validating the presence of an AH in the TMH region of PERK, as well as the identification of additional mutants that would disrupt the membrane-based oligomerization of PERK should help to uncover the mechanism of membrane responsiveness of this human UPR transducer. The membrane-based activation of the UPR provides a new perspective on the role of chronic UPR activation in diseases associated with ER-stress such as type II diabetes or NAFLD.

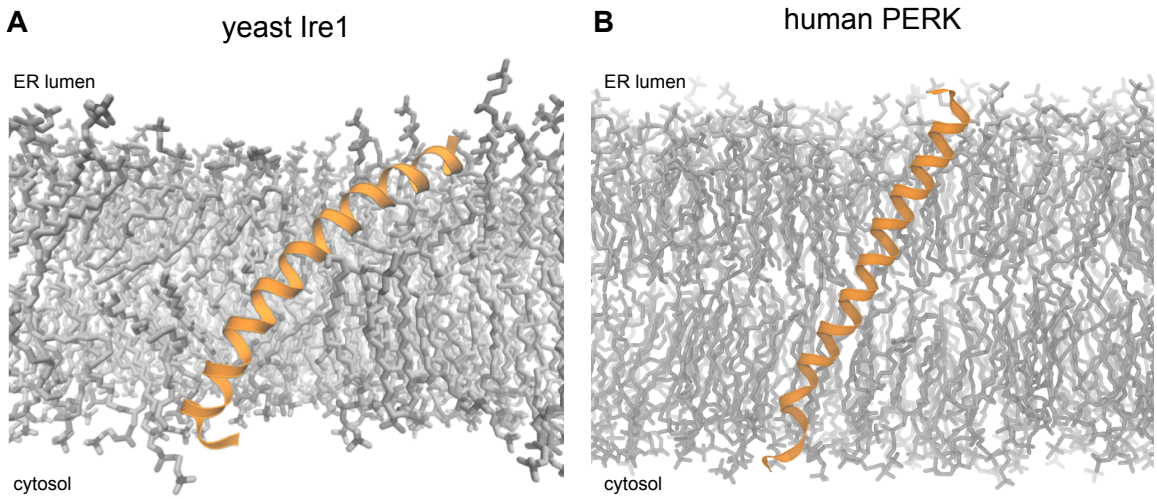

Figure 47: MD simulations of TMH of the yeast Ire1 and the human PERK.

(A) MD simulations of the AH and TMH of the yeast UPR sensor Ire1. (B) MD simulations of the AH and TMH of the human UPR sensor PERK in POPC. MD simulations were performed by Dr. Roberto Covino.

7.8 Conclusion and future perspectives

This work focused on the signal integration of the ER-stress sensors Ire1 and PERK. By performing systematic cysteine scanning and crosslinking of full-length Ire1 in its native environment, it was possible to establish the TMH architecture in Ire1 clusters. It could be shown that different forms of ER-stress converge in a single, signaling-active configuration in the TMH region. The identified X-shaped configuration of the TMHs in the signaling-active clusters of Ire1 reiterates the importance of the AH for the activation of Ire1. The AH plays a crucial role in the activation of Ire1 by lipid bilayer stress by stabilizing the oligomeric state of Ire1.

In the last decade, the membrane-based activation of UPR sensors was an interesting field of study. Here, the two types of stress (proteotoxic stress and lipid bilayer stress) were mostly regarded as independent signals contributing to UPR activation. This work, however, establishes a direct link between lipid bilayer stress and the activation of the UPR by misfolded proteins. The findings presented in this thesis therefore provide an important basis to explore the crosstalk between lipid bilayer stress and the activation of the UPR by unfolded proteins in greater detail.

The mechanism of the membrane-based activation of the UPR sensors is for the most part conserved from yeast to human. The membrane-based activation of PERK relies most probably on the polar face of the AH adjacent to the TMH of PERK. It would be interesting to learn if PERK senses directly specific lipid headgroups. The here established functional relevance of the AH of PERK provides a new angle of attack to better understand diseases

related to obesity such as type II diabetes. Still, further cwEPR experiments and a careful characterization of the *in cellulo* function of PERK are required to fully understand the role of PERK's AH in sensing lipid bilayer stress. The data produced in this thesis provide an important basis to explore the membrane-based activation of PERK in future experiments.

8 References

Adams, C.J., Kopp, M.C., Larburu, N., Nowak, P.R., and Ali, M.M.U. (2019). Structure and Molecular Mechanism of ER Stress Signaling by the Unfolded Protein Response Signal Activator IRE1. Front. Mol. Biosci. *6*, 11.

van Anken, E., Pincus, D., Coyle, S., Aragón, T., Osman, C., Lari, F., Gómez Puerta, S., Korennykh, A. V, and Walter, P. (2014). Specificity in endoplasmic reticulum-stress signaling in yeast entails a step-wise engagement of HAC1 mRNA to clusters of the stress sensor Ire1. Elife *3*, 1–17.

Antonny, B., Vanni, S., Shindou, H., and Ferreira, T. (2015). From zero to six double bonds: phospholipid unsaturation and organelle function. Trends Cell Biol. 1–10.

Aragón, T., van Anken, E., Pincus, D., Serafimova, I.M., Korennykh, A. V, Rubio, C. a, and Walter, P. (2009). Messenger RNA targeting to endoplasmic reticulum stress signalling sites. Nature *457*, 736–740.

Arthur, H., and Watson, K. (1976). Thermal Adaptation in Yeast: Growth Temperatures, Membrane Lipid, and Cytochrome Composition of Psychrophilic, Mesophilic, and Thermophilic Yeasts.

Ballweg, S., and Ernst, R. (2017). Control of membrane fluidity: The OLE pathway in focus. Biol. Chem. *398*.

Ballweg, S., Sezgin, E., Doktorova, M., Covino, R., Reinhard, J., Wunnicke, D., Hänelt, I., Levental, I., Hummer, G., and Ernst, R. (2020). Regulation of lipid saturation without sensing membrane fluidity. Nat. Commun. *11*, 756.

Belyy, V., Tran, N.-H., and Walter, P. (2020). Quantitative microscopy reveals dynamics and fate of clustered IRE1α. Proc. Natl. Acad. Sci. *117*, 1533–1542.

Bertolotti, A., Zhang, Y., Hendershot, L.M., Harding, H.P., and Ron, D. (2000). Dynamic interaction of BiP and ER stress transducers in the unfolded-protein response. Nat. Cell Biol. *2*, 326–332.

Bordignon, E., and Steinhoff, H.-J. (2007). Membrane Protein Structure and Dynamics Studied by Site-Directed Spin-Labeling ESR. In ESR Spectroscopy in Membrane Biophysics, (Boston, MA: Springer US), pp. 129–164.

Botstein, D., and Fink, G.R. (2011). Yeast: An experimental organism for 21st century biology. Genetics *189*, 695–704.

Brooks, A.J., Dai, W., O'Mara, M.L., Abankwa, D., Chhabra, Y., Pelekanos, R. a, Gardon, O., Tunny, K. a, Blucher, K.M., Morton, C.J., et al. (2014). Mechanism of activation of protein kinase JAK2 by the growth hormone receptor. Science *344*, 1249783.

Buzzini, P., Turchetti, B., and Yurkov, A. (2018). Extremophilic yeasts: the toughest yeasts around? Yeast *35*, 487–497.

Calfon, M., Zeng, H., Urano, F., Till, J.H., Hubbard, S.R., Harding, H.P., Clark, S.G., and Ron, D. (2002). IRE1 couples endoplasmic reticulum load to secretory capacity by processing the XBP-1 mRNA. Nature *415*, 92–96.

Chawla, A., Chakrabarti, S., Ghosh, G., and Niwa, M. (2011). Attenuation of yeast UPR is essential for survival and is mediated by IRE1 kinase. J. Cell Biol. *193*, 41–50.

Cho, H., Stanzione, F., Oak, A., Kim, G.H., Yerneni, S., Qi, L., Sum, A.K., and Chan, C. (2019). Intrinsic Structural Features of the Human IRE1α Transmembrane Domain Sense Membrane Lipid Saturation. Cell Rep. *27*, 307-320.e5.

Cohen, N., Breker, M., Bakunts, A., Pesek, K., Chas, A., Argemí, J., Orsi, A., Gal, L.,

Chuartzman, S., Wigelman, Y., et al. (2017). Iron affects Ire1 clustering propensity and the amplitude of endoplasmic reticulum stress signaling. J. Cell Sci. *130*, 3222–3233.

Contreras, F.X., Ernst, A.M., Haberkant, P., Björkholm, P., Lindahl, E., Gönen, B., Tischer, C., Elofsson, A., Von Heijne, G., Thiele, C., et al. (2012). Molecular recognition of a single sphingolipid species by a protein's transmembrane domain. Nature *481*, 525–529.

Cormack, B.P., Bertram, G., Egerton, M., Gow, N.A.R., Falkow, S., and Brown, A.J.P. (1997). Yeast-enhanced green fluorescent protein (yEGFP): a reporter of gene expression in Candida albicans. Microbiology *143*, 303–311.

Cornell, R.B. (2016). Membrane lipid compositional sensing by the inducible amphipathic helix of CCT. Biochim. Biophys. Acta - Mol. Cell Biol. Lipids *1861*, 847–861.

Costantini, L.M., Baloban, M., Markwardt, M.L., Rizzo, M., Guo, F., Verkhusha, V. V, and Snapp, E.L. (2015). A palette of fluorescent proteins optimized for diverse cellular environments. Nat. Commun. *6*, 7670.

Covino, R., Ballweg, S., Stordeur, C., Michaelis, J.B., Puth, K., Wernig, F., Bahrami, A., Ernst, A.M., Hummer, G., and Ernst, R. (2016). A Eukaryotic Sensor for Membrane Lipid Saturation. Mol. Cell 1–11.

Covino, R., Hummer, G., and Ernst, R. (2018). Integrated Functions of Membrane Property Sensors and a Hidden Side of the Unfolded Protein Response. Mol. Cell *71*, 458–467.

Cox, J.S., and Walter, P. (1996). A Novel Mechanism for Regulating Activity of a Transcription Factor That Controls the Unfolded Protein Response. Cell *87*, 391–404.

Cox, J.S., Shamu, C.E., and Walter, P. (1993). Transcriptional induction of genes encoding endoplasmic reticulum resident proteins requires a transmembrane protein kinase. Cell *73*, 1197–1206.

Credle, J.J., Finer-Moore, J.S., Papa, F.R., Stroud, R.M., and Walter, P. (2005). On the mechanism of sensing unfolded protein in the endoplasmic reticulum. Proc. Natl. Acad. Sci. U. S. A. *102*, 18773–18784.

Daleke, D.L. (2003). thematic review Regulation of transbilayer plasma membrane phospholipid asymmetry Supplementary key words flippase • floppase • scramblase • phosphatidylserine. J. Lipid Res. *44*, 233–242.

Diaz-Rohrer, B.B., Levental, K.R., Simons, K., and Levental, I. (2014). Membrane raft association is a determinant of plasma membrane localization. Proc. Natl. Acad. Sci. U. S. A. *111*, 8500–8505.

Ernst, R., Ejsing, C.S., and Antonny, B. (2016). Homeoviscous adaptation and the regulation of membrane lipids. J. Mol. Biol.

Ernst, R., Ballweg, S., and Levental, I. (2018). Cellular mechanisms of physicochemical membrane homeostasis. Curr. Opin. Cell Biol. *53*, 44–51.

Fagone, P., and Jackowski, S. (2009). Membrane phospholipid synthesis and endoplasmic reticulum function. J. Lipid Res. *50 Suppl*, S311–S316.

Falke, J., and Koshland, D. (1987). Global flexibility in a sensory receptor: a site-directed cross-linking approach. Science (80-.). *237*, 1596–1600.

Finger, A., Knop, M., and Wolf, D.H. (1993). Analysis of two mutated vacuolar proteins reveals a degradation pathway in the endoplasmic reticulum or a related compartment of yeast. Eur. J. Biochem. *218*, 565–574.

Frakes, A.E., and Dillin, A. (2017). The UPR ER : Sensor and Coordinator of Organismal Homeostasis. Mol. Cell *66*, 761–771.

Fu, S., Yang, L., Li, P., Hofmann, O., Dicker, L., Hide, W., Lin, X., Watkins, S.M., Ivanov, A.R., and Hotamisligil, G.S. (2011). Aberrant lipid metabolism disrupts calcium homeostasis causing

liver endoplasmic reticulum stress in obesity. Nature *473*, 528–531.

Gardner, B.M., and Walter, P. (2011). Unfolded Proteins Are Ire1-Activating Ligands That Directly Induce the Unfolded Protein Response. Science (80-.). *333*, 1891–1894.

Gautier, R., Douguet, D., Antonny, B., and Drin, G. (2008). HELIQUEST: A web server to screen sequences with specific ??-helical properties. Bioinformatics *24*, 2101–2102.

Ghaemmaghami, S., Huh, W.-K., Bower, K., Howson, R.W., Belle, A., Dephoure, N., O'Shea, E.K., and Weissman, J.S. (2003). Global analysis of protein expression in yeast. Nature *425*, 737–741.

Giménez-Andrés, M., Čopič, A., and Antonny, B. (2018). The Many Faces of Amphipathic Helices. Biomolecules *8*, 45.

Görlach, A., Klappa, P., and Kietzmann, D.T. (2006). The Endoplasmic Reticulum: Folding, Calcium Homeostasis, Signaling, and Redox Control. Antioxid. Redox Signal. *8*, 1391–1418.

Goyal, U., and Blackstone, C. (2013). Untangling the web: Mechanisms underlying ER network formation ☆.

Gutmann, T., Schäfer, I.B., Poojari, C., Brankatschk, B., Vattulainen, I., Strauss, M., and Coskun, U. (2019). Cryo-EM structure of the complete and ligand-saturated insulin receptor ectodomain.

Halbleib, K., Pesek, K., Covino, R., Hofbauer, H.F., Wunnicke, D., Hänelt, I., Hummer, G., and Ernst, R. (2017). Activation of the Unfolded Protein Response by Lipid Bilayer Stress. Mol. Cell *67*, 673-684.e8.

Han, S., Lone, M. a, Schneiter, R., and Chang, A. (2010). Orm1 and Orm2 are conserved endoplasmic reticulum membrane proteins regulating lipid homeostasis and protein quality control. Proc. Natl. Acad. Sci. U. S. A. *107*, 5851–5856.

Harding, H.P., Zhang, Y., and Ron, D. (1999). Protein translation and folding are coupled by an endoplasmic-reticulum-resident kinase. Nature *397*, 271–274.

Haze, K., Yoshida, H., Yanagi, H., Yura, T., and Mori, K. (1999). Mammalian Transcription Factor ATF6 Is Synthesized as a Transmembrane Protein and Activated by Proteolysis in Response to Endoplasmic Reticulum Stress. Mol. Biol. Cell *10*, 3787–3799.

Hetz, C. (2012). The unfolded protein response: controlling cell fate decisions under ER stress and beyond. Nat. Rev. Mol. Cell Biol. *13*, 89–102.

Hetz, C., and Papa, F.R. (2018). The Unfolded Protein Response and Cell Fate Control. Mol. Cell *69*, 169–181.

Ho, N., Wu, H., Xu, J., KOH, J.H., YAP, W.S., Goh, W.W. Bin, Chong, S.C., Taubert, S., and Thibault, G. (2019). ER stress sensor Ire1 deploys a divergent transcriptional program in response to lipid bilayer stress. BioRxiv Cell Biol. 1–20.

Hofbauer, H.F., Gecht, M., Fischer, S.C., Seybert, A., Frangakis, A.S., Stelzer, E.H.K., Covino, R., Hummer, G., and Ernst, R. (2018). The molecular recognition of phosphatidic acid by an amphipathic helix in Opi1. J. Cell Biol. *217*, 3109–3126.

Hollien, J., and Weissman, J.S. (2006). Decay of Endoplasmic Reticulum-Localized mRNAs During the Unfolded Protein Response. Science (80-.). *313*, 104–107.

Holthuis, J.C.M., and Levine, T.P. (2005). Lipid traffic: floppy drives and a superhighway. Nat. Rev. Mol. Cell Biol. *6*, 209–220.

Holthuis, J.C.M., and Menon, A.K. (2014). Lipid landscapes and pipelines in membrane homeostasis. Nature *510*, 48–57.

Hoppe, T., Matuschewski, K., Rape, M., Schlenker, S., Ulrich, H.D., and Jentsch, S. (2000). Activation of a membrane-bound transcription factor by regulated ubiquitin/proteasome-

dependent processing. Cell *102*, 577–586.

Hou, N.S., Gutschmidt, A., Choi, D.Y., Pather, K., Shi, X., Watts, J.L., Hoppe, T., and Taubert, S. (2014). Activation of the endoplasmic reticulum unfolded protein response by lipid disequilibrium without disturbed proteostasis in vivo. Proc. Natl. Acad. Sci. U. S. A. *111*, E2271-80.

Hubert, P., Sawma, P., Duneau, J.-P., Khao, J., Hénin, J., Bagnard, D., and Sturgis, J. (2010). Single-spanning transmembrane domains in cell growth and cell-cell interactions. Cell Adh. Migr. *4*, 313–324.

Inoue, H., Nojima, H., and Okayama, H. (1990). High efficiency transformation of Escherichia coli with plasmids. Gene *96*, 23–28.

Ito, H., Fukuda, Y., Murata, K., and Kimura, A. (1983). Transformation of intact yeast Saccharomyces cerevisiae cells treated with alkali cations. J. Bacteriol. *153*, 163–168.

Jonikas, M.C., Collins, S.R., Denic, V., Oh, E., Quan, E.M., Schmid, V., Weibezahn, J., Schwappach, B., Walter, P., Weissman, J.S., et al. (2009). Comprehensive characterization of genes required for protein folding in the endoplasmic reticulum. Science *323*, 1693–1697.

Kaiser, H.-J., Lingwood, D., Levental, I., Sampaio, J.L., Kalvodova, L., Rajendran, L., and Simons, K. (2009). Order of lipid phases in model and plasma membranes. Proc. Natl. Acad. Sci. *106*, 16645–16650.

Kapust, R.B., and Waugh, D.S. (1999). Escherichia coli maltose-binding protein is uncommonly effective at promoting the solubility of polypeptides to which it is fused. Protein Sci. *8*, 1668–1674.

Karagöz, G.E., Acosta-Alvear, D., Nguyen, H.T., Lee, C.P., Chu, F., and Walter, P. (2017). An unfolded protein-induced conformational switch activates mammalian IRE1. Elife *6*, 152–153.

Kimata, Y., and Kohno, K. (2011). Endoplasmic reticulum stress-sensing mechanisms in yeast and mammalian cells. Curr. Opin. Cell Biol. *23*, 135–142.

Kimata, Y., Kimata, Y.I., Shimizu, Y., Abe, H., Farcasanu, I.C., Takeuchi, M., Rose, M.D., and Kohno, K. (2003). Genetic Evidence for a Role of BiP / Kar2 That Regulates Ire1 in Response to Accumulation of Unfolded Proteins. Mol. Biol. Cell *14*, 2559–2569.

Kimata, Y., Oikawa, D., Shimizu, Y., Ishiwata-Kimata, Y., and Kohno, K. (2004). A role for BiP as an adjustor for the endoplasmic reticulum stress-sensing protein Ire1. J. Cell Biol. *167*, 445–456.

Kimata, Y., Ishiwata-Kimata, Y., Ito, T., Hirata, A., Suzuki, T., Oikawa, D., Takeuchi, M., and Kohno, K. (2007). Two regulatory steps of ER-stress sensor Ire1 involving its cluster formation and interaction with unfolded proteins. J. Cell Biol. *179*, 75–86.

Klose, C., Surma, M.A., and Simons, K. (2013). Organellar lipidomics--background and perspectives. Curr. Opin. Cell Biol. *25*, 406–413.

Kobashi, K. (1968). Catalytic oxidation of sulfhydryl groups by o-phenanthroline copper complex. Biochim. Biophys. Acta - Gen. Subj. *158*, 239–245.

Kono, N., Amin-Wetzel, N., and Ron, D. (2017). Generic membrane-spanning features endow IRE1α with responsiveness to membrane aberrancy. Mol. Biol. Cell *28*, 2318–2332.

Korennykh, A., and Walter, P. (2012). Structural Basis of the Unfolded Protein Response. Annu. Rev. Cell Dev. Biol. *28*, 251–277.

Korennykh, A. V, Egea, P.F., Korostelev, A. a, Finer-Moore, J., Zhang, C., Shokat, K.M., Stroud, R.M., and Walter, P. (2009). The unfolded protein response signals through high-order assembly of Ire1. Nature *457*, 687–693.

Krahmer, N., Guo, Y., Wilfling, F., Hilger, M., Lingrell, S., Heger, K., Newman, H.W., Schmidt-Supprian, M., Vance, D.E., Mann, M., et al. (2011). Phosphatidylcholine Synthesis for Lipid

Droplet Expansion Is Mediated by Localized Activation of CTP:Phosphocholine Cytidylyltransferase. Cell Metab. *14*, 504–515.

De Kroon, A.I.P.M., Rijken, P.J., and De Smet, C.H. (2013). Checks and balances in membrane phospholipid class and acyl chain homeostasis, the yeast perspective. Prog. Lipid Res. *52*, 374–394.

Lee, K.P.K.K., Dey, M., Neculai, D., Cao, C., Dever, T.E., and Sicheri, F. (2008). Structure of the Dual Enzyme Ire1 Reveals the Basis for Catalysis and Regulation in Nonconventional RNA Splicing. Cell *132*, 89–100.

Li, H., Korennykh, A. V, Behrman, S.L., and Walter, P. (2010). Mammalian endoplasmic reticulum stress sensor IRE1 signals by dynamic clustering. Proc. Natl. Acad. Sci. *107*, 16113–16118.

Lin, J.H., Li, H., Zhang, Y., Ron, D., and Walter, P. (2009). Divergent Effects of PERK and IRE1 Signaling on Cell Viability. PLoS One *4*, e4170.

Lingwood, D., and Simons, K. (2010). Lipid Rafts As a Membrane-Organizing Principle. Science (80-.). *327*, 46–50.

Lorent, J.H., Diaz-Rohrer, B., Lin, X., Spring, K., Gorfe, A.A., Levental, K.R., and Levental, I. (2017). Structural determinants and functional consequences of protein affinity for membrane rafts. Nat. Commun. *8*, 1–10.

Mathuranyanon, R., Tsukamoto, T., Takeuchi, A., Ishiwata-Kimata, Y., Tsuchiya, Y., Kohno, K., and Kimata, Y. (2015). Tight regulation of the unfolded protein sensor Ire1 by its intramolecularly antagonizing subdomain. J. Cell Sci. *128*, 1762–1772.

Matthews, E.E., Thévenin, D., Rogers, J.M., Gotow, L., Lira, P.D., Reiter, L.A., Brissette, W.H., and Engelman, D.M. (2011). Thrombopoietin receptor activation: Transmembrane helix dimerization, rotation, and allosteric modulation. FASEB J. *25*, 2234–2244.

McIntosh, P.R., and Freedman, R.B. (1980). Characteristics of a copper-dependent cross-linking reaction between two forms of cytochrome P-450 in rabbit-liver microsomal membranes. Biochem. J. *187*, 227–237.

van Meer, G., Voelker, D.R., and Feigenson, G.W. (2008). Membrane lipids: where they are and how they behave. Nat. Rev. Mol. Cell Biol. *9*, 112–124.

Mori, K. (2009). Signalling Pathways in the Unfolded Protein Response: Development from Yeast to Mammals. J. Biochem. *146*, 743–750.

Mori, K., Ma, W., Gething, M.-J., and Sambrook, J. (1993). A transmembrane protein with a cdc2+CDC28-related kinase activity is required for signaling from the ER to the nucleus. Cell *74*, 743–756.

Nicolson, G.L. (1976). Transmembrane control of the receptors on normal and tumor cells. I. Cytoplasmic influence over cell surface components. BBA - Rev. Biomembr. *457*, 57–108.

Nicolson, G.L. (2014). The Fluid - Mosaic Model of Membrane Structure: Still relevant to understanding the structure, function and dynamics of biological membranes after more than 40 years. Biochim. Biophys. Acta - Biomembr. *1838*, 1451–1466.

Nielsen, J. (2019). Yeast Systems Biology: Model Organism and Cell Factory. Biotechnol. J. *1800421*, 1800421.

Oikawa, D., Kimata, Y., and Kohno, K. (2007). Self-association and BiP dissociation are not sufficient for activation of the ER stress sensor Ire1. J. Cell Sci. *120*, 1681–1688.

Okada, T., Haze, K., Nadanaka, S., Yoshida, H., Seidah, N.G., Hirano, Y., Sato, R., Negishi, M., and Mori, K. (2003). A Serine Protease Inhibitor Prevents Endoplasmic Reticulum Stress-induced Cleavage but Not Transport of the Membrane-bound Transcription Factor ATF6. J. Biol. Chem. *278*, 31024–31032.

Pietzsch, J. (2004). Mind the membrane. Nature *Horizon Sy*, 1–4.

Pineau, L., Colas, J., Dupont, S., Beney, L., Fleurat-Lessard, P., Berjeaud, J.M., Bergès, T., and Ferreira, T. (2009). Lipid-induced ER stress: Synergistic effects of sterols and saturated fatty acids. Traffic *10*, 673–690.

Plumb, R., Zhang, Z.-R., Appathurai, S., and Mariappan, M. (2015). A functional link between the co-translational protein translocation pathway and the UPR. Elife *4*, e07426.

Prischi, F., Nowak, P.R., Carrara, M., and Ali, M.M.U. (2014). Phosphoregulation of Ire1 RNase splicing activity. Nat. Commun. *5*, 3554.

Promlek, T., Ishiwata-Kimata, Y., Shido, M., Sakuramoto, M., Kohno, K., and Kimata, Y. (2011). Membrane aberrancy and unfolded proteins activate the endoplasmic reticulum stress sensor Ire1 in different ways. Mol. Biol. Cell *22*, 3520–3532.

Puth, K., Hofbauer, H.F., Sáenz, J.P., and Ernst, R. (2015). Homeostatic control of biological membranes by dedicated lipid and membrane packing sensors. Biol. Chem. *396*.

Quiocho, F.A., Spurlino, J.C., and Rodseth, L.E. (1997). Extensive features of tight oligosaccharide binding revealed in high-resolution structures of the maltodextrin transport/chemosensory receptor. Structure *5*, 997–1015.

Radanović, T., Reinhard, J., Ballweg, S., Pesek, K., and Ernst, R. (2018). An Emerging Group of Membrane Property Sensors Controls the Physical State of Organellar Membranes to Maintain Their Identity. BioEssays *40*, 1–9.

Rubio, C., Pincus, D., Korennykh, A., Schuck, S., El-Samad, H., and Walter, P. (2011). Homeostatic adaptation to endoplasmic reticulum stress depends on Ire1 kinase activity. J. Cell Biol. *193*, 171–184.

Santos, A.X.S., and Riezman, H. (2012). Yeast as a model system for studying lipid homeostasis and function. FEBS Lett. *586*, 2858–2867.

Schwarz, D.S., and Blower, M.D. (2016). The endoplasmic reticulum: structure, function and response to cellular signaling. Cell. Mol. Life Sci. *73*, 79–94.

Sharpe, H.J., Stevens, T.J., and Munro, S. (2010). A Comprehensive Comparison of Transmembrane Domains Reveals Organelle-Specific Properties. Cell *142*, 158–169.

Sheff, M.A., and Thorn, K.S. (2004). Optimized cassettes for fluorescent protein tagging in Saccharomyces cerevisiae. Yeast *21*, 661–670.

Sidrauski, C., and Walter, P. (1997). The transmembrane kinase Ire1p is a site-specific endonuclease that initiates mRNA splicing in the unfolded protein response. Cell *90*, 1031–1039.

Sidrauski, C., Cox, J.S., and Walter, P. (1996). tRNA Ligase Is Required for Regulated mRNA Splicing in the Unfolded Protein Response.

Singer, S.J., and Nicolson, G.L. (1972). The fluid mosaic model of the structure of cell membranes. Science *175*, 720–731.

Stein, A., Ruggiano, A., Carvalho, P., and Rapoport, T.A. (2014). Key Steps in ERAD of Luminal ER Proteins Reconstituted with Purified Components. Cell *158*, 1375–1388.

Surma, M. a., Klose, C., Peng, D., Shales, M., Mrejen, C., Stefanko, A., Braberg, H., Gordon, D., Vorkel, D., Ejsing, C., et al. (2013). A lipid E-MAP identifies Ubx2 as a critical regulator of lipid saturation and lipid bilayer stress. Mol. Cell *51*, 519–530.

Thibault, G., Shui, G., Kim, W., McAlister, G.C., Ismail, N., Gygi, S.P., Wenk, M.R., and Ng, D.T.W. (2012). The Membrane Stress Response Buffers Lethal Effects of Lipid Disequilibrium by Reprogramming the Protein Homeostasis Network. Mol. Cell *48*, 16–27.

Tirasophon, W., Welihinda, A.A., and Kaufman, R.J. (1998). A stress response pathway from

the endoplasmic reticulum to the nucleus requires a novel bifunctional protein kinase/endoribonuclease (Ire1p) in mammalian cells. Genes Dev. *12*, 1812–1824.

Travers, K.J., Patil, C.K., Wodicka, L., Lockhart, D.J., Weissman, J.S., and Walter, P. (2000). Functional and Genomic Analyses Reveal an Essential Coordination between the Unfolded Protein Response and ER-Associated Degradation. Cell *101*, 249–258.

Voeltz, G.K., Rolls, M.M., and Rapoport, T. a. (2002). Structural organization of the endoplasmic reticulum. EMBO Rep. *3*, 944–950.

Volmer, R., and Ron, D. (2014). Lipid-dependent regulation of the unfolded protein response. Curr. Opin. Cell Biol. *33C*, 67–73.

Volmer, R., van der Ploeg, K., and Ron, D. (2013). Membrane lipid saturation activates endoplasmic reticulum unfolded protein response transducers through their transmembrane domains. Proc. Natl. Acad. Sci. U. S. A. *110*, 4628–4633.

Walter, P., and Ron, D. (2011). The Unfolded Protein Response: From Stress Pathway to Homeostatic Regulation. Science (80-.). *334*, 1081–1086.

Wenzel, M., Vischer, N., Strahl, H., and Hamoen, L. (2018). Assessing Membrane Fluidity and Visualizing Fluid Membrane Domains in Bacteria Using Fluorescent Membrane Dyes. Bio-Protocol *8*.

Westrate, L.M., Lee, J.E., Prinz, W.A., and Voeltz, G.K. (2015). Form Follows Function: The Importance of Endoplasmic Reticulum Shape.

Wiseman, R.L., Zhang, Y., Lee, K.P.K., Harding, H.P., Haynes, C.M., Price, J., Sicheri, F., and Ron, D. (2010). Flavonol Activation Defines an Unanticipated Ligand-Binding Site in the Kinase-RNase Domain of IRE1. Mol. Cell *38*, 291–304.

Ye, J., Rawson, R.B., Komuro, R., Chen, X., Davé, U.P., Prywes, R., Brown, M.S., and Goldstein, J.L. (2000). ER stress induces cleavage of membrane-bound ATF6 by the same proteases that process SREBPs. Mol. Cell *6*, 1355–1364.

Bachelor Thesis, Master Thesis, Diploma Thesis and PhD Thesis:

Bruckert, J. (2016). Reinigung und vergleichende Charakterisierung des Trans-membranhelices von IRE1 and PERK. Bachelor Thesis, Frankfurt University.

Halbleib, K. (2017). Activation of the unfolded protein response sensor Ire1 by lipid bilayer stress. PhD Thesis, Frankfurt University.

Michaelis, J. (2015). Reconstitution of single-pass transmembrane domains of lipid sensing proteins. Diploma Thesis, Frankfurt University.

Stasiuk, I. (2017). Purification and characterization of a set of putative mammalian sensors for membrane properties. Master Thesis, Frankfurt University.

Wolf, S. (2016). Etablierung eines *in-vitro*-Systems zur Charakterisierung des UPR-Sensors Ire1p aus *Saccharomyces cerevisiae*, Bachelor Thesis, Frankfurt University.

9 Supplementary Information

An excess of DTT and heat reduces cysteine crosslinked dimers of Ire1.

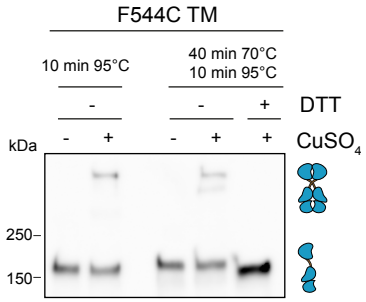

Figure S 1: Cysteine crosslink can be reduced by an excess of DTT and heat.

Cysteine crosslinking in microsomes of the TM stressed cells expressing F544C. Stationary cells were used to inoculate a culture in SCD complete to an OD_{600} of 0.2 and cultivated to an OD_{600} of 0.7. Cells were treated with 1.5 µg/ml TM for 1 h. 80 OD_{600} equivalents were harvested and used for microsomal membrane preparation by differential centrifugation. Microsomes were incubated for 5 min with 10 mM $CuSO_4$ on ice and the crosslinking reaction was stopped by a mix of EDTA, NEM and MSB. One half of the samples were directly analyzed by SDS-PAGE with a previous denaturation step at 95°C and a subsequent immunoblotting using anti-HA antibodies. The other half was incubated with 100 mM DTT, heated up for 40 min at 70°C and then heated up at 95°C for the analysis by SDS-PAGE and a subsequent immunoblotting using anti-HA antibodies.

Purification and size-exclusion chromatography of CPY*.

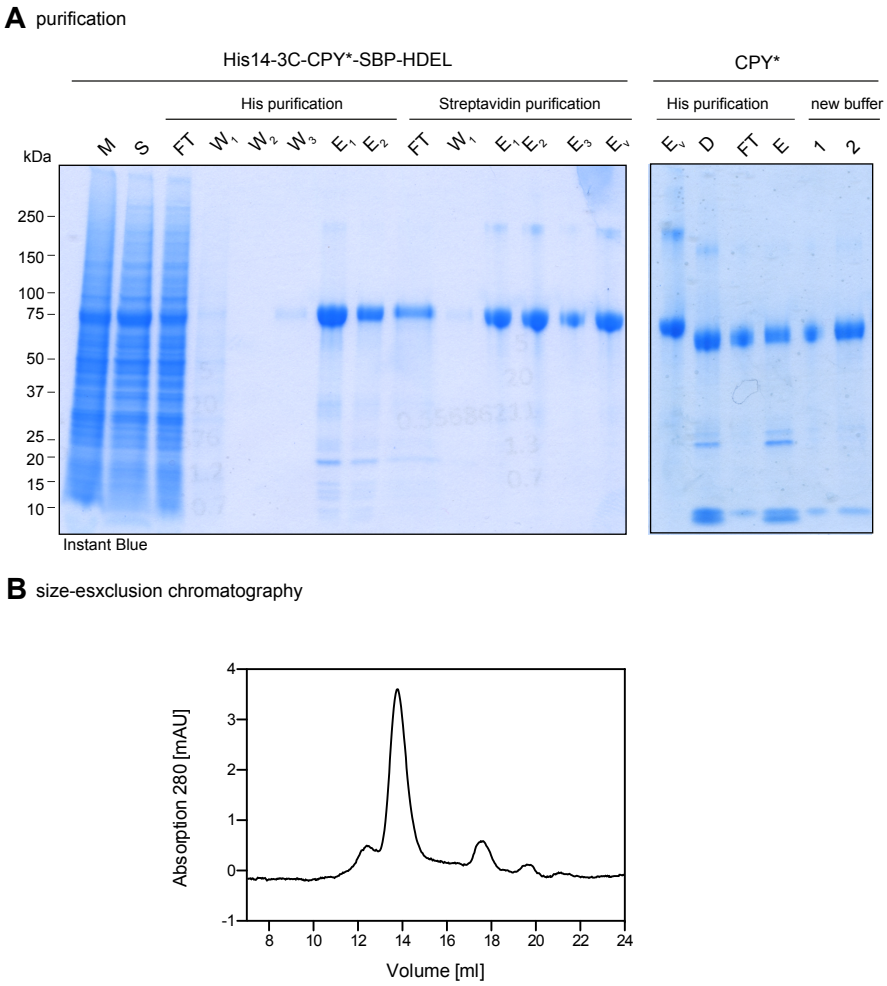

Figure S 2: Purification of CPY*.

(A) Affinity purification of His14-3C-CPY*-SBP-HDEL from *S. cerevisiae*. The purification by Ni-NTA and Streptavidin was monitored by subjecting samples of membrane fraction (M), supernatant (S), flow-through (FT), washing steps (W) and eluate (E). The purification tags were removed by an overnight incubation with TEV and 3C proteases. To remove the proteases, an additional Ni-NTA purification step was performed. CPY* without purification tags was found in the FT. Finally, CPY* was adjusted to new buffer composition using PD10 desalting columns. (C) SEC analysis of purified CPY*. 100 µl of CPY* (0.7 mg/ml) were analyzed on a Superdex 100/300 Column.

Eidesstattliche Erklärung

Ich erkläre hiermit, dass ich mich bisher keiner Doktorprüfung im Mathematisch-Naturwissenschaftlichen Bereich unterzogen habe.

Frankfurt, den .....

(Kristina Väth)

Ich erkläre hiermit an Eides Statt, dass ich die vorliegende Dissertation mit dem Titel

„ Signal integration by the ER-stress sensors Ire1 and PERK”

selbständig angefertigt habe und mich keiner anderen Hilfsmittel bedient habe als der in ihr angegebenen. Insbesondere versichere ich, dass alle Entlehnungen aus anderen Schriften mit Angabe der betreffenden Schrift gekennzeichnet sind.

Ich versichere, die Grundsätze der guten wissenschaftlichen Praxis beachtet, und nicht die Hilfe einer kommerziellen Promotionsvermittlung in Anspruch genommen zu haben.

Frankfurt, den .....

(Kristina Väth)